Experimental and Numerical Modelling of the Flexural Behaviour of Ultra High Performance Fibre Reinforced Concrete (UHPFRC) beams

Kenneth Odero Awinda

The thesis is submitted in partial fulfilment of the requirements for the award of the degree of Doctor of Philosophy of the University of Portsmouth.

January 2018

School of Civil Engineering and Surveying

Abstract

Ultra high performance fibre reinforced concrete is a relatively new material developed by taking advantage of advances in concrete technology and material science to enhance its microstructure. Short, discrete fibres with a high aspect ratio (50-100) substantially improve its ductility. The material's overall performance is therefore superior to other types of reinforced and fibre reinforced concretes with respect to strength, ductility and durability. However, despite its enormous potential, adoption of the material is still relatively low. This is attributed not only to its higher cost but also to a lack of enough experimental data and widely accepted design standards. While some effort is being made to develop numerical models for UHPFRC, many are based on multiscale frameworks requiring the measurement of microscale parameters. Such parameters are difficult to measure whereas for most practical purposes design normally requires material properties measured at the macroscale.

The overall aim of this research therefore is to propose a numerical damage model for UHPFRC that uses material properties from standard tests and that can simulate the flexural behaviour of UHPFRC and predict its failure loads. Initial modelling enabled identification of suitable approaches for estimating the elastic modulus, tensile strength and fracture energy values appropriate for simulating the material's flexural behaviour. A comprehensive experimental investigation undertaken established the existence of size effect on the flexural stress at the end of linearity and flexural strength of notched and un-notched specimens with 2%, 4% and 6% fibre content. The tests also identified the significant effect of fibre content on the elastic modulus, tensile strength and fracture energy values. Therefore the effect of fibre content was incorporated into the proposed damage model by making these three material properties a function of it. This is done by incorporating values of estimated material properties into a bilinear traction separation law thereby also linking the damage to fibre content. The multiple fibre content effects represented include the spacing and number of fibres per unit cross-sectional area. The model adopts a smeared crack approach. It is implemented as a user defined material model in ABAQUS finite element software and written in FORTRAN code. The model's ability to simulate the load deflection response was validated using two case studies. The model's predictions match test data reasonably well for specimens of different sizes, test arrangement and fibre contents. Therefore a validated numerical material model incorporating fibre content is proposed as a simple, practical and economical tool for predicting the material's flexural behaviour thereby achieving the overall aim of the study. This is one of the main contributions of this study. Another contribution is the establishment of size effects on the flexural properties of UHPFRC at 2%, 4% and 6% fibre contents. Finally values of material properties at these fibre contents estimated from

test data and comparisons between the different modelling approaches are a valuable resource for similar studies in future.

Dissemination

1. Effect of fibre content and specimen size on flexural properties of ultra high performance fibre reinforced concrete (UHPFRC)

Harkin, L., Dr Stephanie Barnett, Mr Kenneth Awinda, Kelner, C., Rodriguez, J. & Dr Jiye Chen

10 May 2016

BEFIB 2016: 9th RILEM International Symposium on Fiber Reinforced Concrete. RILEM

2. Investigating geometrical size effect on the flexural strength of the ultra high performance fibre reinforced concrete using the cohesive crack model

Mr Kenneth Awinda, Dr Jiye Chen & Dr Stephanie Barnett

15 Feb 2016

Construction and Building Materials. 105, p. 123–131

3. Modelling behaviour of ultra high performance fibre reinforced concrete

Mr Kenneth Awinda, Dr Jiye Chen, Dr Stephanie Barnett & Dr Dominic Fox

Nov 2014

Advances in Applied Ceramics. 113, 8, p. 502-508

Declaration

Whilst registered as a candidate for the above degree, I have not been registered for any other research award. The results and conclusions embodied in this thesis are the work of the named candidate and have not been submitted for any other academic award.

Word count: 50711

Acknowledgements

First I would like to thank my lead supervisor Dr Jiye Chen for his guidance and support throughout the course of this work. He introduced me to FEA analysis and offered invaluable advice on developing my knowledge and skill in modelling in general. I gained a lot by drawing on his technical knowledge and intuitive understanding of numerical modelling. He kindly offered me information and material that has been used and acknowledged in this study. I am grateful to him for leaving his door open for me to see him whenever I needed to throughout this journey and for the many discussions we had about this work. His feedback on all aspects of this study has been very useful and is much appreciated.

I also owe a debt of gratitude to my second supervisor, Dr Stephanie Barnett, who introduced me to UHPFRC, gave me the idea for this study and offered me a lot of information to start me off. She was very generous in providing me with the data used in the initial modelling and was on hand to provide feedback and support. I also acknowledge her immense help with the preparatory work required for all the laboratory tests. We had many discussions from which I learnt a lot. I thank her also for her feedback on the drafts of this report.

It is with deep sadness that I acknowledge Dr Dominic Fox, my third supervisor and Head of School, who has just passed on a few days before the submission of this work. His help with this work cannot be quantified. His support and encouragement throughout this study was immense. As my line manager, he always sought opportunities to support me in arranging any training I needed and in finding ways of reducing my workload to help me find time to conduct this study. Even when he was unwell, he still sought to provide his help in reading and commenting on my draft reports. I salute Dr Fox, an inspirational leader and great person from whom I learnt a lot.

I would like to acknowledge the help of the following people who I worked with in carrying out the laboratory tests: Lab technicians Trevor Leggett, Gary Etienne and Andrew Brookes. Also thanks to former exchange student Clement Kelner, and former MSc students Liam Harkin and Jorge Rodriguez.

Special thanks must go to my family for their huge sacrifice and patience as I committed time to this study and away from them. To my wife Jackie, children Abigail, Joshua and Caleb, I thank you. Daddy has finally finished the ‘book’.

Finally, and above all, I thank God our Father, our Lord Jesus Christ and His Spirit of grace for sustaining and helping me to complete this work.

Dedication

In honour of my parents, the late Lawrence Gordon Awinda and the late Dorcas Tabitha Awinda.

Table of Contents

Abstract i
Dissemination ii
Declaration iii
Acknowledgements iv
Dedication v
List of Tables x
List of figures xi
Abbreviations xv
Chapter 1 Introduction 1
1.1 Background 1
1.2 Aim & Objectives 4
1.2.1 Initial simulation studies 4
1.2.2 Experiment tests 4
1.2.3 Model development 4
1.3 Research questions 5
1.4 Contributions 5
1.5 Thesis Layout 6
Chapter 2 – Ultra High Performance Fibre Reinforced Concrete (UHPFRC) 8
2.1 Introduction 8
2.2 Constituents of UHPFRC 9
2.2.1 Cement 9
2.2.2 Super-plasticisers 11
2.2.3 Aggregates 12
2.2.4 Silica fume 12
2.2.5 Fibres 13
2.3 UHPFRC stages of deformation 14
2.3.1 Phase I - Linear elastic behaviour 14
2.3.2 Phase II - Strain hardening 16
2.3.3 Phase III - Tension softening 16
2.4 Factors affecting fibre efficiency 17
2.4.1 Effect of fibre length 18
2.4.2 Effect of fibre orientation 20
2.4.3 Effect of fibre content 22
2.5 Mechanical properties of UHPFRC 24
2.5.1 Tensile strength 24

2.5.2 Compressive strength 25
2.5.3 Flexural strength 25
2.5.4 Fracture Energy 28
2.6 Size effect 29
2.6.1 Sources of size effect 29
2.6.2 Quantification of fracture mechanics size effects 30
2.6.3 The size effect equation 31
2.6.4 Size effect in UHPFRC 33
Chapter 3 – Concrete Fracture Models 35
3.1 Introduction 35
3.2 Fracture zone models 35
3.2.1 Cohesive Crack Models 38
3.2.2 Crack Band Models 44
3.2.3 Damage Models 47
3.3 Implementation Concrete models in FEM 50
3.3.1 Cohesive crack model (CCM) 50
3.4 Numerical simulations of UHPFRC behaviour 53
3.5 Initial simulation study 59
3.5.1 Introduction 59
3.5.2 Data Description 59
3.5.3 Estimating material properties 600
a) Elastic Modulus 611
b) Tensile strength 63
c) Fracture Energy 644
3.5.4 Test geometry and model inputs 67
3.5.5 Initial simulation using the Cohesive Crack Model (CCM) 67
3.5.6 Initial simulation using the Concrete Smeared Cracking Model (CSM) 76
3.5.7 Initial simulation using the Concrete Damaged Plasticity Model (CDP) 78
3.5.8 Comparison of CCM, CSM and CDP 82
Chapter 4 – Experimental Investigations 85
4.1 Introduction 85
4.2 Mixing and Casting procedures 85
4.2.1 Mix proportions 85
4.2.2 Specimen sizes 86
4.2.3 Mixing and casting 88
4.3 Testing 90

4.3.1 Overview 90
4.3.2 Notched Three Point Bending (TPB) test 90
4.3.3 Un-notched Three Point Bending (TPB) and Four Point Bending (FPB) test....91
4.3.4 Compression Test....93
4.4 Summary of Results 94
4.4.1 Notched TPB test results....94
4.4.2 Un-notched TPB test results 111
4.4.3 Four Point Bend (FPB) test results 123
4.4.5 Discussion....130
4.5 Size effect analysis 135
4.5.1 Size effect on flexural stress at end of linearity....136
4.5.3 Implications of size effect on estimating tensile strength from flexural tests 145
4.5.4 Size effect on fracture energy....146
4.6 Effect of Fibre content 153
4.6.1 Effect on flexural stress at end of linearity and flexural strength 153
4.6.2 Effect on fracture energy....155
4.6.3 Effect on compressive strength 155
4.6.4 Concluding remarks on the effect of fibre content 157
Chapter 5 – UHPFRC Model Development 159
5.1 Introduction 159
5.2 Key features of the UHPFRC damage model incorporating fibre content (UDMF) 159
5.3 Summary of material property values 160
5.3.1 Elastic modulus 161
5.3.2 Tensile strength 161
5.3.3 Fracture energy....161
5.4 Fibre content....161
5.5 Model formulation....164
5.5.1 Linear elastic behaviour 164
5.5.2 Damage modelling 166
5.5.3 Damage initiation....166
5.5.4 Damage evolution....166
5.6 Implementation of model in ABAQUS 168
5.7 Model verification....176
5.7.1 Problem description....176
5.7.2 Modelling techniques 176
5.7.3 Results....178

5.7.4 Sensitivity analysis 180
5.7.5 Further verification 183
5.8 Model validation 189
5.8.1 CASE STUDY 1 189
5.8.2 CASE STUDY 2 199
Chapter 6 – Conclusions 204
6.1 Overview 204
6.2 Initial modelling 204
6.3 Experimental investigations 204
6.4 UHPFRC damage model incorporating fibre content (UDMF). 206
6.5 Contributions 207
6.6 Recommendations for future work 208
References 210
Appendices 216
1-10 Selected test data
11 Derivation of the damage scale
12 Example of an input file

List of Tables

Chapter 3

Table 3.1: UHPFRC Mixture Proportions 59
Table 3.2: Summary of material properties estimated from test data compared with data from literature 66
Table 3.3: Modelling parameters.....67

Chapter 4

Table 4.1: UHPFRC mix proportions.....86
Table 4.2: Specimen sizes 87
Table 4.3: Three Point Bending test displacement rates 92
Table 4.4: Notched three point bending test load @ end of linearity.....97
Table 4.5: Notched Three Point bending test peak loads.....100
Table 4.6: Average hardening 102
Table 4.7: Post peak flexural toughness 105
Table 4.8: Notched Three Point Bending test average post peak slope 107
Table 4.9: Un-notched three point bending test Load at the end of linearity.....112
Table 4.10: Un-notched three point bending test Peak Loads 113
Table 4.11: Un-notched three point bending test hardening (%).....118
Table 4.12: Un-notched three point bending average slope 118
Table 4.13: Un-notched four point bending test load at the end of linearity 125
Table 4.14: Un-notched four point bending test Peak Load.....126
Table 4.15: Un-notched four point bending test hardening.....127
Table 4.16: Un-notched four point bending test average slope.....128
Table 4.17: Flexural stresses considered 135
Table 4.18: Notched three point bending test flexural stress @ end of linearity 138
Table 4.19: Un-notched three point bending test flexural stress @ end of linearity.....140
Table 4.20: Un-notched three point bending test flexural strength.....142
Table 4.21: Notched three point bending test flexural strength 143
Table 4.22: Average tensile strength values 146
Table 4.23: Fracture energy from notched three point bending tests 149
Table 4.24: Fracture energy values adjusted for weight of the specimen 151
Table 4.25: Compressive strengths.....157

Chapter 5

Table 5.1: Summary of average material property values.....161
Table 5.2: Comparison of model and test average leak load and toughness.....180
Table 5.3: Mesh sensitivity on peak load and flexural toughness 181
Table 5.4: Input values for parametric study.....182
Table 5.5: Some simulation parameters.....184
Table 5.6: No. of elements.....184
Table 5.7: Model predictions of peak load and flexural toughness compared to test.....185
Table 5.8: UHPFRC mix proportions 189
Table 5.9: Some simulation parameters.....191
Table 5.10: Number of elements 191
Table 5.11: Model predictions of peak load and flexural toughness compared to test data.....194
Table 5.12: Input parameters for cohesive modelling compared to CDP's 195

Table 5.13: UHPFRC mix proportions.....199
Table 5.14: Some simulation parameters.....200
Table 5.15: : Model prediction of peak load and flexural toughness compared to test 202

List of figures

Chapter 1

Figure 1.1: UHPFRC in relation to other types of concrete 1
Figure 1.2: Comparison of flexural properties of UHPFRC with conventional FRC and high strength concrete 2

Chapter 2

Figure 2.1: The effect of silica fume in filling voids 12
Figure 2.2: Typical tensile curve for UHPFRC 14
Figure 2.3: Schematic description of a fibre embedded in a matrix, and the deformation and stress fields around it.....15
Figure 2.4: Representation of the 'pinching effect' and interfacial shear stress distribution between fibres in suppressing crack propagation in a matrix 15
Figure 2.5: Idealized representation of an advancing crack in a fibre reinforced cement 16
Figure 2.6: Stress distribution in a fibre and concrete matrix under uniaxial tension 17
Figure 2.7: Relationship between fibre length and transferred stress 19
Figure 2.8: The intersection of an oriented fibre with a crack. 21
Figure 2.9: 3D image of steel fibres 21
Figure 2.10: Examples of tensile constitutive law for UHPFRC 23
Figure 2.11: Schematic description of strain softening, strain hardening and deflection hardening in FRC composites 24
Figure 2.12: Comparison of tensile and flexural behaviour of ideally elastic and ideally elastic 26
Figure 2.13: Correlation between composite flexural strength and matrix strength.....27
Figure 2.14: Variation of flexural strength with fibre volume content 28
Figure 2.15: Illustration of size effect by geometrically similar notched specimens.....31
Figure 2.16: Size effect schematic based on the crack band approach 33
Figure 2.17: Size effect on strength on a bi-logarithmic plot 33
Figure 3.1: Scales for modelling concrete 35
Figure 3.2: Model classification 37

Chapter 3

Figure 3.3: Modes of strain localisation 37
Figure 3.4: a) Cohesive crack model b) Crack band model 38
Figure 3.5: A simple direct tensile test in which crack is replaced by a slit of width w across which stress can still be transferred 38
Figure 3.6: a) The σ-ε curve outside fracture zone b) The σ-ω curve within the fracture zone 40
Figure 3.7: Some physical sources of cohesive crack 41
Figure 3.8: Notched beam in TPB test 43
Figure 3.9: Comparison of σ-ω curves for UHPFRC with other types of concrete.....44

Figure 3.10: correspondence between softening curve of the cohesive crack model and the stress-strain curve of the crack band model 46
Figure 3.11: Inter-element discrete crack element 50
Figure 3.12: Inter-element smeared crack element 51
Figure 3.13: Intra-element crack....51
Figure 3.14: Specimen under tensile stress 52
Figure 3.15: Schematic representation of the RSBM 56
Figure 3.16: Traction-separation constitutive law for the fibre-matrix interface 57
Figure 3.17 : The two-scale analytical-numerical homogenisation approach for UHPFRC. 58
Figure 3.18: Four point bending test arrangement 60
Figure 3.19: Three point bending test arrangement 60
Figure 3.20: Stress-strain relations for cement paste, aggregate and concrete 62
Figure 3.21: Typical stress-strain curve for concrete 63
Figure 3.22: Load-deflection curve for un-notched FPB test specimen with 2% fibre content....64
Figure 3.23: Test geometry 67
Figure 3.24: Simplified traction-separation curve 68
Figure 3.25: Typical damaged response....70
Figure 3.26: Cracked specimens from TPB test 71
Figure 3.27: Deformed shape with stress state of failed specimen....72
Figure 3.28: Final deformed shape with contour of STATUS 72
Figure 3.29: Load deflection curves for 100x100x350 specimen 73
Figure 3.30: Load-deflection curves for different tensile strengths 74
Figure 3.31: Variation of peak load with tensile strength 74
Figure 3.32: Variation of post-peak slope with tensile strength 74
Figure 3.33: Load-deflection curves for different fracture energies 75
Figure 3.34: Effect of fracture energy on Peak Load 75
Figure 3.35: Variation of post-peak slope with fracture energy....75
Figure 3.36: Fracture energy cracking model 77
Figure 3.37 : Deformed shape with stress state. 78
Figure 3.38: Model prediction of Load-deflection curve compared to test curve 78
Figure 3.39: Response of concrete to uniaxial loading in tension (ABAQUS, 2013) 79
Figure 3.40: Post-failure stress-fracture energy curve (ABAQUS, 2013). 80
Figure 3.41: Deformed shape with stress state of failed specimen....81
Figure 3.42: CDP Model prediction compared to test data 81
Figure 3.43: Comparison of load-deflection curves....83

Chapter 4

Figure 4.1: Sequence of mixing and casting specimens....89
Figure 4.2: Three point bending test with notched specimen....92
Figure 4.3: Three point bending test configuration....92
Figure 4.4: a) Un-notched TPB test b) Un-notched FPB test c) Compression test....93
Figure 4.5: Average load deflection curves for all fibre contents....95
Figure 4.6: Notched TPB test average load @ end of linearity against specimen depth 98
Figure 4.7: Notched three point bending test average Peak load against specimen depth....101
Figure 4.8: Peak Load against Load @ end of linearity 102
Figure 4.9: Notched Three Point bending test average hardening....103
Figure 4.10: Post peak response analysis 104

Figure 4.11: Notched Three Point Bending test average toughness against specimen depth 106
Figure 4.12: Notched Three Point Bending test average toughness against fibre content 107
Figure 4.13: Notched Three Point Bending test average slope against specimen depth 108
Figure 4.14: Notched Three Point Bending test average slope against fibre content 109
Figure 4.15: Notched TPB test failed specimen showing main crack (2S1 B1-B5) 110
Figure 4.16: Load deflection curves for Un-notched TPB specimens (2% fibre content) 114
Figure 4.17: Load deflection curves for Un-notched TPB specimens (4% fibre content) 115
Figure 4.18: Load deflection curves for Un-notched TPB specimens 6% fibre content 116
Figure 4.19: Un-notched TPB test average load @ end of linearity against specimen depth 117
Figure 4.20: Un-notched three point bending test average peak load against specimen depth ...119
Figure 4.21 : Un-notched three point bending test average hardening 120
Figure 4.22: Un-notched three point bending test average slope against specimen depth 121
Figure 4.23: Un-notched three point bending test average slope against fibre content 122
Figure 4.24: Un-notched three point bending test failed specimens (4%) 123
Figure 4.25: Un-notched Four Point Bending test Load-deflection curves 124
Figure 4.26: Un-notched FPB test load at the end of linearity against fibre content 125
Figure 4.27: Un-notched four point bending test peak load against fibre content 126
Figure 4.28: Un-notched four point bending test average hardening 127
Figure 4.29: Un-notched four point bending test average slope against fibre content 128
Figure 4.30: Un-notched four point bending test failed specimens (2%) 129
Figure 4.31: Effect of gravitational bias and pour sequence on fibre distribution 132
Figure 4.32 : Failure pattern for beam 4S10B1 133
Figure 4.33: Notched three point bending test S3 specimens from batch 4 134
Figure 4.34: Notched TPB bi-logarithmic plot of flexural stress against Depth 137
Figure 4.35: Un-notched TPB bi-logarithmic plot of flexural stress against depth 139
Figure 4.36: Un-notched TPB test average flexural strength against specimen depth 141
Figure 4.37: Bi-logarithmic plot of flexural strength against depth 144
Figure 4.38: Notched TPB test fracture energy against specimen depth 148
Figure 4.39: Two ways of compensating for energy supplied by weight of beam 149
Figure 4.40: Graphical illustration of effect of weight compensation on load deflection curve ...150
Figure 4.41: Notched TPB test Fracture energy (weight adjusted) with specimen depth 152
Figure 4.42: Notched TPB test flexural strength against fibre content for each specimen size 154
Figure 4.43: Average fracture energy against fibre content 155
Figure 4.44: Compression test specimens after test 156
Figure 4.45: Compressive strength against fibre content 156

Chapter 5

Figure 5.1: Traction separation curve incorporating fibre content 160
Figure 5.2: Fibre content effect on material properties 163
Figure 5.3: Defining the damaged response 167
Figure 5.4: overview of ABAQUS solution process 170
Figure 5.5: Overview of UDMF process 172
Figure 5.6: UDMF process in updating Jacobian 173
Figure 5.7: Load arrangement geometry 176
Figure 5.8: Un-deformed mesh 176
Figure 5.9: Deformed shape with stress state 178
Figure 5.10 : Testing of specimen 4S4B4 to failure 178

Figure 5.11: Comparison of model and test load-deflection curve for 100x100x350 specimen....179
Figure 5.12: Mesh sensitivity study cases....180
Figure 5.13: Mesh sensitivity study....181
Figure 5.14: Effect of convergence aids....181
Figure 5.15: Variation in elastic modulus....182
Figure 5.16: Variation in tensile strength....183
Figure 5.17: Variation in fracture energy....183
Figure 5.18: Load and support geometry....184
Figure 5.19: Model prediction for 100mm deep specimens with 2%, 4% and 6% fibre content....186
Figure 5.20: Model prediction for 150mm deep specimens with 2%, 4% and 6% fibre content....187
Figure 5.21: Comparison of model prediction for a) 2% b) 4% and c) 6% fibre content....188
Figure 5.22: Load and support arrangement....190
Figure 5.23: Traction separation curve from tensile test....190
Figure 5.24: Load and support arrangement....191
Figure 5.25: Typical un-deformed mesh diagram....191
Figure 5.26: Typical deformed shape with stress state....192
Figure 5.27: Model prediction compared to test and CDP....193
Figure 5.28: Peak load against specimen size....195
Figure 5.29: Toughness against specimen size....195
Figure 5.30: Traction separation response of UDMF compared to CDP....196
Figure 5.31: Comparison of predictions by different models with test....197
Figure 5.32: Comparing stress at peak load between UDMF and CDP....198
Figure 5.33: Four point bending test arrangement....199
Figure 5.34: Load and support arrangement....200
Figure 5.35: Typical un-deformed mesh diagram....200
Figure 5.36: Typical deformed mesh with stress state....201
Figure 5.37: UDMF predictions compared to test for different fibre contents (fc)....202
Figure 5.38: Model prediction of fibre content effect on flexural strength compared to test....203

Abbreviations

AFGC	Association Francaise De Genie Civil
BK	Benzeggah-Kenane
CCM	Cohesive crack model
CDP	Concrete damaged plasticity
CE	Cohesive elements
CIE	Cohesive interface elements
CMOD	Crack mouth opening displacement
COH2D4	Two dimensional four node cohesive element
CPE4I	Four node plane strain incompatibility element
CRC	Compact reinforced composites
CSH	Calcium silicate hydrate
CSM	Concrete smeared cracking model
CPU	Central processing unit
FCM	Fictitious crack model
FE	Finite elements
FEA	Finite element analysis
FEM	Finite element method
FPB	Four point bending
FRC	Fibre reinforced concrete
GGBFS	Ground granulated blast furnace slag
HPFRC	High performance fibre reinforced concrete
ITZ	Interfacial transition zone
JSCE	Japanese Society of Civil Engineers
LEFM	Linear elastic fracture mechanics
LVDT	Linear variable differential transformer
NFM	Non-linear fracture mechanics
NR	Newton-Raphson
PFA	Pulverised fuel ash
RPC	Reactive powder concrete
TPB	Three point bending
UDMF	UHPFRC damage model incorporating fibre content
UHPC	Ultra high performance concrete

UHPFRC	Ultra high performance fibre reinforced concrete
UMAT	User defined material model
μXCT	Micro X-ray computed tomography

Chapter 1 Introduction

1.1 Background

Concrete-based materials have many important applications within building and civil engineering construction. However, their brittleness makes crack formation and growth critical to their mechanical behaviour and has in many cases limited the way in which they can be used. Ultra high performance fibre reinforced concrete (UHPFRC) is a material consisting of a cementitious matrix reinforced by steel fibres designed in such a way as to achieve higher strength and ductility compared to other types of concrete (Fig.1.1). These properties have been developed by taking advantage of advances in concrete technology and material science. Typically, it has compressive strengths of 150-200MPa (AFGC-SETRA, 2013). The direct tensile strength of UHPFRC is also typically greater than 7MPa. However, its name makes reference to ultra high 'performance' because in addition to strength it has both superior ductility due to the fibres and durability due to its enhanced microstructure. The high fibre/matrix bond strength arising out of the enhanced microstructure of UHPFRC makes possible the incorporation of relatively high dosages (≥2%) of short fibres with high aspect ratios.

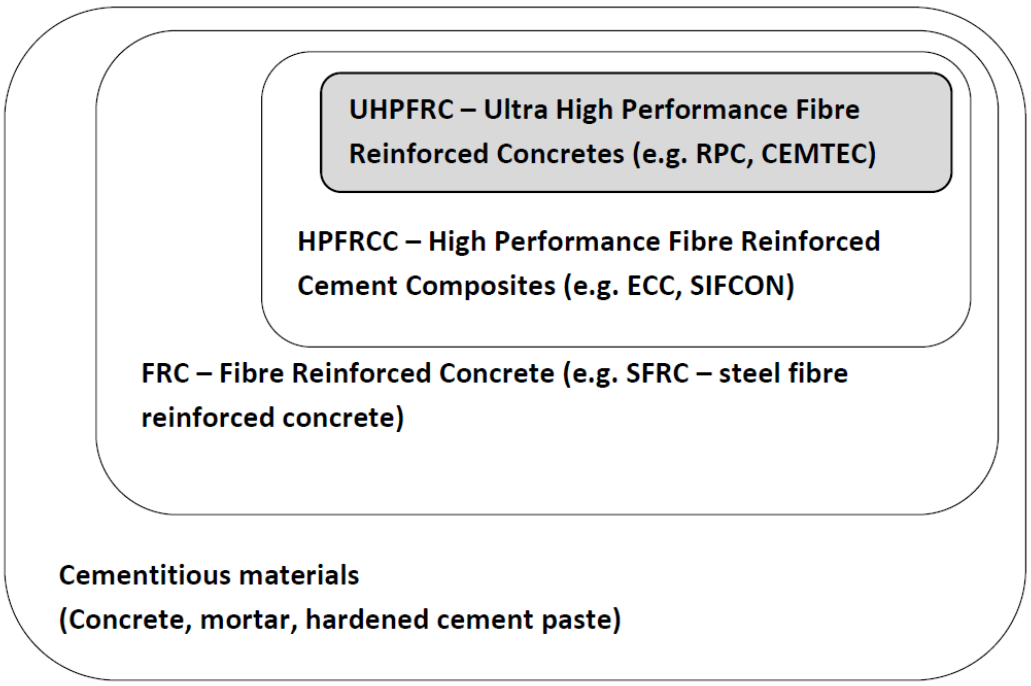

Figure 1.1: UHPFRC in relation to other types of concrete (Habel, 2004)

The above factors combine to produce another feature that distinguishes UHPFRC from other types of concrete namely the considerably higher strain hardening in tension and/or deflection hardening in bending (Fig.1.2).

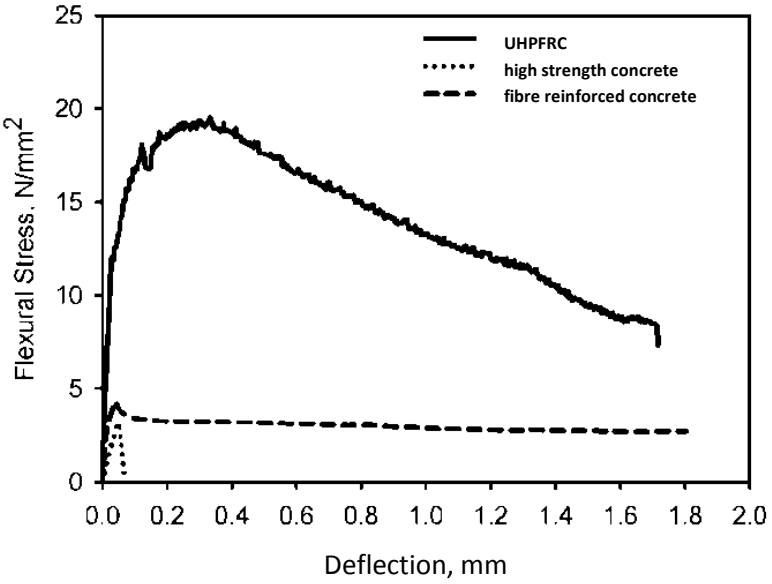

Figure 1.2: Comparison of flexural properties of UHPFRC with conventional FRC and high strength concrete (Barnett et al., 2007a)

Strain hardening in tension (or deflection hardening in bending) means that increased tensile (or flexural) loading is required to cause further strain (or deflection in bending) above the loading at first crack (Bentur and Mindess, 2007).

Since the mid-1990s, several ultra high performance concrete (UHPC) products have been developed commercially in different countries including:

- Reactive Powder Concrete (RPC) developed in France by Bouygues (Richard and Cheyrezy, 1994)
- Ductal concrete developed in France by Bouygues, Lafarge and Rhodia (Acker and Behloul, 2004). It is one of the main types of ultra high performance concrete used in Europe, Asia, Australia and North America
- Compact Reinforced Composites(CRC) developed by Aalborg Portland Denmark (Aarup, 2004)
- CEMTEC multiscale concrete developed by LCPC in France (Rossi, 1997)

Due to its enhanced fracture properties, UHPFRC has many potential applications both in the construction of new (Ikeda et al., 2004) and rehabilitation of old structures (Bruhwiler and Denarie, 2008). The dense micro-structure achieved by homogeneity and compactness makes it resistant to abrasion, corrosion and chemical attacks giving it excellent durability properties (Li and Stang (2004), Magureanu et al. (2012)).This property together with its high strength and ductility make it very useful in the repair and rehabilitation of structures such as bridges (Habel, 2004). Dispensing with passive

reinforcement bars substantially increases the strength to weight ratio (Adeline and Behloul, 1996) but also enables it to be made into thinner and more sophisticated shapes finding application in more innovative ways in both new building and civil engineering construction (Perry and Seibert, 2008). Its high fracture energy has also seen it increasingly applied in blast protection (Barnett et al., 2007b).

Despite the many potential applications provided by these enhanced properties, the current use of UHPFRC is limited. For example in the UK, known applications of the material were initially in constructing a couple of staircases to showcase its potential (Marcinkiewitcz and Wells, 2014). Apart from its high cost, this limited use of UHPFRC has been attributed to several factors including a limited understanding of its mechanical behaviour and a lack of widely accepted design standards (Kang et al. (2010), Lappa (2007), Qsymah et al. (2017)). One of the factors limiting a fuller understanding of its mechanical behaviour could be due to the cost of testing UHPFRC which is considerably more compared to normal concrete for several reasons including:

- The method of preparation (which may require heat treatment) requires more time and effort. After specimens are demoulded, they would typically be cured at room temperature for about 2 days. Heat treatment could then be applied by steam-curing the specimens at a temperature of 90^0C for a further 2-3 days (Kang et al, 2017).

- Cement is normally the most expensive constituent of concrete and for the same size specimen, UHPFRC requires about twice the quantity of cement compared to normal concrete.

While more experiment tests are necessary, the limitations highlighted above mean that the role of numerical modelling will become increasingly important in providing more insight into the behaviour of the material in general and crack propagation in particular. Numerical modelling and simulation has the potential to significantly reduce the number of experiment tests required for UHPFRC. One area where simulation can have a significant contribution is the investigation of the effect of size on the mechanical behaviour of UHPFRC. Simulation can be used more cost effectively to investigate the influence on the mechanical response of specimens of varying factors such as test methods, specimen size and fibre content. Therefore, simulation used in this way provides an important basis for developing tools for informing the design of structures with UHPFRC. In comparison to the other factors, studies on the size effects in UHPFRC seem most limited (Mahmud et al., 2013) most likely due to the high cost involved in testing the wide range of sizes required for their proper evaluation. Of the studies done, there are significant inconsistencies with some finding a strong size effect and others little.

Generally, in addition to size effects, the influence of factors such as fibre type, content and distribution on UHPFRC's material properties are still being studied using both experimental and numerical modelling. Studying the influence of these factors on the flexural properties of UHPFRC has been identified as a vital step towards exploring the material's potential applications (Barnett et al. (2007a).

1.2 Aim & Objectives

This is an experimental and numerical modelling study of the flexural behaviour of UHPFRC with the aim of proposing an appropriate UHPFRC numerical concrete damage model. Only Mode I fracture is considered as it is the most common in concrete bending (Bažant and Planas, 1998). An initial simulation study evaluates the suitability of existing concrete material models in simulating the flexural behaviour of UHPFRC. Observations from this initial simulation study and from further tests are the basis for proposing a UHPFRC concrete damage model incorporating fibre content. The model is applied in the progressive failure analysis of UHPFRC by simulating crack initiation and crack propagation. The validated model is then used in predicting the flexural behaviour of UHPFRC. It is also used in studying the effect of size and fibre content, and their influence on the prediction of the loading capacity of UHPFRC. The validated model is proposed as a predictive tool for numerical analysis and design of UHPFRC. Therefore, this project consists of the following three stages: An initial simulation study, experimental investigations and further UHPFRC model development. The objectives of each of these stages are summarised below.

1.2.1 Initial simulation study

The objectives of this stage are:

a) Identification of appropriate methods to estimate material properties of UHPFRC

b) Study and identification of appropriate modelling approaches for UHPFRC

1.2.2 Experiment investigations

The main objectives of this stage are to enable the following:

a) Detailed fibre content and size effect study

b) Material property estimates incorporating fibre content for use in modelling

1.2.3 UHPFRC model development

The main objective of this stage is to develop a validated UHPFRC numerical damage model incorporating fibre content.

1.3 Research questions

UHPFRC was developed by improving its material structure especially at the microscale and mesoscale. It is the reason for its much better performance compared to normal reinforced and fibre reinforced concrete not only in terms of strength but also other aspects such as durability. One of its main advantages over normal reinforced or fibre reinforced concrete is its significantly enhanced crack resistance. This is achieved mainly by incorporating fine fibres within the matrix which make the concrete significantly more ductile than normal concrete. A few numerical models using multiscale frameworks have been developed specifically for UHPFRC to take into account its unique characteristics (Qsymah et al. (2017); Zhang et al. (2018)). However, these all require measurement of microscale and/or mesoscale parameters.

A primary research question in this study relates to the viability of adopting a modelling approach that is simpler and more economical than the classical multiscale approach. In order to answer this question, the following aspects of UHPFRC flexural behaviour need to be established by numerical modelling and experiment:

1. Viability of incorporating the influence of fibre content on UHPFRC material properties within the proposed model
2. Whether or not there is a size effect on the flexural response at different fibre contents

1.4 Contributions

At the end this study a UHPFRC damage model incorporating fibre content is presented and used to accurately simulate the flexural response of un-notched and notched test specimens of different sizes and fibre contents, and to predict their failure loads. A size effect is observed on the flexural stress at linearity and flexural strength of geometrically similar UHPFRC specimens with 2%, 4% and 6% fibre content. This contributes to the limited studies available on the size effect on UHPFRC. Values of elastic modulus (E), tensile strength (σ_t) and fracture energy (G_f) at 2%, 4% and 6% fibre content are estimated from standard tests and confirmed as appropriate inputs for modelling UHPFRC using a bilinear $\sigma - w$ curve. Comparisons are presented between the cohesive crack model using cohesive elements (CCM), ABAQUS concrete smeared crack model (CSM) and ABAQUS concrete damaged plasticity (CDP) in simulating the flexural response of UHPFRC. Both the values of estimated material properties and the comparative study of different modelling approaches mentioned above are useful resources for related future studies on UHPFRC.

1.5 Thesis Layout

Chapter 1 – Introduction

A background presents a justification for this study as a basis for setting out its aim & objectives, and its research questions. This is followed by an outline of the thesis layout in this section.

Chapter 2 – Ultra High Performance Fibre Reinforced Concrete (UHPFRC)

The principles of UHPFRC design and development are reviewed within the context of the constituents of UHPFRC. In the development of UHPFRC these constituents have been carefully selected in order to achieve an internal structure that leads to its enhanced mechanical properties. Therefore, in order to analyse UHPFRC and to predict its performance under load, the internal structure of its matrix and of the fibre-matrix interface are also be reviewed.

Chapter 3 – Concrete Fracture Models

A literature review of existing concrete material models is undertaken with a view to investigating the possibilities of using them for simulating the flexural behaviour of UHPFRC. Three modelling approaches are reviewed namely the cohesive crack models, crack band models and damage models. Their implications in modelling UHPFRC are discussed by reviewing previous numerical modelling and simulation studies in which they have been used to analyse fibre content, distribution and orientation.

In the initial study, the cohesive crack model (CCM), concrete smeared crack model (CSM) and concrete damaged plasticity model (CDP) in ABAQUS are used to simulate progressive crack propagation and failure mechanism of UHPFRC test specimens, and to predict their load capacities. These predictions are be compared with test data available from an earlier study carried out by Barnett et al. (2007a). The suitability of above modelling approaches is assessed with a view to selecting the most appropriate features for further model development.

Chapter 4 – Experimental Investigation

The production of UHPFRC is described involving mixing and casting of specimens with varying sizes and fibre content (2% - 6%) required for the study. This is followed by a description of the test methods adopted including the three point bending test on notched specimens and the four point bending test on un-notched specimens. The test results are then analysed in terms of size and fibre content effect on both the pre- and post-peak load-deformation responses. The effect of fibre content is then linked to material properties measured at the macroscale.

Chapter 5 – UHPFRC Model Development

This includes a description of the development of a proposed UHPFRC concrete damage model. The effect of fibre content determined from tests is incorporated into a smeared damage model. Thus a UHPFRC concrete damage model incorporating fibre content (UDMF) is proposed. The model is verified and validated by comparing predictions with test data from this study and from literature respectively.

Chapter 6 – Conclusions

The main findings linked to the objectives of the study are outlined. This is followed by a presentation of the study's contributions relating to each of the three stages of the research. Finally, the study's limitations are described and some recommendations are made for future work.

Chapter 2 – Ultra High Performance Fibre Reinforced Concrete (UHPFRC)

2.1 Introduction

The development of UHPFRC can be viewed within a historical context of continuing efforts to improve the strength, rheology and crack resistance of cement based materials (Richard and Cheyrezy, 1994). The compressive strength of cementitious materials like concrete has traditionally been increased by lowering the water-cement ratio (w/c). For normal concrete the corresponding reduction in its workability is overcome by the addition of plasticisers which work by enhancing the dispersion of water within the concrete mix hence reducing the overall water requirement. However, it was the development of very efficient water reducers known as super-plasticisers that enabled the production of High Strength Concrete (HSC). The high compressive strength of HSC (60-100 MPa) was the result of achieving a relatively low w/c ratio of 0.3-0.4 (Aitcin, 1998). Despite its relatively high strength, HSC was still very brittle. Hence it was the addition of fibres to the HSC matrix to enhance its ductility that led to the development of High Performance Fibre Reinforced concrete (HPFRC). Emphasis then shifted from just strength to performance in general because the resulting concrete was enhanced not only in strength but in other properties such as ductility.

However, the bond between the cement paste and the fibres is still relatively weak in both normal and high performance fibre reinforced concrete due to the inherent porous nature of the cement paste at the interface with fibres and aggregates (Bentur and Mindess, 2007). This is the reason for modifying either the surface texture or shape of the fibres in order to enhance their mechanical anchorage within the interfacial cement paste. Therefore in addition to the above concrete technology advances, the development of UHPFRC required the application of material science in modifying the internal structure of the matrix.

The design of UHPFRC is therefore based on principles that aim to minimise defects such as micro-cracks and pore spaces in order to exploit a bigger proportion of the ultimate load carrying capacity provided by the constituents (Richard and Cheyrezy, 1995). This is achieved by:

- Super-plasticisers which improve workability while maintaining a low w/c ratio
- Enhanced homogeneity through optimisation of particle size distribution resulting in the use of only fine aggregates (silica sand)
- High compactness through addition of silica fume to fill pore spaces
- Addition of fibres which bridge micro-cracks and significantly improve ductility

As a further option, post-set heat treatment has been found to enhance the microstructure of the concrete matrix.

As these principles are the basis on which UHPFRC mixes are designed they are now reviewed below within the context of the role performed by the constituents of UHPFRC. Cement and super-plasticisers are reviewed first emphasising the initial step in increasing strength by reducing the water/cement ratio while maintaining a high workability. However, in order to achieve an even higher performance it is necessary to modify the aggregates, add silica fume and introduce fibres. In the development of UHPFRC these constituents have been carefully selected to achieve an internal structure that leads to its enhanced mechanical properties. Therefore in order to analyse UHPFRC and to predict its performance under load, the internal structure of its matrix and of the fibre-matrix interface are also reviewed.

2.2 Constituents of UHPFRC

A typical UHPFRC mix would consist of cement, water, silica sand, silica fume, super plasticiser and fibres. The role of these constituents is reviewed briefly in relation to their contribution to enhancing the mechanical properties of UHPFRC.

2.2.1 Cement

Portland cement is the most commonly used type of cement and is produced by heating limestone and a small amount of clay to temperatures of about 1500^0C. This temperature is just enough to fuse the limestone and the clay together without liquefying them. The resulting paste 'clinker' consists of tiny granules that are ground and mixed with gypsum (hydrated calcium sulphate) to produce Portland cement.

Portland cement is made up of several compounds but calcium silicates (C_3S and C_2S) make up more than ¾ of its total mass (Aitcin, 1998). When it comes into contact with water cement forms a paste that acts as a binder for the other constituents of concrete. This cement paste is formed as the anhydrous silicate compounds react with water during the process of hydration. An example of the hydration process is represented by the chemical equation below in which a calcium silicate hydrate (C-S-H) product is formed:

$$2C_3S + 6H \rightarrow C_3S_2H_3 + 3CH \qquad (2.1)$$

The usual chemistry notation is used in the above equation where C is calcium oxide (CaO) and S is silicon dioxide (SiO_2). C-S-H is the main product that is responsible for the development of strength in concrete. As they are formed, these products gradually occupy the space left by the water being used up during hydration. Any spaces left unoccupied after hydration will remain as voids or capillary pores. A higher w/c ratio makes more water available for hydration leading to more crystalline products. As a result of their

relatively angular shape and large size, crystals result in more voids or pores being formed within the cement paste. On the other hand, less crystalline products associated with lower w/c result in less voids or pores within the cement paste. Due to the fact that strength within the hydrated cement paste is generated mainly by Van der Waals forces of attraction, the less crystalline the hydration products the stronger they will be (Taylor, 1997). It follows then that the strength of the hydrated cement paste is mainly influenced by its porosity which is in turn dependent on the relative volumes of water, cement and entrapped air as follows (Neville, 2012):

$$f_c' = k\left(\frac{c}{c+w+a}\right)^2 \qquad (2.2)$$

where f_c' is the compressive strength of the hydrated paste, c, w and a are the volumes of the cement, water and air respectively, and k is a constant. The term in brackets in Eq. 2.2 is a proportion representing a material's porosity and therefore has no units. The constant *k* has the same units as compressive strength f_c' and depends on the type of cement.

Dividing the top and bottom terms of Eq.2.2 by c reduces the expression to:

$$f_c' = k\frac{1}{1+(w/c)^2+(a/c)^2} \qquad (2.3)$$

Hence to increase compressive strength, porosity has to be reduced by lowering as much as possible the water/cement (w/c) ratio and the entrapped air in the fresh cement mix. However, because the air content is relatively small (1-2%), Eq.2.3 is commonly reduced to:

$$f_c' = k\frac{1}{1+(w/c)^2} \qquad (2.4)$$

When the *w/c* ratio is reduced, the cement particles come closer together in the fresh cement mix reducing porosity and thereby increasing compressive strength. Hence achieving the lowest possible w/c is crucial in producing both high strength concrete (HSC) and ultra high performance concrete (UHPC). In addition to pores, hydration results in a contraction in volume of its products of up to 10% producing many micro-cracks in the process (Taylor, 1997). The extent of this micro-cracking can be reduced by lowering the *w/c* ratio to achieve a reduction in the quantity of anhydrous silicates being hydrated. In normal concrete the w/c ratio is relatively high so that the hydration process results in the formation of pores and micro-cracks within the cement paste at the interface between cement particles and aggregates. The paste at this interface is referred to as the interfacial transition zone, ITZ (Fehling et al., 2015). With the pores and micro-cracks within it, this ITZ is therefore the weakest link in normal concrete where failure would first

occur. In UHPFRC however, with the very low w/c ratio (<0.3), pores and micro-cracks resulting from hydration are significantly reduced.

In addition to reducing the water requirement, in UHPFRC the w/c ratio is further reduced by the very high cement content. The effect of increasing the cement content while at the same time reducing the available water is that not all the cement particles will be hydrated. The un-hydrated cement in UHPFRC is responsible for its self-healing properties. It reacts with any water finding its way through micro-cracks to close them thus further enhancing the material's durability (Aitcin, 1998). Several studies have indicated that cement types CEM I and CEM II 42.5 or 52.5 are suitable for producing UHPFRC (Karihaloo and De Vriese, 1999).

In order to reduce the cost of UHPFRC and enhance its sustainability, several studies have successfully reduced the cement content by replacement with pozzolanic industrial by-products such as Granulated Blast Furnace Slag (GBFS) and Pulverised Fuel Ash (PFA) (Le, 2008). These cement replacement products have also been found to enhance resistance of the material against chemical attacks. Incorporation of these products which also have the same 'binding' effect as cement therefore requires that reference should now made to a more inclusive water/binder ratio (*w/b*) rather than just *w/c*.

2.2.2 Super-plasticisers

While lowering the *w/c* ratio increases compressive strength it also leads to reduced workability. This happens because the surface of cement particles have an electrical charge that attracts oppositely charged water particles resulting in flocculation whereby some water is trapped between cement particles (Neville, 2012). This means that the trapped water is not available for lubrication necessitating the addition of water in excess of the quantity required to hydrate all the cement particles. This excess water makes the hydrated cement paste more porous thereby weakening the mechanical properties of concrete. Addition of chemical admixtures can reduce flocculation by neutralising the electrical charges on the surface of cement particles and so enhance the dispersal of water within the mix. Unlike in normal concrete where ordinary organic plasticisers can be used as the admixture, in UHPFRC super-plasticisers have to be used because they have synthetic molecules that are more effective in dispersing water particles thereby enabling a significant reduction in the amount of water added. Super-plasticiser molecules are adsorbed into the surface of cement particles by Van der Waals forces where they cause electrostatic repulsion between cement particles thereby reducing flocculation (Aitcin, 1998). It is the addition of super-plasticisers that enables the achievement of a very low *w/b* ratio (<3%) and hence a very high compressive strength. In UHPFRC, polycarboxylate-based polymers have been found to be more efficient than the sulfonate-based polymer (Soutsos et al., 2005)

2.2.3 Aggregates

In UHPFRC, homogeneity is significantly enhanced by eliminating coarse aggregates while only retaining fine aggregates. This is because the size, shape and texture of coarse aggregates encourage local water retention thereby preventing its uniform dispersion throughout the mix. As a result, the ITZ tends to have a higher w/c ratio than the rest of the cement paste which in turn produces more pores and voids. In UHPFRC, however, the combination of low *w/c* ratio and fine aggregates further reduces defects in the ITZ. In addition to enhancing water dispersion within the mix, fine aggregates have fewer inherent pores and defects hence are much stronger. Silica sand is normally used as the fine aggregate in UHPFRC because of its high silica content and lack of impurities. Hence both its physical and chemical properties are valuable in enhancing both homogeneity and strength (Fehling et al., 2015).

2.2.4 Silica fume

Though retention of only fine aggregates enhances homogeneity of UHPFRC, particle size distribution is still not ideal leaving some voids within the matrix which are filled by the addition of silica fume. Silica fume consists of ultra-fine silica (SiO_2) particles that are a by-product of the process of producing silicon metal and alloys. With diameters of 0.1-0.2µm they are about 100 times smaller than the average cement particles (Aitcin, 1998). Due to this fine nature, silica fume particles can fill the voids between the larger cement particles that have been de-flocculated by the action of a superplasticiser (Fig.2.1). These particles are also spherical in shape, a property that is thought to enhance its lubrication effect and rheology within the fresh concrete mix (Neville, 2012).

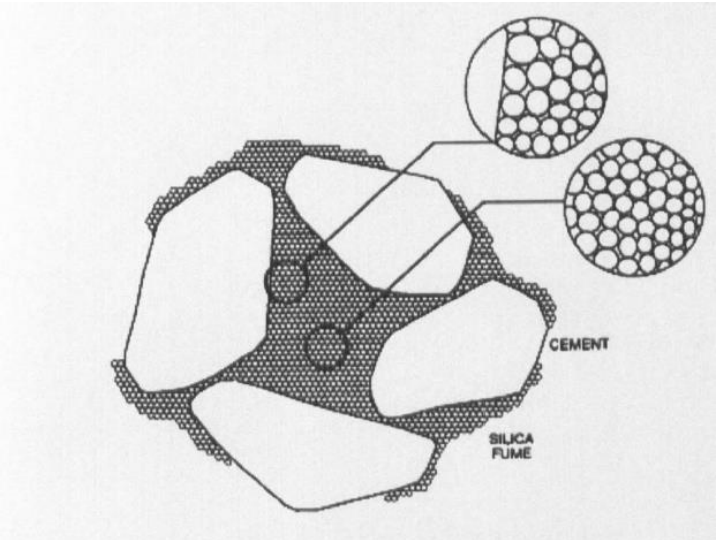

Figure 2.1: The effect of silica fume in filling voids (Bache, 1981)

Hydration of Portland cement produces a large amount of lime ($Ca(OH)_2$) which can be easily leached out by water and make the cement paste even more porous (Aitcin, 1998). Silica is very reactive and can combine with this lime at room temperature in the presence

of water to produce calcium silicate hydrate (C-S-H) similar to that produced when Portland cement is hydrated. Therefore the addition of silica fume produces a very dense microstructure that has a very strong bond between aggregates and the hydrated cement paste.

2.2.5 Fibres

The above enhancements to the microstructure of UHPFRC result in an ITZ virtually free of defects (Fehling et al., 2015). As the bond between the cement paste within the ITZ and other inclusions is very strong, the ITZ is no longer the weakest link. While the enhanced micro-structure leads to higher strengths, it is the addition of fibres to the matrix that significantly improves the ductility of UHPFRC. They do this by bridging micro-cracks within the matrix thereby maintaining load transfer in cracked zones. Because of the very strong bond between the cement paste and the fibres within the ITZ, short straight fibres (6-15mm long) can be used unlike in other types of concrete where longer fibres are required with modification in their shape or texture to enhance their mechanical anchorage within the matrix (Bentur and Mindess, 2007).This is explained further in section 2.4.1. Short straight fibres also have less negative effects on workability compared to deformed ones. The absence of coarse aggregates enables much higher fibre dosages to be incorporated within the matrix without 'balling' during mixing further enhancing ductility (Le, 2008).

Fibres are very effective in enhancing the mechanical properties of UHPFRC due to their significant adhesive and frictional bonds with the matrix within the ITZ. Enhancement by fibres in the mechanical properties of UHPFRC takes effect initially during the pre-cracking stage where they suppress initiation and propagation of cracks thereby increasing first crack load. However, the crack-bridging action at the post-cracking stage is the main reason for incorporating fibres in UHPFRC. At this stage fibres within UHPFRC can do the following (Bentur and Mindess, 2007):

- Transfer stresses and loads across cracks in the matrix thereby increasing ultimate strength. This is referred to as strain/deflection hardening because the stress/flexural load continue to increase with strain/deflection beyond first crack.
- Provide energy absorption mechanisms through de-bonding and pull-out as fibres bridge cracks even during strain softening when stresses decrease with strain beyond first crack.

The above two processes have been described in detail by Bentur and Mindess (2007). Their approach has been adopted in this study whereby the fibre-matrix stress transfer and crack bridging for straight and smooth fibres is analysed by considering the shear stresses that develop across the fibre-matrix interface. Based on this analysis, efficiency

of short and randomly oriented fibres in UHPFRC can be predicted. In the following section only aspects relevant to this study are reviewed in relation to mechanisms involved in stress transfer which are the basis for predicting the stress-strain curve and mode of failure of UHPFRC.

2.3 UHPFRC stages of deformation

The material's stages of deformation can be described with reference to its tensile/flexural response (Fig.2.2).

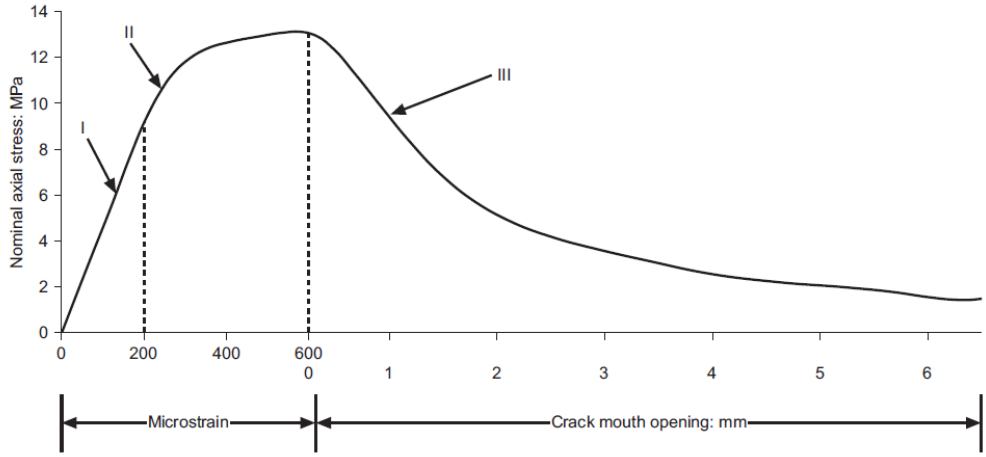

Figure 2.2: Typical tensile curve for UHPFRC (Benson and Karihaloo, 2005)

2.3.1 Phase I - Linear elastic behaviour

Prior to any cracking, stress transfer is predominantly elastic so that there is compatibility in the displacements between the fibre and matrix (Bentur and Mindess, 2007). The shear stress developed at the interface distributes the external load between the fibres and matrix which have different moduli of elasticity. As a result, the strains in the fibres and matrix stay the same at the interface (Fig.2.3a). This elastic shear stress transfer is responsible for determining the elastic range and first crack of UHPFRC. The distribution of this stress along the fibre-matrix is not uniform. The shear stress distribution at the interface and the tensile stress distribution in the fibre are shown in Fig.2.3b. The maximum shear stress is found at the ends of the fibre and it is in these regions that stress is transferred from the matrix to the fibre wherein tensile stress gradually increases.

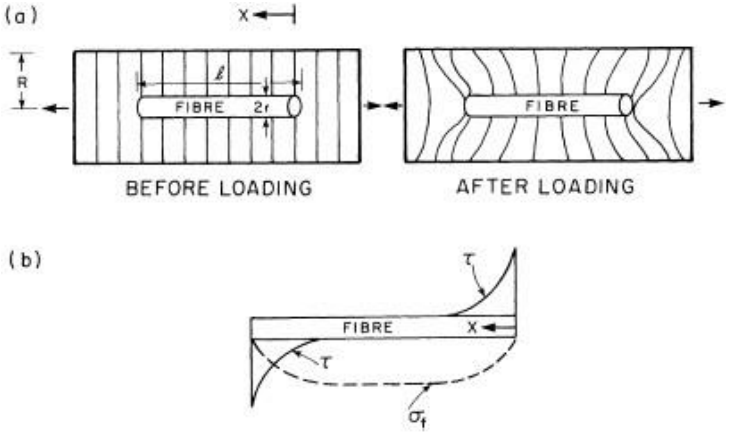

Figure 2.3: Schematic description of a fibre embedded in a matrix, and the deformation and stress fields around it: (a) geometry of the fibre and the deformation in the matrix around the fibre prior to and after loading; (b) elastic shear stress distribution at the interface (τ) and tensile stress distribution in the fibre (σ) (Bentur and Mindess, 2007)

Fibres also increase the first cracking stress through crack suppression in cases where there are existing defects (e.g. pores or micro-cracks) in which stress concentrations could be induced under tensile loading (Bentur and Mindess, 2007). According to the prediction of Romualdi and Batson (1963) surrounding fibres through their interfacial shear bond stresses apply opposing 'pinching' forces which reduce the stress concentrations at crack tips (Fig.2.4). As a result a higher stress would now be required to initiate cracking within the matrix. This stress has been found to be inversely proportional to the spacing between fibres. The fibre spacing is in turn influenced by the fibre content, geometry, orientation and bond with matrix. Hence a higher fibre content, interfacial frictional shear strength and fibre aspect ratio would lead to a higher first cracking stress.

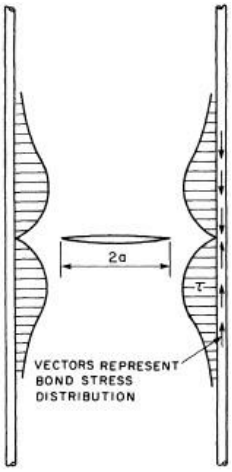

Figure 2.4: Representation of the 'pinching effect' and interfacial shear stress distribution between fibres in suppressing crack propagation in a matrix (Romualdi and Batson, 1963)

2.3.2 Phase II - Strain hardening

Fibres also respond to the onset of first cracking in order to prevent or stop the cracks from propagating in an unstable manner. This is also referred to as crack stabilisation. This response is the result of the bridging action of fibres on micro-cracks which prevents their growth and coalescence (Karihaloo and Wang, 2000a).This fibre bridging action involves stress being transferred by frictional slip of the fibres. In addition to this action some stress is transferred within the matrix in front of the advancing crack through aggregate interlock (Fig.2.5). The density of the micro-cracks increases with increasing tensile/flexural loading until it reaches a saturation level at peak. The extent of strain hardening is determined by both the microstructure of the cementitious matrix and the volume fraction and bond strength of the fibre (Bentur and Mindess, 2007).

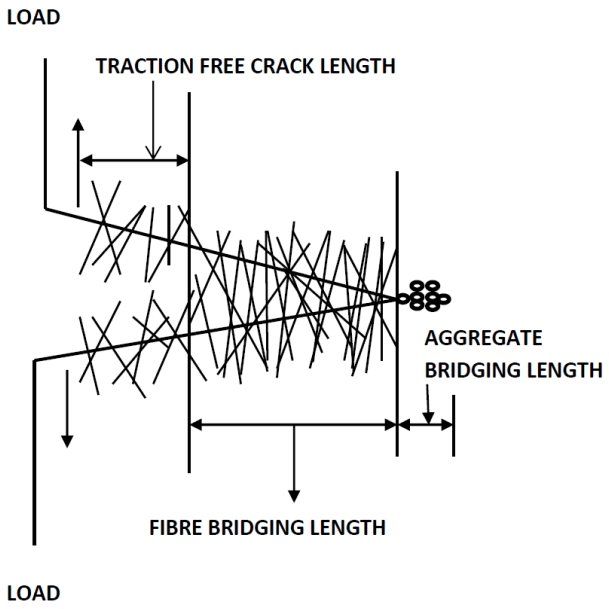

Figure 2.5: Idealized representation of an advancing crack in a fibre reinforced cement (from Wecharatana and Shah (1983))

2.3.3 Phase III - Tension softening

When the strain hardening capacity has been exhausted (i.e. tensile/flexural strength of the composite has been reached), some of the fibres begin to de-bond from the matrix resulting in the localisation of deformation along the eventual failure plane (Karihaloo and Wang, 2000b). The localisation is seen in the opening of the cracks along this plane but without their actual coalescence. The increased deformation is due to progressive de-bonding of fibres under decreased applied loading resulting in the opening and growth of fragmented cracks. The de-bonding occurs when the shear stress due to applied load exceeds the shear strength of the interface. At this point frictional slip becomes the means of transferring stress across the interface during which relative displacements take place between the fibre and the matrix (Bentur and Mindess, 2007). This frictional shear stress

transfer is a major influence on the post-cracking stage when fibre-bridging action takes place across cracks. This mode of stress transfer determines the ultimate strength and deformation of UHPFRC.

The main difference between the stress-transfer pre- and post-cracking is that whereas in the former the maximum shear stress at the interface occurs at the ends of the fibre (Fig.2.3b), in the latter the maximum shear stress occurs where the fibre enters the matrix (Fig.2.6). The fraction of fibres that remain elastically bonded to the matrix progressively decreases during this phase until all the fibres have de-bonded resulting in the coalescence of crack fragments to form a through crack. Thereafter, the residual tensile carrying capacity is determined entirely by the frictional contact between the fibres and the matrix until the fibres are completely pulled out of the matrix and failure occurs.

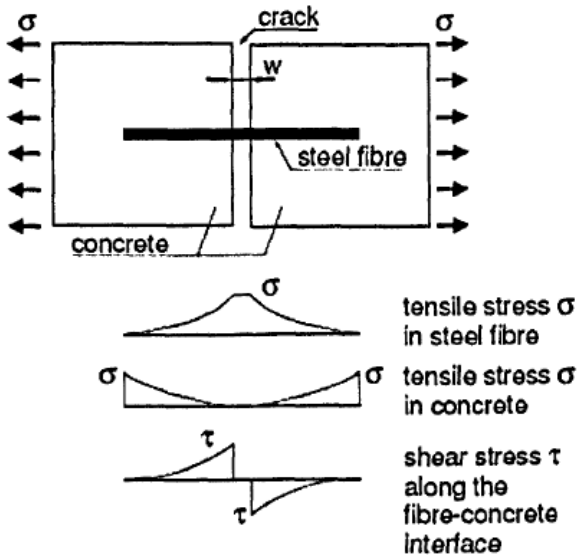

Figure 2.6: Stress distribution in a fibre and concrete matrix under uniaxial tension (Markovic, 2006)

2.4 Factors affecting fibre efficiency

While a fibre can accommodate the transfer of tensile stress equal to its tensile strength, in practice the influence of several factors on fibre efficiency determines the actual value of stress that is transferred. Therefore strength efficiency can be defined as the ratio of the average stress transferred along the fibre relative to its tensile strength (Bentur and Mindess, 2007). How efficiently the tensile stress will be transferred to the fibres will depend on the value of shear stresses that will develop at the interface. The development of these shear stresses is dependent on the combined effects of fibre length, orientation and content.

2.4.1 Effect of fibre length

Based on the stress transfer mechanism discussed above, the minimum length of a fibre needed for build-up of a stress equal to its strength σ_{fu} is defined as the critical fibre length, L_c (Fig.2.7). However, this stress is not uniform along the fibre length but varies from 0 at the ends to a maximum in the middle (Fig.2.6). This tensile stress within the fibre is built up from the shear stress developed at the fibre interface which also varies from 0 to a maximum value. L_c is therefore obtained by equating the average load transferred along the length of a fibre of radius *r* to its tensile load capacity as follows:

$$2\pi r L_c \left(\frac{0+\tau_{fu}}{2}\right) = \pi r^2 \sigma_{fu} \qquad (2.5)$$

where *r* is the fibre radius, τ_{fu} is the maximum shear stress and σ_{fu} is the fibre tensile strength. In the above expression, the term in brackets is the average stress transferred along the fibre. It is assumed that variation in the stress is linear according to Fig.2.7.

Simplifying Eq. 2.5 gives

$$L_c = \frac{\sigma_{fu} r}{\tau_{fu}} \qquad (2.6)$$

If fibre length is less than L_c then the embedded length is not enough to generate a stress equal to the fibre strength (Fig.2.7). The stress in the fibre will reach its yield or tensile strength only if the length of the fibre exceeds L_c. In fact to obtain strength efficiency above 90%, the fibre needs to be 4-5 times longer than its critical length (Bentur and Mindess, 2007). This can be achieved by controlling the geometry of the fibre (higher aspect ratio) or by enhancing the fibre-matrix interaction (i.e. higher τ_{fu} for the case of frictional bond).

Eq.2.6 is also useful in explaining why the fibres in normal FRC are often deformed or surface textured to induce mechanical anchorage while in most UHPFRC mixes this is not necessary. Typical interfacial shear strength in UHPFRC is 5 times or more than that in normal FRC (Tjiptobroto and Hansen, 1993) and the example below aims to illustrate the significance of this difference in determining the common use of straight smooth fibres in UHPFRC rather than deformed ones.

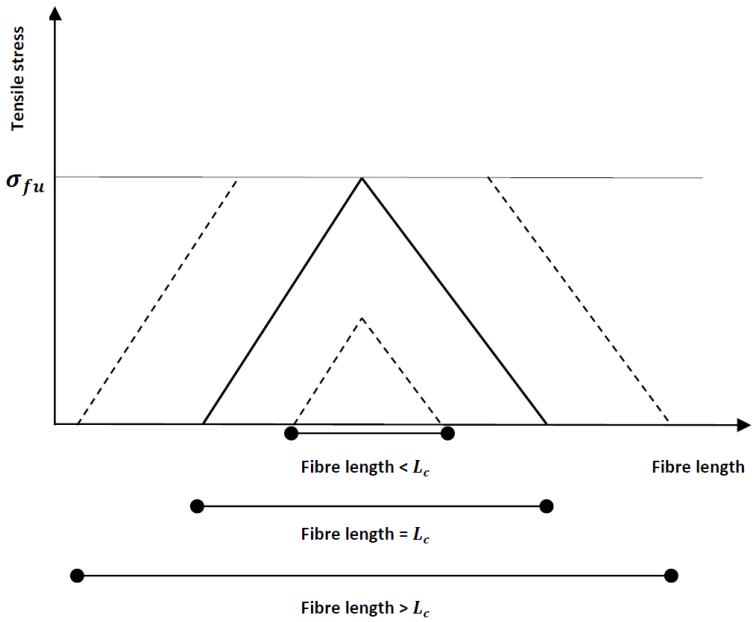

Figure 2.7: Relationship between fibre length and transferred stress (Adapted from Bentur and Mindess (2007))

In theory σ_{fu} would be equal to the tensile strength of the fibre which is here taken to be about 1000MPa. This value is typical of steel fibres used in many FRC mixes (Le et al., 2008). Taking as an example steel fibres of diameter *d* = 0.3mm in a FRC mix with a typical interfacial shear stress τ_{fu} of 1MPa (Tjiptobroto and Hansen, 1993), Eq. 2.6 would give an L_c of 150mm. A fibre with these dimensions would have a fibre aspect ratio (L_c/d) of 500. However, in practice the fibre aspect ratio needs to be less than 100 to achieve sufficient workability and uniform distribution. The fibre considered above can be brought to within the required aspect ratio by either reducing its length and/or increasing its diameter. Typically, fibres used in FRC are less than 50mm long. In this case by reducing the fibre length (L) to 30mm an upper bound aspect ratio of 100 is obtained. Re-arranging Eq. 2.6 then enables an estimate of the tensile stress that can be transferred by the new fibre length as follows:

$$\sigma_{fu} = \frac{\tau_{fu} L}{r} \qquad (2.7)$$

A value of 200MPa is obtained from Eq. 2.7 which is well below the assumed fibre tensile strength of about 1000MPa. In addition to several simplifying assumptions in the above calculation, production and other factors often cause the tensile stress values that can be transferred by the interfacial shear stress to be much less than that obtained in this estimate. Thus in order to complement the ability of interfacial shear stress to transfer stress to the fibres in normal FRC, fibres are deformed or surface coated in order to induce additional mechanical anchorage.

In UHPFRC however, the fibre-matrix bond strength has already been significantly enhanced by modification of the microstructure to minimise defects within the ITZ. Hence typical interfacial shear strength values of UHPFRC are 5-7.5MPa (Tjiptobroto and Hansen, 1993). Inserting the lowest τ_{fu} value of 5MPa and the same fibre radius as in the above FRC example into Eq. 2.6 gives L_c in the order of 30mm. The fibre aspect ratio obtained is also within the upper limit of 100 required for workability. In fact a typical fibre diameter used in UHPFRC is less than 0.2mm enabling the use of even shorter fibres which would still be able to transfer stress values in the order of their tensile strength. Therefore straight and smooth fibres can be used adequately without any need to induce additional mechanical anchorage by deforming or altering their surface texture. It also means that relatively short fibres (typically 6-15mm long) can be used while maintaining a high aspect ratio (typically 50-100) therefore providing a significant advantage in workability (Fehling et al., 2015). The above observations were confirmed in tests carried out by Yoo et al. (2016) to compare flexural properties of a UHPFRC mix incorporating straight smooth fibres with that having deformed fibres. They found that for the same fibre aspect ratio, the flexural strength of the mix with smooth fibres was the same as that with deformed fibres. They attributed this observation to the high frictional bond strength due to the dense ITZ which made any improvements in bond strength from the deformed shape insignificant.

2.4.2 Effect of fibre orientation

The ideal fibre orientation for UHPFRC is where the fibres are aligned to the maximum principal stress. In practice this is rarely achieved despite adoption of casting methods aimed at influencing fibre alignment for example relative to direction of flow. In most cases where the process of mixing aims at achieving a uniform fibre distribution and random orientation, fibres that are not parallel to the load direction will be less efficient in contributing to the mechanical properties i.e. strength and toughness.

Orientation of fibres in relation to the load direction reduces their efficiency in contributing to the elastic modulus at the pre-cracked stage and to strength post-cracking. It is reasonable to assume that a fibre's orientation remains constant when considering its contribution to the elastic modulus within an un-cracked region (Fig.2.8a). After cracking however, some fibres will develop local bending around the crack resulting in flexural stresses in the fibres and local compressive stresses in the matrix (Fig.2.8b). This dowel action will lead to increased pull-out resistance which may make up for the reduction in fibre efficiency caused by fibre orientation angle. This dowel action has been observed to increase with increasing fibre content (Fehling et al., 2015).

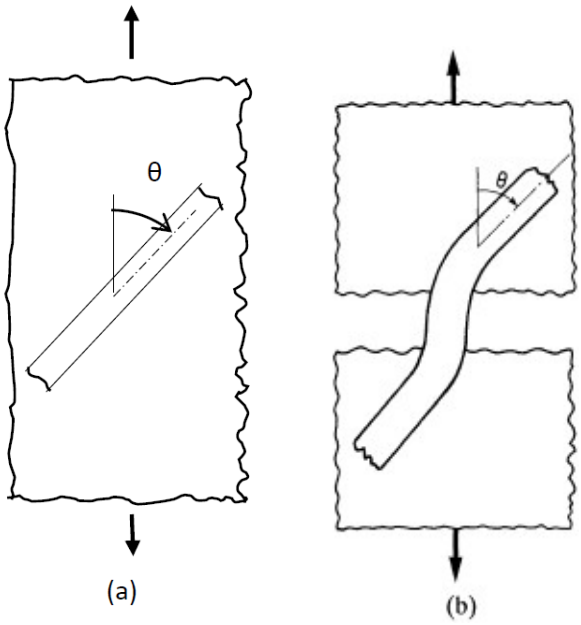

Figure 2.8: The intersection of an oriented fibre with a crack assuming (a) constant fibre orientation in un-cracked region; (b) local fibre bending around the crack (Adapted from Bentur and Mindess (2007)).

Qsymah et al. (2017) investigated the effect of fibre orientation on the elastic modulus of UHPFRC using μXCT images of 20mm UHPFRC cube samples to characterise the overall orientation of fibres (Fig.2.9). The orientation angle of each fibre with respect to a global axis (x, y or z) was calculated based on the coordinates of its centreline. By calculating an overall orientation factor based on the above angles, it was observed that a majority of the fibres in their UHPFRC specimen tended to align along one of the axes (fibre volume ratio of 60:40:20 for x, y, z axis respectively) in Fig.2.9. The elastic modulus was observed to be slightly more along the dominant x-axis compared to the y and z axes. The differences in elastic moduli between the most and least dominant axis were observed to be less than 5%.

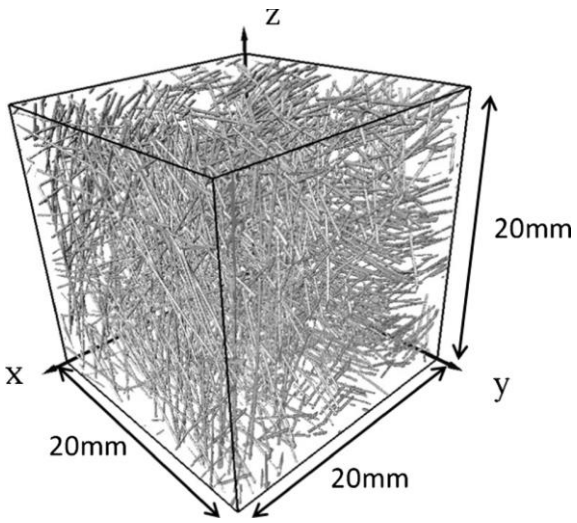

Figure 2.9: 3D image of steel fibres (Qsymah et al., 2017)

In order to investigate the effect of fibre orientation through numerical modelling, the μXCT images were converted to 3D FE meshes. For computational efficiency, the fibres were replaced by 1 D truss elements embedded in the mortar along the coordinates of the fibre centreline as described above. By fixing the fibre orientation to 0^0 relative to the most dominant axis while leaving it random relative to the other two axes, the difference in the elastic moduli increased significantly to 34% between the most and least dominant axis.

The casting method is generally acknowledged to have a significant influence on the orientation that the fibres finally assume in the UHPFRC specimen or structure. Several studies on UHPFRC beams have indicated that fibres tend to align to the direction of flow (Le, 2008; Wille and Parra-Montesinos, 2012). However, Barnett et al. (2010) found that in round panels fibres aligned perpendicular to the direction of flow. In addition, fibres will be aligned parallel to the formwork surfaces thus producing a skin layer with different properties to the rest of inner material. This can introduce a size effect in relatively smaller specimens where this skin layer forms a significant proportion of the cross-sectional area.

2.4.3 Effect of fibre content

As mentioned in section 2.3.1, increasing fibre content results in a higher first crack load by enhancing the crack suppression mechanism. Higher fibre content also enhances the post-cracking bridging action of the fibres by increasing the pull-out resistance through a dowel action when inclined fibres cross a crack (Fig.2.8b). This effect partly counteracts the reduction in efficiency from non-alignment of fibres with load direction. Applying the rule of mixtures to a UHPFRC mix, the load at first cracking can be written as (Bentur and Mindess, 2007):

$$E_m \varepsilon_m V_m + nE_f \varepsilon_f V_f \qquad (2.8)$$

where n represents total efficiency factors relating to fibre length and orientation. E_m, ε_m, V_m and E_f, ε_f, V_f are the elastic moduli, strain and volume content of the matrix and fibres respectively. As this load on the composite is transferred to the fibres at first cracking, the load capacity of the fibres must be able to bear it in order for failure not to occur i.e.

$$n\sigma_f V_f > E_m \varepsilon_m V_m + nE_f \varepsilon_m V_f \qquad (2.9)$$

where σ_f is the fibre strength.

The fibre volume needs to be high enough for Eq.2.9 to be satisfied. When that happens then first cracking does not lead to failure but to a transfer of load from the matrix to the bridging fibres (Fehling et al., 2015). Further loading would only result in more cracks referred to as multiple cracking.

Therefore a critical fibre volume (V_{fcrit}) can be defined such that fibre contribution to strength will only be significant when $V_f > V_{fcrit}$. Critical fibre volume for short fibres has been found to be a function of fibre aspect ratio and fibre-matrix bond. For measured τ_{fu} values 1-10Mpa and typical fibre aspect ratios 50-100, the critical fibre volume is between 1-3% (Bentur and Mindess, 2007). In contrast to normal fibre reinforced concrete (FRC) where these represent maximum fibres volumes that can be used, in UHPFRC fibre volumes higher than these can be easily attained due to enhancements in its internal structure. Typical fibre contents for UHPFRC are in the range 2-6% (Barnett et al., 2007a). This is the main reason for the considerably higher strain or deflection hardening in UHPFRC compared to normal FRC (Fig.1.2). Strain hardening occurs when increased tensile loading is required to cause further strain after the first crack. Similarly, deflection hardening is defined in bending such that increased flexural loading is required to produce increased deflection after the first crack.

Three types of stress-crack width curves for UHPFRC are presented by AFGC-SETRA (2013) for use in classifying UHPFRC in terms of the degree to which they exhibit strain hardening (Fig.2.10). For strain hardening to occur, the post-cracking tensile strength of the composite must be higher than the tensile strength of the matrix (i.e. stress at first crack). A strain hardening UHPFRC mix will also display deflection hardening in bending (Naaman and Reinhardt, 2015). A strain softening UHPFRC can also still be deflection hardening in bending as long as its residual post-cracking tensile stress is greater than about 1/3 that of the tensile strength of the matrix (Bentur and Mindess, 2007) as per Fig. 2.13. It also therefore follows that the critical volume required for deflection hardening is less than that required for strain hardening.

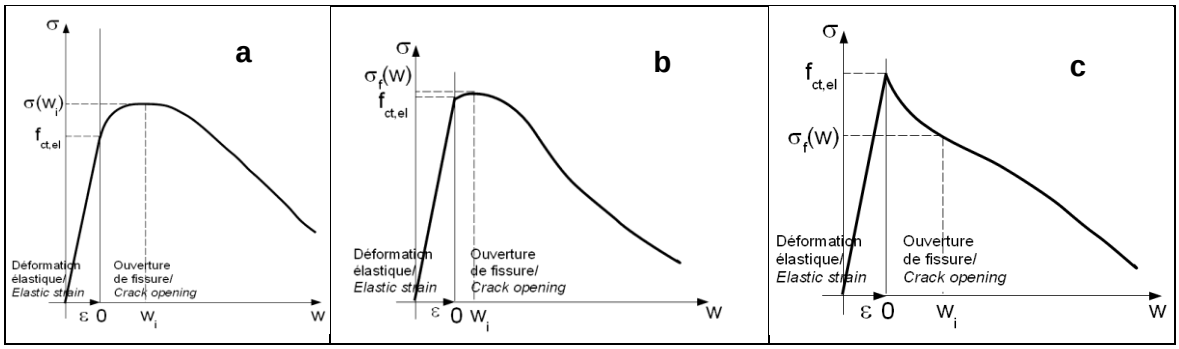

Figure 2.10: Examples of tensile constitutive law for UHPFRC a) strain-hardening b) low strain-hardening c) strain softening material (AFGC-SETRA, 2013)

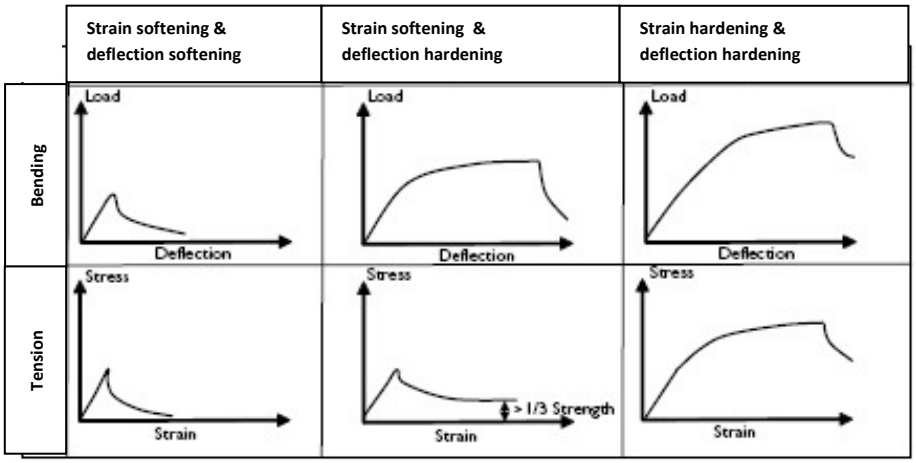

Figure 2.11: Schematic description of strain softening, strain hardening and deflection hardening in FRC composites (Bentur and Mindess, 2007)

2.5 Mechanical properties of UHPFRC

2.5.1 Tensile strength

In a brittle material such as concrete the tensile strength is observed to decrease with increased porosity, and with increased size and non-homogeneity of the material grains (Aitcin, 1998). For UHPFRC, as discussed in section 2.2, significant enhancements in relation to both reduced porosity and increased homogeneity result in relatively high tensile strengths. Due to the fact that the ITZ in UHPFRC is very strong and compact, the strength of the fibre-matrix bond is significantly increased. Therefore the enhanced capacity for load transfer from the matrix to the fibres results in an increase of the elastic region and corresponding load capacity in tension (Le, 2008).

According to AFGC-SETRA (2013), the tensile strength of UHPFRC is typically above 7 MPa. Though challenging, some attempts have been made to determine UHPFRC's tensile strength by direct tensile tests. In a method involving the use of dog-bone specimens of UHPFRC with 2% fibre content, Hassan et al. (2012) obtained an average direct tensile strength value of 9.07 MPa. Graybeal and Baby (2013) on the other hand tested prismatic specimens in a method employing tapered aluminium plates fixed to the sides of the specimens for enhanced grip. In their analysis of the tensile response, they distinguished between the average strength at first crack (5.91-9.09 MPa for 2% fibre content) and maximum tensile strength (8.56-11.56 MPa for 2% fibre content).

Due to the difficulty of conducting reliable direct tensile tests the tensile response is commonly obtained by inverse analysis of flexural tests adjusted for scale effects (AFGC-SETRA, 2013). Using this approach, Chanvillard and Rigaud (2003) obtained average tensile strength values of 10.8 MPa from four point bending test of UHPFRC with 2% fibre content .

2.5.2 Compressive strength

The extremely low porosity of UHPFRC is the main source of its very high compressive strength. Reduction of its maximum grain size through retention of only fine aggregates and the infilling of any voids by silica fume produces a very compact microstructure which further increases its compressive strength. Compressive strength is much higher than tensile strength because while only a few cracks need to be propagated to cause failure by applied tensile stress, failure by compressive stress only occurs after a critical number of tensile cracks have been joined together (Aitcin, 1998).

The compressive strength of UHPFRC subjected to a post-set heat treatment at 90^0C has been observed to vary between 150 and 250 MPa (Richard and Cheyrezy, 1994). The reaction of cementitious materials (Eq. 2.1) is accelerated by high temperature producing more calcium silicate hydrates (C-S-H). The result is that the microstructure of the concrete matrix is enhanced even further significantly increasing the compressive strength of UHPFRC (Richard and Cheyrezy, 1995). Based on tests to cylindrical specimens, Graybeal (2007) obtained average 28 day compressive strength values of 126 and 193 MPa on standard cured and heat-treated specimens respectively. On the other hand, Kazemi and Lubell (2012) tested 50mm cube UHPFRC specimens with 2-5% fibre content air-cured at ambient temperature and obtained compressive strength values of 147-174 MPa.

As for tensile strength, the increased bond strength between the fibres and the cement paste also enhances load carrying capacity. However, studies indicate that only fibre volumes equal to or greater than 2% have a significant influence on compressive strength. For example compared to an identical mix without fibres, compressive strength was observed to increase by about 15% at a fibre content of 2.5% by volume (Fehling et al., 2015). The other effect of fibres is that the failure of UHPFRC in compression is not as explosive as that of HSC for example because the steel fibres in UHPFRC hold the cracked pieces together (Le, 2008).

2.5.3 Flexural strength

The flexural strength σ_b is normally used to represent the bending capacity of a beam. It is based on the ultimate bending moment of a beam under loading (M_u) applying simple bending theory. Therefore the flexural strength is calculated as follows for a beam:

$$\sigma_b = 6M_u/bh^2 \qquad (2.10)$$

where b and h are cross-sectional width and height respectively.

The flexural strength is equal to the ultimate tensile strength only in a perfectly elastic material with a linear elastic stress distribution (Bentur and Mindess, 2007). Hence in a perfectly elastic material failure will occur once the load reaches the elastic limit. However,

UHPFRC can continue to carry additional load even after it cracks under tensile stress due to stress redistribution whereby the neutral axis moves up the stress block with a corresponding change in shape of the tensile stress distribution to rectangular (Fig.2.12). Therefore the load-deflection curve of UHPFRC continues to rise beyond the elastic limit so that σ_b will be greater than its tensile strength. It is the enhanced ductility of UHPFRC that increases its load bearing capacity represented by its flexural strength (σ_b). Additional fibres that do not increase the ultimate tensile strength can still increase σ_b by enhancing post-cracking ductility. The value of σ_b will depend on both the ultimate tensile strength and the post-cracking ductility of UHPFRC.

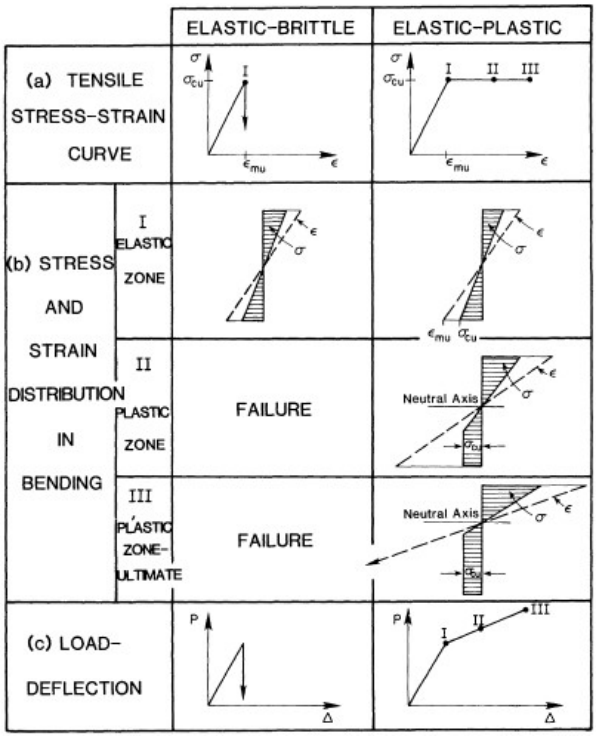

Figure 2.12: Comparison of tensile and flexural behaviour of ideally elastic and ideally elastic–plastic materials a) tensile stress-strain response b)stress and strain distribution in bending c) Flexural load–deflection curves (Bentur and Mindess, 2007)

Richard and Cheyrezy (1994) report results of early studies done in France with UHPFRC flexural tensile strength values of between 50-102 MPa depending on the type of hot-curing applied and the amount of steel fibres used (from 2% to 6% by volume). Barnett et al. (2007a) also tested specimens of UHPFRC with similar fibre contents under both three and four point bending tests and found flexural tensile strength values ranging between 15-41MPa. Le (2008) investigated the properties of UHPFRC through testing and FEA modelling as part of a study to assess its viability for production of paving flags. He reports values of flexural strength between 10-40 MPa depending on fibre dosage, size and heat treatment of the specimens. Fibre content has been shown to be a major influence on flexural strength of UHPFRC (Yoo et al., 2013).

Expressions of the form of Eq. 2.11 below have been used to estimate flexural strength by taking into account both matrix and fibre contributions in accordance with the rule of mixtures (Bentur and Mindess, 2007).

$$\sigma_b = A\sigma_{bm}(1 - V_f) + BV_f\, L/d \qquad (2.11)$$

In the above equation σ_{bm} is the flexural strength of the matrix, L and d are the fibre length and diameter respectively. The first term on the right hand side of Eq. 2.11 relates to the matrix contribution to the composite flexural strength and A is a dimensionless constant. The second term on the right hand side of the same equation is the fibre contribution to the overall strength. B is a constant with a stress dimension associated with the fibres. Since failure in FRC mainly occurs through failure of the interfacial shear bond well before the fibre strength is reached, B would normally be a function of this shear strength. Dividing each side of Eq. 2.11 by the term $V_f\, L/d$ reduces it to a linear form convenient for plotting as follows:

$$\sigma_b/(V_f\, L/d) = A\sigma_{bm}(1 - V_f)/(V_f\, L/d) + B \qquad (2.12)$$

Regression analyses of flexural strength values of FRC from experimental data have shown close correspondence to the above equation (Fig.2.13). Eq. 2.11 has been successfully applied to UHPFRC by Kang et al. (2010) who showed that for a constant fibre aspect ratio (L/d) the flexural strength increases linearly with fibre volume content between 1-5% (Fig.2.14).

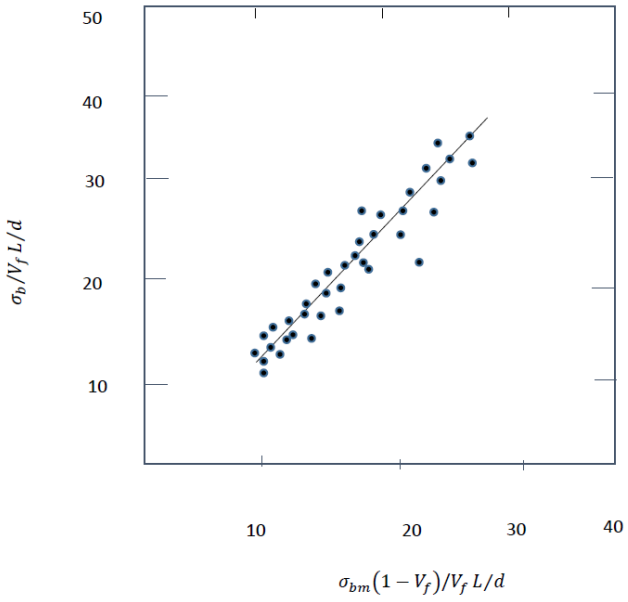

Figure 2.13: Correlation between composite flexural strength and matrix strength based on equation 2.12 (Bentur and Mindess, 2007)

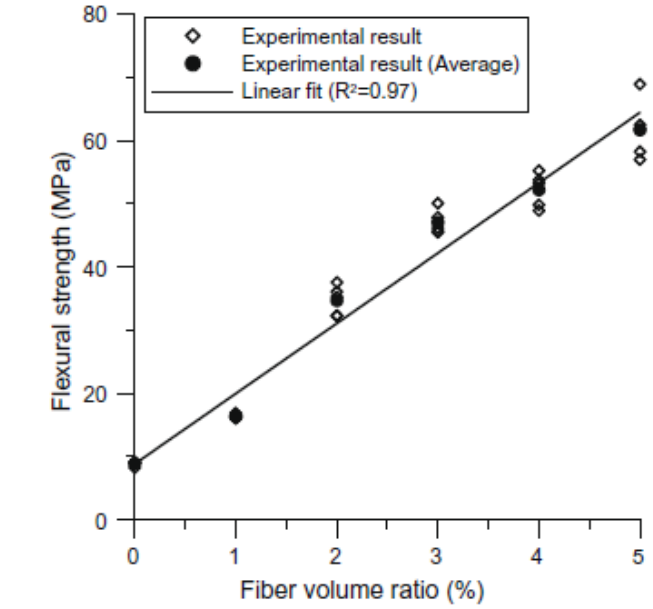

Figure 2.14: Variation of flexural strength with fibre volume content (Kang et al, 2010)

2.5.4 Fracture Energy (or toughness)

Fracture energy refers to the energy required to create a unit area of crack and is represented by the area below the stress-separation (σ-ω) curve. Fracture energy as commonly measured (for example by RILEM (2002) procedure), utilises the three point bending test on a notched specimen because the tensile stress field near the notch has been observed to be similar to that in a tensile test specimen (Bažant and Planas, 1998).

Because of the prominent role performed by fibres, the fracture energy of UHPFRC refers to the energy required for crack opening rather than just crack formation (Spasojević, 2008). The fibre-bridging action across fibres enables load transfer within cracked zones thus significantly enhancing the material's post-peak response. Richard and Cheyrezy (1994) reported fracture energy values of between10-40 KJ/m^2 obtained from the area under the Load-Deflection curve up to a deflection of 1/150 of span. This approach has its origins from the Japanese standards for testing fracture toughness of FRC (JSCE-SF4). The results they obtained were dependent on the type of hot-curing applied and the amount of steel fibres used (from 2% to 6% by volume). Barnett et al. (2007a) also tested specimens of UHPFRC with similar fibre contents under both three and four point bending tests and found fracture energy values of between 18-55KJ/m^2 depending on the specimen size. Le (2008) on other hand found that fracture energy values varied between 19-38KJ/m^2.

2.6 Size effect

Size effect refers to a phenomenon in which the strength of a structure is observed to depend on its size. Classical theories such as limit analysis in which material failure is based on stress or strain criteria ignore this size effect in their prediction of a structure's load capacity (Bažant and Planas, 1998). However, this is not a true reflection of concrete and other brittle or quasi-brittle structures in which structural strength has been observed to decrease as the size increases and vice versa (Mier, 2013).

2.6.1 Sources of size effect

The sources of size effect which may be of practical significance to concrete include (Bažant and Planas, 1998):

1. Boundary layer (wall) effect

This arises because the concrete layer (about the size of maximum aggregate) adjacent to the walls of the formwork has less large aggregates but more cement and mortar than the inner concrete. This boundary layer which is therefore stronger is a bigger proportion of the cross-section of smaller structures in which they produce a more noticeable size effect. In FRCs such as UHPFRC, this wall effect has been attributed to fibres adjacent to the formwork aligning parallel to it therefore forming a stronger layer on the surface of the structure (Barnett et al., 2007a) .

2. Diffusion phenomena

This arises because diffusion half-times are proportional to the square of the size of structure. So for example, hydration heat produces higher temperatures in thicker members. Also the diffusion process (heat conduction or pore water transfer) changes the material properties and produces residual stresses which can induce inelastic strains and cracking. Drying for example can produce tensile cracking in the surface layer of the concrete. Due to the different drying times and stored energies, the extent and density of cracking may differ between small and large members resulting in differences in response.

3. Statistical size effect

This is caused by randomness of material strength. Application of Weibull's theory in which failure occurs in the weakest link of a chain means that failure in a concrete material would occur at a point with the minimum strength. The statistical size effect arises because the larger the size of the structure the higher the likelihood of encountering a point with a lower strength. While this theory was previously thought to explain most size effects in concrete, a better understanding of the mechanics of failure of concrete structures has proved it inapplicable. Unlike in metals where growth of a micro-crack into a macro-crack could be enough to cause failure, concrete structures fail only after a large stable growth of crack zones (Mier, 2013). The resulting stress redistributions and strain

energy release then produce a more dominant size effect relative to any statistical size effect. In addition, just before failure this stable crack growth would normally be localised in a small zone so that random strength values outside of this zone would not have any effect.

4. Fracture mechanics size effect

The fracture mechanics size effect is caused by the fact that larger structures release more strain energy per unit crack extension compared to smaller ones. Hence crack propagation and failure in larger structures would be expected to occur at lower nominal stresses. Brittle materials exhibit a stronger size effect because they have no mechanism to restrict crack growth with the resulting strain energy released being used to further propagate cracks. Ductile materials on the other hand can inhibit crack propagation by dislocation for example whereby adjacent layers of atoms are able to slide relative to each other first before the onset of fracture. Concrete size effect response lies between that of purely ductile materials which exhibit no size effect and that of pure brittle materials that have a strong and constant size effect as shown if Fig.2.17 (Bažant and Planas, 1998).

2.6.2 Quantification of fracture mechanics size effects

Following from the definition mentioned previously, an assessment of size effect on a structure is based on quantifying the variation of its strength with size. The strength of a structure normally refers to its nominal stress at peak load. The nominal stress σ_N refers to the load per unit cross-sectional area as follows:

$$\sigma_N = C_N \frac{P}{bD} \qquad (2.13)$$

where P is the applied load, b the thickness of the structure, D the characteristic dimension of the structure or specimen (such as depth or span), and C_N a coefficient introduced for convenience. Where 2D similarity is intended in experimental tests, then b needs to be the same for all specimen sizes which also minimises size effect from diffusion phenomena (Bažant and Planas, 1998) mentioned previously. The coefficient C_N can be chosen to make Eq.2.13 consistent with any relevant theory. For example for a simply supported beam of span S and depth h loaded at mid-span by load P, σ_N may be chosen to coincide with the elastic bending formula for the maximum normal stress in the beam and the beam depth as the characteristic dimension ($D = h$) so that:

$$\sigma_N = \frac{3PS}{2bh^2} = C_N \frac{P}{bD} \qquad (2.14)$$

where

$$C_N = 1.5 \frac{S}{h} \qquad (2.15)$$

From Eq. 2.15 above, C_N depends on the span-to-depth ratio so that size effect can only be consistently defined by considering geometrically similar specimens or structures of different sizes, with geometrically similar notches or initial cracks. Without geometrical similarity, the size effect would be contaminated by the effects of varying structure shape.

2.6.3 The size effect equation

That the fracture mechanics size effect is caused by larger structures releasing more strain energy per unit crack extension than smaller ones can be illustrated by an example of two sizes of geometrically similar notched specimens (Fig.2.15). Therefore for geometrical similarity between the two specimens, the notch to depth ratio is the same ($\frac{a_1}{d_1} = \frac{a_2}{d_2}$) as is the depth to span ratio ($\frac{d_1}{S_1} = \frac{d_2}{S_2}$). In both specimens the crack is extended by the same length Δ_a from the notch tip:

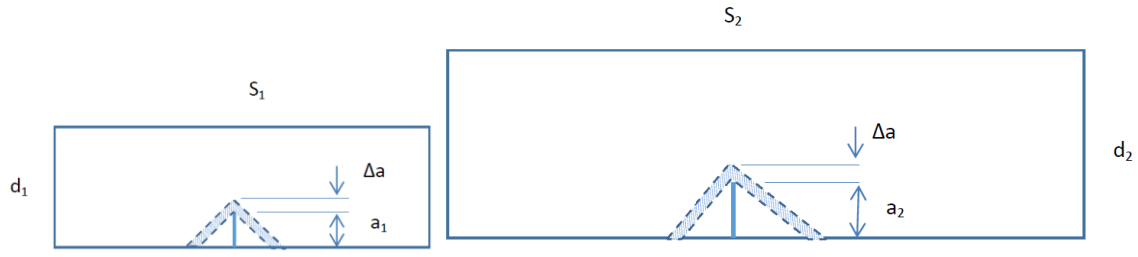

Figure 2.15: Illustration of size effect by geometrically similar notched specimens

The energy required to extend the crack per unit length is the same in both specimens. This is the fracture energy (G_f) which can be considered a material property. However, when the crack extends by Δ_a, the strain energy that is released can be reasonably considered as coming from the shaded area defined by the dashed diagonal lines in Fig.2.15. Assuming that the failure modes are also geometrically similar, the shaded area in the larger specimen is also larger but with the same slope. More strain energy is released from the larger shaded area in the larger specimen than in the smaller specimen by the same extension of crack. This is the source of the fracture mechanics size effect according to Bažant and Planas (1998).

Where there is no notch, the same argument about geometrical similarity of the failure modes can be applied whereby for the same crack extension a longer crack band is formed in the larger specimen at failure than in in the smaller specimen (Fig.2.16). The strain energy per unit volume released by extending the crack band of length a_0 by Δ_a when a nominal stress σ_N corresponding to the peak load is applied is given by $\frac{\sigma_N^2}{2E}$. This additional strain energy can be reasonably assumed to be released from the hatched strip in Fig.2.16.

The area of the hatched strip is given by:

$$h_f\Delta_a + 2k * \left[{}^1\!/_2\,(a_0+\Delta_a)^2 - {}^1\!/_2\,a_0^2\right] = h_f\Delta_a + 2k\left[a_0\Delta_a + {}^1\!/_2\,\Delta_a^2\right] \qquad (2.16)$$

Assuming the term Δ_a^2 is small enough to be ignored, the nominal stress σ_N can be obtained by equating the strain energy released by the hatched strip of thickness b to that required to extend the crack as follows:

$$\frac{\sigma_N^2}{2E} b[h_f\Delta_a + 2ka_0\Delta_a] = G_f b\Delta_a \qquad (2.17)$$

$$\sigma_N = \sqrt{\frac{2G_fE}{h_f+2ka_0\Delta_a}} \qquad (2.18)$$

The above is the size effect equation which Bažant and Planas (1998) re-write for convenience as follows:

$$\sigma_{Nu} = \frac{Bf_t}{\sqrt{1+D/D_0}} \qquad (2.19)$$

where f_t is the tensile strength of the material and B is a dimensionless constant such that

$$Bf_t = \sqrt{\frac{2G_fE}{h_f}} \qquad (2.20)$$

In the above equation G_f is the fracture energy, *E* the elastic modulus and h_f the width of the structure band front considered to be independent of structure size. D_0 is a constant with a length dimension such that:

$$D_0 = \frac{h_fD}{2ka_0} \qquad (2.21)$$

D_0 depends on the structure shape through the constant k but is independent of the structure size if the structures are geometrically similar (D/a_0 is constant). Eq. 2.19 provides a basis for quantifying size effect in structures of different materials. This can be done, for example, using bi-logarithmic plots of nominal strength against structure or specimen depth (Fig. 2.17). Size effect in concrete is observed to be transitional between that of classical failure strength theory (no size effect) and that of purely brittle behaviour predicted by LEFM (strong size effect).

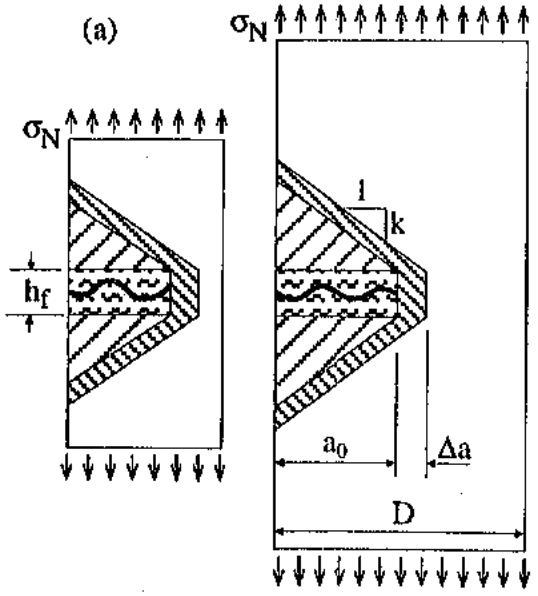

Figure 2.16: Size effect schematic based on crack band approach according to Bažant and Planas (1998)

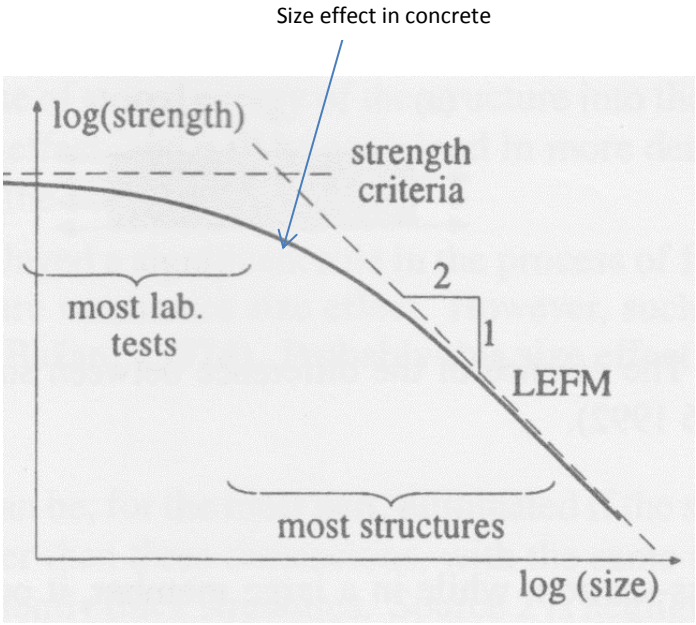

Figure 2.17: Size effect on strength on a bi-logarithmic plot (Adapted from Bažant and Planas (1998))

2.6.4 Size effect in UHPFRC

While research of the size effect on flexural strength of normal concrete has received a great deal of attention, Mahmud et al. (2013) observed a serious lack of sufficient and reliable experimental data in relation to UHPFRC on this aspect. This may be due to the high cost of testing of a large range of sizes required for proper establishment of size effects.

However, of the limited studies of size effect reported for UHPFRC, there are significant inconsistencies with some finding a significant size effect ((Le, 2008)) and others little (Spasojevic et al. (2008);Wille and Parra-Montesinos (2012)).

An experimental study by Le (2008) involving three point bending tests on notched specimens of UHPFRC with 2% fibre content indicated the existence of a size effect on flexural strength. On the other hand, based on UHPFRC specimens with 0-5% fibre content, Yoo et al. (2013) found a definite size effect at 0% fibre content which decreased with increased fibre content so that at 2% fibre content the size effect was negligible.

In both studies cited above, however, the range of specimen depths used (50-150mm) was too narrow to definitively establish the existence of size effect. Mahmud et al. (2013) used a wider range of specimen depths (30-150mm) and concluded that there was little size effect on the beam nominal strength of UHPFRC specimens due to the material's high ductility. However, the specimens used were geometrically similar only in their notch/depth ratio but not in their overall span/depth ratio. Bažant and Planas (1998) state that in order to properly investigate size effect, both the depth to span ratio and the notch to depth ratio need to be kept constant to avoid contaminating the results with shape effects.

A more recent study by Yoo et al. (2016) found a significant size effect on flexural properties of UHPFRC including flexural strength. However, they argued that this size effect was due to a variation in the fibre distribution characteristics within the specimens tested. By analysing high resolution photographs taken at crack surfaces, their study seemed to indicate that the observed size effect was due to poor fibre orientation in larger specimens in which the influence of the formwork surfaces (also called skin or wall effect) was less. By carrying out further tests, they found that UHPFRC beam specimens with similar fibre distribution characteristics were significantly less sensitive to size effects. However, these additional tests were limited to 3 UHPFRC specimens of depths 50,100 and 150mm all with 2% fibre content.

Chapter 3 – Concrete Fracture Models

3.1 Introduction

UHPFRC, like other types of concrete is a composite material whose properties and behaviour are mainly influenced by the characteristics of its constituents and their interaction with each other at different scales. Models for concrete can be formulated at four scales namely the microscale, mesoscale, macroscale and structural scale (Fig.3.1) as proposed by Mier (2013).

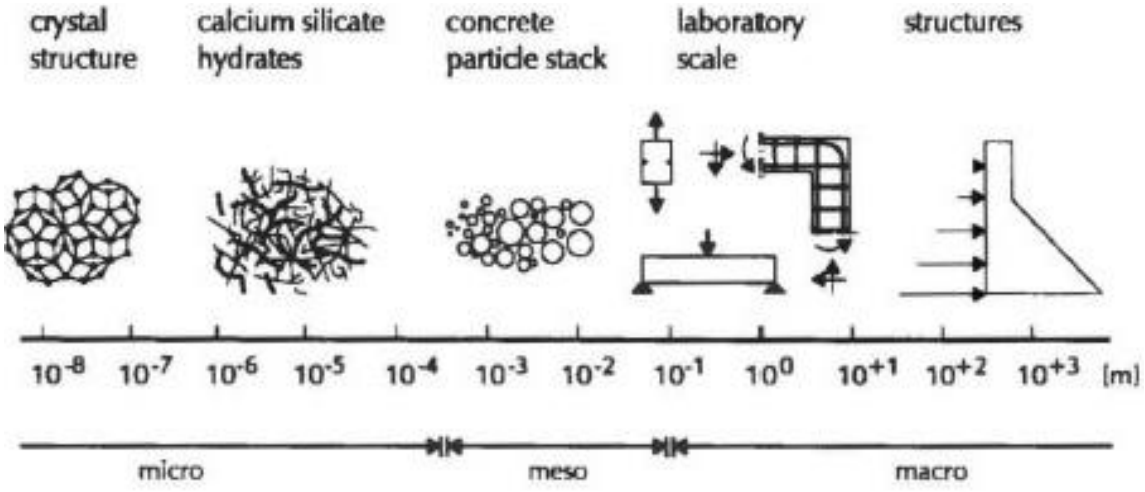

Figure 3.1: Scales for modelling concrete (Mier, 2013)

At the microscale, models describe the structure of the hardened cement paste in terms of material science of hydration products for example. Mesoscale models assume concrete to be heterogeneous with cement paste, aggregates, pores and water as its constituents. On the macroscale, models consider concrete to be homogeneous and rely on input of mechanical properties also measured at the same scale. Finally, structural scale models are concerned with the structural response of a concrete structure or element. The interaction between the above levels can also be represented by multiscale models which acknowledge the influence of lower scales on higher scales and propose suitable parameters to link appropriate length scales.

The models discussed in this chapter are at the macroscale as are the experiments to determine the input material properties. However, in the previous chapter a review of UHPFRC properties included explanations of the mechanisms and interactions of its constituents at lower scales (microscale and mesoscale). This is in line with the rationale that properties observed at a macroscale can be explained by interactions at the levels below.

3.2 Fracture zone models

UHPFRC has been developed by taking advantage of advances in concrete technology and material science in such a way as to achieve enhanced resistance to fracture failure.

Therefore fracture mechanics provides a logical framework within which to propose models to explain the observed experimental facts and to provide additional insight into the behaviour of UHPFRC. However, linear elastic fracture mechanics (LEFM) approaches adopt the concept of stress singularity which applied to a material with cracks and subjected to load results in infinite stresses at the crack tips. This is contrary to real materials in which the area directly in front of the crack (also called fracture or cohesive zone) would already be partially damaged significantly reducing the stresses therein (Petersson, 1981). In concrete materials, these stresses decrease with increasing strain resulting in a response within the fracture zone referred to as strain softening.

In practice, the size of the fracture zone relative to the rest of the material or structure determines whether or not linear elastic fracture mechanics can be used reliably. For most concrete materials and structures, the relative size of the fracture zone has been observed to be significant and hence requires approaches other than LEFM that take the influence of this zone into consideration (Bažant and Planas, 1998). Non-linear Fracture Mechanics (NFM) can be used to propose a theoretical framework for the modelling of this zone and of its influence on the overall behaviour of materials such as UHPFRC. The development of the fracture zone at the microscale is extremely complex. However, at the macroscale, understanding of crack propagation can be enhanced by modelling the strain localisation within the fracture zone using simpler criterion.

Elices and Planas (1989) have proposed a framework for classifying concrete models based on the damage mechanisms occurring within and outside the fracture zone (Fig. 3.2). In their framework, softening takes place in the fracture zone as the bulk material outside of this zone unloads. Localisation criteria specify the shape and size of the fracture zone. Hence for a fracture model to be complete it must describe a material's behaviour within both the fracture zone and the bulk material, and also prescribe the localisation criteria to be adopted.

In theory, damage can occur within both the fracture zone and the bulk material in the form of stiffness (Fig.3.2A-b) and/or stress degradation (Fig.3.2B-c). Stiffness degradation is where unloading occurs to the origin whereas stress degradation results in irreversible strain. General damage refers to where both types of degradation take place (Fig.3.2 A-a and B-a). Despite the fact that unloading in the bulk material has to accompany strain localisation most models assume an elastic behaviour within the bulk material (Fig.3.2A-c). This is because of the observation that including dissipation within the bulk in many cases only results in a small refinement in accuracy. Similarly, due to the fact that displacements within the fracture zone in concrete materials are monotonic , there is little practical difference between adopting any of the damage mechanisms (Bažant and Planas, 1998).

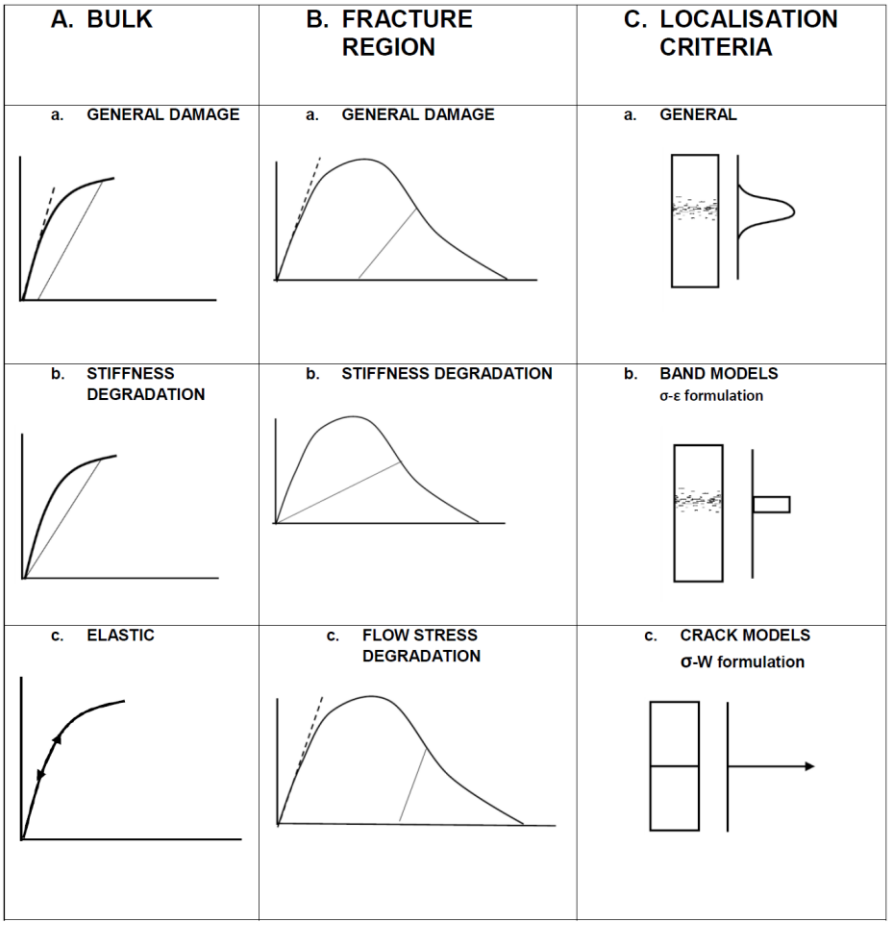

Figure 3.2: Model classification (Elices and Planas, 1989)

Though strain localisation is most realistically represented as a gradual process (Fig.3.3), simpler criteria are adopted whereby it is assumed to occur either within a band (Bažant and Oh, 1983) or along a line (Hillerborg et al., 1976) (Fig.3.4). The main difference between these two approaches is not in their concept but in their mathematical formulation (Elices and Planas, 1989).

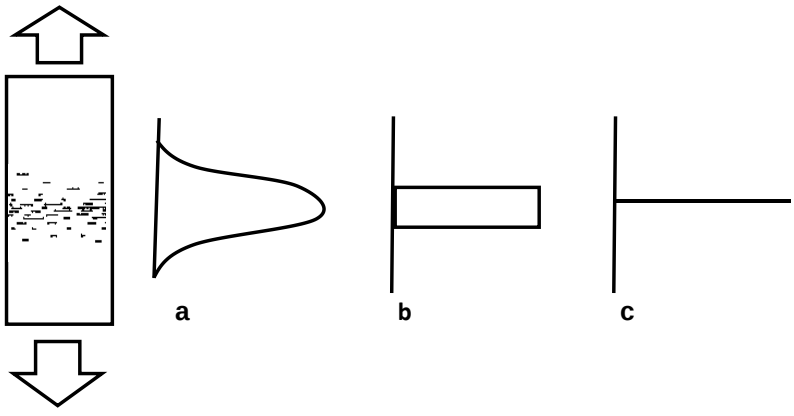

Figure 3.3: Modes of strain localisation a) smooth arbitrary shape b) within a band c) into a crack line (Elices and Planas, 1989).

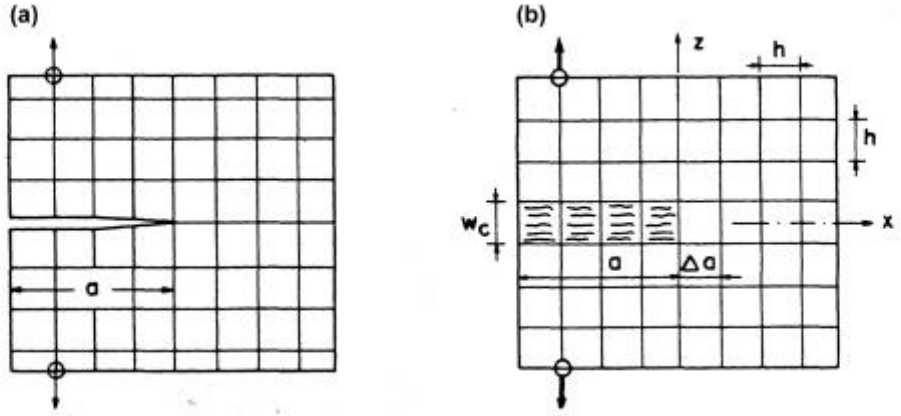

Figure 3.4: a) Cohesive crack model b) Crack band model (Bažant and Planas, 1998)

3.2.1 Cohesive Crack Models

These are mostly based on the fictitious crack model (FCM) developed in quasi-brittle materials by Hillerborg et al. (1976). Observations of stable tensile tests for concrete clearly indicated that some stress could still be transferred where a visible crack had occurred in the fracture zone possibly due to some aggregate interlock (Petersson, 1981). The fictitious crack model (FCM) for concrete replaces the whole fracture (cohesive) zone with a single 'fictitious' crack that has the ability to transfer cohesive stress. In the above study a simplified tensile test model is used to demonstrate the effect of the fracture zone in determining material properties (Fig.3.5).

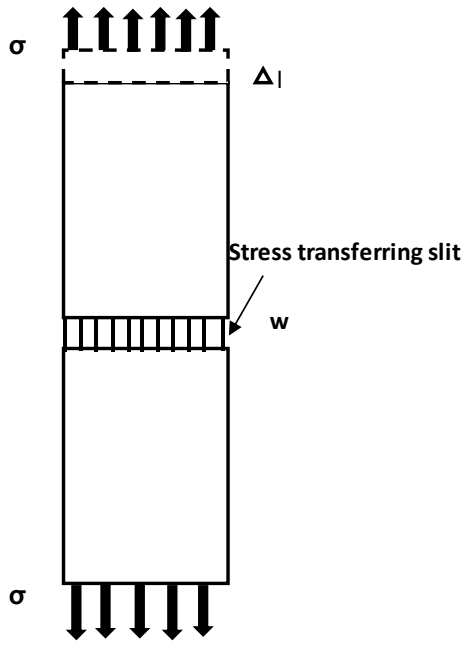

Figure 3.5: A simple direct tensile test in which crack is replaced by a slit of width w across which stress can still be transferred (Petersson, 1981).

A specimen of length L and cross-sectional A is subject to a tensile load P producing an extension of Δl before the onset of cracking. The stress-strain (σ-ε) relation is an important property of materials when loaded within the elastic range and up to their peak load. The elastic strain ε_e is then given by:

$$\varepsilon_e = {}^{P}/_{EA} \qquad (3.1)$$

where E is the elastic modulus.

Beyond the peak load, however, cracks localise in the fracture zone represented in Fig. 3.5 by a single slit of width w. The total strain ε_{total} is then given by:

$$\varepsilon_{total} = \varepsilon_e + {}^{w}/_{L} \qquad (3.2)$$

Eq.3.2 can also be written as:

$$\varepsilon_{total} = {}^{P}/_{EA} + {}^{w}/_{L} \qquad (3.3)$$

When $w = 0$, strain is wholly elastic (P/EA) and is independent of L. However, when the crack begins to widen (w is non-zero), the total strain in Eq. 3.3 is now dependent on L. From this point onwards $\sigma - \varepsilon$ relation is no longer a material property. Therefore in FCM, a direct post-post peak measure is made of the change in w with σ. The $\sigma - \omega$ curve so produced is defined by the tensile strength (maximum stress), maximum crack width and the shape of the curve. The shape of the curve can be defined by a function f such that:

$$\sigma = f(w) \qquad (3.4)$$

The $\sigma - \omega$ curve defined by the above function is also called a softening curve as σ decreases with ω. Hence the elastic range is characterised by $\sigma - \varepsilon$ while the post peak behaviour by $\sigma - \omega$ which is considered a material property since it is independent of L (Fig.3.6). When a material is loaded beyond the elastic limit and peak load, the fracture zone (represented by a single crack in FCM) starts to widen according to Eq. 3.4 while the rest of the bulk material unloads.

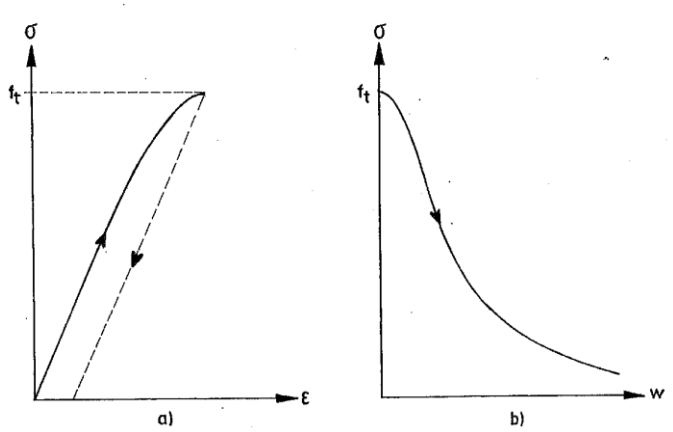

Figure 3.6: a) The σ-ε curve determines material deformation properties outside fracture zone b) The σ-ω curve determines material deformation properties within the fracture zone (Petersson, 1981).

Hillerborg et al. (1976) therefore proposed the description of the material deformation properties using two relations:

i) The stress-strain relation ($\sigma - \varepsilon$) for the bulk material outside the fracture zone (fig.3.6a)

ii) The stress-deformation ($\sigma - w$) for the fracture zone. The fracture zone is replaced by a crack that can transfer stress depending on its width according to this $\sigma - w$ curve. (fig.3.6b).

In the simplest and most commonly used case, the fracture zone starts developing at one location when the first principal stress reaches the tensile strength (σ_t) and it then develops perpendicular to this stress. The energy required to create a unit area of crack is called the fracture energy (G_f) and is represented by the area below the $\sigma - \omega$ curve such that:

$$G_f = \int \sigma dw \qquad (3.5)$$

Hence the complete definition of a cohesive crack model includes the definition of the bulk behaviour, the specification of the condition for crack formation and the specification of the equations for crack evolution as per the framework proposed by Elices and Planas (1989). Based on the above material properties, a single characteristic length l_{ch} can be used to define the brittleness of a material (Petersson, 1981). This is done by equating the energy consumed in the fracture zone in propagating a crack to the elastic energy released from the material outside the fracture zone at the peak tensile load. Hence the characteristic length is given by:

$$l_{ch} = G_f E / \sigma_t^2 \qquad (3.6)$$

where G_f, E and σ_t are the fracture energy, elastic modulus and tensile strength respectively. It is an indicator of the length of specimen required to make strain energy released for crack propagation at maximum load equal to that in the fracture zone. It means then that the lower the l_{ch} the more prone to crack propagation the material will be making it more brittle (Petersson, 1981).

FCM was initially applied to plain concrete in which physical processes within the matrix such as aggregate interlock were responsible for the stress transfer within the fracture zone (Fig.3.7a). It was later extended by Hillerborg (1980) to fibre reinforced concrete (FRC) in which fibres now played a prominent role in the stress transfer by a crack bridging action (Fig.3.7b). As a result the softening curve for FRC is now much longer and can be conveniently represented by crack bridging functions whereby the fracture energy for UHPFRC is now defined as the energy required for crack opening while the energy needed for crack formation is negligible in comparison (Spasojević, 2008).

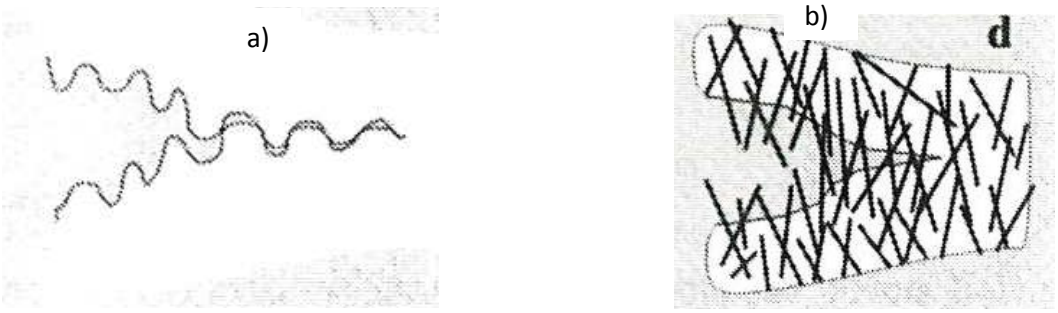

Figure 3.7: Some physical sources of cohesive crack a) aggregate frictional interlock b) fibre bridging (Adapted from Planas et al. (1995))

All these models adopt cohesive crack concepts and therefore fall under the broader cohesive crack models. In FRC the action of fibres is incorporated into the cohesive crack model by its effect on the softening curve. In the simplest cohesive crack model, the following assumptions are made (Bažant and Planas, 1998):

1. The behaviour of the bulk material is isotropic linearly elastic described only by the elastic modulus E and Poisson's ratio v
2. A crack forms when the maximum principal stress at a point reaches the tensile strength (σ_t). The crack forms perpendicular to the direction of maximum stress.
3. For a monotonic pure opening mode, the stress transferred between the crack faces is given by softening curve $\sigma = f(w)$

Limitations of the Cohesive Crack Models

One of the limitations of the Cohesive Crack Model is the difficulty of determining from experiments the parameters required as material inputs. While the direct tensile test is the ideal way to obtain both the tensile strength and $\sigma - \omega$ curve, it has been found to be difficult for several reasons including (Bažant and Planas, 1998):

- In testing prismatic or cylindrical specimens, the location of the crack is not known *a priori*
- Concrete heterogeneity may lead to multiple cracking even in tapered /dog-bone specimens
- In notched specimens where a single crack is formed, the specimens tend to shift to an asymmetric mode of fracture due to either rotation in the supports or internal elastic rotations in the specimen itself
- Even when rotations are avoided using short specimens and a very stiff machine the cracks growing from both sides of the specimens do not meet each other so that a true single crack is not obtained

Due to the difficulties observed in achieving a stable tensile test, indirect tests are commonly used from which these properties are obtained. Some common indirect methods to obtain the tensile strength include the split tensile test (Lofgren et al., 2004) and the flexural tensile test (Einsfeld and Velasco, 2006). The tensile stress field near a notch in a three point bending (TPB) test specimen has been found to be similar to that in a tensile test specimen (Bažant and Planas, 1998) from which the raw stress-crack width ($\sigma - \omega$) curve can be obtained by inverse analysis. While in reality every concrete mix will have its own $\sigma - \omega$ curve, it has been observed that these curves are similar in shape for different mixes of ordinary concrete. Therefore raw $\sigma - \omega$ curves can be idealised into simpler shapes that are easier to implement in models.

Unlike for normal concrete where a bilinear softening curve is generally accepted as providing good results, there is still a lack of agreement as to which curve is best for UHPFRC with different shapes proposed in literature including linear, bilinear, trilinear and exponential. Studies by Spasojević (2008) and Le (2008) adopted linear softening curves successfully to simulate the flexural behaviour of UHPFRC. Kang et al. (2010) carried out inverse analysis based on data from notched three-point bending (TPB) tests of specimens with varying fibre contents and proposed a tri-linear cohesive stress-crack width softening relation as being most appropriate for UHPFRC. However, following a similar approach based on inverse analysis of data from TPB test specimens with fibre

contents between 1- 4%, Yoo et al. (2013) concluded that bilinear softening relations were just as accurate as tri-linear relations for FE simulations of UHPFRC. If the shape of the σ-ω curve is known, the curve can be fully established by just measuring σ_t and G_f (Hillerborg, 1980). G_f is commonly estimated by measuring the area under the full load deflection curve from stable TPB test on notched specimens (RILEM, 2002). G_f is then calculated as the work done divided by the initial ligament area so that:

$$G_f = \frac{1}{BD}\int P d\delta \qquad (3.7)$$

where B is the specimen width, D is its depth, P is the applied load and δ is the deflection.

However, fracture energy values obtained directly from the commonly used three point bending test on notched specimens have been observed to be affected by spurious energy dissipations from sources such as not including the final portion of the load-displacement curve (Bažant and Planas, 1998). Denneman et al. (2011) proposed a technique for determining fracture energy (G_f) of High Performance Fibre Reinforced Concrete (HPFRC) by extrapolating the load-displacement curves which they then used to define an exponential softening function by parameter fitting of results from TPB tests.

The initial slope of the softening curve has been found to control important structural properties (Bažant and Planas, 1998). This is because in cases where a structure or specimen does not undergo large softening, a linear approximation to the softening curve is very accurate (Fig.3.8). This is indeed the case for notched specimens and un-notched specimens with typical laboratory test sizes. This fact was observed by Spasojević (2008) to be applicable to modelling UHPFRC post peak behaviour thereby justifying the use of a linear softening curve (Fig.3.9).

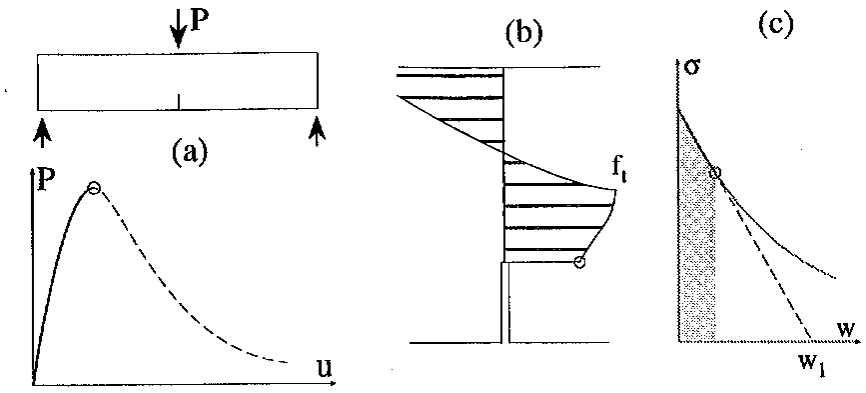

Figure 3.8: Notched beam in TPB test *a*) Peak load on load displacement curve *b*) Stress profile along the ligament at peak *c*) Softening at peak load by the material at the notch tip (Elices and Planas, 1996)

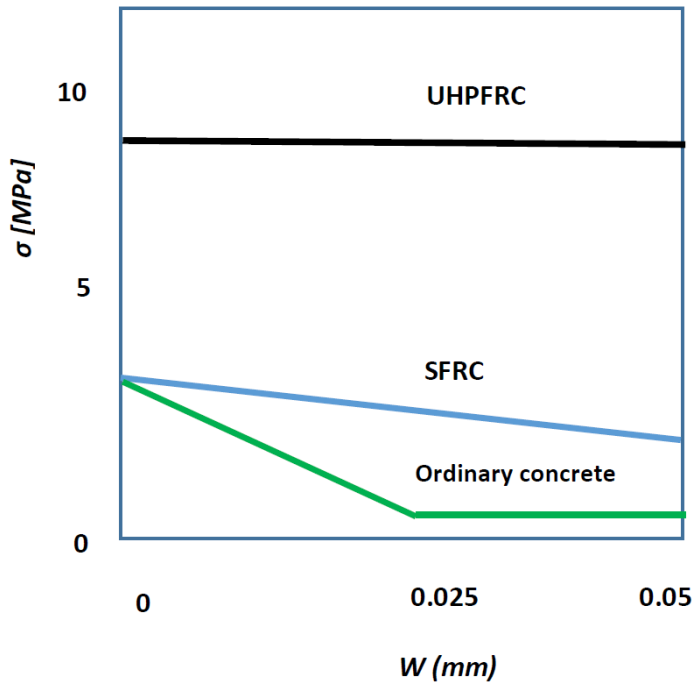

Figure 3.9: Comparison of σ-ω curves for UHPFRC with other types of concrete (Spasojević, 2008)

3.2.2 Crack Band Models

These were originally proposed by Bažant and Oh (1983) as a fracture zone model that took advantage of the strengths of the then already popular smeared crack models while overcoming their inherent difficulties. Like the original smeared crack models, the crack band model assumes that an infinite number of parallel cracks of small opening are distributed (smeared) over the finite element (Fig.3.4b). Fracture is then modelled by reducing the material stiffness and strength in the direction normal to the cracks after peak strength of the material is reached. Modelling cracking like this by reducing the material stiffness can be easily implemented within a finite element framework and was the main reason for the wide adoption of the smeared crack approach.

However, as mentioned in the description of CCM in the previous section, fracture involves softening so that modelling fracture by the $\sigma - \varepsilon$ curve alone as per the original smeared cracking model does not produce objective results as they are found to be sensitive to the adopted mesh. In theory, continued refining of the mesh should produce increasingly better results but in practice this leads to instabilities below a certain mesh size. These are caused by the difficulties of the smeared cracking in localising in arbitrarily small sizes. The crack band model overcomes these difficulties by limiting the smallest element size within which a smeared crack can localise. It does this by introducing an additional material property called the reference length (h_c) which must be specified when a softening stress-strain ($\sigma - \varepsilon$) curve is used in modelling (Bažant and Planas, 1998).

Basic assumptions

The crack band model can also completely be defined within the framework provided by Elices and Planas (1989) by specifying the bulk behaviour, the condition for crack band formation and crack band evolution. In addition, the thickness of the softening band (h_c) which is assumed to be a material parameter must be given. Hence in the simplest case, materials with no bulk dissipation must also have elastic bulk behaviour. For concrete this is generally assumed to be isotropic linear elastic and therefore defined by an elastic modulus, E and a Poisson's ratio ν. For isotropic materials the behaviour at a point is usually assumed to be elastic until the maximum principal stress reaches the tensile strength (σ_t). Thereafter, the fracture starts as an array of densely and uniformly distributed cracks normal to the maximum tensile stress direction, and distributed over the band thickness, h_c.

The crack orientation within the crack band remains fixed and it is assumed that the stress tensor and the strain tensor remain uniform through the band thickness. Stresses and strains are related through a constitutive equation or stress-strain relationship displaying softening. As in CCM it is usually assumed that the traction vector acting on crack planes depends upon the average crack opening per unit band thickness. For the simple case described above, it has been found that the crack band model is numerically equivalent to CCM (Bažant and Planas, 1998) as reviewed below. The width of the band cannot be lower than a characteristic value, h_c. Thus for linear behaviour followed by softening, the expression for fracturing elongation can be equated to the cohesive crack opening (w) as follows:

$$h_c \varepsilon^f = w \qquad (3.8)$$

where ε^f is the inelastic fracturing strain.

Hence if the softening curve of stress against fracturing strain $\phi(\varepsilon^f)$ is equated to the softening curve of stress against cohesive crack opening then the stress-elongation curve for the crack band model becomes the same as that of the cohesive crack model (Fig.3.10):

$$\phi(\varepsilon^f) = f(w) = f(h_c \varepsilon^f) \qquad (3.9)$$

Eq.3.9 can also be written as:

$$f(w) = \phi(w/h_c) \qquad (3.10)$$

where $f(w)$ is the function for the cohesive crack model.

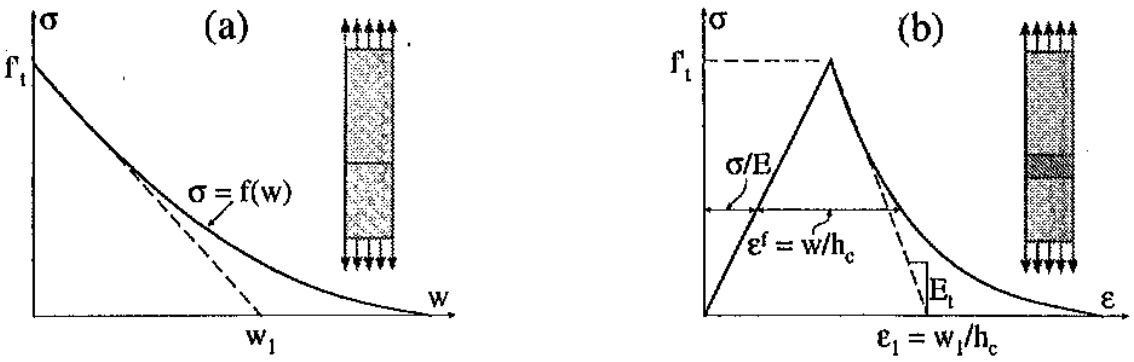

Figure 3.10: correspondence between softening curve of the cohesive crack model and the stress-strain curve of the crack band model (Bažant and Planas, 1998)

The above figure also shows that the initial linear approximation for the crack band softening curve will be just as good as that of the cohesive crack model as the horizontal intercept $\varepsilon_1 = w_1/h_c$. Similarly the energy required to form a complete crack (fracture energy G_f) is the same as that required for a fully softened crack band with $w = w_f$ and a fracture energy density γ_f as follows:

$$G_f = \frac{W_f}{A} = h_c \gamma_f \qquad (3.11)$$

The characteristic length l_{ch} can also be expressed in terms of the properties of the crack band model as follows:

$$l_{ch} = \frac{EG_f}{\sigma_t^2} = h_c \frac{E\gamma_f}{\sigma_t^2} \qquad (3.12)$$

In many practical situations characteristic reference width (h_c) is much smaller than the overall specimen length (L) so that for engineering purposes there is no difference between the cohesive crack and the crack band models (Bažant and Planas, 1998). In reality, cracking begins earlier before tensile strength is reached so that there is energy dissipation within the bulk. For concrete materials where there is one main crack neglecting the pre-peak nonlinearity is acceptable for practical engineering purposes because the large post peak strains dominate over the pre-peak deformation. However, where there are no sharp localisations, the pre-peak nonlinearity may need to be included due to its increased dominance. This would indeed be the case where the UHPFRC has a large strain hardening after first cracking as modelled analytically by Spasojević (2008).

Limitations of the crack band model

The limitations of the crack band model have been discussed in detail by Elices and Planas (1989) and only selected aspects are reviewed in this section. Stress-strain constitutive equations that display softening lead to predictions that are mesh-sensitive unless a localisation 'limiter' is specified such as h_c. However, there is no direct experimental evidence of a softening band of constant thickness (h_c) and uniform strain through its thickness. Only indirect evidence is available of a h_c value of about 3 aggregate sizes as suggested by Bažant (2002). Further, it appears that numerical predictions of behaviour are largely insensitive to band thickness when the same softening relation $\sigma - w$ curve is used. This aspect is discussed further in section 3.32 in relation to its implementation in the finite element method. Analytical studies by Habel (2004) and Lappa (2007) and numerical work by Le (2008) on modelling UHPFRC cite the difficulty in determining the appropriate reference length as being a significant limitation in applying the smeared crack approach to UHPFRC. It is also not possible to satisfy compatibility and equilibrium conditions at every point within the band when a constant strain throughout the band thickness is assumed. It is only possible to satisfy compatibility and equilibrium on average. This requires a well-defined algorithm taken as being of a band-type so that the minimum size of elements to be considered is a band of thickness h_c.

3.2.3 Damage Models

Stress-strain relations based on continuum damage mechanics are always associated with localisation criteria to eliminate mesh-objectivity. Damage concepts can also be used to generate stress-crack displacement formulations for the crack approaches. However, as mentioned above, retaining the continuum mechanics framework lends itself to easier finite element formulation and is therefore more convenient for structural analysis. Developments in the formulation of high level constitutive equations have led to many models based on the internal variables concept (Elices and Planas, 1989). Lemaître and Chaboche (1994) have discussed in detail the concepts underlying such formulations drawing from both continuum mechanics and thermodynamics. Damage is described as the evolution between a virgin or initial best state and initiation of a macro-crack. In concrete this evolution occurs through brittle fracture by which the cohesion between atoms or crystals is destroyed by monotonic loading without producing much irreversible deformations. At a macroscopic level it is difficult to distinguish between a virgin and a fully damaged material so that the deteriorated state can only be represented by imaginary internal state variables called damage variables.

Damage represents surface discontinuities in the form of micro-cracks or volume discontinuities in the form of cavities (voids). For isotropic damage, the cracks and cavities

have an orientation distributed uniformly in all directions. The damage variable does not depend on the orientation of any surface normal and the damaged state is completely characterised by a scalar D. The damage variable (D) can be defined by considering a representative element of finite volume from such a damaged solid. If the total initial surface area was S before and effective area S' after damage (cracks, cavities, stress concentrations and interaction between defects), then the difference is given by:

$$S_D = S - S' \tag{3.13}$$

The mechanical measure of local damage (D) can be given by:

$$D = S_D/S \tag{3.14}$$

Therefore the damage variable is a representation of the relative area of cracks and cavities and falls within the range $0 \leq D < 1$ where

D=0 corresponds to the non-damaged or virgin state
D=1 corresponds to the fully damaged state.

It is then possible to calculate the effective stress as that stress over the section which effectively resists the forces. Hence if a uniaxial force (F) is applied on a representative section of a solid, then stress would normally be given by:

$$\sigma = F/S \tag{3.15}$$

If there is isotropic damage (D) then the effective area of resistance is:

$$S' = S - S_D = S(1 - D) \tag{3.16}$$

The effective stress σ' then becomes:

$$\sigma' = \sigma S/S' \text{ or } \sigma' = \sigma/(1 - D) \tag{3.17}$$

Evidently, $\sigma' \geq 0$ and for a virgin material $\sigma' = \sigma$ while at the point of fracture $\sigma' \to \infty$. For multiaxial isotropic damage, the term $(1 - D)$ is the same in all directions since the ratio S/S' is not dependent on the orientation of load application. Therefore the effective stress becomes:

$$\sigma' = \sigma/(1 - D) \tag{3.18}$$

The normal assumption is that the deformation behaviour of the material is only affected by damage in the form of effective stress. Therefore the constitutive laws of the virgin material behaviour in which the usual stress is replaced by the effective stress can be used to represent any deformation behaviour of the damaged material.

Hence for the uniaxial case, the linear elastic law of a damaged material can be given by:

$$\varepsilon_e = \frac{\sigma'}{E} = \frac{\sigma}{(1-D)E} \qquad (3.19)$$

The general damage continuum models have three main features (Elices and Planas, 1989) :

1. A set of independent internal variables P_k that with the infinitesimal strain tensor ε (or stress tensor σ) are assumed to characterise uniquely the instantaneous state of the body at a given point. They can be related to kinematic or structural features

2. A set of equations relating the stress to the strain and to the internal variables:

$$\sigma = \Lambda(P_k)\varepsilon - \boldsymbol{T}(P_k) \qquad (3.20)$$

where $\Lambda(P_k)$ is a fourth-order tensorial function depending only on internal variables, and $\boldsymbol{T}(P_k)$ is a second-order tensorial function of the internal variables. When $\boldsymbol{T}$ is 0 and $\Lambda(P_k) = \Lambda_0$ (i.e. constant), the behaviour is purely elastic. When $\boldsymbol{T}$ varies and $\Lambda(P_k) = \Lambda_0$ (i.e. constant) then the model displays flow-stress degradation without stiffness degradation. When $\boldsymbol{T}$ is 0 but $\Lambda(P_k)$ varies then model displays stiffness degradation and always unloads to the origin. General damage occurs when both $\Lambda(P_k)$ and $\boldsymbol{T}(P_k)$ are variable.

3. A set of 'flow rules' which specify the way in which the internal variables increase when loading proceeds. Flow rules must contain conditions that are irreversible (2nd law of thermodynamics). They may be specified at many different levels. An example includes use of one or more loading functions from the plasticity theory. A multi-yield surface type formulation is also possible. Restricted flow rules can be generated from special loading cases, the monotonic loading case being the simplest and most useful.

A widely used example of continuum damage model is the Scalar Damage Model (Mazars, 1981; Mazars, 1985). In this model the only primary internal variable is a scalar damage variable 'D' which varies between 0 and 1 such that $D = 0$ for no damage and $D = 1$ for complete failure. Eq. 3.20 is then written as:

$$\sigma = (1 - D)\, \Lambda_0 \varepsilon \qquad (3.21)$$

where Λ_0 is the elastic (undamaged) stiffness tensor

3.3 Implementation of concrete models in FEM

3.3.1 Cohesive crack model (CCM)

Three basic approaches are currently used with cohesive cracks implemented in FEM (Bažant and Planas, 1998):

1. Discrete inter-element crack approach

Here the crack extends between elements in which the cohesive forces are most commonly simulated by using interface elements connecting the nodes on both sides of the crack (Fig.3.11). In modelling discrete cohesive crack propagation, there are generally two approaches that are used in mesh generation (Su, et al., 2010):

a) Mode I fracture specimens in which the crack path is known a priori can be easily simulated by pre-inserting or pre-embedding elements with cohesive zone formulation between the finite elements in the initial mesh (Bažant and Planas, 1998).
b) If the crack path is not known in advance then re-meshing techniques would be required whereby the meshes are constantly changed as cracks propagate.

The choice of the approach to be used can be based on several factors including computational efficiency and complexity of crack patterns to be modelled.

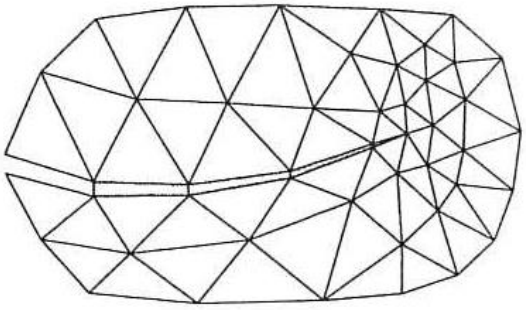

Figure 3.11: Inter-element discrete crack element (Bažant and Planas, 1998)

2. Smeared crack approach

In this approach, conventional finite element formulations are used with element-dependent stress-strain relations obtained by smearing the crack opening displacement *w* in the element intersected by the crack (Fig.3.12).The advantage of this approach is that the mesh topology is not changed during crack growth. The formulation resulting from the smeared crack concept is very close to the crack-band model which is implemented in many commercial FE codes.

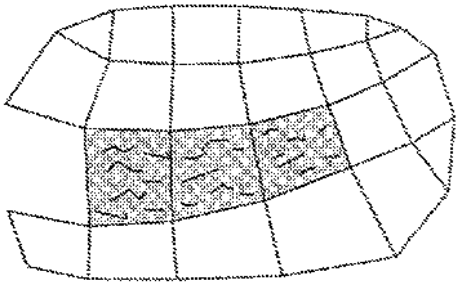

Figure 3.12: Inter-element smeared crack element (Rots, 1989)

3. Discrete intra-element crack approach

In the above meshing approaches, the crack boundaries coincide with those of the element necessitating continuous re-meshing where the crack path is not known in advance. For complex crack patterns this can be computationally costly. In the discrete intra-element crack approach, the crack geometry is independent of the mesh so that a crack can propagate within an element (Fig.3.13). They have a common feature in that after localisation, the stress-strain constitutive relation is replaced by a softening relation with stress and displacement as in the cohesive crack model. The numerical implementation of the intra-element crack essentially consists in introducing discontinuous shape functions into an element. An example of the use of this approach in UHPFRC is provided by Li (2016). He embedded the cohesive zone model into the extended Finite Element Method (XFEM) which he then used successfully to simulate crack propagation in a notched UHPFRC specimen under the TPB test.

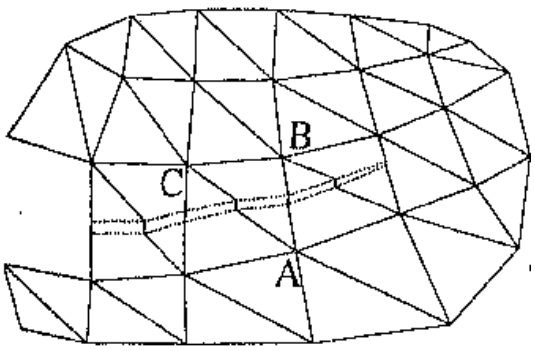

Figure 3.13: Intra-element crack (Oliver, 1995)

3.3.2 Crack band model

A strict application of the crack band model as formulated by Bažant and Oh (1983) where h_c is a material constant would require a finite element mesh in which the crack band has exactly a width of h_c. Hence if the crack band location is not known in advance, all the finite elements would have to be of width h_c. However, in practice this is not necessary

because the most important macroscopic parameter that is explicitly required is fracture energy (G_f) and h_c is only a contributor to it as follows:

$$G_f = h_c \gamma_F \tag{3.22}$$

Hence if a finite element size larger than h_c is required, the same response can be maintained as long as the fracture energy is kept constant (Fig. 3.14). This is achieved by distributing the fracturing strain uniformly over the element and rescaling the softening part of the stress-strain curve to keep G_f constant. The rescaled stress-strain curve will depend on the element size as follows:

$$h^{(e)} \gamma_F^{(e)} = h_c \gamma_F \tag{3.23}$$

where $h^{(e)}$ is the size of the element and $\gamma_F^{(e)}$ is the density of fracture energy to be used for this element. For models with elastic-softening stress-strain curves scaling is done with reference to Fig.3.14 as follows:

$$\varepsilon^{f(e)} = \frac{h_c}{h^{(e)}} \varepsilon^f \tag{3.24}$$

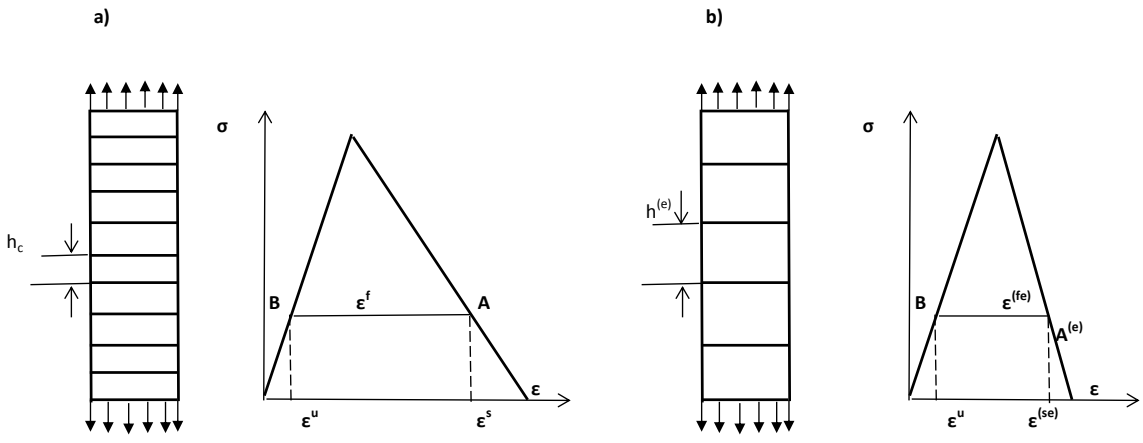

Figure 3.14: a) Specimen under tensile stress with finite elements of width h_c b) Same specimen but with finite elements of arbitrary width $h^{(e)}$ (Adapted from Bažant and Planas (1998))

3.4 Numerical simulations of UHPFRC behaviour

The framework for classifying concrete models proposed by Elices and Planas (1989) discussed previously is based on the damage mechanisms occurring within and outside the fracture zone and the adopted crack localisation criteria. Damage within the fracture zone will always result in energy dissipation from the surrounding material. However, the linear elastic assumption within the material bulk is adopted in many commonly used concrete models where the effect on the overall result is observed to be small. Models incorporating this assumption have been used successfully with both discrete crack (Hillerborg et al., 1976) and crack band (Bažant and Oh, 1983) localisation approaches to simulate the load-deflection response and predict failure loads for UHPFRC test specimens. For example the concrete smeared model in ABAQUS used by Le (2008) to simulate the flexural response of UHPFRC test specimens uses the crack band localisation approach. The model also assumes that damage involves only stiffness degradation so that unloading occurs to the origin. The concrete damaged plasticity (CDP) model in ABAQUS used by Mahmud et al. (2013) to simulate the TPB test on UHPFRC specimens on the other hand adopts general damage within both the material bulk and fracture zone involving both stress and stiffness degradation. Though CDP adopts a crack band (smeared crack) localisation approach, it can be also be classified as a 'damage model' in that its constitutive formulation uses internal variables which are more sophisticated in representing real life materials.

However, analytical studies by Habel (2004) and Lappa (2007) and numerical work by Le (2008) on modelling UHPFRC cite the difficulty in determining the appropriate reference length as being a significant limitation in applying the smeared crack approach to UHPFRC with a suggestion that the use of CCM may be more appropriate for eliminating this difficulty. It has also been suggested that discrete crack approaches could be more appropriate in cases where macro-cracks with strong discontinuity need to be modelled thereby lending themselves to the use of cohesive elements in finite element methods (Su et al. (2010); Yang et al. (2009)).

A variety of idealised σ-w curve shapes have been used as an input for the general concrete models discussed previously and used in different numerical studies to simulate the mechanical behaviour of UHPFRC. These studies have been carried out to investigate the influence of factors such as fibre content, distribution, and orientation as well as the effect of size on the mechanical behaviour of UHPFRC. Kang et al (2010) investigated the influence of fibre content on the fracture properties of UHPFRC. Using tri-linear softening relations in their finite element (FE) simulations they found that the flexural tensile strength of UHPFRC increases linearly with increasing content and that the rule of mixtures could be applied to UHPFRC.

Yoo et al. (2013) on the other hand adopted bilinear softening relations in their finite element (FE) simulations. They investigated the effect of fibre content on the strength and deflection capacity of UHPFRC both in tension and compression, and on the bond strength and pull-out energy of embedded fibres. They found that compressive load carrying capacity and elastic modulus improved with increase in fibre content up to 3%. On the other hand, fibre bond strength and pull-out energy improved with increased fibre content but only up to 2% and then deteriorated. In relation to the flexural response of UHPFRC, the first cracking load and corresponding deflection and crack mouth opening displacement (CMOD) did not change with fibre content. However at peak load the flexural strength, deflection and CMOD were observed to increase almost linearly with increase in fibre content as observed by Kang et al. (2010) which they attributed to improvement in the fibre bridging effect.

There are several studies that have investigated the effect of fibre orientation and distribution on flexural behaviour of UHPFRC. Kang and Kim (2012) made use of test data from image analysis to estimate the fibre distribution in three point bending tests on notched specimens with different fibre orientation. They then adopted a cohesive crack model (CCM) implemented using interface elements to model crack propagation at the notch in order to predict flexural behaviour considering differences in the fibre orientation and distribution. They found that fibre orientation and distribution have a strong influence on flexural behaviour of UHPFRC especially on deflection hardening. Their finite element analysis which adopted a post-cracking curve combining matrix softening and fibre-bridging (determined from probabilistic fibre orientation distribution) produced results which matched the test results well.

Denneman et al. (2011) developed a method for carrying out numerical simulation of Mode I (opening mode) fracture in High Performance Fibre Reinforced Concrete (HPFRC) that considered size effect for use in analysis and design of pavement structures. Using an exponential softening implemented in a CCM referred to as the ‘embedded discontinuity method’ they simulated the flexural behaviour of geometrically similar TPB specimens in order to study their size effect. The numerical model satisfactorily simulated the opening mode fracture behaviour of HPFRC under TPB tests. They also found that HPFRC is subject to size effect though simulation could not match experiment data satisfactorily. They attributed this discrepancy to the fact that their model could only predict size effect due to fracture mechanics and not from other sources like specimen preparation.

Building on their previous work, Denneman et al. (2012) conducted another study to demonstrate that fracture mechanics material parameters could be used to accurately predict the flexural capacity of HPFRC specimens of different sizes and geometry. Test data was obtained from HPFRC specimens of different sizes subject to TPB testing and from centrally loaded round panels. Exponential softening curves were obtained from parameter fitting of results for both flexural beam and tensile splitting tests. Numerical simulations of the flexural tests on the beams and panels were done using the cohesive crack approach and implemented using two finite elements software for comparison. The first FE approach used embedded discontinuity method (EDM) implemented in Opensees software and was said to have an advantage over other CCM FE models 'in that it allowed cracks to propagate through elements independent of nodal positions and element boundaries'. The second used ABAQUS FE software brittle cracking model that had a damage evolution according to CCM. They found that the exponential cohesive softening functions adopted could be used reliably to predict the flexural behaviour of beams of different sizes and also of centrally loaded panels. The simulation of the TPB tests using these softening curves satisfactorily matched the test results for both Opensees and ABAQUS software. The numerical simulation of the round panels provided accurate predictions of the pre-peak, peak load and early post-peak behaviour of the specimens. Hence they concluded that fracture mechanics models adopted based on CCM could be used to generalise the parameters obtained from one specimen size to reliably predict flexural behaviour of specimens with different sizes and geometry. It is worth noting that their conclusions cannot be directly applied to UHPFRC which only has fine aggregates compared to HPFRC which also includes coarse aggregates as a constituent.

The simulation studies reviewed above involved the use of softening curves representative of UHPFRC in general concrete models in-built within commonly used FEA software. While this approach is useful, it in effect describes procedures for characterising and simulating the behaviour of specific UHPFRC mixes. In cases where equations describing these softening curves are proposed as general UHPFRC models, they don't provide insight into reasons for the material's behaviour.

However, a few numerical models have been developed specifically for UHPFRC to take into account its unique characteristics. Many of these use the general framework for multiscale modelling developed by Kabele and Li (1998) which is based on the observed hierarchical influence of different length scales on each other. Multiscale modelling using this framework has been adopted by several studies to propose models to simulate the behaviour of UHPFRC for specific applications (Radtke et al. (2010), Ellis et al. (2014)). For example the multiscale model proposed by Ellis et al. (2014) was used to simulate the behaviour of UHPFRC panels subject to impact blast loads. Their model first

simulated the fracture of the UHPC matrix and subsequent fibre pull-out at the fibre length scale to estimate material properties related to the meso-structure attributes of the constituents. It is this information that was then used to simulate the behaviour of UHPFRC panels subject to impact blast loads at the structural scale. A key feature of their work was a 2 element rigid body spring model (RBSM) used to generate a traction separation response for an interface bridged by fibres. Randomly oriented fibres required to make up to 2% volume fraction were introduced between the two elements (Fig.3.15). By restraining one element and applying a deformation δ to the other, a traction separation law was obtained by summing up the forces in each fibre. This law was assumed to account for a multiple fibre length scale incorporating the effects of fibre orientation, length, volume fraction and force end slip relations. The RSBM consisted of a pre-cracking and a post cracking phase. The pre-cracking phase was defined by an elastic modulus determined by a relation conforming to a rule of mixtures incorporating factors for embedded fibre length and orientation. In the post-cracking phase tensile strength was calculated by summing up the pull-out resistance of each fibre crossing a crack plane. The fibre pull-out strength was obtained by using an analytical relation proposed by Li et al. (1990) based on experimental data.

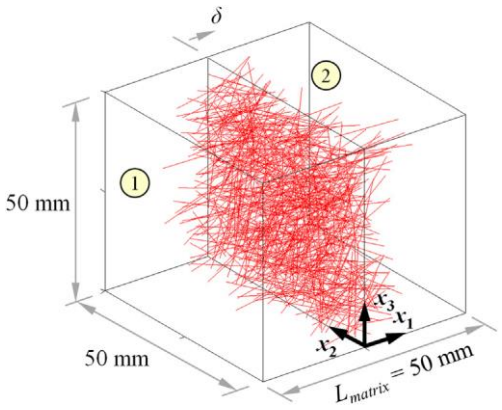

Figure 3.15: Schematic representation of the RSBM (Ellis et al., 2014)

The average tensile strength, T and dissipated fracture energy, G^c (calculated as the area under the traction separation response) obtained from several runs of the RBSM deformation described above were adopted as material properties for use at the structural scale. This was the primary means used by this multiscale model to link the two length scales. At the structural scale, the model was made up of bulk elements bonded together by zero thickness cohesive elements assumed to have a bilinear traction separation law according to Fig.3.16. In the figure T is the traction, δ is the separation, K is the stiffness, and G_c is the work of separation equal to the integral of traction from zero separation δ^0 to separation at failure δ^f. The normal and two tangential directions are denoted by n, s, t respectively. This model, implemented as a VUMAT in ABAQUS/Explicit was able to

make good predictions relative to test data of structural scale UHPFRC panels subject to blast loading. However, only fibre contents of up to 2% by volume were considered.

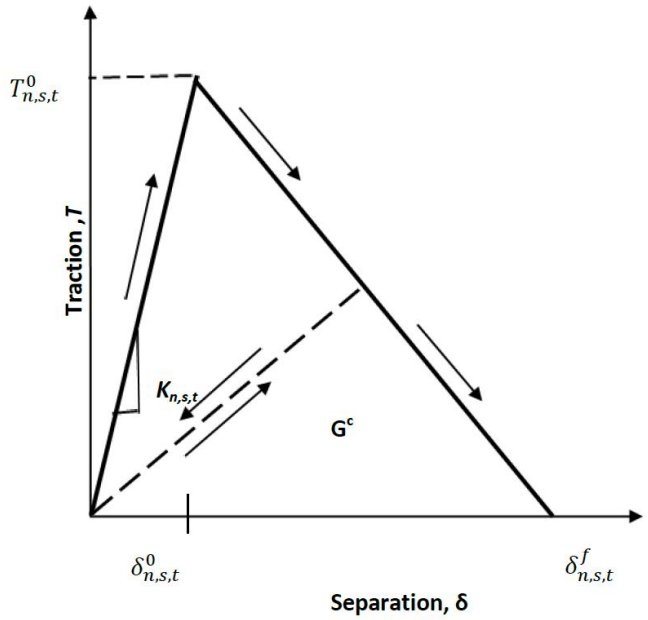

Figure 3.16: Traction-separation constitutive law for the fibre-matrix interface (Ellis et al., 2014)

.

Qsymah et al. (2017) developed a two-step homogenisation approach for the prediction of elastic properties of UHPFRC (Fig.3.17). Micro X-ray computed tomography (μXCT) scans were used to obtain a 3D microstructure image of a 20mm UHPFRC cube sample. A statistical analysis of the pore sizes from these images then provided the basis for developing the two-step homogenisation approach. In their approach the first step consisted of mortar homogenised from three phases: cement paste, silica sand and a large number of small pores (less than 600μm). In this step an analytical approach was adopted based on the Mori Tanaka average stress theory which was convenient for the large number of small pores. The second step was the homogenised UHPFRC consisting of the mortar, fibres and small number of large pores (larger than 600μm). Here a numerical homogenisation approach was adopted by making use of 3D FE meshes transformed directly from the μXCT images shown in Fig.2.9. The average homogenised elastic modulus was found to overestimate the experimental values by about 28%. This was attributed to the uncertainties in the micro-indentation tests observed through the relatively high standard deviation in the elastic moduli of cement paste (±24.4%) and silica sand (±16.3%). Indeed a recalculation to account for the high standard deviations in the elastic moduli of the constituent materials produced values much closer to test data. In addition the volume fraction of the fibres was not found to have a significant effect on the elastic modulus.

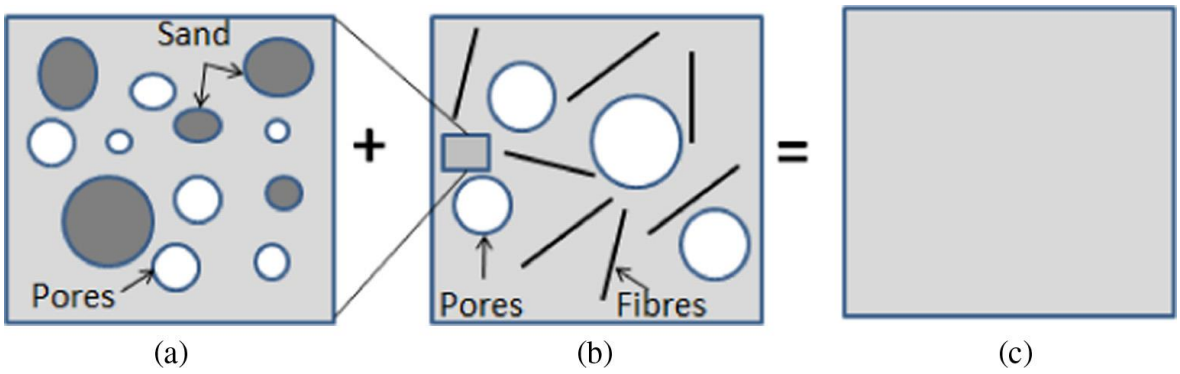

Figure 3.17 : The two-scale analytical-numerical homogenisation approach for UHPFRC: (a) analytical homogenisation of mortar at microscale (b) numerical homogenisation at mesoscale (c) homogenised macroscale UHPFRC (Qsymah et al., 2017).

While the above approach has so far only been applied to elastic properties of UHPFRC, Zhang et al. (2018) developed a discrete-continuum coupled modelling approach to simulate nonlinear damage and fracture behaviour of fibre reinforced concrete at the mesoscale. The main constituents considered individually by the model at this scale were the fibres, the mortar and the interfacial transition zone. The fibres were simulated by beam elements with elastic-plastic properties and the mortar matrix by solid elements with continuum damaged plasticity mechanics. The fibre-matrix interfaces were simulated by zero-thickness cohesive elements with softening bond-slip relations.

The fibres were modelled using two-noded beam elements incorporating elastic-plastic stress-strain laws with yielding, strain hardening and rupture. The mortar matrix was modelled by 4-noded plane-stress isoperimetric elements whose behaviour was described by the concrete damaged plasticity (CDP) model in ABAQUS. The fibre-matrix interfacial behaviour was simulated by the cohesive crack model and was implemented in ABAQUS as zero-thickness cohesive elements. In the first step of mesh generation, the fibres and mortar were set as separate parts in ABAQUS. The fibres were then merged into the mortar using a Boolean operation. In the second step, by means of a MATLAB code zero-thickness cohesive elements were inserted between pairs of fibre and matrix elements to model the fibre-matrix interface.

The simulation results from the above modelling approach were shown to be reasonably close to independent test data used for validation. In addition, the modelling approach was able to simulate typical failure mechanisms in FRC such as fibre pull-out, yielding and rupture, interfacial de-bonding, and matrix cracking and spalling.

3.5 Initial simulation study

3.5.1 Introduction

This section builds on the concepts discussed in the previous sections with the aim of identifying a suitable modelling approach for UHPFRC including appropriate methods for estimating the relevant material properties. The cohesive crack model (CCM) using cohesive elements, the concrete smeared crack model (CSM) and the concrete damaged plasticity model (CDP) are used to simulate progressive crack propagation and failure mechanism of UHPFRC test specimens, and predict their load capacities. These predictions are compared with test data available from an earlier study. The suitability of the above approaches for modelling the flexural behaviour of UHPFRC is assessed with a view to selecting the most appropriate features for further development of a model specific to UHPFRC.

3.5.2 Data Description

Initial simulation presented in this section relied on data generated in the study of Barnett et al. (2007a) on flexural strength of UHPFRC. The mix adopted in their study incorporated 2% fibre content by volume consisting of straight high tensile steel fibres 13mm long and 0.2mm in diameter (Table 3.1). As has been done in several studies aimed at enhancing UHPFRC's sustainability, some Portland cement was replaced by slag cement which is pozzolanic. While this has no noticeable effect on strength, it enhances the material's resistance to chemical attack. The load-deflection data from the above mentioned study was obtained from deformation controlled four point bending (FPB) tests on un-notched 100X100X350 mm UHPFRC specimens (Fig.3.18) and three point bending (TPB) tests on notched specimens with depths between 50-150mm (Fig. 3.19). Ultimate loads were also obtained from compression tests on 100x100x100 cubes from which compressive strength was calculated.

Table 3.1: UHPFRC Mixture Proportions ((Barnett et al., 2007a)

UHPFRC constituent	kg/m^3 (lb/yd^3)
13 mm fibres	157 (265)
Cement	657 (1107)
Microsilica	119 (201)
Slag cement	418 (705)
Silica sand	1051 (1772)
High range water reducer	40 (67)
Water	185 (312)

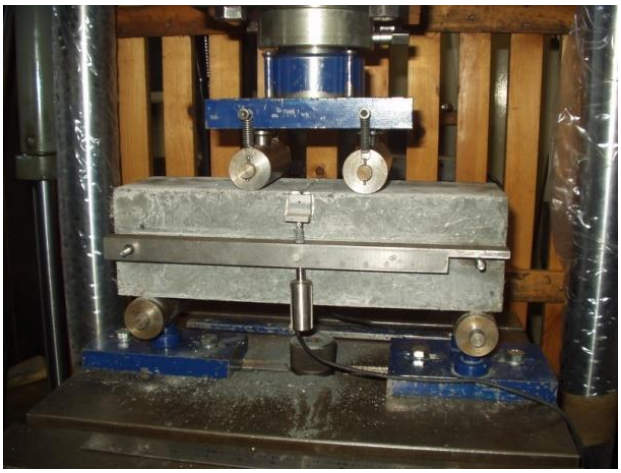

Figure 3.18: Four point bending test arrangement (Barnett et al., 2007a)

Figure 3.19: Three point bending test arrangement (Barnett et al., 2007a)

3.5.3 Estimating material properties

Under tensile stress normal concrete is considered to behave elastically prior to failure. This elastic phase typically occurs at very low strains of 0.001-0.005 (Neville, 2012). Therefore, for most practical purposes linear elasticity is normally assumed and implemented in many concrete models. This assumption would still be reasonable in UHPFRC mixes with either small or no strain hardening (AFGC categories b & c in Fig.2.10). However, in cases where there is a significant strain hardening (category a), the initial phase may be best represented for example by a multi-linear curve as proposed by Wuest et al. (2008). In this section, the initial phase of UHPFRC was assumed to be linearly elastic characterised by an elastic modulus (E).

As previously discussed, failure in concrete under tensile stress occurs when cracks localise within a fracture zone. The post-failure behaviour is characterised by the $\sigma - \omega$ curve which is considered a material property. While in reality every concrete mix will have

its own $\sigma - \omega$ curve, it has been observed that these curves are similar in shape for different mixes of ordinary concrete. Therefore raw $\sigma - \omega$ curves can be idealised into simpler shapes that are easier to implement in models. If the general shape of the $\sigma - w$ curve for concrete based material is known, a good estimate of the curve for a specific mix can be made from a determination of fracture energy and tensile strength (Hillerborg, 1980). Unlike for normal concrete where a bilinear softening curve is generally accepted as providing good results, there is still a lack of agreement as to which curve is best for UHPFRC with different shapes proposed in literature including linear, bilinear, trilinear and exponential. In cases where a structure or specimen does not undergo large softening as in notched and un-notched specimens of typical laboratory test size range, a linear approximation to the softening curve is very accurate (Bažant and Planas, 1998). This fact was observed by Spasojević (2008) to also be applicable to modelling UHPFRC post peak behaviour (Fig.3.9). Therefore in this initial simulation a linear softening curve was adopted and determined by an estimation of the tensile strength σ_t and fracture energy, G_f.

In view of the above assumptions, a macroscale numerical model of a concrete-based materials like UHPFRC would require input of three basic properties i.e. E, G_f and σ_t. The most common way to estimate the value of these properties is directly from experiment tests or indirectly from literature. Attempts have also been made by other researchers to estimate values of these properties for UHPFRC from theoretical micro-structural relations based on the mix and fibre parameters. For example earlier studies by Lange-Kornbak and Karihaloo (1998) developed mathematical expressions relating the elastic modulus (E), fracture energy ($G_{f)}$ and tensile strength (σ_t) to the water/cement ratio, volume fraction of constituents and fibre dimensions. As mentioned in the previous section more recent attempts have been made by Qsymah et al. (2017) to estimate values of some of these properties from multiscale analytical-numerical homogenisation studies of UHPFRC. For the initial simulation studies in this chapter, values of material properties were estimated from test data as outlined below.

a) Elastic Modulus (E)

The assumption of linear elasticity in the stress-strain curve of concrete prior to cracking is only an approximation. In reality, the slope varies at different points along this curve (Fig.3.20). The reason for this slope variation is the cement paste at the interface between the aggregates and cement particles which is prone to micro-cracking. Progressive development of cracks at the interfaces increases local stress intensity making strain to increase at faster rate than the applied stress (Neville, 2012).

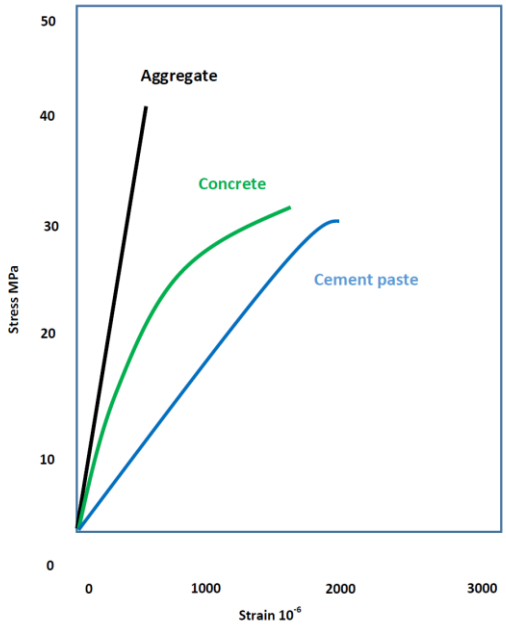

Figure 3.20: Stress-strain relations for cement paste, aggregate and concrete (Neville, 2010)

This makes it difficult to determine a tangent modulus straight from a stress-strain curve. For this reason a common method aims to determine a secant modulus from a test involving repeated loading and unloading. The secant modulus of the unloading curve has been observed to be close to the initial tangent modulus (Fig. 3.21). The secant modulus has also been observed to increase with the strength of concrete probably because both are influenced by the porosity within the cement paste at the interface between the aggregates and cement particles. Hence several empirical relations have been proposed to estimate the elastic modulus from the strength of concrete. For example, Neville (2010) states that the modulus of elasticity of concrete E_c in GPa increases approximately with the cube root of cube strength f_{cu} in MPa such that:

$$E_c = 9.1{f_{cu}}^{0.33} \qquad (3.25)$$

The above expression was used with the test data from Barnett et al. (2007a) to obtain an elastic modulus of 47.55GPa. Ductal, a proprietary UHPFRC mix similar to that adopted in this study is reported to have E values of 47GPa (VSL, 2008).

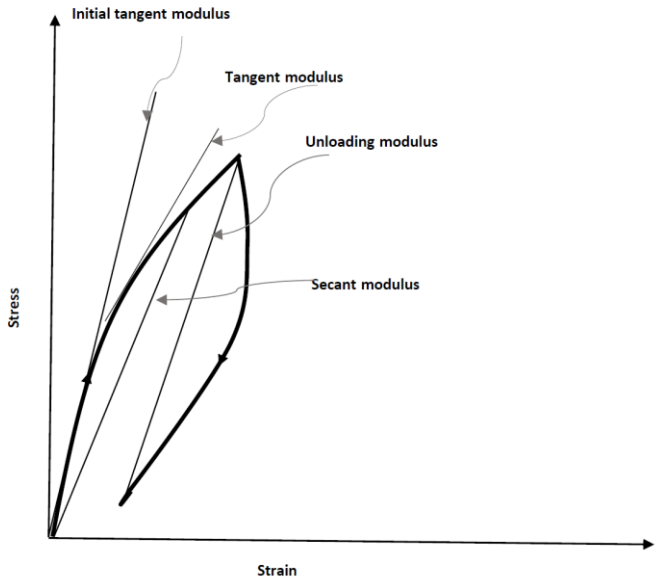

Figure 3.21: Typical stress-strain curve for concrete (Neville, 2010)

b) Tensile strength (σ_t)

Because of the difficulties of carrying out a reliable direct tensile test highlighted in previous sections, AFGC-SETRA (2013) recommends that the tensile strength should be obtained from a flexural test using an inverse procedure. A four point bending test on an un-notched UHPFRC specimen is preferred to a three point bending test because it induces pure bending in the middle third of the span unlike the latter which also introduces a shear stress (Chanvillard and Rigaud, 2003). An un-notched specimen also increases the likelihood of failure occurring along the weakest plane rather than forcing it to originate from the notch tip. Therefore, an un-notched specimen is more appropriate for estimating tensile strength since its failure is more representative of real life structures.

The common practice in concrete design standards in determining tensile strength of a material is to use the flexural strength of the matrix which corresponds to the flexural stress at the end of the elastic phase. In UHPFRC, this flexural stress value is increased by strong bonds between the cement paste and inclusions within the interfacial transition zone (ITZ). The action of fibres through the crack suppression mechanism also increases the stress at first crack thereby increasing this value further.

The flexural stress at the end of the elastic phase (σ_f) for a beam of length L, depth d and width b subjected to the four point bending (FPB) test can be calculated from the load P corresponding to this point as follows:

$$\sigma_f = \frac{PL}{bd^2} \tag{3.26}$$

However, this flexural stress at the end of the elastic range is still observed to be higher than the direct tensile strength. This discrepancy between the flexural and tensile strength is attributed to a scale effect produced by the existence of a fracture zone created to allow stress transfer between the compressive and tensile stress fields introduced by flexural tests (Chanvillard and Rigaud, 2003)**.** Therefore, in order to obtain the correct tensile strength (σ_t), AFGC-SETRA (2013) adjusts the above stress value (σ_f) to account for scale effects as follows:

$$\sigma_t = \sigma_f * \frac{\alpha * (a)^{0.7}}{1 + \alpha * (a)^{0.7}} \qquad (3.27)$$

where α = 0.08 and a is the depth of the specimen in mm.

Load-deflection curves from deformation controlled four point bending (FPB) tests on un-notched 100X100X350 mm UHPFRC specimens (Fig.3.22) were used to estimate tensile strength of the mix following guidance in AFGC-SETRA (2013). Using the above expressions, an average tensile strength (σ_t) value of 8.56MPa was obtained compared to 8MPa reported for a propriety UHPFRC mix Ductal (VSL, 2008). Hassan et al. (2012) obtained a tensile strength value of 9 MPa from direct tensile tests on dog-bone specimens.

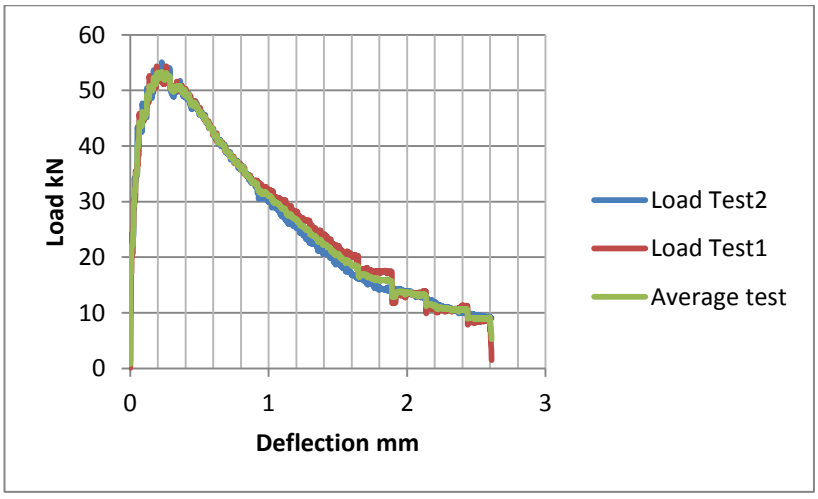

Figure 3.22: Load-deflection curve for un-notched FPB test specimen with 2% fibre content

c) Fracture Energy (G_f)

Fracture energy (G_f) is defined as the energy required to create and open a unit area of crack. Because defining the location of the tip of a propagating crack is difficult, measuring G_f in practice involves measuring the total energy consumed from the time a crack is initiated to when it is propagated right through the specimen (Petersson, 1981). Therefore

to achieve reliable results, it is essential to minimise any energy consumed by dynamic effects or outside of the fracture zone. Ensuring that the crack propagates in a stable manner is the key to avoiding energy consumption by dynamic effects. The notched three-point bending specimen is the simplest type of specimen that can be used to obtain stable crack propagation. This must be used with displacement controlled testing as load controlled testing will result in an unstable fracture as soon as the maximum load is achieved. The aim is for the crack to be able to consume both the energy that is supplied by the applied load and also that is released from the beam as the crack propagates at every point of the load-deflection curve.

The fracture energy G_f is calculated as the area under the full load-deflection curves as suggested by Abdalla and Karihaloo (2003). However, for UHPFRC, the fibre bridging activated after crack localisation makes it difficult to achieve the full load deflection curve as a very large crack width is required to cause complete de-bonding of the fibre from the matrix. Hence measures of G_f are adopted by common test standards that only utilise a proportion of the deflection. For example, the Japanese Society of Civil Engineers method of test for flexural strength and toughness of steel fibre reinforced concrete recommends measuring deflection up to $1/150$ of span (JSCE-SF4) . Though very useful for comparing different FRC mixes, these measures are not suitable for modelling material behaviour.

As is typical of UHPFRC test specimens, the post peak section of the load-deflection curves from the data used in this initial study generally had relatively steep slopes and long tails. Where possible, the average test curves were extrapolated to obtain an estimate of the area under the full load deflection curve which was then divided by the effective crack area to obtain the fracture energy values. Fracture energy (G_f) was estimated from the three point bending 100x100x350 mm specimen with 33mm notch on the tension face. (Fig.3.19). The fracture energy G_f was calculated as the area under the load-deflection curves as follows (Abdalla and Karihaloo, 2003):

$$G_f = \frac{1}{(w-a)b} \int P d\delta \qquad (3.28)$$

where w is the specimen depth, a the notch length, b the specimen thickness, P the applied load, and δ the displacement of the load point. However, as stated earlier the softening part of the load-deflection curves from three point bending tests of UHPFRC specimens had long tails.

Therefore, the average test curves were extrapolated to obtain an estimate of the area under the full load deflection curve. As per Eq. 3.28, the area was then divided by the effective crack area to obtain the fracture energy. Fracture energy from the 100x100x350 mm notched three point bending specimen was estimated as 16.9 kJ/m^2. Richard and Cheyrezy (1994) reported fracture energy values for UHPFRC of 10-40 kJ/m^2 while Le (2008) found values between 19-38kJ/m^2.

Values of the three material properties estimated using test data from Barnett et al. (2007a) were compared to those from literature in Table 3.2 below. The values from the above mentioned test data were reasonably close to those from literature. In the following initial simulation study material property values estimated from the test data were used.

Table 3.2: Summary of material properties estimated from test data compared with data from literature

	Data from Literature		**From tests by Barnett et al. (2007a)**
Elastic Modulus E (GPa)	**44**	(Lange-Kornbak and Karihaloo, 1998)	47.5
	47	(VSL, 2008)	
	48	(Qsymah et al., 2017)	
Fracture Energy G_f (kJ/m^2)	**10-40**	(Richard and Cheyrezy, 1994)	16.9
	15-18	(Lange-Kornbak and Karihaloo, 1998)	
	19-38	(Le, 2008)	
Tensile Strength σ_t (MPa)	**8**	(VSL, 2008)	8.56
	11-16	(Lange-Kornbak and Karihaloo, 1998)	
	9	(Hassan et al., 2012)	

3.5.4 Test geometry and model inputs

The three point bending (TPB) test on a 100x100x350 specimen with 33mm notch on the tension face was simulated as shown in Fig. 3.23 and the corresponding test results used for verification. Simulation was carried out using the values estimated as described above and summarised in Table 3.3. In addition, a Poisson's ratio value of 0.2 was adopted.

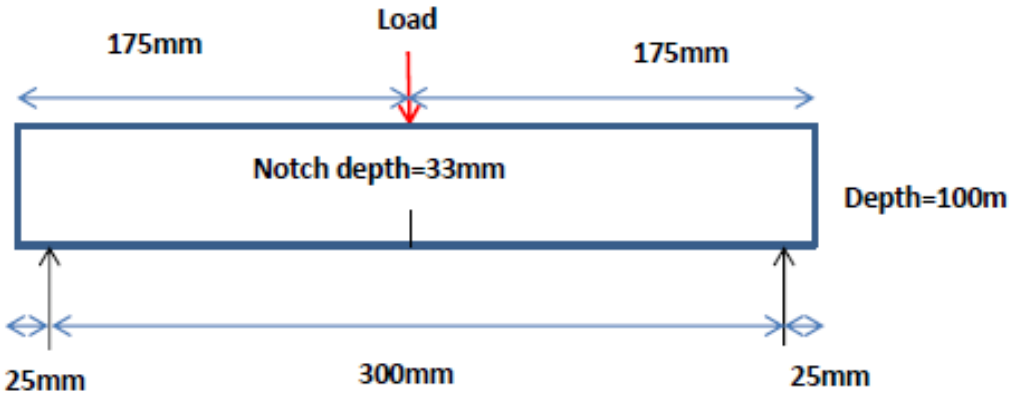

Figure 3.23: Test geometry

Table 3.3: Modelling parameters

Parameter	Value
Elastic Modulus E	47.5GPa
Poisson's ratio υ	0.2
Fracture Energy G_f	16.9kJ/m^2
Tensile Strength σ_t	8.56 MPa

3.5.5 Initial simulation using the Cohesive Crack Model (CCM)

As the crack path was known in advance, cohesive elements were used within the cohesive crack model to simulate progressive crack propagation and failure mechanism of UHPFRC test specimens, and to predict their load capacities.

- **Constitutive laws of cohesive elements**

Cohesive elements can simulate several types of behaviours at interfaces where the interface load carrying capability is lost (Chen, 2009).The cohesive elements in ABAQUS FE software have been adopted in this study as they are based on the cohesive crack model by Hillerborg et al. (1976). The cohesive elements used in this study are formulated using a stress-crack width curve that is typically characterized by a nominal peak strength ($\sigma_{n(max)}$) and fracture energy (G_f) as shown in Fig. 3.24 (ABAQUS, 2013). .

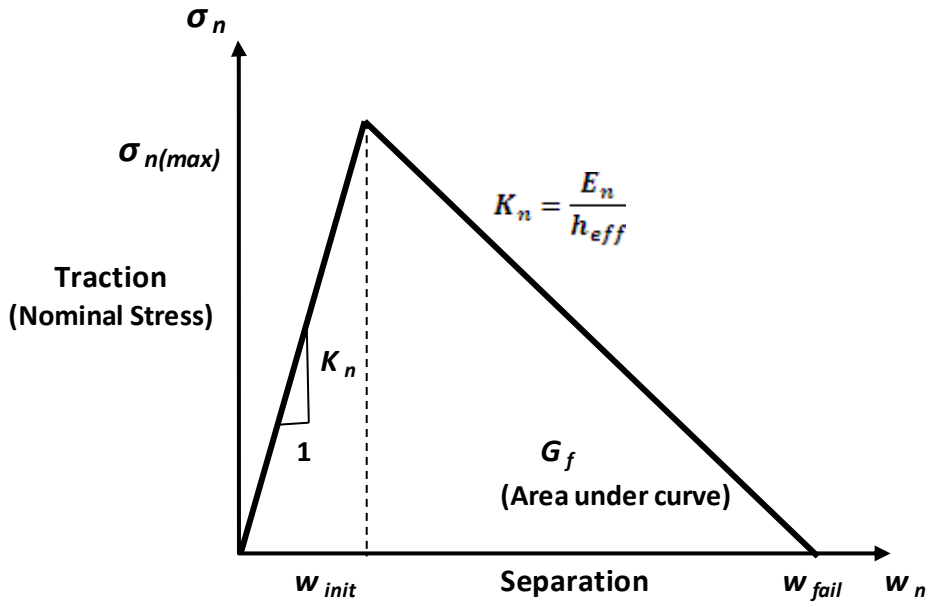

Figure 3.24: Simplified traction-separation curve

These cohesive elements are based on an initial linearly elastic response followed by damage as described below.

- Pre-Damage response

Linear elasticity defines behaviour before initiation of damage with nominal stress and strain quantities used by ABAQUS for the traction separation law. Hence a unit thickness is specified for the element so that the nominal strain corresponds to the separation value. The elastic modulus for traction separation law is interpreted as a penalty stiffness K_n such that for the normal direction

$$K_n = \frac{\sigma_{n(max)}}{w_{init}} \qquad (3.29)$$

where $\sigma_{n(max)}$ is the maximum normal stress and w_{init} is the initial separation.

- Damage initiation

The Quadratic nominal stress criterion was used and has the following formulation (ABAQUS, 2013):

$$\left[\frac{\langle\sigma_n\rangle}{\sigma_{n(max)}}\right]^2 + \left[\frac{\sigma_s}{\sigma_{s(max)}}\right]^2 + \left[\frac{\sigma_t}{\sigma_{t(max)}}\right]^2 = 1 \qquad (3.30)$$

where the nominal and maximum principal stresses in the normal directions are σ_n and $\sigma_{n(max)}$ respectively and the corresponding stresses in the shear directions are: σ_s & $\sigma_{s(max)}$ and σ_t & $\sigma_{t(max)}$.

- Damage evolution

Damage evolution describes the rate of degradation of material stiffness once initiation criterion is satisfied (ABAQUS, 2013). The formulation is based on a scalar damage approach whereby post damage-initiation stress (σ_1) is related to stress without damage (σ_E) as follows (Fig.3.25):

$$\sigma_1 = (1 - D)\sigma_E \qquad (3.31)$$

where D is the scalar damage variable which incorporates the combined effect of all damage mechanisms. D increases monotonically from $D = 0$ when the material is undamaged to $D = 1$ when the material is fully damaged.

The initial stiffness is,

$$K_0 = \sigma_E / w_1 \qquad (3.32)$$

Substituting σ_E from Eq.3.32 into Eq.3.31 and re-arranging gives the scalar damage variable as follows:

$$D = 1 - K/K_0 \qquad (3.33)$$

where $K = \sigma_1 / w_1$.

Damage evolution is based on either energy or displacement requiring specification of either the total fracture energy or the post damage-initiation effective displacement at failure.

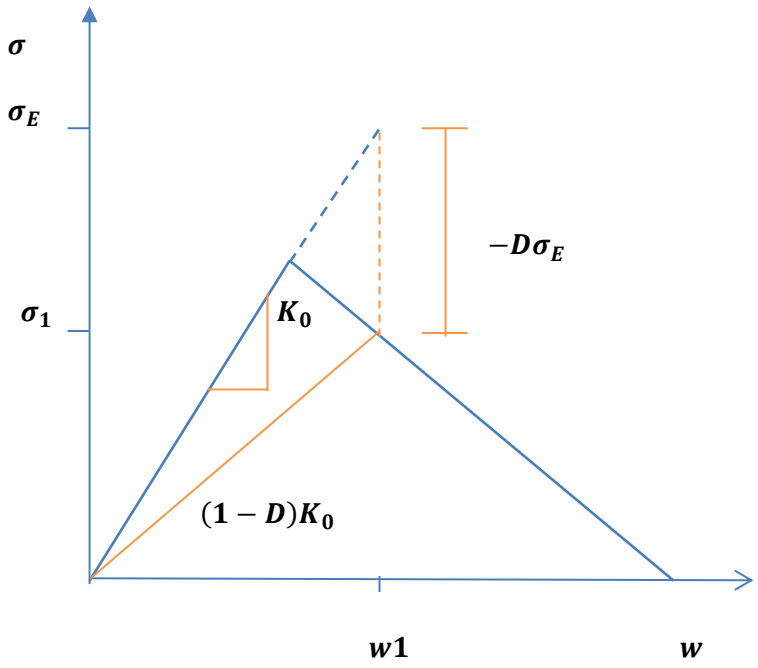

Figure 3.25: Typical damaged response

It may depend on mode mix which may be defined either in terms of energy or traction. Energy-based damage evolution was used whereby the fracture energy can be defined as a function of mode mix using the Benzeggagh-Kenane (BK) analytical form (Benzeggagh and Kenane, 1996):

$$G_f^I + \left(G_f^{II} - G_f^I\right)\left(\frac{G_f^S}{G_f^T}\right)^{\eta} = G_f \qquad (3.34)$$

where G_f is the total mixed-mode fracture energy, G_f^I is the normal strain energy release rate, G_f^{II} and G_f^{III} are the shear strain energy release rates in the two other directions respectively and $G_f^S = G_f^{II} + G_f^{III}$. The total strain energy release rate, $G_f^T = G_f^I + G_f^S$. The above BK law is suitable for the case when G_f^{II}=G_f^{III}. Hence for isotropic failure the response is insensitive to the value of η allowing the use of any valid value for it. The Benzeggagh-Kenane (BK) analytical form was selected as the mixed-mode behaviour with η =2.284. In the absence of more detailed information about the specimens, the fracture energy was assumed to be equal for all the three modes so that $G_f = G_f^I = G_f^{II} = G_f^{III}$. Once G_f has been determined as described above, D is defined by Eq.3.33. The value of the initial stiffness K_0 is a function of the elastic modulus and the element width adopted in the model. The value of K depends on the slope of the post peak curve in Fig.3.25 which in turn is determined from G_f.

- **Simulation techniques**

As confirmed by experimental observation (Fig.3.26), the centreline of the specimen directly above the specimen was the cracking path into which cohesive elements were inserted (Fig.3.27). Cohesive elements (COH2D4) were assigned to the interface using shared nodes. A viscosity parameter of 0.001 was needed to aid convergence.

Figure 3.26: Cracked specimens from TPB test

The bulk of the beam model was meshed with first order plane strain incompatible mode elements (CPE4I). These elements work well in bending and are compatible with cohesive elements when using shared nodes (ABAQUS, 2013). For the cohesive elements linear elastic properties were defined using the traction type. The initial damage scale w_{init} and hence the stiffness was estimated in relation to the stress-separation response shown in Fig. 3.24.

Hence

$$w_{init} = \sigma_{n(max)}/K_n \qquad (3.35)$$

and

$$K_n = E_n/h_{eff} \qquad (3.36)$$

Assuming effective thickness of cohesive elements $h_{eff} = 1$ gives

$$K_n = E_n \qquad (3.37)$$

The value of $K_n = 47500N/mm$ was used in the simulation.

- **Results**

The deformed shape and contour with stress distribution is shown in Fig.3.27. The status of cohesive elements is shown in Fig.3.28 where the status is 1.0 if an element is active and 0.0 if it is not. The cohesive elements failed along the length of the interface.

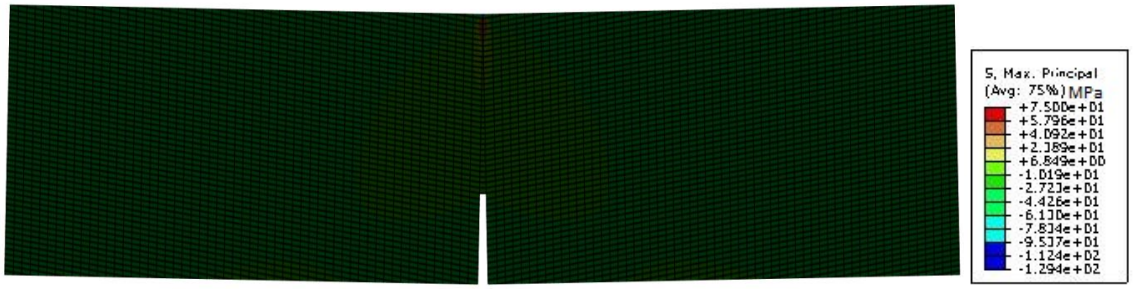

Figure 3.27: Deformed shape with stress state of failed specimen

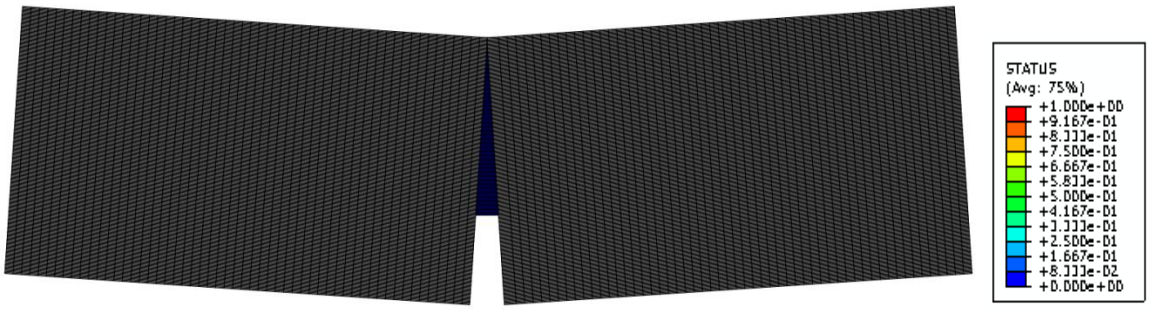

Figure 3.28: Final deformed shape with contour of STATUS

The cohesive crack model with a bi-linear $\sigma - w$ curve produced a load-deflection curve whose shape closely matched those from test results in the elastic, hardening and softening phases (Fig.3.29). The tests by Barnett et al. (2007a) were conducted only up to a deflection equal to $1/150$ of span in accordance to JSCE. The model ignored the spread of cracks in the specimens and only simulated the dominant crack path. This approach was justified because the dominant crack path was known in advance enabling the model to predict the average curve with accuracy and computational efficiency. Each of the phases could be explained in terms of the gradual engagement of the fibres to bridge micro-cracks after the linear elastic stage. From this point to the peak load, the energy provided by the externally applied load was not enough to overcome the fibre bridging action resulting in the formation of more micro-cracks in the strain hardening phase. However, beyond the peak load, the fibres de-bonded from the matrix leading to the softening phase and finally to failure through complete pull-out. No fibre breakage was reported during the tests by Barnett et al. (2007a).

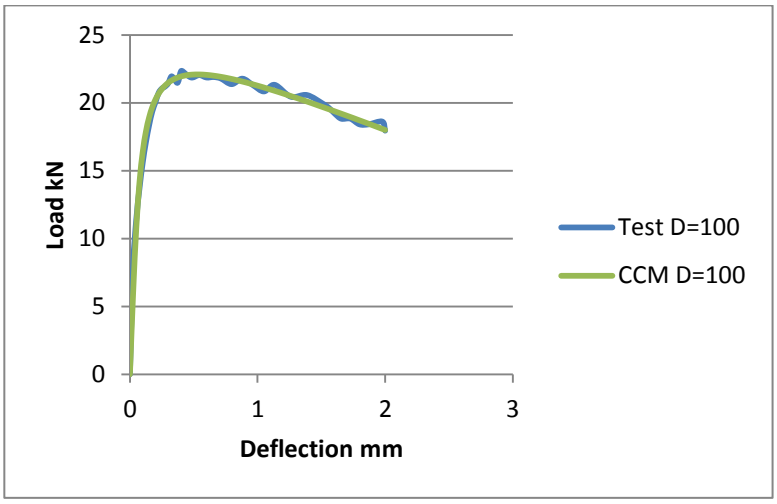

Figure 3.29: Load deflection curves for 100x100x350 specimen

- **Sensitivity study**

The values of tensile strength (σ_t=8.5MPa) and fracture energy (G_f =16.9KJ/m^2) used in the model were estimated as described in section 3.5.3. The sensitivity of the Load-deflection curve predicted by the model to variation in the tensile strength (σ_t) and fracture energy (G_f) was investigated as described below.

- Tensile strength (σ_t)

The effect of varying the tensile strength between 6-16 MPa while maintaining a constant fracture energy (G_f=16.9 KJ/m^2) is presented in Fig.3.30 below. The test data had a maximum deflection of 2mm corresponding to 1/150 of the span (JSCE-SF4). The response of peak load to variation in the input tensile strength was significant and almost linear with a tensile strength increase of only 1MPa causing a 7KN increase in peak load (Fig.3.31). An increase in the tensile strength also produced a steeper post-peak slope and the response was almost exponential (Fig.3.32).

- Fracture Energy, G_f

The effect of varying the fracture energy values between 9-40 KJ/m^2 representing the range of values quoted in literature (Table 3.2) is shown in Fig.3.33 below. The tensile strength was kept constant at 8.56MPa. Change in the peak load with variation of fracture energy was also exponential but less sensitive relative to that of tensile strength with a 10KJ/m^2 increase in input fracture energy producing only a 4KN increase in peak load (Fig.3.34). Not only did increasing the G_f increase the material's toughness seen in the enhanced post peak response but it also produced deflection hardening after the linear elastic stage as discussed in chapter 2. This also explained why a bilinear stress-crack opening response was enough to simulate deflection hardening. However, an increase in

the input fracture energy produced an exponential decrease in the post-peak slope (Fig.3.35). The sensitivity study suggested that the elastic modulus, tensile strength and fracture energy values estimated in section 3.5.3 were appropriate for this UHPFRC material as they produced good model prediction relative to the test results.

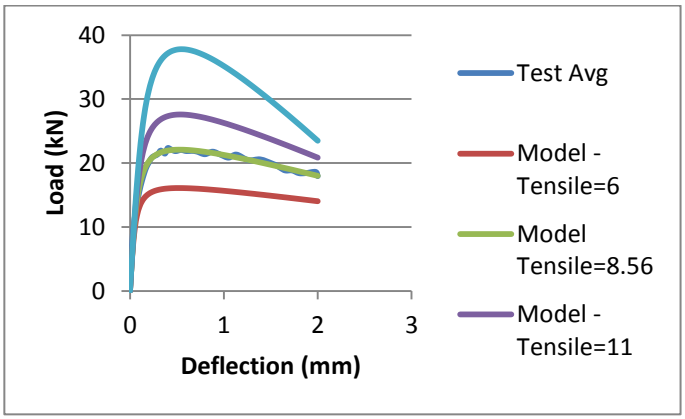

Figure 3.30: Load-deflection curves for different tensile strengths

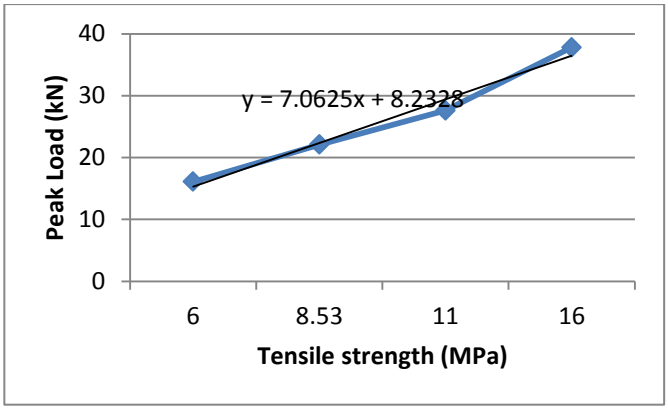

Figure 3.31: Variation of peak load with tensile strength

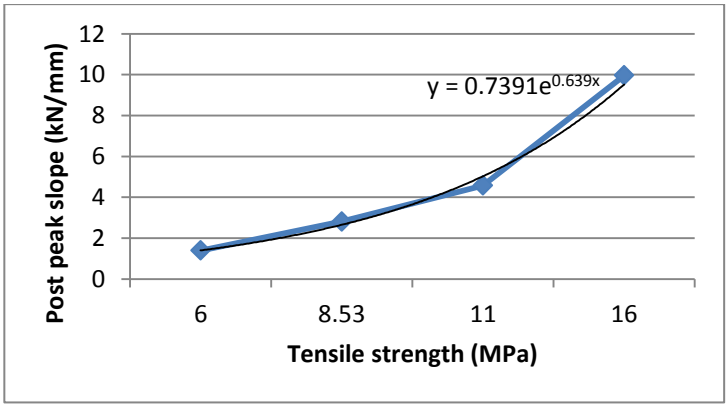

Figure 3.32: Variation of post-peak slope with tensile strength

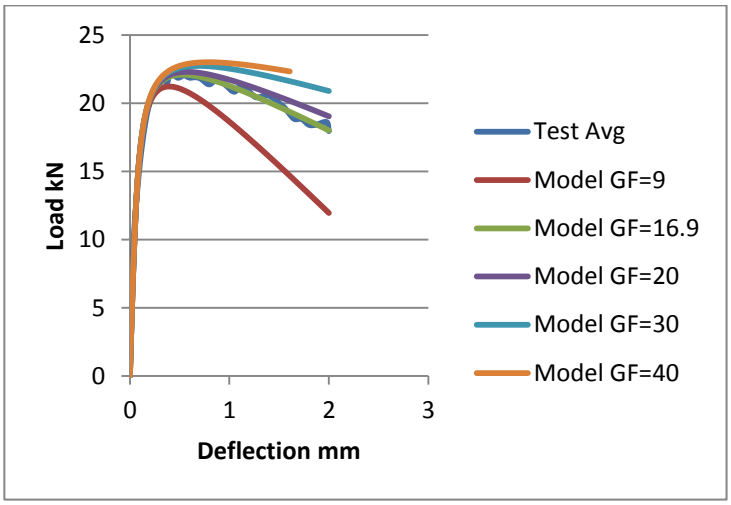

Figure 3.33: Load-deflection curves for different fracture energies

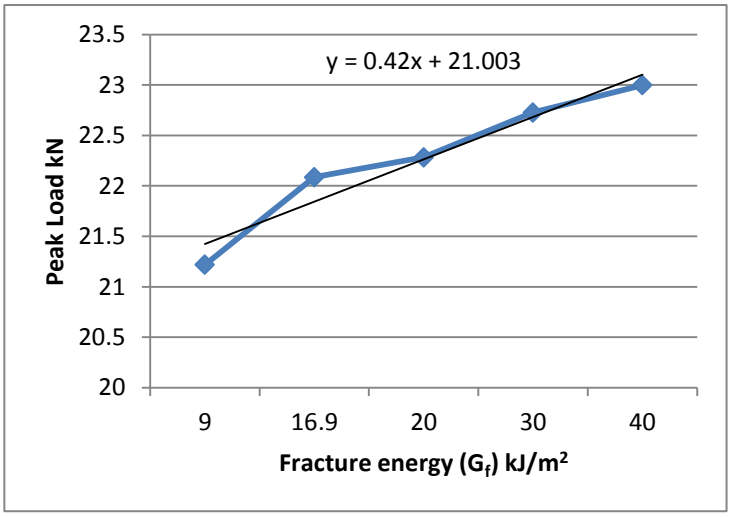

Figure 3.34: Effect of fracture energy on Peak Load

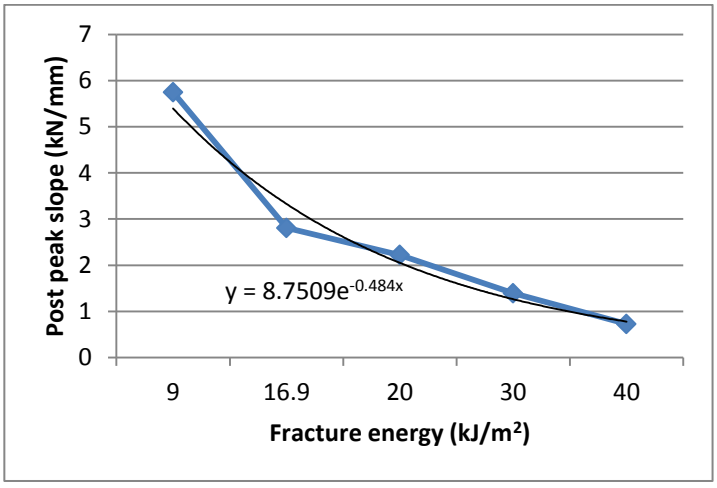

Figure 3.35: Variation of post-peak slope with fracture energy

3.5.6 Initial simulation using the Concrete Smeared Cracking Model (CSM)

Concrete smeared cracking model is available in ABAQUS/Standard for general modelling of concrete in all types of structures (ABAQUS, 2013). It was used successfully by Le (2008) to simulate the behaviour of UHPFRC paving flags under flexural loading. A detailed description of this model is provided in the ABAQUS theory manual (ABAQUS, 2013) and only selected aspects relating to treatment of concrete response to tensile loading are reviewed briefly below.

The model is designed primarily for cases in which the concrete is subject to monotonic loadings with low confining pressures. It assumes that cracking is the most dominant aspect of concrete's behaviour and hence representation of cracking and post-cracking response is emphasised. However, as individual 'macro' cracks are not tracked reference is made to the 'smeared crack model'. Calculations of the constitutive response are carried out independently at each integration point of the FE model and the influence of cracks is taken into account through their effect on the stress and material stiffness relating to that integration point. When subjected to uniaxial tensile loading, the concrete response is elastic up to a maximum stress at which cracking failure occurs. The model assumes that this failure is due to a degradation of the elastic stiffness. Though the cracks are permanent, the strains associated with them are not so that cracks can be closed completely if the stresses across them become compressive.

The ABAQUS concrete smeared cracking model uses 'tension stiffening' to model the post-failure behaviour arising out of the application of a direct strain across cracks. Tension stiffening involves defining the strain-softening response of cracked concrete. This provides a simple way of simulating the effects of the interaction between reinforcement and the concrete matrix. Tension stiffening can be specified by a post-failure stress-strain relation or a fracture energy approach. However, as was noted in previous sections, the use of a post-failure stress-strain relation alone would in most cases introduce mesh sensitive outcomes with no unique solution as mesh refinement leads to narrower crack bands. In order to retain the use of a post-failure stress-strain relation (which is convenient for FE application) the band in which the cracks are allowed to localise needs to be limited in some way (Bažant and Planas, 1998). This effectively makes the post-failure stress-strain relation equivalent to the stress-displacement relation which is considered a material property according to Hillerborg et al. (1976). This gives rise to the definition of fracture energy as energy required to create a unit area of crack calculated from the area below the stress-displacement curve:

$$G_f = \int \sigma_t du \qquad (3.38)$$

In this approach, the maximum displacement u_0 at which the linear approximation of the strain-softening curve gives zero stress is specified (Fig.3.36).

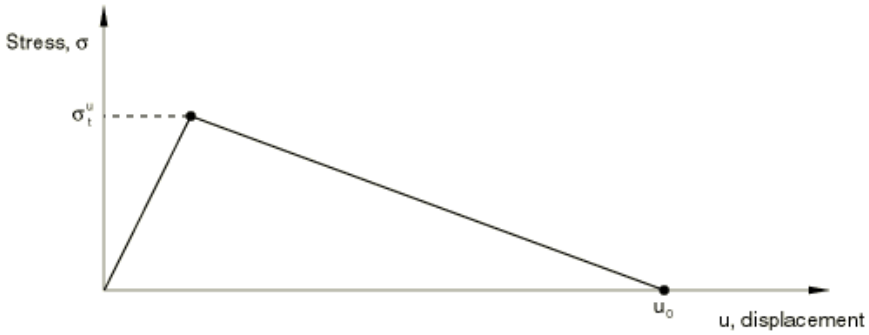

Figure 3.36: Fracture energy cracking model (ABAQUS, 2013)

The failure stress (σ_t^u) is the maximum stress. The strain at which it occurs is the failure strain and is equal to the failure stress divided by the elastic modulus. Post failure, the stress decreases and becomes zero at the maximum displacement (u_0). Unlike the strain, this displacement value is independent of specimen length. Therefore the tensile stress-strain curve obtained from cracked concrete needs to be converted to a stress-displacement one. This is done by multiplying the strain at each integration point by a characteristic length, l_c (Crisfield, 1986)). l_c is defined relative to an element geometry and formulation. For example, for a first order element, it is a typical length across the element.

- **Simulation techniques**

The model uses a plasticity based failure surface for crack detection. This was implemented using the absolute value of the ratio (r_t^σ) of the uniaxial tensile stress at failure σ_t to the ultimate uniaxial compressive stress σ_c as follows:

$$r_t^\sigma = {}^{\sigma_t}/_{\sigma_c} \qquad (3.39)$$

In addition in order to satisfy the description of compressive behaviour, an inelastic strain of 0.004 was specified at a compressive stress of 170 MPa (Le, 2008). Tension stiffening using a fracture energy approach was adopted whereby the ultimate displacement, u_0, was estimated from the fracture energy per unit area, G_f, as follows:

$$u_0 = 2G_f/\sigma_t^u \qquad (3.40)$$

where σ_t^u is the maximum tensile stress that can be carried by the concrete material. The Newton-Raphson technique was used for the non-linear solution within ABAQUS/Standard.

- **Results**

The deformed shape and contour of the stress distribution is shown if Fig.3.37.

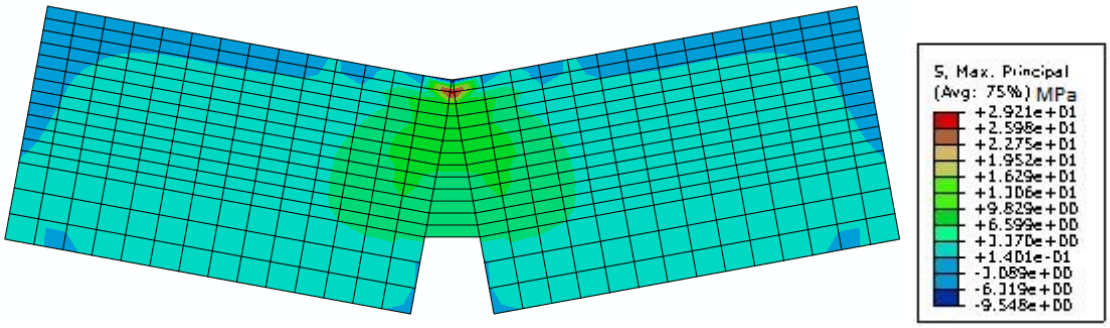

Figure 3.37 : Deformed shape with stress state.

The concrete smeared cracking model prediction of the load-deflection curve matched the test average closely in the pre-peak, peak and post-peak phases (Fig.3.38). Mesh density made little noticeable difference to the predictions.

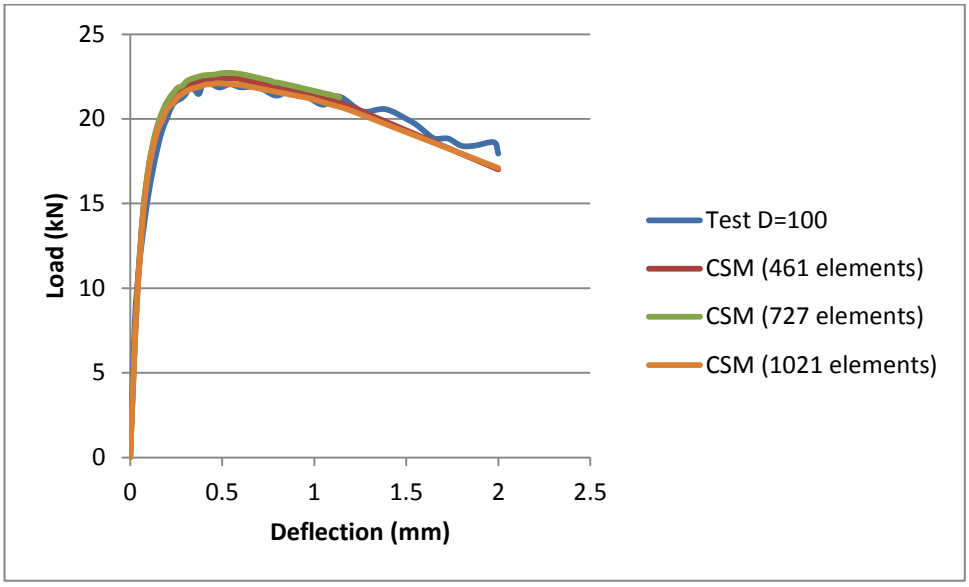

Figure 3.38: Model prediction of Load-deflection curve compared to test curve

3.5.7 Initial simulation using the Concrete Damaged Plasticity Model (CDP)

Based on the work of Lubliner et al. (1989), the concrete damaged plasticity (CDP) model uses concepts of isotropic damaged elasticity in combination with isotropic tensile and compressive plasticity to represent the inelastic behaviour of concrete. It is designed for applications in which concrete is subjected to monotonic, cyclic, and/or dynamic loading under low confining pressures (ABAQUS, 2013). It can be used in conjunction with a viscoplastic regularization of the constitutive equations in ABAQUS/Standard to improve the convergence rate in the softening regime. It requires that the elastic behaviour of the

material be isotropic and linear as in the concrete smeared cracking model. Concrete plasticity in the model is defined by flow potential, yield surface, and viscosity parameters and the formulation is detailed in the ABAQUS theory manual (ABAQUS, 2013). .

The model assumes that the uniaxial tensile response of concrete is characterized by damaged plasticity (Fig.3.39). $\tilde{\varepsilon}_t^{pl}$ is referred to as the tensile equivalent plastic strain. Under uniaxial tension the stress-strain response follows a linear elastic relationship until the value of the failure stress σ_{t0} is reached. The failure stress corresponds to the onset of micro-cracking in the concrete material. Beyond the failure stress the formation of micro-cracks is represented macroscopically with a softening stress-strain response, which induces strain localization in the concrete structure.

As shown in Fig.3.39, when the concrete specimen is unloaded from any point on the strain softening branch of the stress-strain curves, the unloading response is weakened. The elastic stiffness of the material appears to be damaged (or degraded). The degradation of the elastic stiffness under tensile loading is characterized by damage variables, d_t taking values from zero, representing the undamaged material, to one, which represents total loss of strength. To avoid potential numerical problems, ABAQUS enforces a lower limit on the post-failure stress equal to one-hundredth of the initial failure stress $\sigma_t \geq \sigma_{t0}/100$. Material models exhibiting softening behaviour and stiffness degradation often lead to severe convergence difficulties in implicit analysis programs, such as ABAQUS/Standard. A common technique to overcome some of these convergence difficulties is the use of a viscoplastic regularization of the constitutive equations, which causes the consistent tangent stiffness of the softening material to become positive for sufficiently small time increments (Niazi et al., 2013).

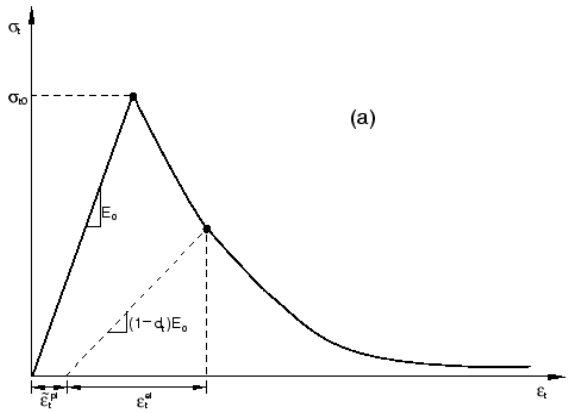

Figure 3.39: Response of concrete to uniaxial loading in tension (ABAQUS, 2013) .

The concrete damaged plasticity model can be regularized in ABAQUS/Standard using viscoplasticity by permitting stresses to be outside of the yield surface. The stress-strain relation of the viscoplastic model is given as:

$$\sigma = (1 - d_v)\mathbf{D}_0^{el} : \left(\varepsilon - \varepsilon_v^{pl}\right) \qquad (3.41)$$

where d_v is a viscous stiffness degradation variable, $\mathbf{D}_0^{el}$ is the initial elastic stiffness matrix and ε_v^{pl} is the viscoplastic strain. Using the viscoplastic regularization with a small value for the viscosity parameter (small compared to the characteristic time increment) usually helps improve the rate of convergence of the model in the softening regime, without compromising results.

Application of the fracture energy approach as proposed by Hillerborg et al. (1976) in which a stress-strain relation is replaced by a stress-displacement response as a material property means that for a concrete specimen under tensile load, the crack opening does not depend on the specimen's length. This fracture energy cracking model can be invoked by specifying the fracture energy, G_f directly as a material property. This model assumes a linear loss of strength after cracking such that the cracking displacement at which complete loss of strength takes place is $u_{t0} = 2G_f/\sigma_{t10}$ (Fig.3.40). The stress-displacement relation is obtained from a stress-strain one by multiplying the strain associated with an integration point by a characteristic length l_c as previously defined.

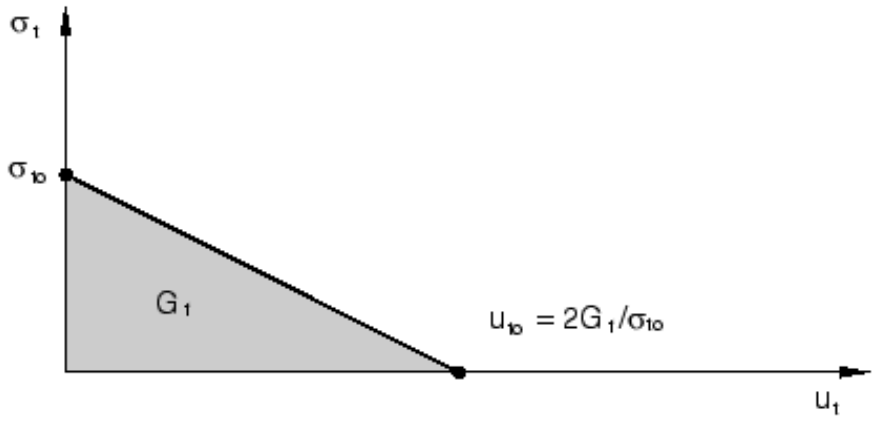

Figure 3.40: Post-failure stress-fracture energy curve (ABAQUS, 2013).

- **Simulation techniques**

As recommended in ABAQUS analysis manual default values were adopted for plasticity based parameters required by the model including a zero value for the viscosity parameter. These default values have also been used successfully by Mahmud et al (2012) to simulate the flexural behaviour of UHPFRC. In addition, in order to satisfy description of compressive behaviour, an inelastic strain of 0.004 was specified at a compressive stress of 170 MPa (Le, 2008). Newton-Raphson non-linear solution was employed within ABAQUS/Standard with control of geometrical non-linearity from large displacements. A mesh sensitivity study was also carried out using three mesh sizes consisting of 461,792 and 1021 elements.

- **Results**

The model deformed shape and contour with stress distribution is shown in Fig.3.41. The model predicted the initial elastic phase and peak load very well but slightly under-predicted the post peak response (Fig.3.42). The different mesh sizes did not produce any noticeable difference in the predictions.

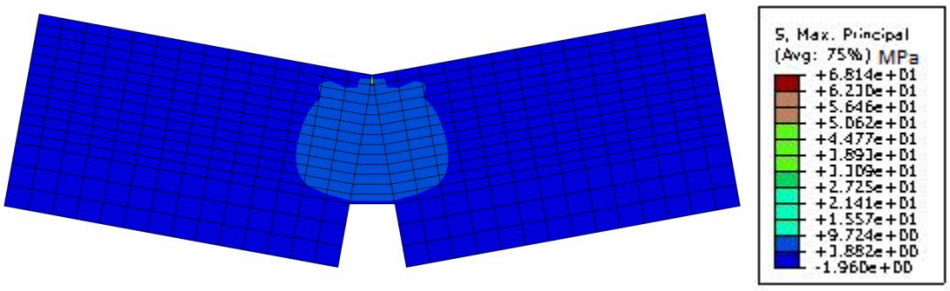

Figure 3.41: Deformed shape with stress state of failed specimen

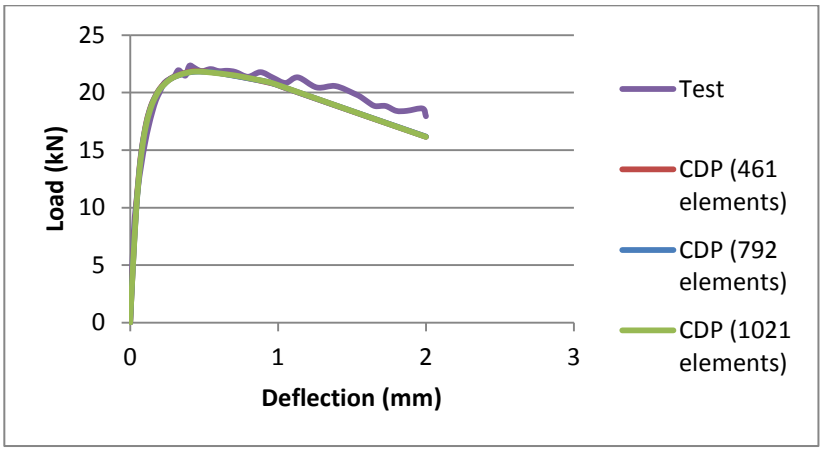

Figure 3.42: CDP Model prediction compared to test data

3.5.8 Comparison of CCM, CSM and CDP

Drawing on the experience of using the three modelling approaches, they were compared below with the main emphasis being the observations made during the simulation study. CCM employed cohesive elements within the crack ligament and plain strain incompatible elements (CPE4I) in the bulk of the model. Both CSM and CDP used plain strain incompatible elements (CPE4I) on the whole model according to the smeared crack approach. Newton-Raphson technique was used for non-linear solutions within ABAQUS/Standard in all the three models.

- Localisation criteria and damage mechanism

The three modelling approaches were compared using the framework developed by Elices and Planas (1989) which was discussed in section 3.2. Cohesive elements were incorporated into a bulk material such that the fracture zone localised in a discrete crack. On the other hand, in both CSM and CDP within ABAQUS/Standard the crack was smeared over an element whose minimum size was limited. Both cohesive elements and CSM incorporated stiffness degradation only whereby the crack could close under compressive stress and all strains could be recovered. In CDP however, both stiffness degradation and plasticity were possible such that irrecoverable strains could result. This is useful when modelling cyclic modelling in concrete. All the above models assumed linear elasticity prior to the onset of cracking.

- Discrete vs diffuse cracking

Initial simulation of cracking using cohesive elements was justified by the fact that the dominant crack path was known in advance enabling the average curve to be predicted with computational efficiency. Cohesive cracks in ABAQUS also had an enhanced ability to study propagation of individual cracks through tracking of ‘damage status’. While CCM assumed a homogeneous and isotropic material at the macro-level, the scatter of the test results indicated the inherent heterogeneity of the material at the micro- or meso-level. The model also ignored the spread of cracks in the specimens and only simulated the dominant crack path. Attempts have been made by others (Yang et al., 2009) to simulate the complex crack patterns in concrete by pre-inserting cohesive elements within very fine and elaborate meshes. On the other hand, both CSM and CDP could be applied to all the elements making them suitable for simulating diffuse cracking.

- Prediction accuracy

Predictions of the load deflection curve by all the three models closely matched test data. (Fig.3.43). The cohesive crack and smeared crack approaches used in these models were found to be equivalent under conditions of described by Eq. 3.9.

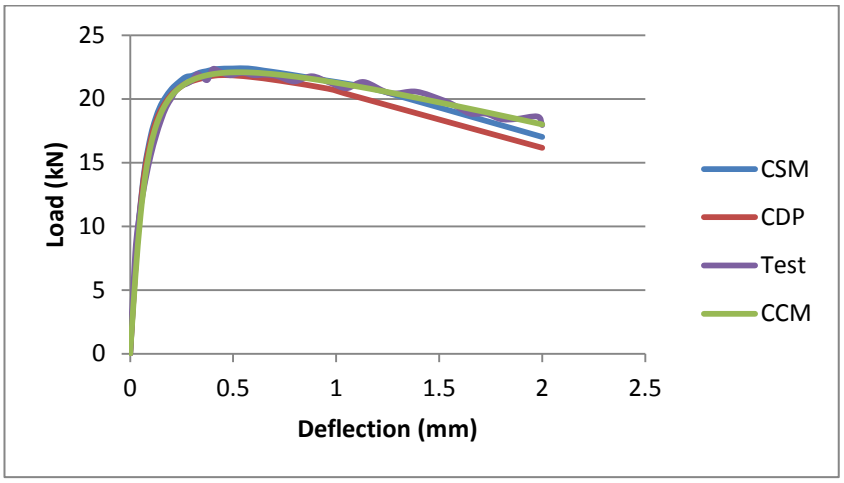

Figure 3.43: Comparison of load-deflection curves

- Convergence

The CDP model was found to the quickest in achieving convergence compared to both CCM and SCM. This may be because of the fact that in order to avoid potential numerical problems, ABAQUS enforces a lower limit on the post-failure stress (σ_t) equal to one-hundredth of the initial failure stress (σ_{t0}): $\sigma_t \geq \sigma_{t0}/100$. CCM was observed to have the most difficulties in achieving convergence also requiring a much finer mesh compared to the other models. Material models exhibiting softening behaviour and stiffness degradation often lead to severe convergence difficulties in implicit analysis programs, such as ABAQUS/Standard. One technique to overcome some of these convergence difficulties is the use of a viscoplastic regularization of the constitutive equations, which causes the consistent tangent stiffness of the softening material to become positive for sufficiently small time increments. Both the concrete damaged plasticity (CDP) and cohesive elements model can be regularized in ABAQUS/Standard using viscoplasticity by permitting stresses to be outside of the yield surface. Using the viscoplastic regularization with a small value for the viscosity parameter (small compared to the characteristic time increment) usually helps improve the rate of convergence of the model in the softening regime, without compromising results. A viscosity parameter of 0.01 was required to aid convergence in CCM while CDP did not require any regularisation. CSM

however, did not seem to have an easy way to directly incorporate viscous regularisation hence limiting the options available to aid its convergence. Instead where local cracking causes unstable behaviour in the model, ABAQUS analysis manual recommends the use of more tension stiffening to obtain a numerical solution (ABAQUS, 2013). However, increasing tension stiffening in this way makes it more of an estimate to achieve convergence rather than being based directly on measured values of fracture energy.

Yang and Chen (2005) adopted a local arc-length algorithm to solve system equations characterised by material softening. They used this approach within a finite element model incorporating re-meshing for simulation of multiple discrete crack propagation in reinforced concrete (RC) beams. In their findings they recommended the use of secant instead of tangential iterative stiffness matrices. They noted the fact that the secant stiffness was always positive during loading-unloading iterations, leading to better numerical convergence and stability.

Conclusions

Based on the results of initial simulation, the following observations were made as a basis for further development of a model suitable for simulating the flexural behaviour of UHPFRC in chapter 5.

- A bilinear $\sigma - \omega$ curve using a fracture energy approach was able to accurately predict the load-deflection response of UHPFRC. The material's G_f was high enough to be able to simulate deflection hardening.
- The methods/approaches adopted in this study for estimating material properties produced appropriate values of elastic modulus, tensile strength and fracture energy
- Prediction of the load-deflection curve by the concrete smeared cracking model (CSM) was almost as accurate as that of the cohesive crack model with cohesive elements (CCM). This is useful as the smeared cracking approach is easier to implement in the finite elements method.
- However, the concrete smeared crack model could benefit from being implemented with viscous regularisation as an aid to convergence.

Chapter 4 – Experimental Investigations (Preparation, Testing and Results)

4.1 Introduction

The initial simulation study presented in the previous chapter was useful in identifying appropriate approaches for simulating the flexural behaviour of UHPFRC and suitable methods for estimating its material properties. However, the data employed was of a limited range in both specimen size and fibre contents considered. Therefore in this chapter, a comprehensive experimental study is presented in order to achieve the following objectives:

- Extend the range of sizes considered in order to be able to establish size effect on flexural strength of UHPFRC. In addition size effects on the flexural stress at the end of linearity and fracture energy are investigated.
- Extend the range of fibre contents examined in order to study the effect of fibre content on the above mentioned parameters
- Estimate UHPFRC material properties from test data that can be used as inputs for a proposed UHPFRC numerical model
- Provide data that can be used to verify the above UHPFRC model

In the following sections, the mixing and casting of UHPFRC specimens of varying sizes and fibre contents are described. This is followed by descriptions of the test methods adopted including the three point bend test on notched and un-notched specimens and four point bending test on un-notched specimens. The test results are then analysed in terms of size and fibre content effects on both pre- and post-peak load-deformation responses. This leads to discussions of the implications of size effects and fibre content on the estimation of material properties from flexural tests.

4.2 Mixing and Casting procedures

4.2.1 Mix proportions

The mix proportions adopted in this study (Table 4.1) was based on the work by Soutsos et al. (2005) and Le et al. (2007) who carried out extensive studies to find optimal quantities of the various constituents of UHPFRC. Other studies (Barnett et al., 2007a) have also successfully used similar mix proportions to study the flexural properties of UHPFRC. As a basis for achieving a high strength, the mix had a very low water/cement (w/c) ratio (0.16) in accordance with the UHPFRC design principles discussed in chapter 2. However, such a low w/c required a high dosage of super-plasticiser (40kg/m^3) to improve its workability.

Fine silica sand (<600µm) was used as the only aggregate thus enhancing its homogeneity. Incorporation of 8-11% by weight of silica fume (microsilica) further improved its microstructure by making it dense and compact. Le et al (2007) and Barnett (2007) found that this dosage of silica fume provided an optimal balance between compressive and flexural strength enhancement, and cost. 13mm long high yield strength steel fibres of 0.16mm in diameter were used to enhance the ductility of the mix. 2% fibre content by volume is commonly used in commercial UHPFRC mixes as a trade-off between improvement in mechanical properties and cost (Barnett, 2007). In addition to 2% fibre content, this study also included mixes with 4% and 6% contents in order to investigate the effect of fibre content on the flexural behaviour of UHPFRC.

Table 4.1: UHPFRC mix proportions

kg/m^3	2% fibres	4% fibres	6% fibres	Manufacturer's specification
cement	1075	1075	1075	Hansons High strength Portland cement (BS EN 197-1 CEM 1 52.5N cement)
silica fume	119	119	119	Elkem Microsilica MS 940U (Average particle size 0.1µm)
silica sand	1050	1050	1050	Average particle size : 270µm
fibres	157	314	471	Dramix steel wire fibres from BEKAERT for concrete reinforcement (15kg bags)
superplasticiser	40	40	40	FOSCROC AURACAST 200 High Range Water Reducing Superplasticing Admixture EN934-2:T3.1/3.2
water	173	173	173	

4.2.2 Specimen sizes

Establishment of the existence or otherwise of size effects was a major consideration in the selection of specimen sizes (Table 4.2). In order to determine size effects conclusively, specimen sizes were carefully selected based on the following criteria:

- A range of specimens of depths between 25-250mm was adopted exceeding the minimum ratio 8:1 between the largest and smallest size as recommended by Bažant and Kazemi (1990).

- All the notched UHPFRC specimens had a notch/depth and depth/span ratios of 1/3 hence satisfying the geometrical similarity necessary to consider size effects (Bažant and Planas, 1998)

- All specimens had a fixed width (50mm) in order to capture only size effects due fracture mechanics and minimise other sources of size effects. (Bažant and Planas, 1998)

The specimens were designated sizes S1 (depth=250mm) to S11 (depth=25mm) (Table 4.2)

Table 4.2: Specimen sizes

MATERIAL PROPERTY	TEST	FIBRE CONTENT	SPECIMEN SIZES FOR EACH FIBRE CONTENT (mm)	SIZE DESIGNATION	No. OF SPECIMENS FOR EACH SIZE	TOTAL No. OF TESTS
Fracture energy	Three point bending test on notched specimens	2% 4% 6%	50wx250dx850l 50wx200dx700l 50wx150dx550l 50wx100dx350l 50wx50dx200l 50wx25dx125l	S1 S2 S3 S4 S5 S6	5 no.	90
Flexural tensile strength	Three point bending tests on un-notched specimens	2% 4% 6%	50wx125dx425l 50wx100dx350l 50wx50dx200l 50wx25dx125l	S7 S8 S10 S11	5 no.	60
Flexural tensile strength	four point bending tests on un-notched specimens	2%,4%,6 %	50wx75dx275l	S9	5 no.	15
Compressive strength	Compression test on cube specimens	2% 4% 6%	100x100x100		5 no.	15

4.2.3 Mixing and casting

Several studies have presented various mixing sequences and timelines for UHPFRC (Bonneau et al. (1997); Graybeal (2005)). An initial trial mix was prepared based on the work of Le et al (2007). However, 24hrs after casting, the specimens were observed to still be soft and easily warped on the removal from the moulds. This problem was found to be due to the addition of all the super-plasticiser in one dosage. Morin (2011) recommended the addition of the super-plasticiser in two separate dosages. They stated that while the first addition humidifies the dry particles helping in mixing, the second addition is responsible for the mix fluidity and ultimately workability. Therefore this recommendation to add the super-plasticiser in two separate dosages was adopted in the final process of preparing UHPFRC described below with reference to Fig 4.1. Each material constituent was carefully weighed according to the mix proportion in Table 4.1. A dry mix of silica fume, cement and sand respectively was added into a horizontal pan mixer and mixed for about 5 minutes. Blending the dry particles prior to adding the liquid superplasticizers and water helped in preventing their tendency to agglomerate (Maca et al., 2013). In addition the blades in the mixer were observed to be very useful in breaking down lumps of the material. However, beyond this stage, it was found that the capacity of the motor in the horizontal pan mixer was not sufficient to handle the relatively high volume of concrete required to cast all the specimens from a single mix batch. Hence the dry mix was transferred to a drum mixer when it had no more lumps.

About 90% of the superplasticiser mixed with water was first added into the drum mixer which was then switched on. The dry mix from the pan mixer was then transferred into the drum mixer gradually over a period of 10-15minutes. The UHPFRC paste was observed to pass through three distinct phases before it became easily workable. In the first phase immediately after the dry mixed constituents had been added to the combination of water and super-plasticiser, it remained dry for 2-3 minutes (Fig. 4.1). In the second phase, the UHPFRC paste transitioned into relatively big lumps (≈50mm) that become gradually smaller as the paste was mixed for about 3-8 minutes. It is in the third and final phase that the paste became easily workable. The fibres were then proportionately added according to the desired fibre content followed by continued mixing, gradually adding the remaining 10% of the super-plasticiser and water. During this process the mix was observed to become steadily fluid. The mixing was continued further for 5 minutes to ensure that the fibres were uniformly dispersed throughout the mix. Prior to casting, the timber moulds, made according to sizes in Table 4.2, were prepared by applying a de-moulding agent (WD40 oil) to their inner surfaces. The mix was then poured directly from the mixer into the middle of the moulds and allowed to flow outwards. The specimens were cast sequentially, starting with the largest to the smallest size. The cast specimens were then put on a vibrating table for 90-120 seconds until all the air bubbles had been removed.

They were allowed to set for 24 hours at room temperature. The specimens were then removed from their moulds and placed in a curing tank at room temperature for 28 days in accordance with BS EN 12390-2: 2009 (BSI, 2009).

1. Weighing constituent materials

2a. Stage 1 dry mixing

2b. Stage 2 mixing including water, superplasticiser and fibres

3. Placing concrete in moulds

4. Vibrating the concrete

5. Curing the concrete

Figure 4.1: Sequence of mixing and casting specimens

4.3 Testing

4.3.1 Overview

A total of 5 no. batches of each mix were prepared and each batch used to cast all specimen types and sizes for each test. The choice of 5 replicate tests for each specimen was justified by the need to minimise the influence of potential experimental anomalies. The tests were carried out for each specimen size and type as follows (Table 4.2):

a) Three point bending (TPB) tests on notched beam specimens with depths between 25-250 mm to estimate fracture energy, and to study size and fibre content effects. Notches on specimens for notched TPB tests were cut mid-span and full width using 3mm circular saws to 1/3 the depth of the specimens. These were designated sizes S1 to S6.

b) Three point bending (TPB) tests on un-notched beam specimens to estimate flexural strength. These were designated sizes S7, S8, S10 and S11.

c) Four point bending (FPB) tests on un-notched 75mm deep beam specimens to estimate flexural and tensile strength. These were designated size S9.

d) Compression tests on 100mm cube specimens to determine compressive strength and estimate elastic modulus

The naming convention adopted for each test specimen was as follows:

Fibre content size number batch number

For example, 4S3B5 represented 4% fibre content; size designation S3; Batch number 5.

4.3.2 Notched three point bending (TPB) test

The three point bending (TPB) test was carried out on a Zwick/Roell Z250 Universal Testing Machine with a load capacity of 250kN (Fig. 4.2). A frame arrangement was used to mount two linear variable differential transformers (LVDTs) with one LVDT on either side used to measure mid-span deflection (Fig. 4.3). Deflection of the specimen was adopted as an average of the readings from the 2 LVDTs mounted on either side of the specimen. Mounting the LVDTs in this way is in accordance to AFGC (2013) recommendations and has been used successfully in several studies on UHPFRC (Yoo et al. (2013), Trivedi (2015), Kang et al. (2010), Yoo (2014) and Mahmud et al. (2013)). The LVDTs were set against aluminium metal clips glued on the sides of the specimens. In addition a crack width gauge was set within the notch in order to provide measurements of the crack mouth opening displacement (CMOD).

In order to achieve a stable crack growth necessary for measurement of the fracture energy, displacement controlled loading was adopted. Displacement control facilitates a stable crack growth by regulating the energy supplied for crack propagation and therefore minimising energy dissipation outside the fracture zone (Petersson, 1981). While fracture energy determination requires a full load-deflection curve, the post peak softening curves for UHPFRC typically have long tails. Therefore a strategy was devised to achieve full curves in a timely manner while maintaining the required level of precision.

Crack initiation and initial propagation is the most significant stage in the analysis of fracture. In order to ensure crack stability and ensure accurate measurements during this stage, a very slow initial displacement rate was adopted in each test (Table 4.3). Beyond the initial stage, the displacement rate was proportionately increased relative to the deflection to span ratio in order to test all the specimens within a reasonable time frame. The initial rate was maintained up to a deflection of 1/100 of span. It was then tripled and the loading continued up to a deflection of 2.5/100 of span had been reached. At this point the LVDTs were removed in order to safeguard them against damage that could arise by loading them beyond their measurement limit. The displacement measurement was then switched to crosshead travel and the displacement rate was increased 10 times and loading continued to the end. Just before removing the LVDTs, the mid-displacement rate was compared to the crosshead travel rate and they were found to be the same. This ensured a smooth transition between the two measurement methods as their displacement rates at that point were equivalent. The crack width gauge was left in place and just allowed to safely fall off after loading to a point when the crack was too wide to retain it. In order to maintain consistency and accuracy in measurements across different specimen sizes, these displacement rates were also scaled accordingly relative to size. Table 4.3 shows the displacement rates adopted for specimen sizes S1-S5. This loading strategy allowed a testing duration of about 1hr for each specimen which was reasonable given that 90 specimens had to be tested in total.

4.3.3 Un-notched three point bending (TPB) and four point bending (FPB) tests

Testing of both un-notched TPB (Fig. 4.4a) and FPB (Fig. 4.4b) specimens was carried out using the same machine as above. Displacement controlled loading was implemented. The tests were carried out in accordance with BS EN 12390-5 (2009) with a pre-load of 100N and a test speed of 0.05 mm/s. The crosshead travel was used as measure of deflection. This method is less accurate than use of LVDTs because readings could be affected by settlement at the loading points. However, these settlements are normally relatively small and occur in the initial stages of loading followed by the much longer elastic phase whose end can therefore still be easily identified. The specimens were not loaded on their unformed sides as an additional precaution to limit these settlements.

Figure 4.2: Three point bending test with notched specimen

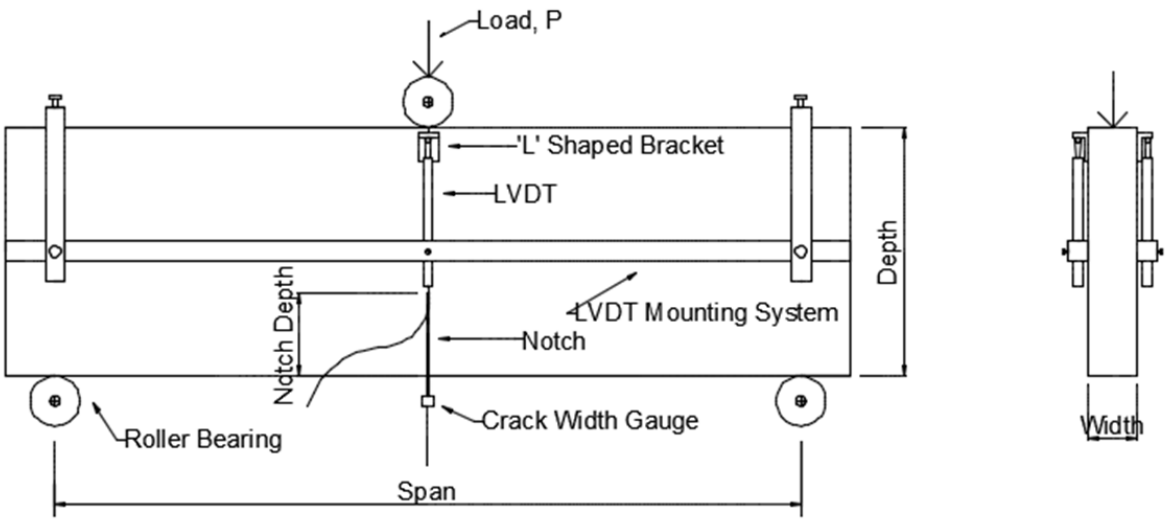

Figure 4.3: Three point bending test configuration

Table 4.3: Three Point Bending test displacement rates

	Start Rate	Change speed @ deflection =	2nd Speed	Remove devices and change speed @ deformation =	Final Speed
Size	(mm/min)	(mm)	(mm/min)	(mm)	(mm/min)
1	0.25	7.50	0.75	20.0	7.50
2	0.20	6.00	0.60	16.0	6.00
3	0.15	4.50	0.45	12.0	4.50
4	0.10	3.00	0.30	8.0	3.00
5	0.05	1.50	0.15	4.0	1.50

4.3.4 Compression Test

Compressive strength tests were carried according to BS EN 12390-3-2009 on 100x100x100mm cube specimens (Fig. 4.4c) from each of the 5 no. batches with 2%, 4% and 6% fibre content mixes. The specimens were tested in a universal strength test machine at a rate of 3KN/s to a maximum load from which the compressive strength could be calculated. These tests were important in identifying variability within the concrete matrix between the batches as the influence of fibres on compressive strength is relatively small. Density of the samples was also determined to give an indication of the relative consolidation of the batches either from self-compaction or vibration.

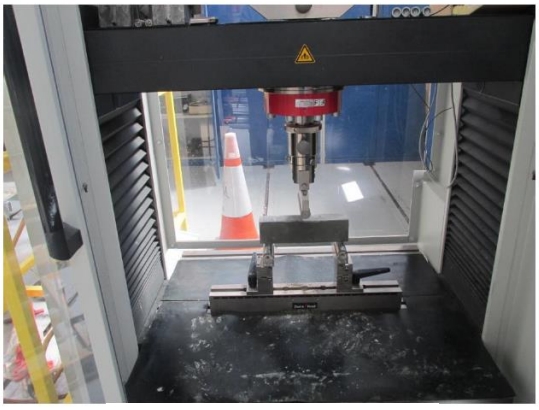

a) Un-notched TPB test

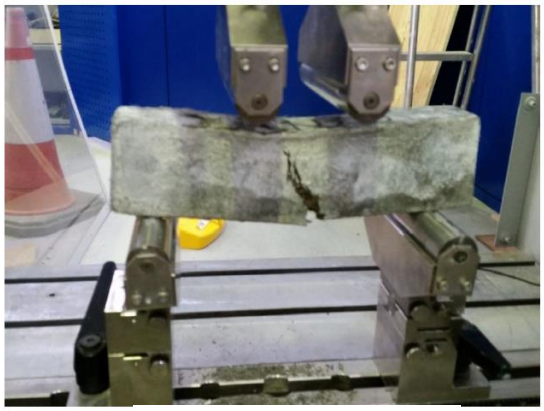

b) Un-notched FPB test

c) Compression test

Figure 4.4: a) Un-notched TPB test b) Un-notched FPB test c) Compression test

4.4 Summary of Results

4.4.1 Notched TPB test results

- **Overview**

In theory the fracture energy (G_f) should be calculated as the area below the full load-deflection or CMOD curve (Lee and Lopez, 2014). However, as the tail of the curve can often be very long, it is normally stopped at an arbitrary deflection typically equal to a proportion of the span. A correction factor is then applied when calculating G_f to account for the effect of the missing tail. As described in section 4.3.2 both deflection and crack mouth opening displacement (CMOD) were measured. However, the CMOD could only be obtained up to a certain loading point beyond which the crack width gauge fell off when the crack became too wide to retain it. On the other hand the loading strategy adopted enabled the full load deflection curves to be captured. Hence these full curves enabled the fracture energy to be determined without the need to estimate the effect of the tail. It is mainly for this reason that load-deflection curves were preferred in the analysis over the load-CMOD curves. The other reason for their use was that it enabled a comparison between notched and un-notched specimens. This is because the crack width gauge is only suitable where the location of the crack is known in advance as in the notched specimens. However, the use of load-deflection curves was also complemented by qualitative descriptions of the failure pattern in all the specimens which identified localised crack behaviour.

A summary of the load deflection curves from average test data is presented in Fig.4.5. The average test data was obtained by calculating the average loads over deflection intervals of 0.1mm which were then allocated to deflection values corresponding to the middle of the intervals. Generally, they had a straight pre-peak initial slope followed by a short hardening phase up to the peak. The point at first crack was not distinct and the transition from the linear elastic phase to hardening was gradual. The post-peak slope had an initial steep and straight portion which gradually transitioned into a long tail.

The load deflection curves from each batch presented in Appendix 1(a-c) show that the actual response was much more irregular than indicated by the smoothed average test curves. The irregularity of the curves was mainly due to the correction by the deflection control every time there was a drop due to cracking. Some tests were aborted before the full load deflection curves could be attained due to clips against which the LVDTs were set becoming unstuck where the crack path coincided with their point of attachment.

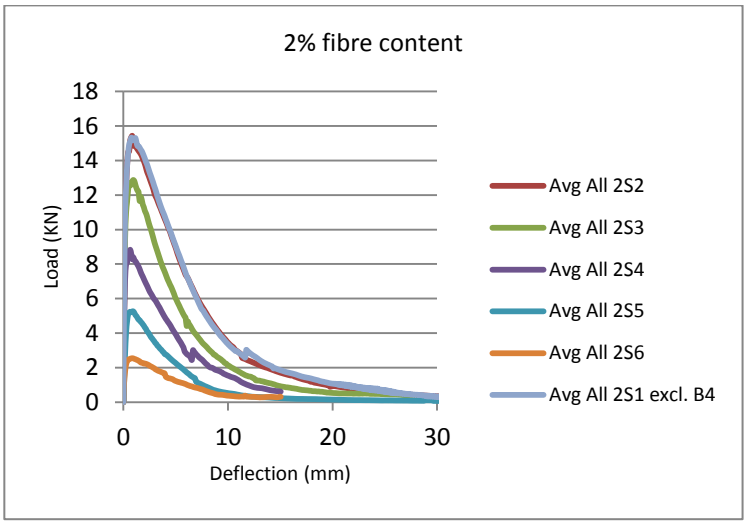

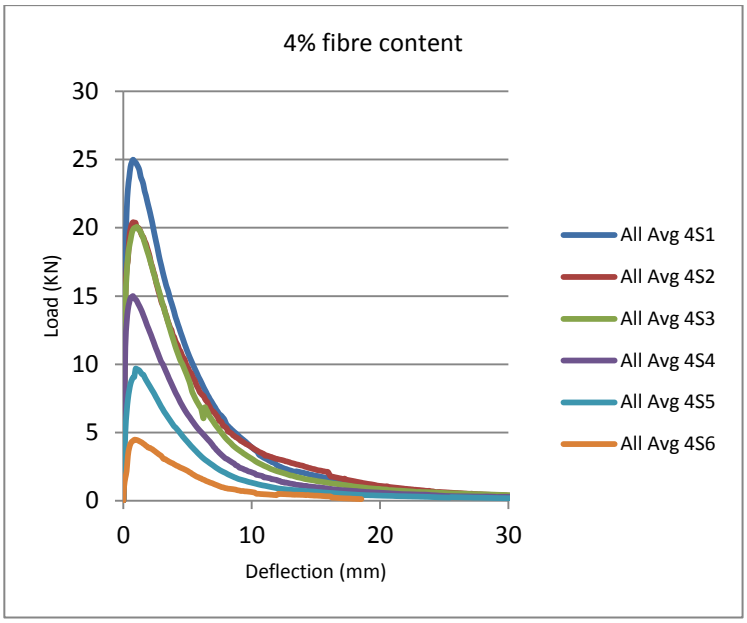

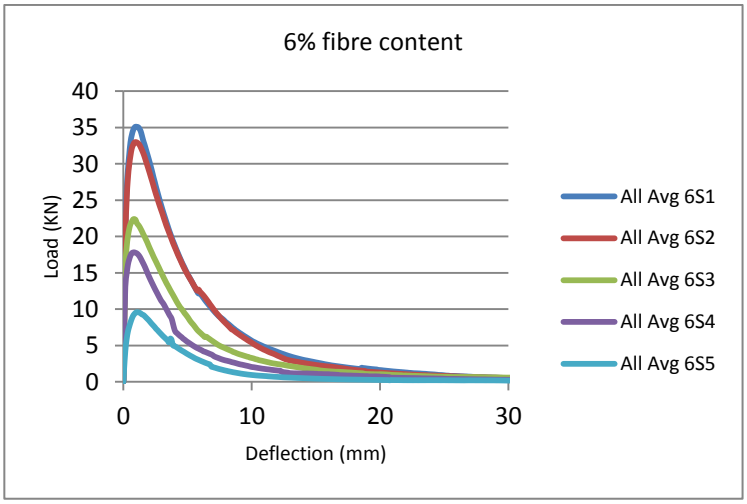

Figure 4.5: Average load deflection curves for all fibre contents

There was also a noticeable scatter between curves from different batches of the same specimen size typical of UHPFRC (Fehling *et al*, 2004). This is normally attributed to the variability in the orientation of the fibres which is mainly influenced by production factors. The load-deflection curves were generally less scattered the higher the fibre content. Apart from specimens with 2% fibre content, the scatter also seemed to increase the smaller the specimen. The scatter in the largest sizes with 2% fibre content (2S1 and 2S2) was made worse because some of the batches had curves with substantially lower peak loads. In the following sections, the elastic and hardening phases of the material are examined in terms of loads at the end of linearity and peak loads, while the flexural toughness concept is adapted to compare the post peak response.

- **Elastic phase**

The average slopes of the initial part of the curves from different batches were roughly the same and linear. However, the linearity of the slopes was only approximate due to the variability in the elastic modulus of the cement paste. The point at which linearity was lost was characterised by a sudden drop in load. This point may sometimes correspond to the occurrence of first cracking but not always as some cracks may also develop earlier in UHPFRC prior to this point (Sadegh and Lubell, 2012). Hence the vicinity of this point was initially identified by a visual examination of the curves. A comparison of slopes between two consecutive points within this vicinity then enabled the determination of the point more precisely. The point at the end of linearity was identified as that preceding the occurrence of a negative slope corresponding to the drop in load.

The loads at the end of linearity identified as above are presented in Table 4.4 and figures in Appendix 2. The average load increased with specimen size for all fibre contents as expected (Fig.4.5). However, the rate of increase in load was observed to decrease with size. An analysis of the batches was therefore undertaken to identify reasons for this decreasing rate of load increase. In batch 1 of specimens with 2% fibre content, there was a uniform increase in load with specimen depth up to a depth of 200mm then a drop at depth 250mm (Appendix 2a). It was this sharp drop in load of the largest specimen of this batch that most affected the average load (Fig.4.6). In the rest of the batches there was a general trend of the load increasing with specimen depth, though this was not uniform with some loads showing a drop. The scatter in the loads also seemed to increase with specimen size.

Table 4.4: Notched three point bending test load @ end of linearity

				Load @ end of linearity (kN)		
size	**Depth (mm)**	**Span (mm)**	**Batch No.**	**2% fibre content**	**4% fibre content**	**6% fibre content**
S1	250	750	1	15.80	25.74	20.81
			2	13.72	27.58	34.60
			3	6.14	21.20	27.78
			4	6.28	19.34	24.94
			5	15.06	15.83	23.76
S2	200	600	1	20.18	17.38	27.49
			2	6.91	24.30	34.48
			3	-	15.26	24.49
			4	14.15	16.43	28.18
			5	6.96	20.77	24.22
S3	150	450	1	14.28	16.97	15.37
			2	9.25	17.66	16.99
			3	14.17	15.09	20.16
			4	5.69	13.43	17.77
			5	9.62	19.75	17.25
S4	100	300	1	9.21	16.01	13.64
			2	-	12.13	14.52
			3	-	12.36	12.07
			4	-	9.33	17.25
			5	4.76	10.84	12.73
S5	50	150	1	6.31	6.63	7.66
			2	3.00	9.36	8.46
			3	3.26	7.36	7.26
			4	5.67	7.58	5.42
			5	5420.26	8070.09	9065
S6	25	75	1	2973.64	-	7023
			2	-	2806.86	4796
			3	1633.39	2114.77	7484
			4	-	4030.72	6015
			5	1645.22	4027.17	4277

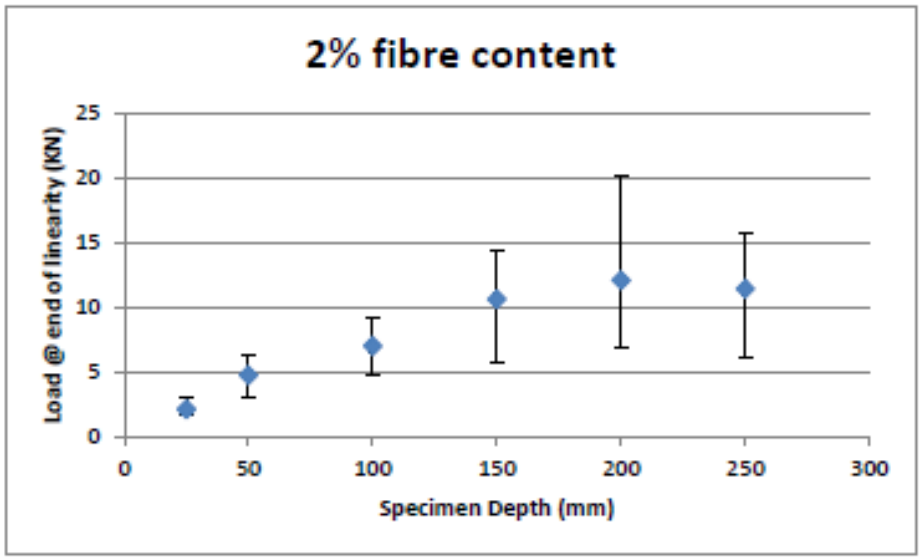

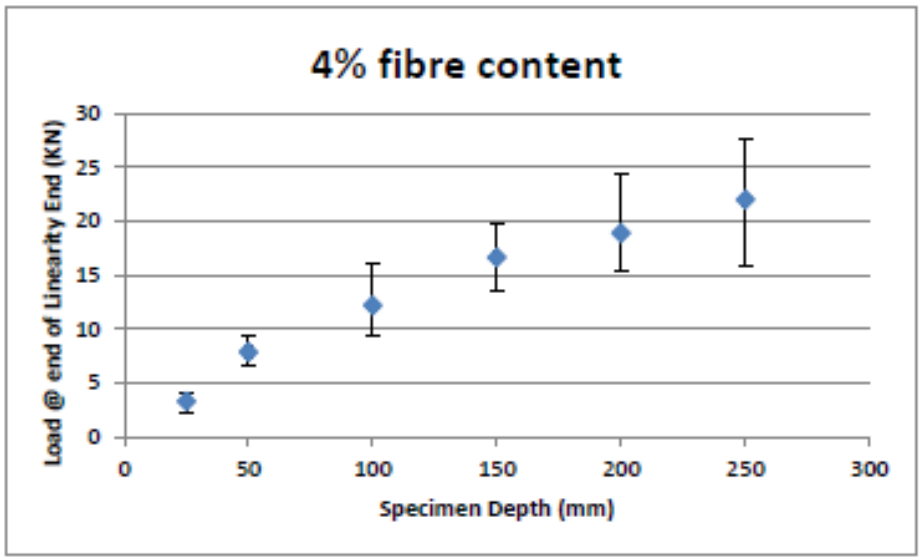

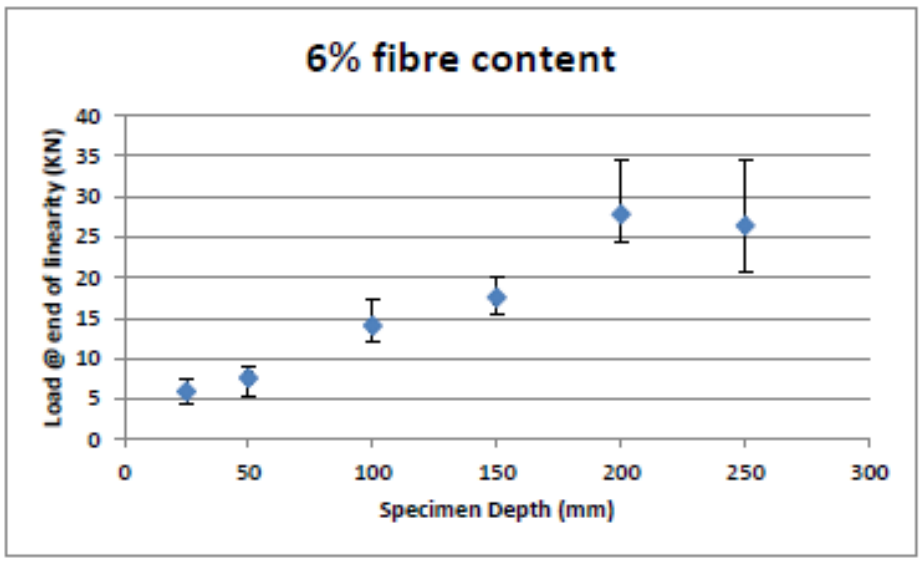

Figure 4.6: Notched Three Point Bending test average load @ end of linearity against specimen depth

For specimens with 4% fibre content, loads generally increased fairly uniformly with specimen depth in batches 2, 3 and 4 (Appendix 2b). Batch 1 also showed the same trend but the increase in load was not as uniform. In Batch 5 the loads also increased uniformly with size up to a depth of 200mm but dropped at depth 250mm. The decreasing rate of increase in average load therefore was mainly due to the drop in load in batch 5. The scatter in the load also showed an increase with specimen size (Fig.4.6). In specimens with 6% fibre content, the load increase with depth was mostly uniform in all the batches (Appendix 2c). The decreasing rate of increase in the average load was however attributed to batch 3 in which the load dropped off at the largest depth of 250mm (Fig.4.6).

- **Hardening phase (Peak Load analysis)**

After the end of proportionality, the loads continued to rise with increasing deflection. However, the rise was very irregular and was marked by several brief drops in load. This was the hardening phase caused by multiple cracking and the corresponding intervention of fibres through bridging action. The peak load marked the end of this phase and the values are presented in Table 4.5. It is clear from the plot of average peak loads against specimen depth that the trend was similar to that of the load at the end of linearity with a decreasing rate of increase in the average peak load with size (Fig.4.7).

Again an analysis of the peak loads of each batch (see figures in Appendix 3) identified the batches responsible for this trend. In batches 2 and 4 of specimens with 2% fibre content, peak load increased with specimen depth as expected (Appendix 3a). However, in batches 1, 3 and 5 peak load also increased with specimen depth up to depth of about 200mm then dropped sharply. The drop in load was reflected in the average peak load with scatter also increasing with specimen size (Fig.4.7). Except for batch 5 of specimens with 4% fibre content, peak load increased with specimen size (Appendix 3b). Batch 5 followed the same trend up to a depth of 200mm after which there was a significant drop. The average load increased with specimen size as did the scatter (Fig.4.7). In all the batches with 6% fibre content there was an increase in peak load with specimen size (Appendix 3c). In batch 1, however, there was a drop in the peak load of the largest size (depth=250mm). Despite this, the average peak load showed an increase with specimen size and less scatter compared to the lower fibre contents (Fig.4.7).

Table 4.5: Notched Three Point bending test peak loads

				Peak Load (kN)		
size	**Depth (mm)**	**Span (mm)**	**Batch**	**2% fibre content**	**4% fibre content**	**6% fibre content**
S1	250	750	1	17.84	31.15	27.52
			2	16.73	30.67	40.04
			3	10.73	24.41	33.85
			4	6.28	24.53	38.10
			5	17.00	16.99	38.82
S2	200	600	1	23.23	21.89	34.51
			2	14.29	28.41	36.56
			3	16.05	21.10	32.38
			4	15.64	20.50	33.67
			5	9.95	23.87	29.77
S3	150	450	1	16.75	25.95	18.67
			2	12.76	20.74	22.08
			3	16.30	18.24	25.79
			4	9.08	14.62	23.73
			5	11.26	21.74	23.54
S4	100	300	1	10.07	21.88	17.40
			2	-	13.31	20.40
			3	11.97	15.31	17.58
			4	6.72	12.26	20.53
			5	7.36	13.77	14.34
S5	50	150	1	6.70	7.82	12.42
			2	4.48	12.13	11.04
			3	3.35	10.54	9.51
			4	6.68	8.62	6.18
			5	5.78	9.43	10.54
S6	25	75	1	3.48	6.16	9.74
			2	3.16	3.73	5.92
			3	1.64	2.42	8.37
			4	2.53	6.25	8.26
			5	2.70	4.99	4.95

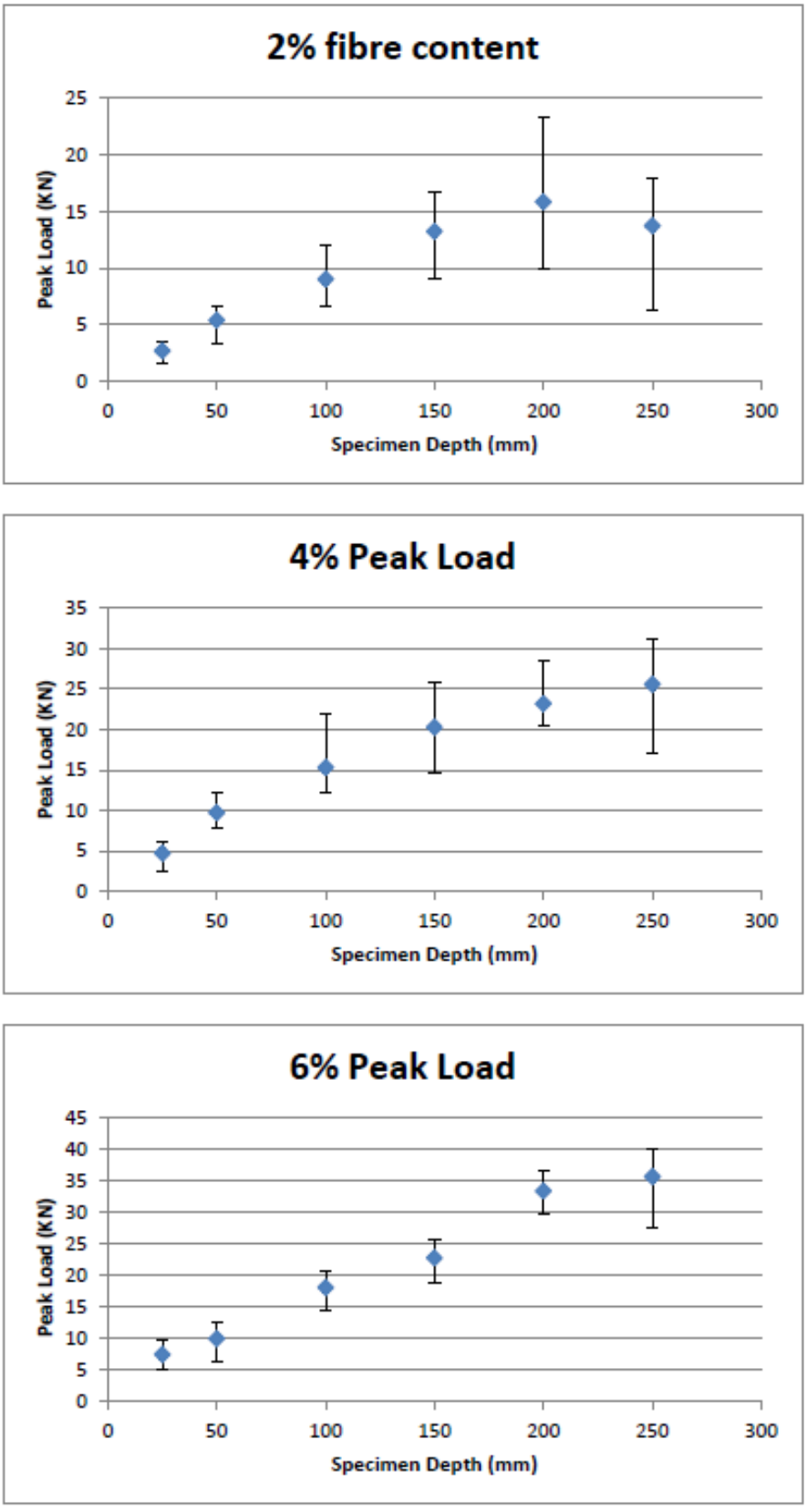

Figure 4.7: Notched three point bending test average Peak load against specimen depth

An important aspect of the hardening property is the increase in the material's load carrying capacity compared to if it did not have hardening. Therefore in order to evaluate the degree of hardening, the increase in load from loss of linearity to the peak was expressed as a percentage of the load at the loss of linearity as follows:

Hardening (%) = (Peak load – load at end of linearity)/load at end of linearity*100

The hardening response calculated as above is presented in Table 4.6 and Fig.4.9.

Deflection hardening was observed in all the specimens apart from Specimen 2S1B4 which did not display a noticeable hardening response. Generally, scatter in the hardening response for all fibre contents seemed to be much higher for the biggest sizes (S1 and S2). This could be related to the significant drop in loads for these sizes as discussed in section above. Scatter seemed to decrease with higher fibre contents. Despite the above, both size and fibre content did not seem to have any noticeable effect on the hardening response. In all the fibre contents there was a strong linear correlation between the load at end of linearity and the peak load (Fig.4.8).

Table 4.6: Average hardening

			Average Hardening (%)		
Size	**Depth**	**Span**	**2% fibre content**	**4% fibre content**	**6% fibre content**
S1	250	750	20.31	16.46	35.22
S2	200	600	31.40	22.98	20.20
S3	150	450	24.78	22.19	30.02
S4	100	300	29.25	26.17	28.52
S5	50	150	14.08	24.46	31.19
S6	25	75	27.01	31.66	25.42

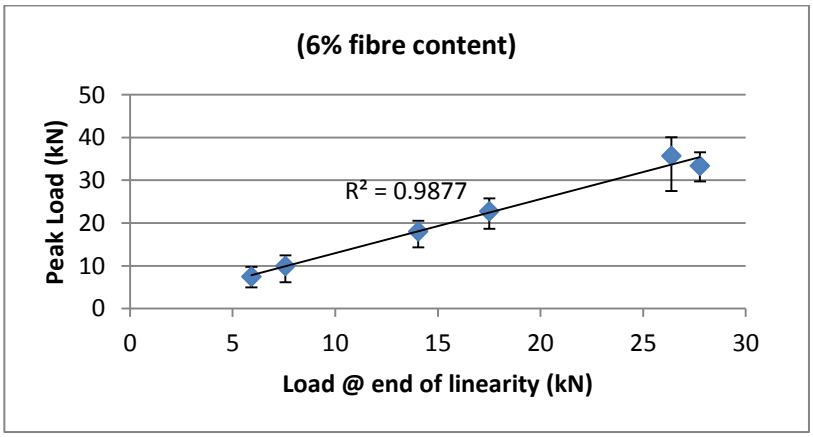

Figure 4.8: Peak Load against Load @ end of linearity

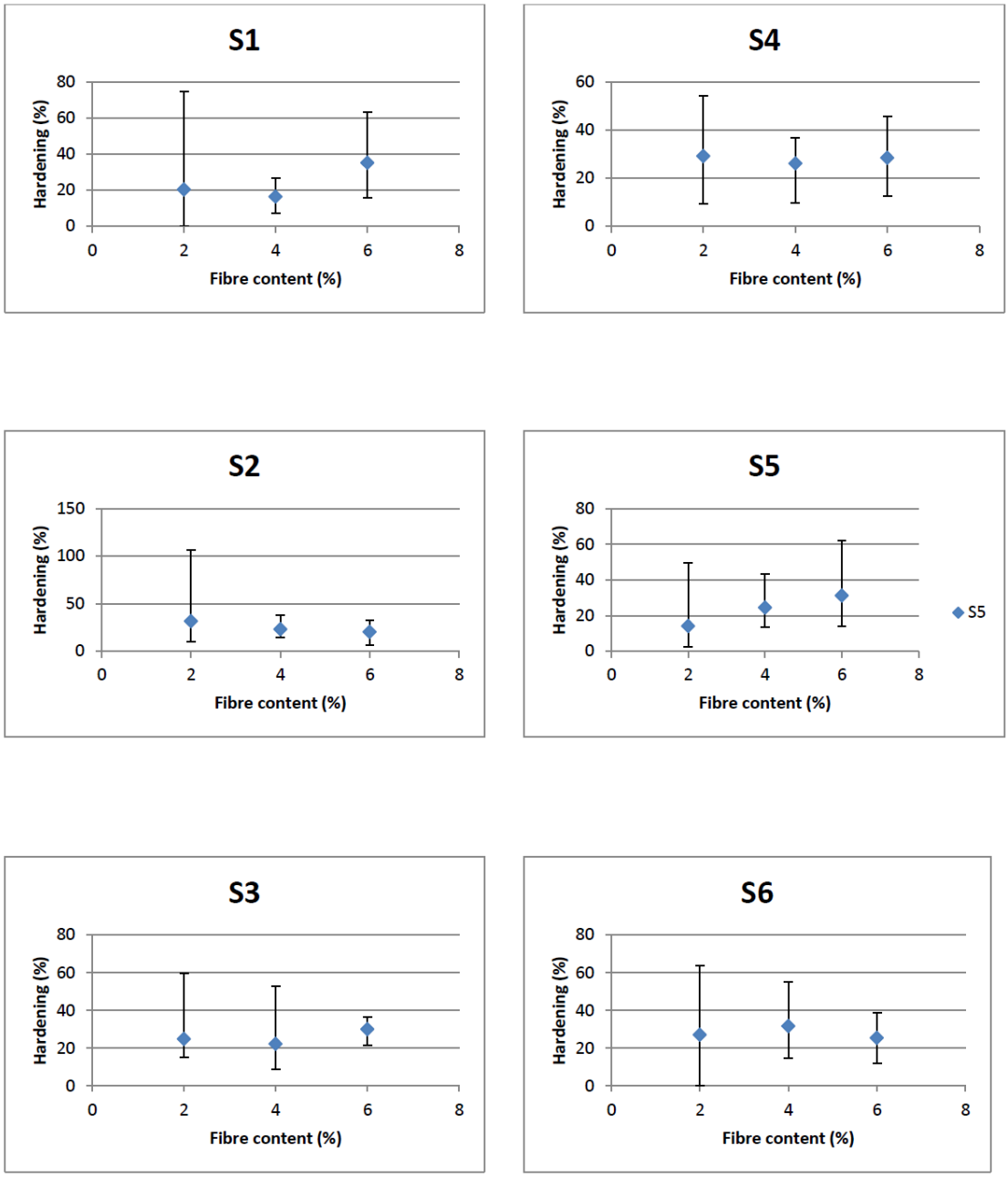

Figure 4.9: Notched Three Point bending test average hardening

- **Post Peak phase**

Beyond the peak, the curve had an initially steep descending slope which gradually transitioned into a long tail. Two approaches were considered in comparing the post peak response (Fig.4.10):

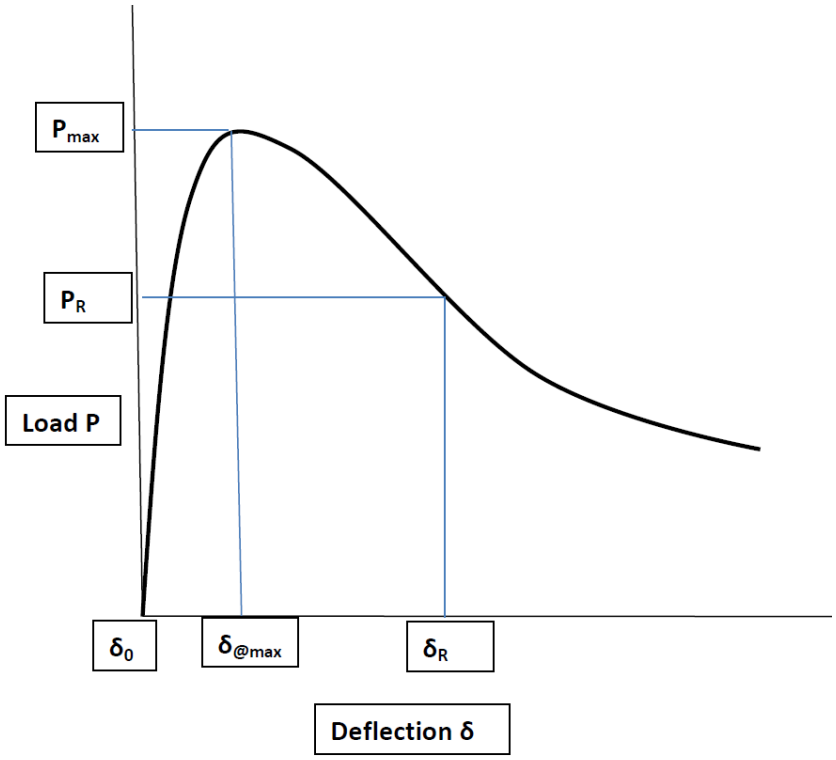

Figure 4.10: Post peak response analysis

i) Area under the load deflection curve between $\delta_{@max}$ and δ_R.

Calculating the area under the load deflection curve is the approach normally used in estimating a material's flexural toughness or fracture energy. The latter is normally adopted where the full load-deflection curve is available. However, as noted previously, in some of the batches, the test had to be stopped before the full curve was obtained. Therefore in this section, the batches are compared using an approach adapted from that of flexural toughness. Standards that adopt the flexural toughness approach estimate the area under the load deflection curve from zero deflection (δ_0) up to a deflection equal to a proportion of the span. For example the Japanese standard recommends using a deflection of up to 1/150 of span (JSCE-SF4). In order to compare only the post peak response of all the batches on the same basis, the area under the load deflection curve was calculated between the deflection at peak load (δ_0) and deflection equal to 1/150 of span (δ_R).This area was estimated by the trapezoidal rule implemented as a formula in excel whereby consecutive load measurements were averaged and multiplied by the interval in their deflection measurements. The modified post peak flexural toughness presented in Table 4.7 was then calculated as follows:

$$Toughness = \frac{(Area\ between\ \delta_{@max}\ and\ \delta_R)}{X - sectional\ area\ of\ crack\ ligament}$$

The X-sectional area of crack ligament equals the product of specimen width and overall depth less notch depth. In Fig.4.11 and 4.12 it can be observed that in using this approach the influence of peak load dominated the moderating effect of size making it difficult to assess only the post peak response. The resulting toughness measure was hence strongly dependent on specimen size mirroring the peak load response discussed in the previous section.

Table 4.7: Post peak flexural toughness

						Flexural toughness (N/mm)				
Fibre content (%)	**Size**	**Depth (mm)**	**Ligament (mm)**	**Span (mm)**	**1/150 of Span**	**Batch 1**	**Batch 2**	**Batch 3**	**Batch 4**	**Batch 5**
2	S1	250	167	750	5	8.37	7.46	4.45	2.68	8.06
	S2	200	133	600	4	11.23	6.23	7.49	6.92	4.81
	S3	150	100	450	3	11.02	5.61	7.70	4.58	5.23
	S4	100	67	300	2	4.83	-	5.83	3.52	3.83
	S5	50	33	150	1	3.79	2.57	1.70	3.64	3.09
	S6	25	17	75	0.5	1.96	1.74	0.79	0.41	1.51
4	S1	250	167	750	5	11.84	11.30	9.22	9.51	6.85
	S2	200	133	600	4	9.18	0.00	9.31	9.28	10.40
	S3	150	100	450	3	15.01	10.01	8.84	8.64	12.71
	S4	100	67	300	2	11.06	6.53	7.94	6.55	6.88
	S5	50	33	150	1	0.00	6.94	6.18	4.84	5.37
	S6	25	17	75	0.5	3.48	2.13	1.32	3.49	2.83
6	S1	250	167	750	5	9.69	14.20	13.57	15.32	14.90
	S2	200	133	600	4	15.77	15.39	13.86	13.25	12.98
	S3	150	100	450	3	9.25	9.14	11.34	12.03	10.56
	S4	100	67	300	2	8.56	10.55	8.86	10.01	7.01
	S5	50	33	150	1	11.24	6.20	4.77	3.49	6.09
	S6	25	17	75	0.5	5.54	3.31	4.69	4.73	2.79

ii) Average slope between peak load P_{max} and residual load P_R

This approach considered the relative slope of the post peak curve between P_{max} and P_R (Fig.4.10). However, as the slope was not constant, it only gave an indication of the average slope so that the higher the ratio, the less ductile a response and vice versa. The values are presented in Table 4.8. From Figs.4.13 and 4.14, both increasing specimen size and fibre content resulted in steeper post peak slopes implying a reduction in ductility and vice versa. Whereas increasing specimen size and fibre content increased the peak loads they also increased brittleness. This demonstrated the opposing effects of strength

and ductility on each other so that an in seeking to enhance both properties simultaneously an optimal balance must be found.

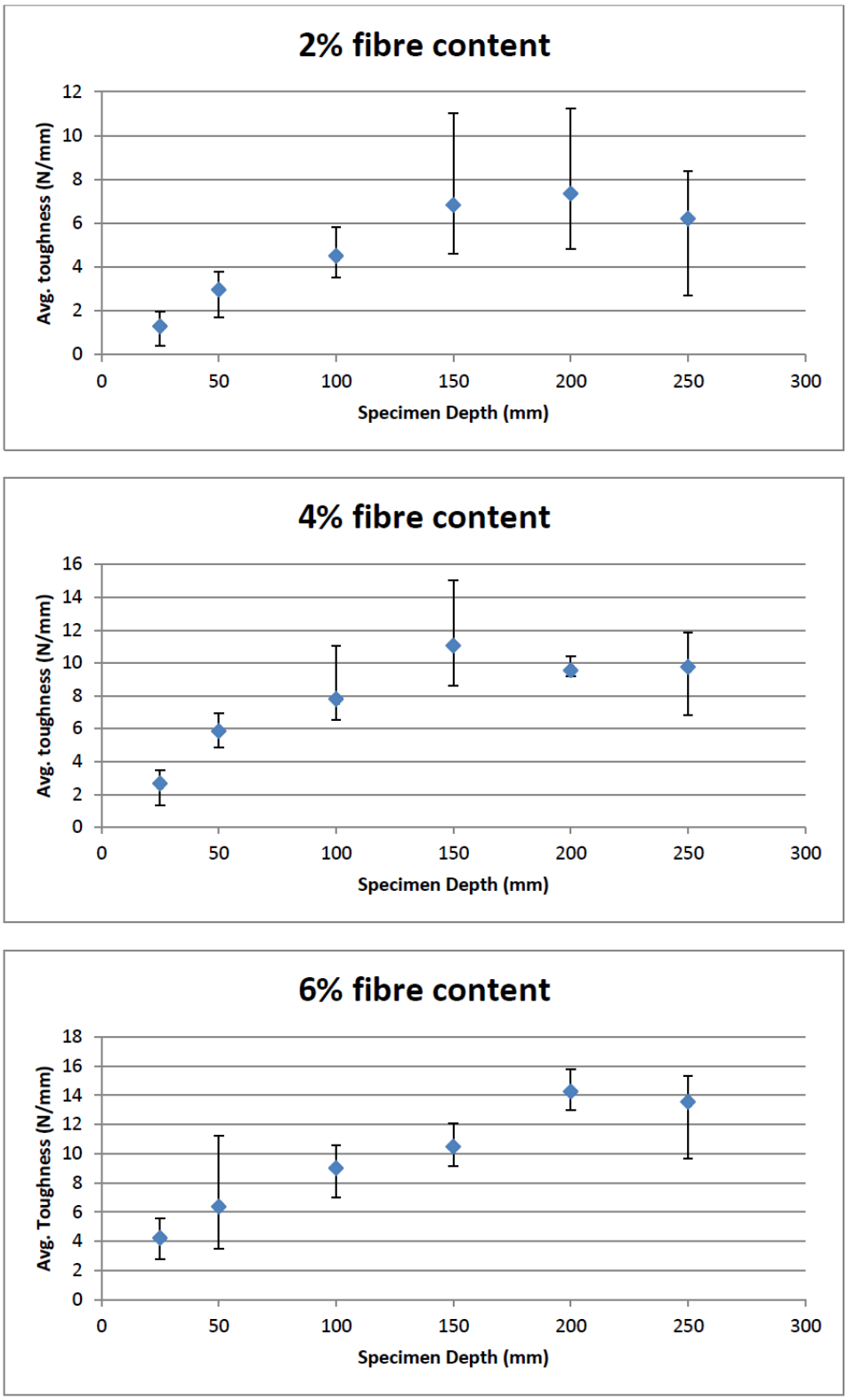

Figure 4.11: Notched Three Point Bending test average toughness against specimen depth

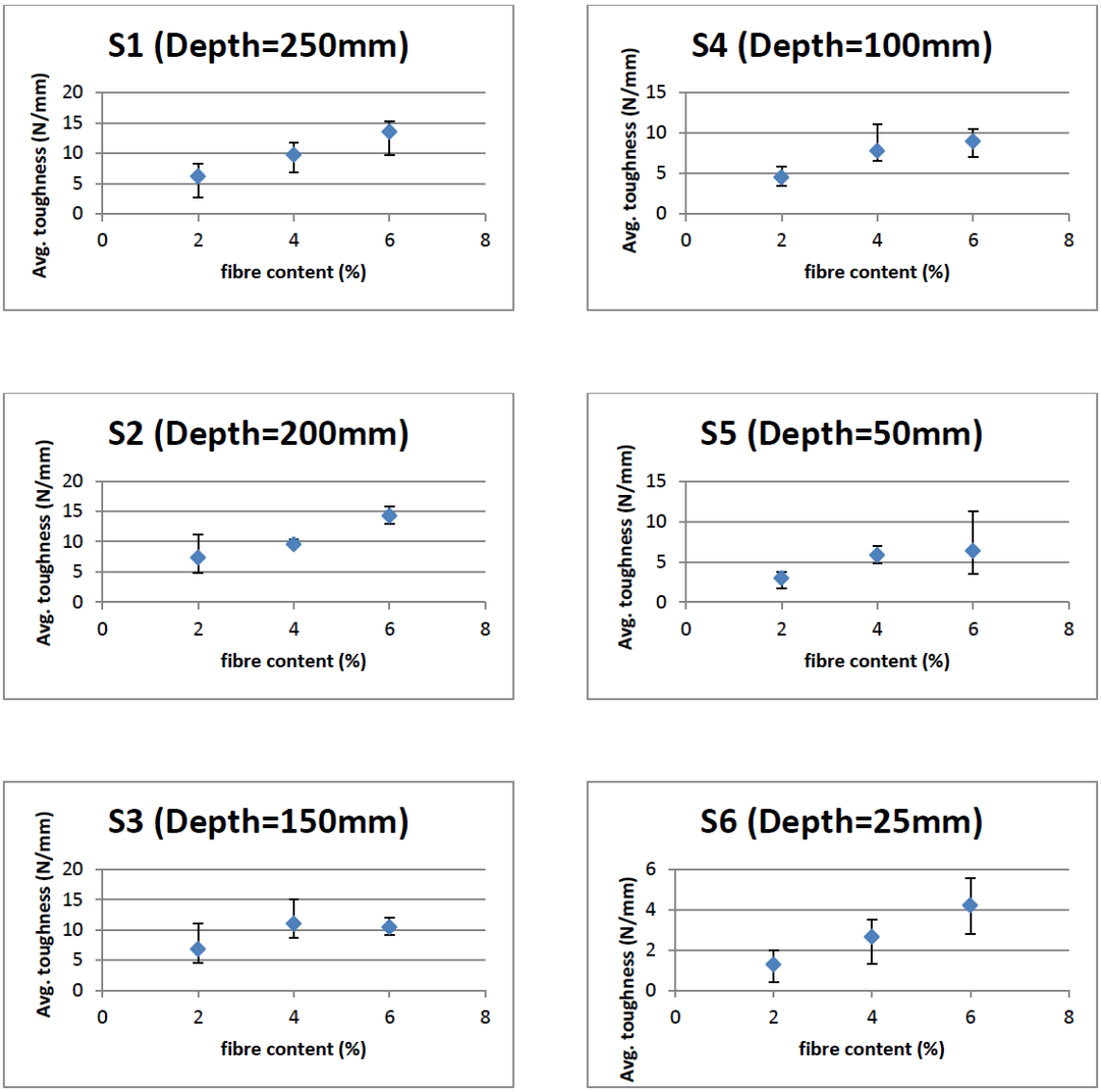

Figure 4.12: Notched Three Point Bending test average toughness against fibre content

Table 4.8: Notched Three Point Bending test average post peak slope

					Average slope		
Size	**Depth (mm)**	**Ligament (mm)**	**Span (mm)**	**1/150 of Span**	**2% fibre content**	**4% fibre content**	**6% fibre content**
S1	250	167	750	5	1408.50	3315.51	4841.89
S2	200	133	600	4	1762.96	3734.68	4675.13
S3	150	100	450	3	1807.79	3394.17	3562.70
S4	100	67	300	2	1325.27	2315.67	3663.22
S5	50	33	150	1	871.34	2542.35	1298.58
S6	25	17	75	0.5	419.50	685.51	1247.67

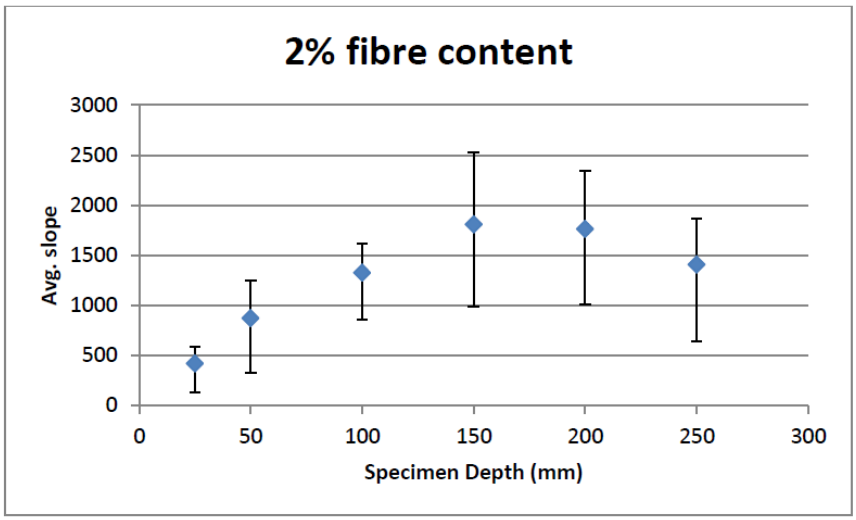

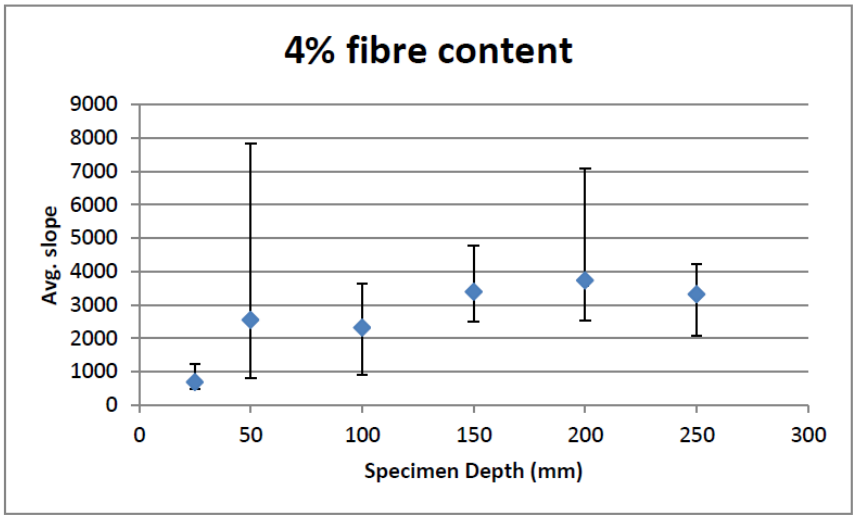

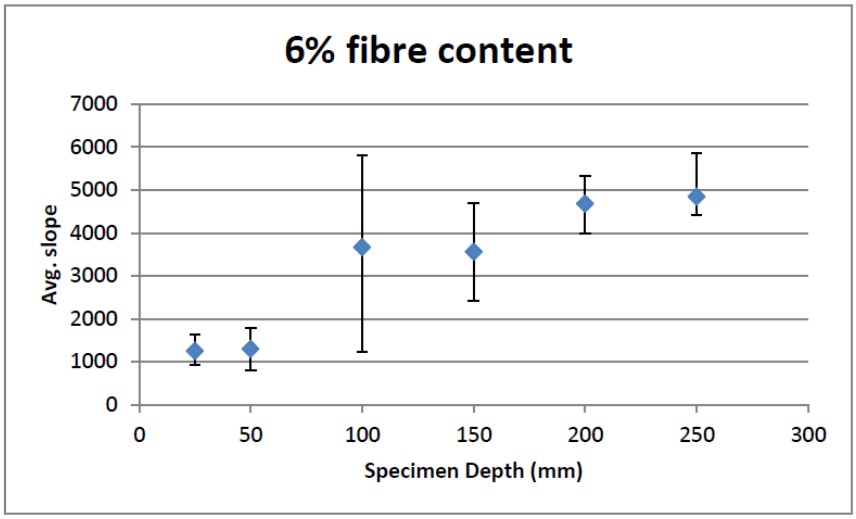

Figure 4.13: Notched Three Point Bending test average slope against specimen depth

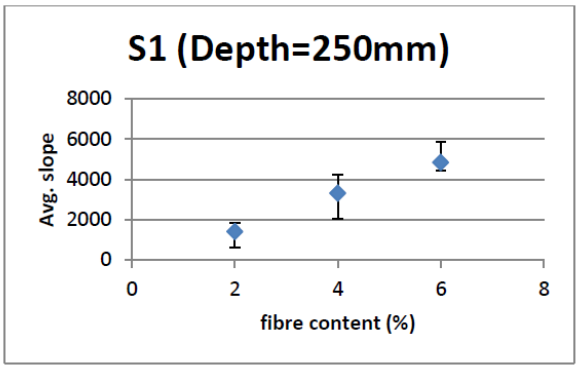

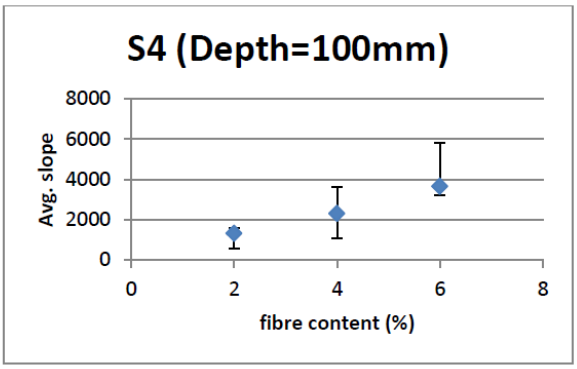

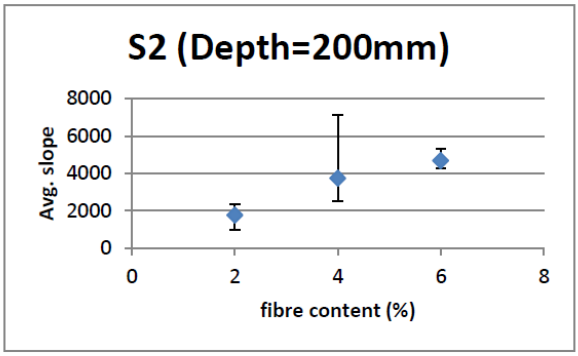

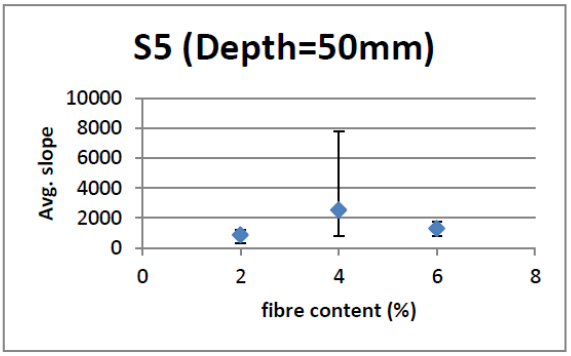

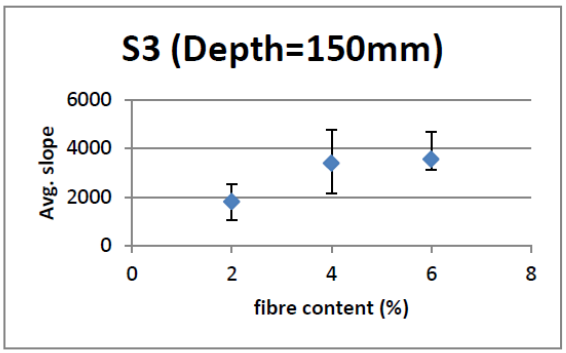

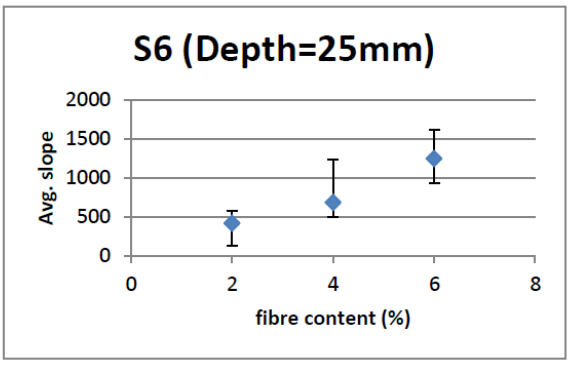

Figure 4.14: Notched Three Point Bending test average slope against fibre content

- **Failure pattern**

Typical failed specimens showed that a single dominant crack was formed in the middle of the specimen directly above and roughly vertical to the notch (Fig.4.15). However the cracks were irregular and tortuous with the crack faces held together by fibres bridging across them. A closer observation of the cracks also gave an indication of the variability in the content, distribution and orientation of the fibres which could account for the scatter in the load-deflection curves. For example, Fig.4.15 shows the main cracks in the specimen S1 (depth=250mm) from all the batches (B1-B5) with 2% fibre content. Clearly, batches 3 and 4 had much less fibres on the crack faces which were less tortuous compared to the rest of the batches. This could be the main reason for their much reduced pre-peak and post-peak performance described in the previous section.

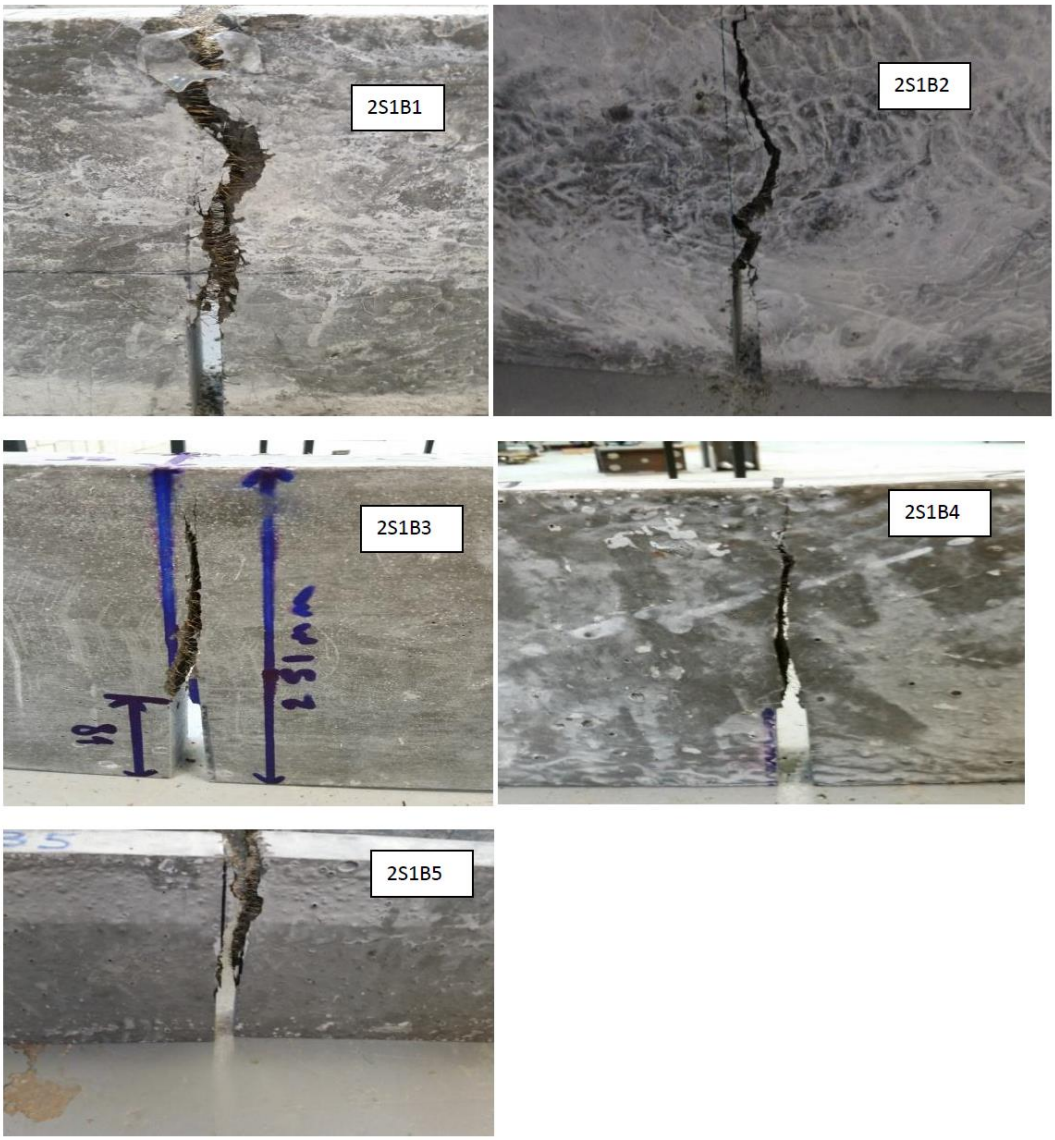

Figure 4.15: Notched three point bending test failed specimen showing main crack (2S1 B1-B5)

4.4.2 Un-notched TPB test results

- **Overview**

All the load-deflection curves for the un-notched three point bending test can be seen in Fig.4.16. The initial pre-peak slope generally ended at a distinct point corresponding to the first crack load. This was followed by a sharp drop before a pick-up launching the hardening phase which was irregular all the way to the peak. This was because of the multiple cracking associated with this phase. The post peak slope however was generally smoother because the main mechanisms involved fibre de-bonding and slippage. An initial shallow slope could be observed most distinctly in curves for specimens 2S11B2, 4S7B4, 4S8B3, 6S8B2 and 6S10B1 but also to a lesser extent in the other curves. This could be attributed to some local deformation at the load application point and in some cases crushing of the concrete. For example, in 4S8B3, the long shallow but irregular slope was most likely due to local crushing at points of loading (Fig.4.24). No difference was noticeable between the three fibre contents in relation to scatter of the curves.

- **Elastic phase (1st Crack analysis)**

Generally, the point at which linearity was lost, characterised by a sudden drop in load also corresponded to the occurrence of first cracking making it much easier to determine compared with TPB specimens. These loads are presented in Table 4.9. As expected the average load increased uniformly with specimen size in all the fibre contents (Fig.4.19). The same trend was observed in plots of load against depth for all the batches from all fibre contents (Appendix 4.a-c). In specimens with 2% fibre content a relatively small scatter in the loads was observed. However, in specimens with 4% and 6% fibre content, the scatter in the largest sizes was larger relative to that of the smallest sizes (Fig.4.19).

- **Hardening phase (Peak Load analysis)**

After the initial drop in load at end of linearity, the load started to rise again during the hardening phase until it reached a peak load. Table 4.10 presents the peak loads for each batch of all the fibre contents. A plot of the average peak load against specimen size also showed an almost uniformly increasing trend for all fibre contents (Fig.4.20). A larger scatter was also observed in the largest sizes. An analysis of the trends in each batch from all the fibre contents is presented in Appendix 5.a-c. The only difference from the general trend was observed in specimens with 6% fibre content in which only batches 3

and 5 have a uniform increase in load with size. In the rest of the batches, the increase in load was also observed but there was a drop in load at the largest size. The degree of hardening represented by the proportional increase in load bearing capacity between load at linearity and peak load (Table 4.11) showed too wide a scatter to indicate any influence of size or fibre content on it (Fig.4.21).

Table 4.9: Un-notched three point bending test Load at the end of linearity

						Load @ end of linearity (kN)		
Size	**Depth (mm)**	**Span (mm)**	**Width (mm)**	**Specimen**	**Batch no.**	**2%**	**4%**	**6%**
S7	125	375	50	S7B1	1	23.50	32.11	21.90
S7	125	375	50	S7B2	2	23.59	27.97	28.15
S7	125	375	50	S7B3	3	21.12	23.79	30.56
S7	125	375	50	S7B4	4	21.49	-	30.04
S7	125	375	50	S7B5	5	22.54	24.58	28.18
S8	100	300	50	S8B1	1	18.32	19.33	-
S8	100	300	50	S8B2	2	20.18	18.46	26.10
S8	100	300	50	S8B3	3	19.64	-	22.42
S8	100	300	50	S8B4	4	17.75	17.12	29.19
S8	100	300	50	S8B5	5	18.93	19.11	22.51
S10	50	150	50	S10B1	1	11.00	13.25	-
S10	50	150	50	S10B2	2	10.73	-	12.04
S10	50	150	50	S10B3	3	10.90	10.52	0.00
S10	50	150	50	S10B4	4	9.51	11.85	11.74
S10	50	150	50	S10B5	5	11.72	12.34	13.31
S11	25	75	50	S11B1	1	5.20	6.62	11.15
S11	25	75	50	S11B2	2	6.23	6.80	8.59
S11	25	75	50	S11B3	3	4.14	6.42	11.58
S11	25	75	50	S11B4	4	6.35	5.75	9.37
S11	25	75	50	S11B5	5	5.93	5.48	8.63

- **Post peak analysis**

Like in notched specimens, the average slope was observed to increase with both size and fibre content (Table 4.12 and Fig.4.22 & 4.23) indicating the dominant effect of higher peak load on reducing ductility over other counteracting factors such as the fibre bridging action.

Table 4.10: Un-notched three point bending test Peak Loads

						Peak Load (kN)		
Size	**Depth (mm)**	**Span (mm)**	**Width (mm)**	**Specimen**	**Batch no.**	**2% fibre content**	**4% fibre content**	**6% fibre content**
S7	125	375	50	S7B1	1	32.92	45.94	35.15
S7	125	375	50	S7B2	2	30.84	44.21	43.74
S7	125	375	50	S7B3	3	30.94	44.23	48.84
S7	125	375	50	S7B4	4	21.50	41.67	40.66
S7	125	375	50	S7B5	5	26.45	35.92	34.06
S8	100	300	50	S8B1	1	30.05	33.09	35.46
S8	100	300	50	S8B2	2	25.66	30.69	46.87
S8	100	300	50	S8B3	3	21.66	38.12	36.93
S8	100	300	50	S8B4	4	17.75	30.35	49.52
S8	100	300	50	S8B5	5	23.47	27.81	31.36
S10	50	150	50	S10B1	1	11.00	17.43	21.24
S10	50	150	50	S10B2	2	16.25	19.44	15.16
S10	50	150	50	S10B3	3	13.15	20.18	19.64
S10	50	150	50	S10B4	4	14.53	14.77	16.39
S10	50	150	50	S10B5	5	13.52	14.34	20.00
S11	25	75	50	S11B1	1	6.13	11.26	11.98
S11	25	75	50	S11B2	2	6.23	9.68	11.15
S11	25	75	50	S11B3	3	4.64	8.59	12.07
S11	25	75	50	S11B4	4	6.49	7.99	11.44
S11	25	75	50	S11B5	5	5.93	10.20	9.95

- **Failure pattern**

Generally a single dominant but irregular crack was formed within the middle third of the span with the fibres bridging the two crack faces (Fig.4.24). However, branches of other minor cracks could also be observed from the main crack. In all the three point bending specimens the main crack developed from the bottom vertically up to the load application point. The exception was in one of the specimens from the second smallest size where a crack developed at 45^{o} from the support to the load application point (Fig.4.32). This may have been caused by shear failure due to the short span relative to the size of the rollers applying the load.

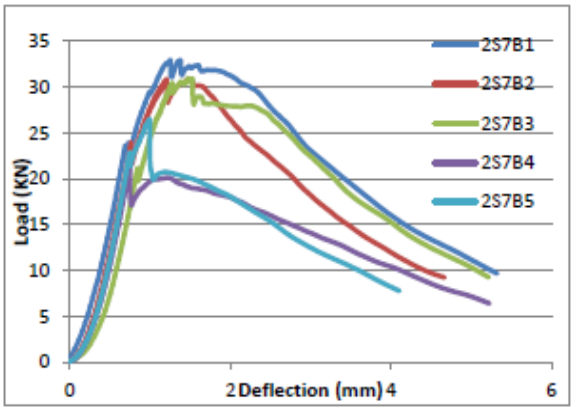

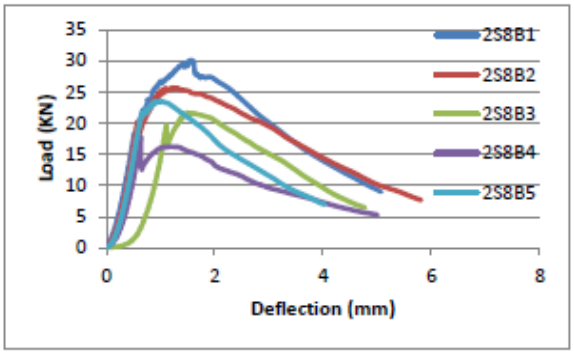

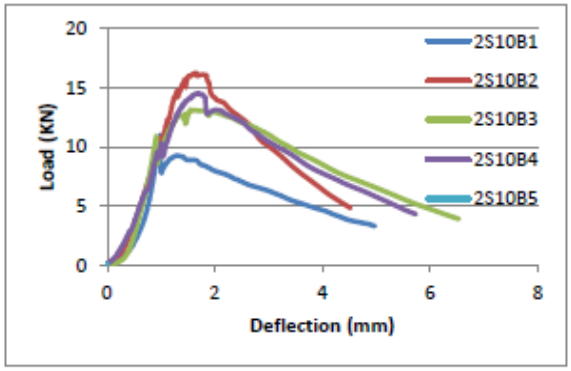

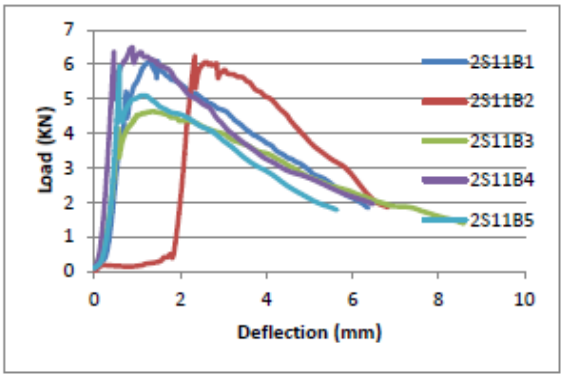

Figure 4.16: Load deflection curves for Un-notched three point bending specimens (2% fibre content)

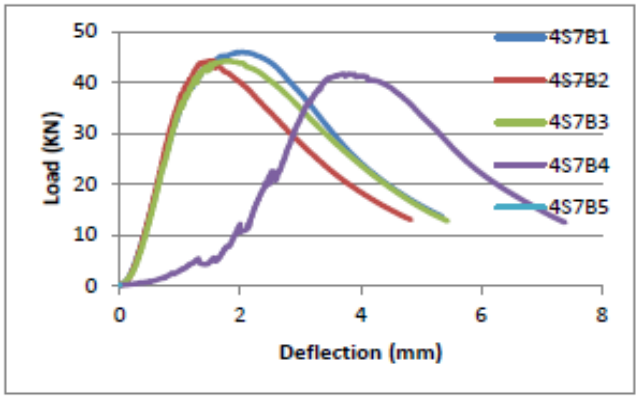

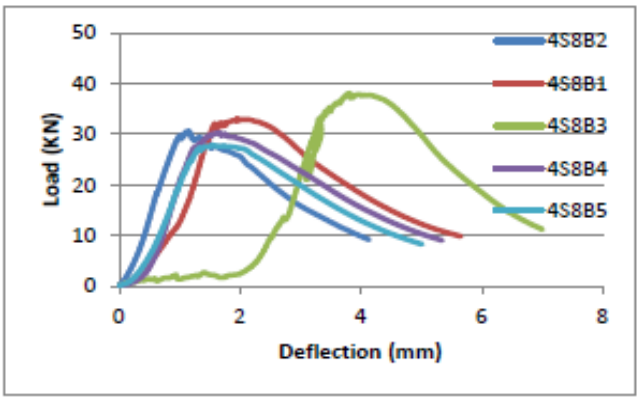

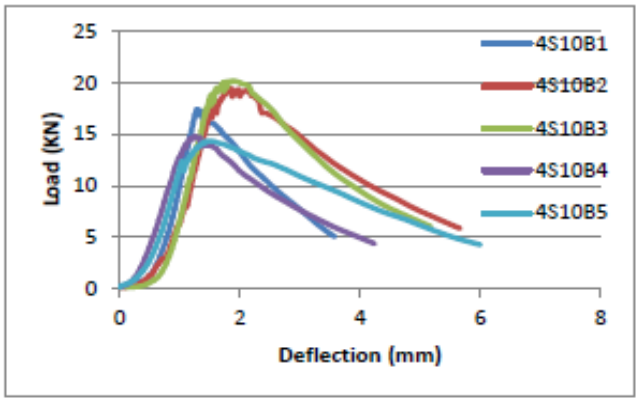

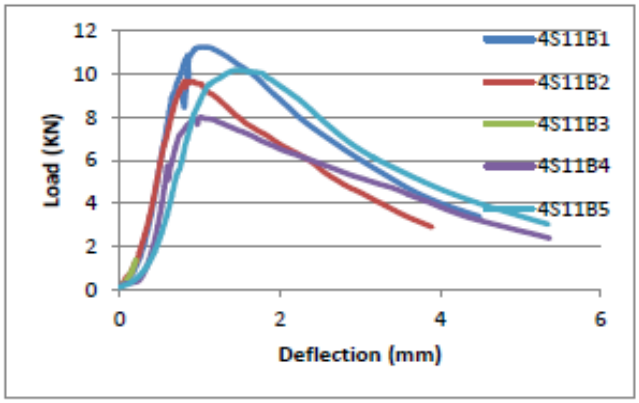

Figure 4.17: Load deflection curves for Un-notched three point bending specimens (4% fibre content)

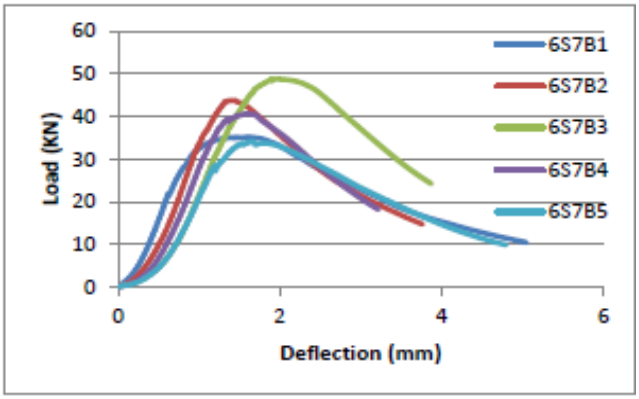

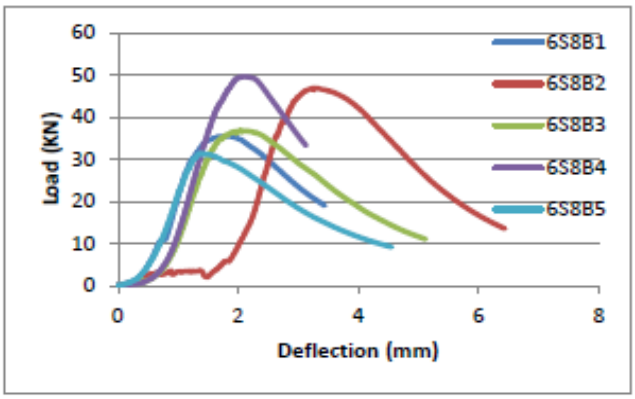

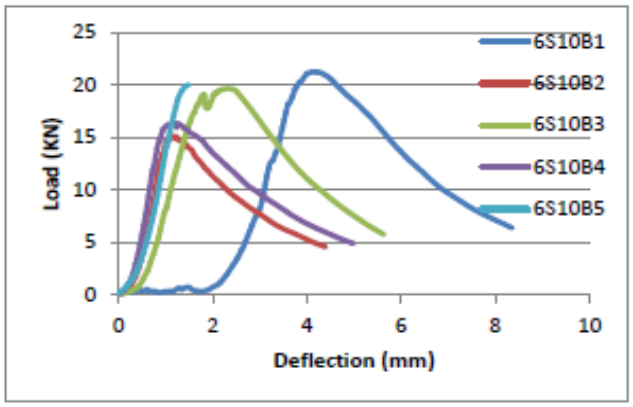

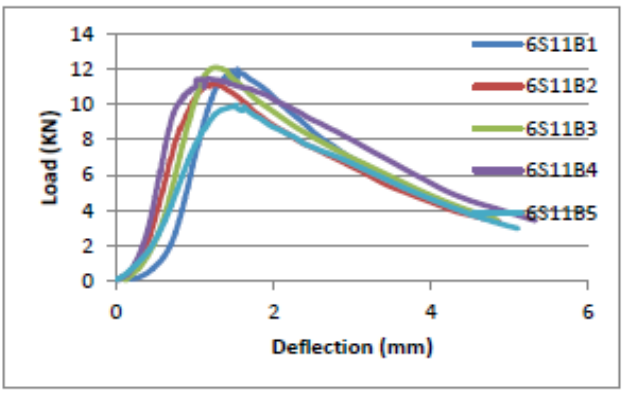

Figure 4.18: Load deflection curves for Un-notched three point bending specimens 6% fibre content

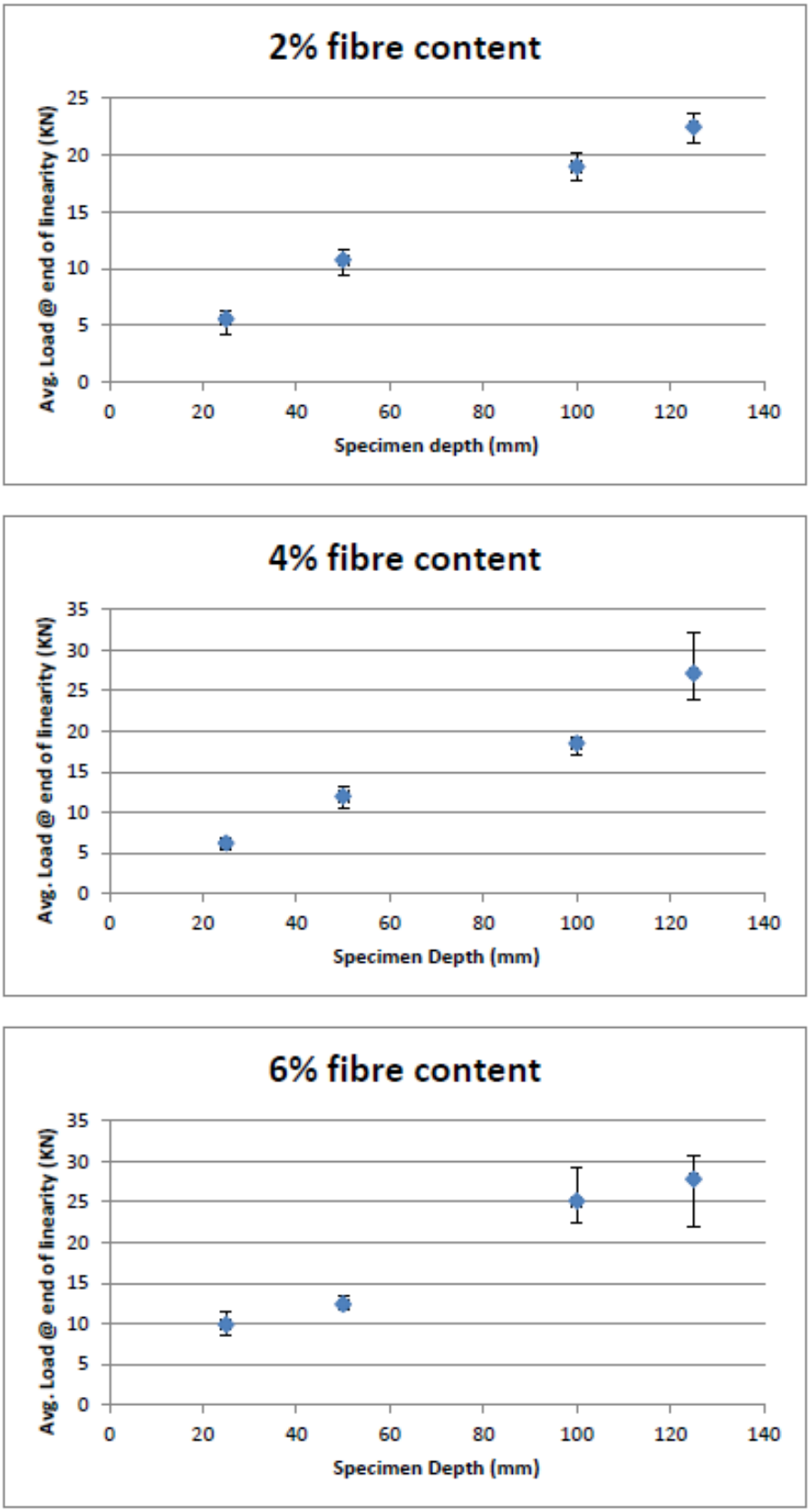

Figure 4.19: Un-notched three point bending test average load @ end of linearity against specimen depth

Table 4.11: Un-notched three point bending test hardening (%)

						Hardening (%)		
Size	**Depth (mm)**	**Span (mm)**	**Width (mm)**	**Specimen**	**Batch no.**	**2% fibre content**	**4% fibre content**	**6% fibre content**
S7	125	375	50	S7B1	1	40.11	43.07	60.49
S7	125	375	50	S7B2	2	30.73	58.02	55.36
S7	125	375	50	S7B3	3	46.47	85.91	59.82
S7	125	375	50	S7B4	4	0.04	-	35.35
S7	125	375	50	S7B5	5	17.33	46.13	20.90
					Average	27.09	56.35	45.83
S8	100	300	50	S8B1	1	64.04	71.19	-
S8	100	300	50	S8B2	2	27.17	66.23	79.62
S8	100	300	50	S8B3	3	10.30	-	64.68
S8	100	300	50	S8B4	4	0.00	77.33	69.66
S8	100	300	50	S8B5	5	23.93	45.53	39.30
					Average	25.07	72.99	59.76
S10	50	150	50	S10B1	1	0.00	31.55	-
S10	50	150	50	S10B2	2	51.48	-	25.90
S10	50	150	50	S10B3	3	20.63	91.85	-
S10	50	150	50	S10B4	4	52.79	24.62	39.55
S10	50	150	50	S10B5	5	15.42	16.23	50.29
					Average	27.11	43.72	49.53
S11	25	75	50	S11B1	1	17.96	70.05	7.44
S11	25	75	50	S11B2	2	0.00	42.42	29.75
S11	25	75	50	S11B3	3	12.01	33.91	4.26
S11	25	75	50	S11B4	4	2.29	38.93	22.20
S11	25	75	50	S11B5	5	0.00	86.25	15.34
					Average	5.66	53.63	14.76

Table 4.12: Un-notched three point bending average slope

				Average slope (N/mm)		
Size	**Depth (mm)**	**Span (mm)**	**1/150 of Span**	**2% fibre content**	**4% fibre content**	**6% fibre content**
S7	125	375	2.5	5066.2	9518.6	11002.8
S8	100	300	2	4155.5	6968.1	10980.4
S10	50	150	1	2660.0	4224.4	4156.6
S11	25	75	0.5	875.2	1707.5	2792.6

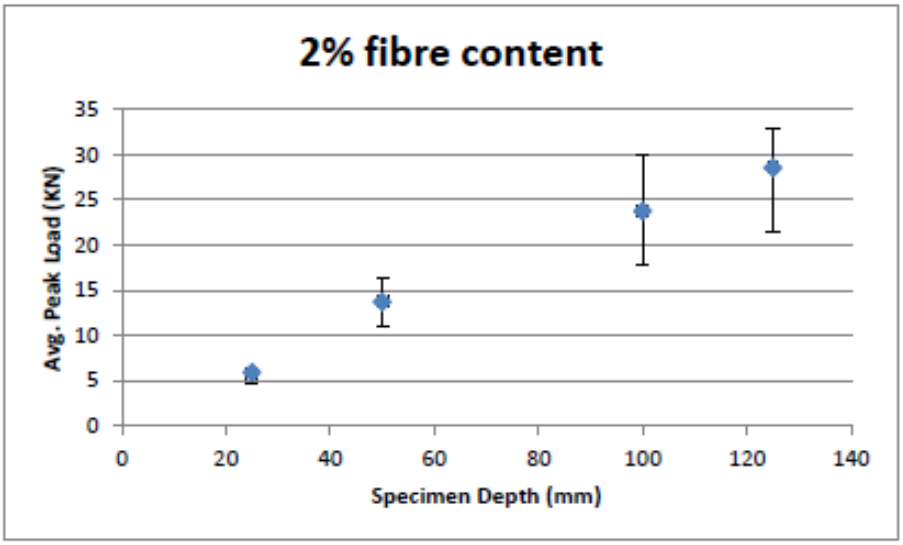

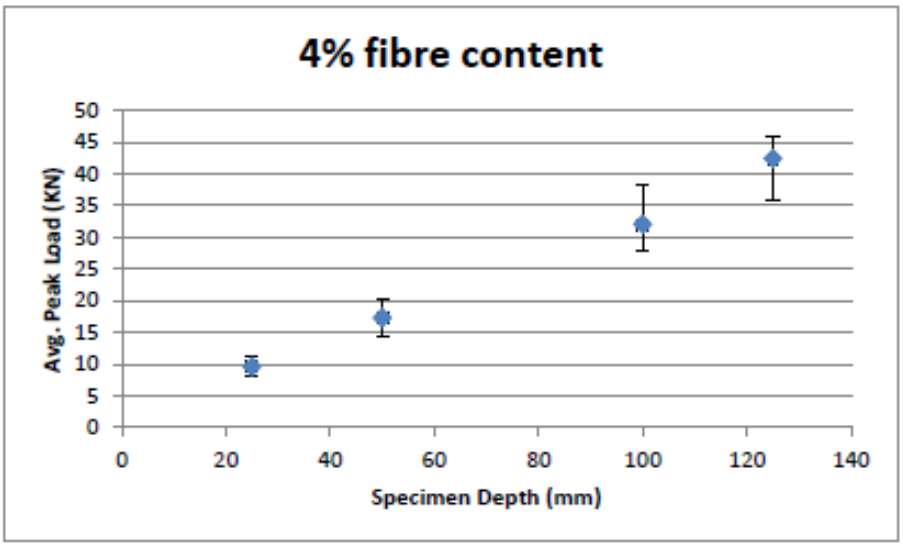

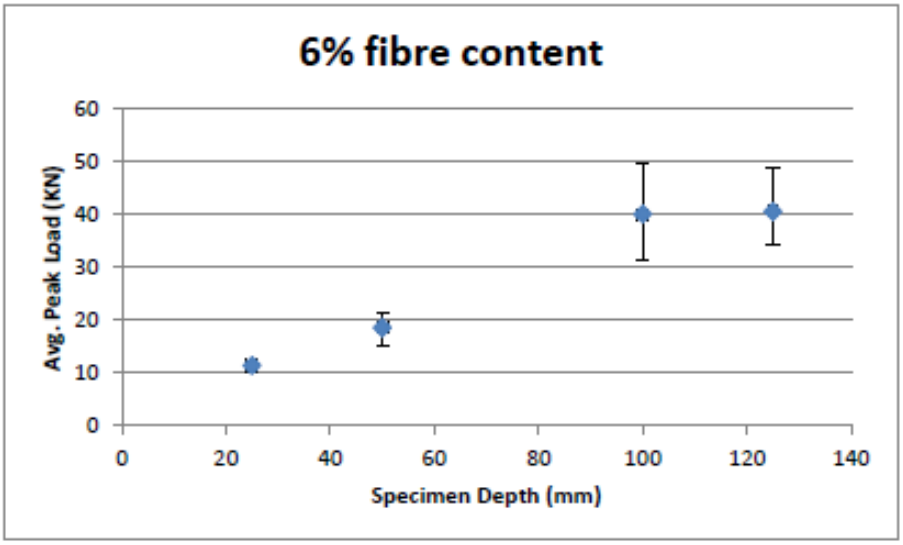

Figure 4.20: Un-notched three point bending test average peak load against specimen depth

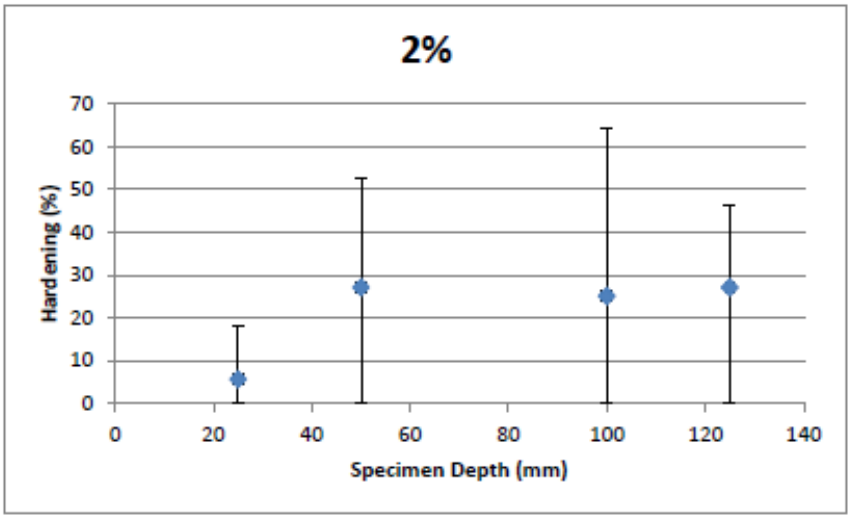

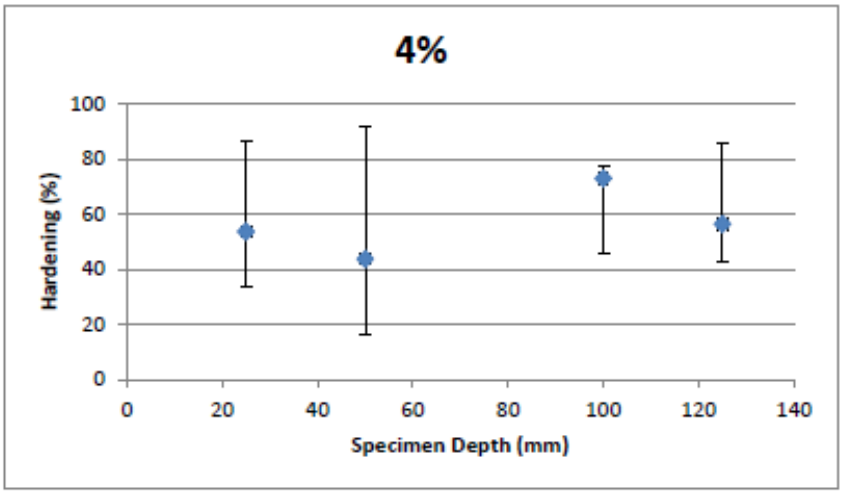

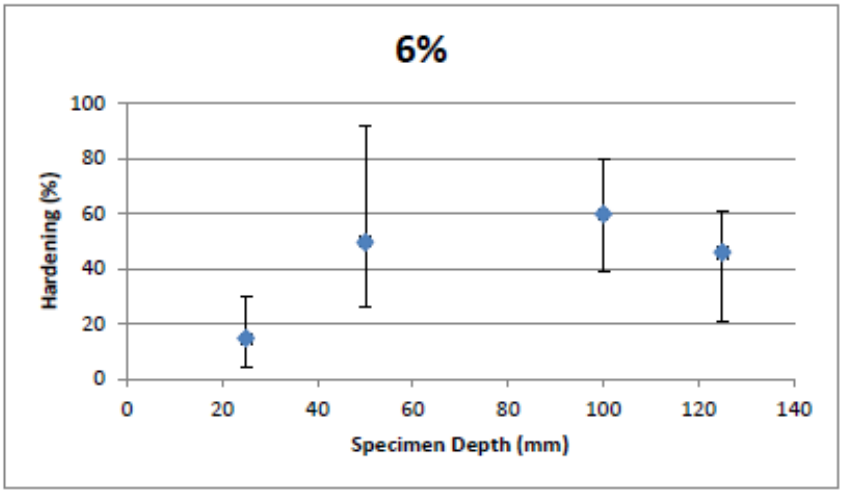

Figure 4.21 : Un-notched three point bending test average hardening

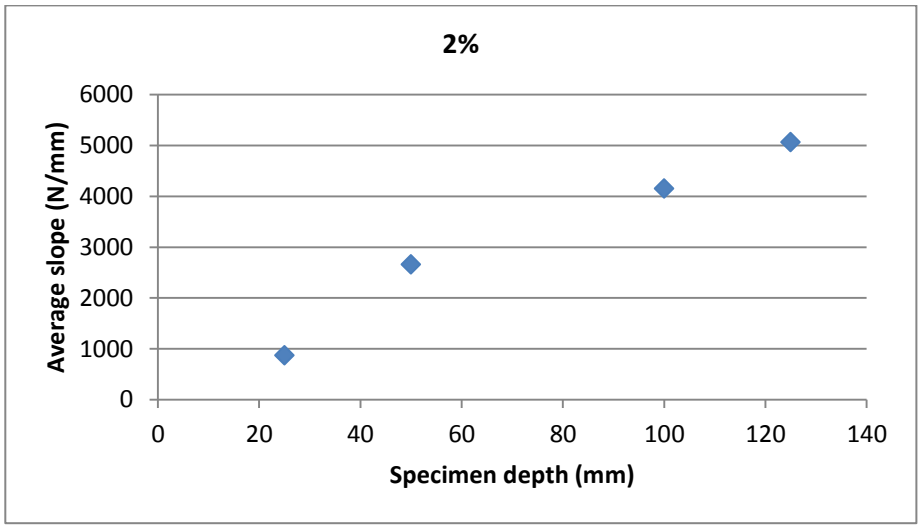

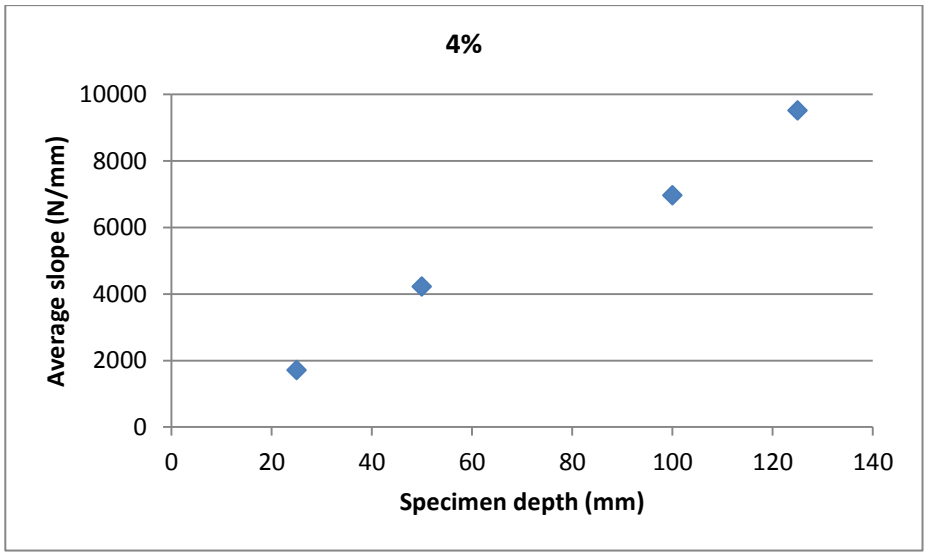

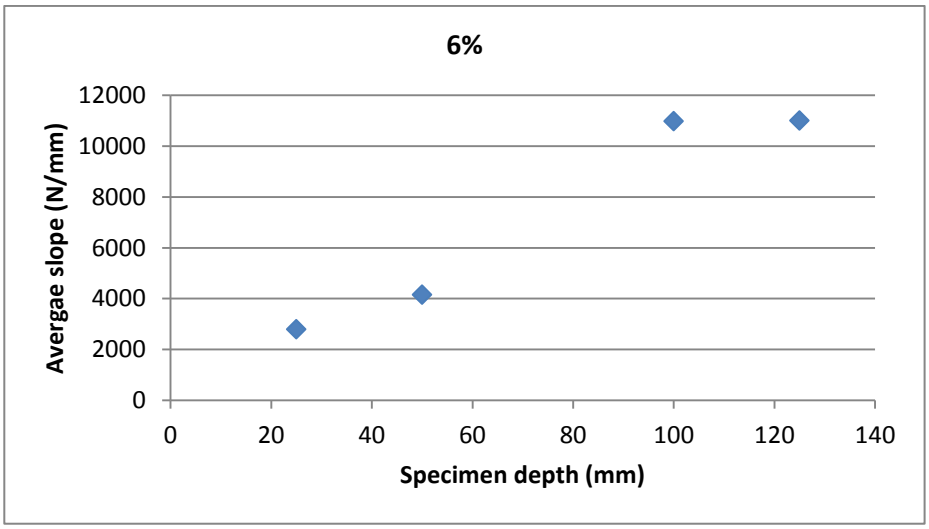

Figure 4.22: Un-notched three point bending test average slope against specimen depth

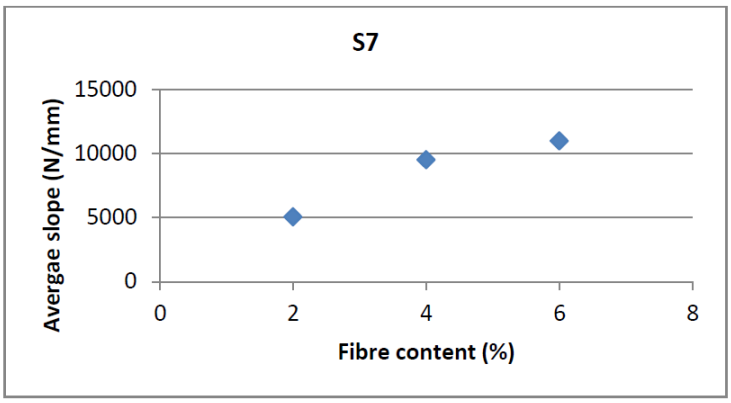

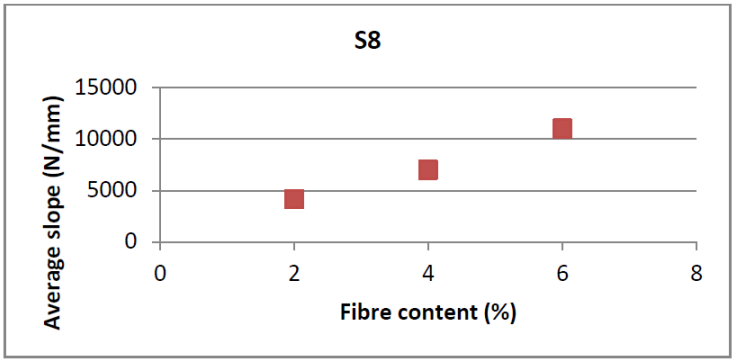

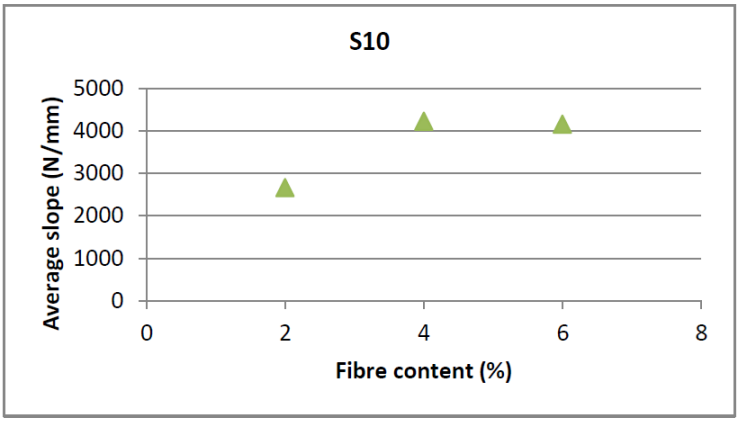

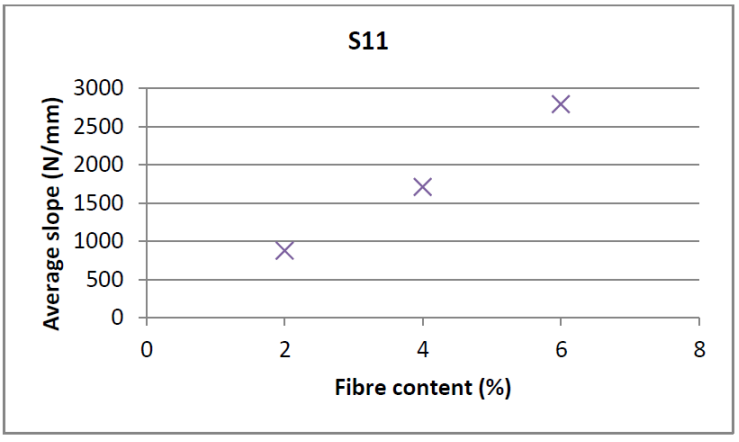

Figure 4.23: Un-notched three point bending test average slope against fibre content

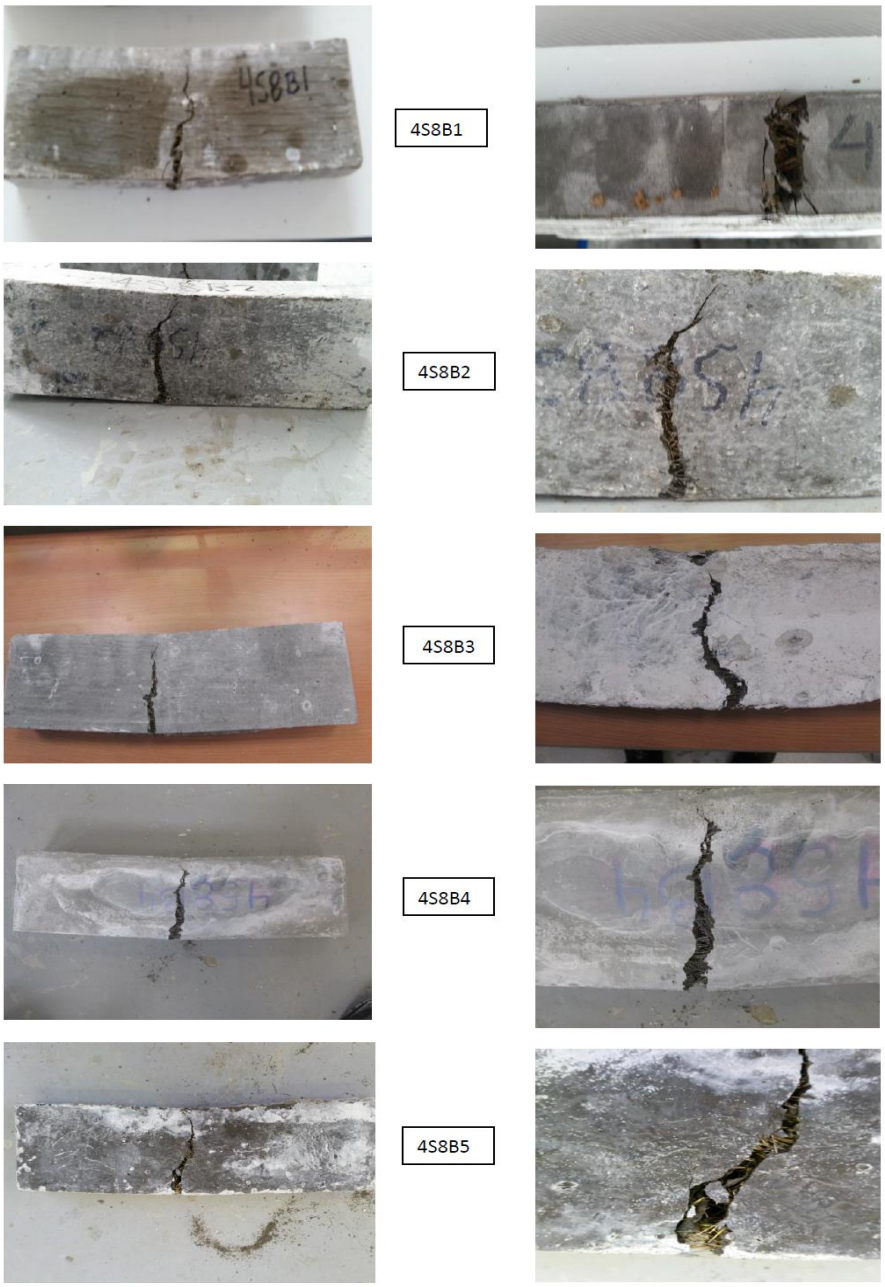

Figure 4.24: Un-notched three point bending test failed specimens (4%)

4.4.3 Four Point Bend (FPB) test results

- **Overview**

The load deflection curves typically involved an initially smooth pre-peak phase up to a distinct point corresponding to the first crack load (Fig.4.25). This was followed by a slight drop in load before the beginning of the hardening phase characterised by irregularity due to multiple cracking. The post peak slope on the other hand was smoother as the failure mechanism at this stage involved fibre de-bonding and slipping.

An initial shallow slope could be observed most distinctly in the batch 3 curve but also to a lesser extent in the other curves. No difference was immediately noticeable between the three fibre contents in relation to scatter in the curves.

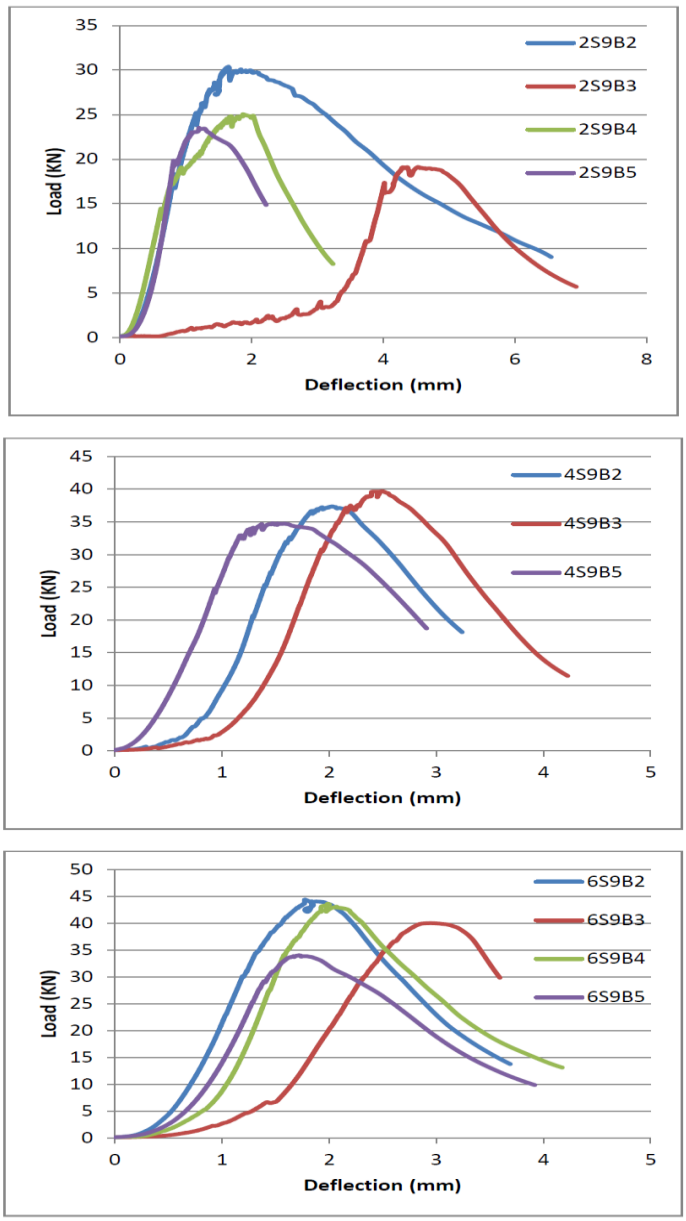

Figure 4.25: Un-notched Four Point Bending test Load-deflection curves

- **Elastic phase**

Generally, the, point at the end of linearity on the load-deflection of un-notched FPB specimens was quite distinct and corresponded to that at which the 1st crack occurred therefore making it easier to determine compared to that in the notched TPB specimens. The loads at the end of linearity are presented in Table 4.13 and Appendix 6a. The average load at end of linearity increased with fibre content with largest scatter observed in the 2% fibre content specimen (Fig.4.26).

Table 4.13: Un-notched four point bending test load at the end of linearity

Fibre content (%)	Size	Depth (mm)	Span (mm)	Width (mm)	Specimen	Batch no.	Load @ end of linearity (kN)	Average Load (kN)	Standard deviation (%)
2	S9	75	225	50	2S9B1	1	-		
		75	225	50	2S9B2	2	18.31	17.36	16.4
		75	225	50	2S9B3	3	10.77		
		75	225	50	2S9B4	4	14.17		
		75	225	50	2S9B5	5	19.61		
4	S9	75	225	50	4S9B1	1			
		75	225	50	4S9B2	2	20.69	22.47	7.5
		75	225	50	4S9B3	3	22.26		
		75	225	50	4S9B4	4	22.18		
		75	225	50	4S9B5	5	24.76		
6	S9	75	225	50	6S9B1	1			
		75	225	50	6S9B2	2	22.78	24.04	11.9
		75	225	50	6S9B3	3	20.77		
		75	225	50	6S9B4	4	27.30		
		75	225	50	6S9B5	5	25.30		

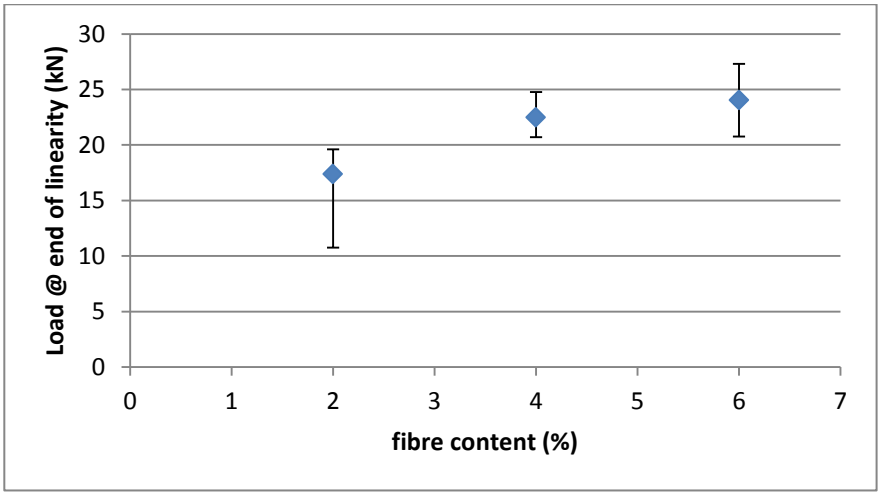

Figure 4.26: Un-notched four point bending test load at the end of linearity against fibre content

- **Hardening phase**

In most specimens, deflection hardening occurred resulting in peak load that was higher than the load at the end of linearity (Table 4.14 and Appendix 6b). An increase in the average peak load with fibre content was observed (Fig.4.27) and generally there was more scatter in the peak load than in the load at the end of linearity. As in the notched and un-notched TPB specimens, the average hardening response evaluated as a percentage of the load at end of linearity showed no correlation with fibre content (Table 4.15 and Figs. 4.28)

Table 4.14: Un-notched four point bending test Peak Load

Fibre content (%)	Size	Depth (mm)	Span (mm)	Width (mm)	Specimen	Batch no.	Peak Load (kN)	Average Peak Load (kN)	Standard Deviation (%)
2	S9	75	225	50	2S9B1	1			
		75	225	50	2S9B2	2	30.39	24.52	18.9
		75	225	50	2S9B3	3	19.12		
		75	225	50	2S9B4	4	25.05		
		75	225	50	2S9B5	5	23.52		
4	S9	75	225	50	4S9B1	1			
		75	225	50	4S9B2	2	37.37	34.07	19.7
		75	225	50	4S9B3	3	39.68		
		75	225	50	4S9B4	4	24.44		
		75	225	50	4S9B5	5	34.79		
6	S9	75	225	50	6S9B1	1			
		75	225	50	6S9B2	2	44.45	40.56	11.7
		75	225	50	6S9B3	3	40.04		
		75	225	50	6S9B4	4	43.66		
		75	225	50	6S9B5	5	34.07		

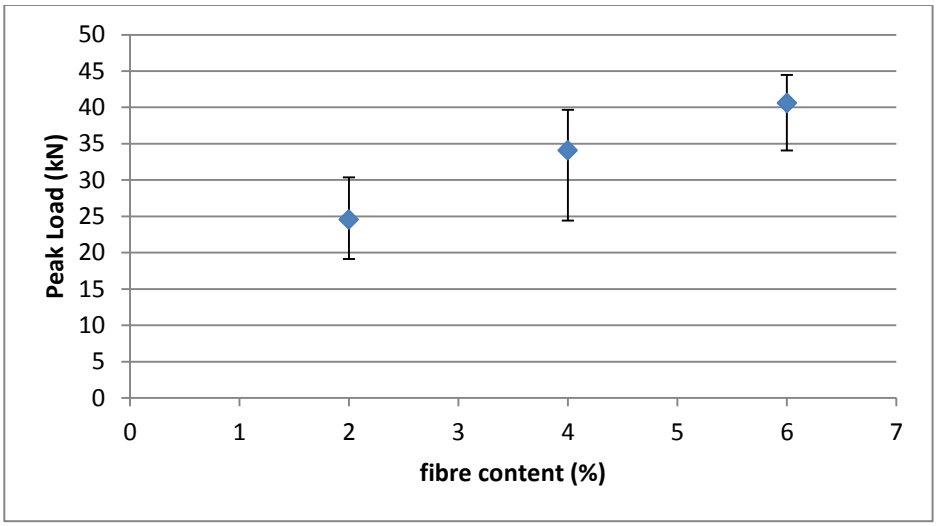

Figure 4.27: Un-notched four point bending test peak load against fibre content

Table 4.15: Un-notched four point bending test hardening

Fibre content (%)	Size	Depth (mm)	Span (mm)	Width (mm)	Specimen	Batch no.	Hardening (%)
2	S9	75	225	50	2S9B1	1	-
		75	225	50	2S9B2	2	65.93
		75	225	50	2S9B3	3	77.54
		75	225	50	2S9B4	4	76.79
		75	225	50	2S9B5	5	19.95
4	S9	75	225	50	4S9B1	1	-
		75	225	50	4S9B2	2	80.60
		75	225	50	4S9B3	3	78.28
		75	225	50	4S9B4	4	10.17
		75	225	50	4S9B5	5	40.49
6	S9	75	225	50	6S9B1	1	-
		75	225	50	6S9B2	2	95.13
		75	225	50	6S9B3	3	92.78
		75	225	50	6S9B4	4	59.95
		75	225	50	6S9B5	5	34.679

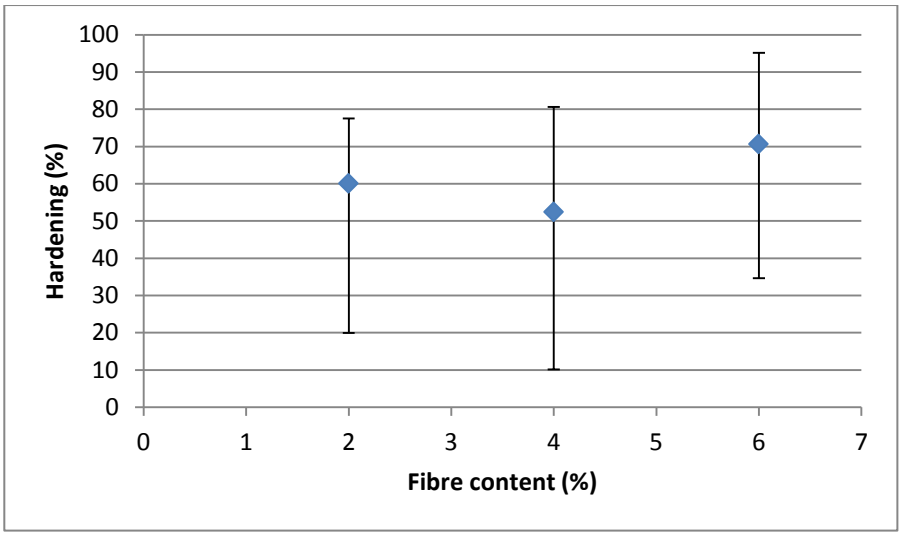

Figure 4.28: Un-notched four point bending test average hardening

- **Post peak phase**

Despite the large scatter, the upward trend in the post peak average slope was still evident (Table 4.16 and Fig.4.29) indicating as in previous specimen types a decreasing ductility with fibre content.

Table 4.16: Un-notched four point bending test average slope

Fibre content (%)	Size	Depth (mm)	Span (mm)	Width (mm)	Specimen	Batch no.	Post peak slope (N/mm)
2	S9	75	225	50	2S9B1	1	-
		75	225	50	2S9B2	2	3663.62
		75	225	50	2S9B3	3	6146.43
		75	225	50	2S9B4	4	12300.06
		75	225	50	2S9B5	5	8486.01
Average							7649.03
4	S9	75	225	50	4S9B1	1	
		75	225	50	4S9B2	2	15849.36
		75	225	50	4S9B3	3	17108.73
		75	225	50	4S9B4	4	7703.73
		75	225	50	4S9B5	5	11189.46
Average							12962.82
6	S9	75	225	50	6S9B1	1	
		75	225	50	6S9B2	2	17188.70
		75	225	50	6S9B3	3	15926.11
		75	225	50	6S9B4	4	16640.96
		75	225	50	6S9B5	5	12034.91
Average							15447.67

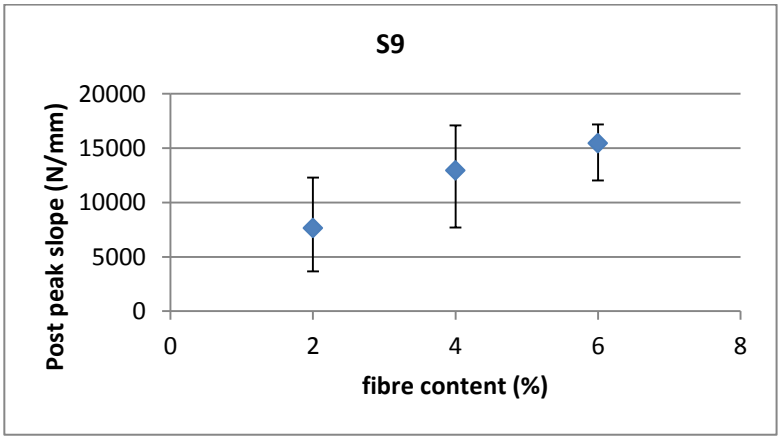

Figure 4.29: Un-notched four point bending test average slope against fibre content

- **Failure pattern**

Failure typically involved multiple cracking within the middle third of the span with fibres bridging the tortuous crack faces (Fig.4.30). In batches 3, 4 & 5 with 2% fibre content a dominant crack within the middle third followed a tortuous path up the specimen. However, branches of other minor cracks could also be observed from the main crack. The varying orientations of the fibres could be seen from the crack edges. Batch 3 also showed crushing of the concrete at loading points and this was the most likely reason for the initial shallow slope in the pre-peak phase. Batch 2 on the other hand had multiple cracking with two dominant cracks from which emanated other minor cracks. It is worth noting that this batch also has the highest peak load.

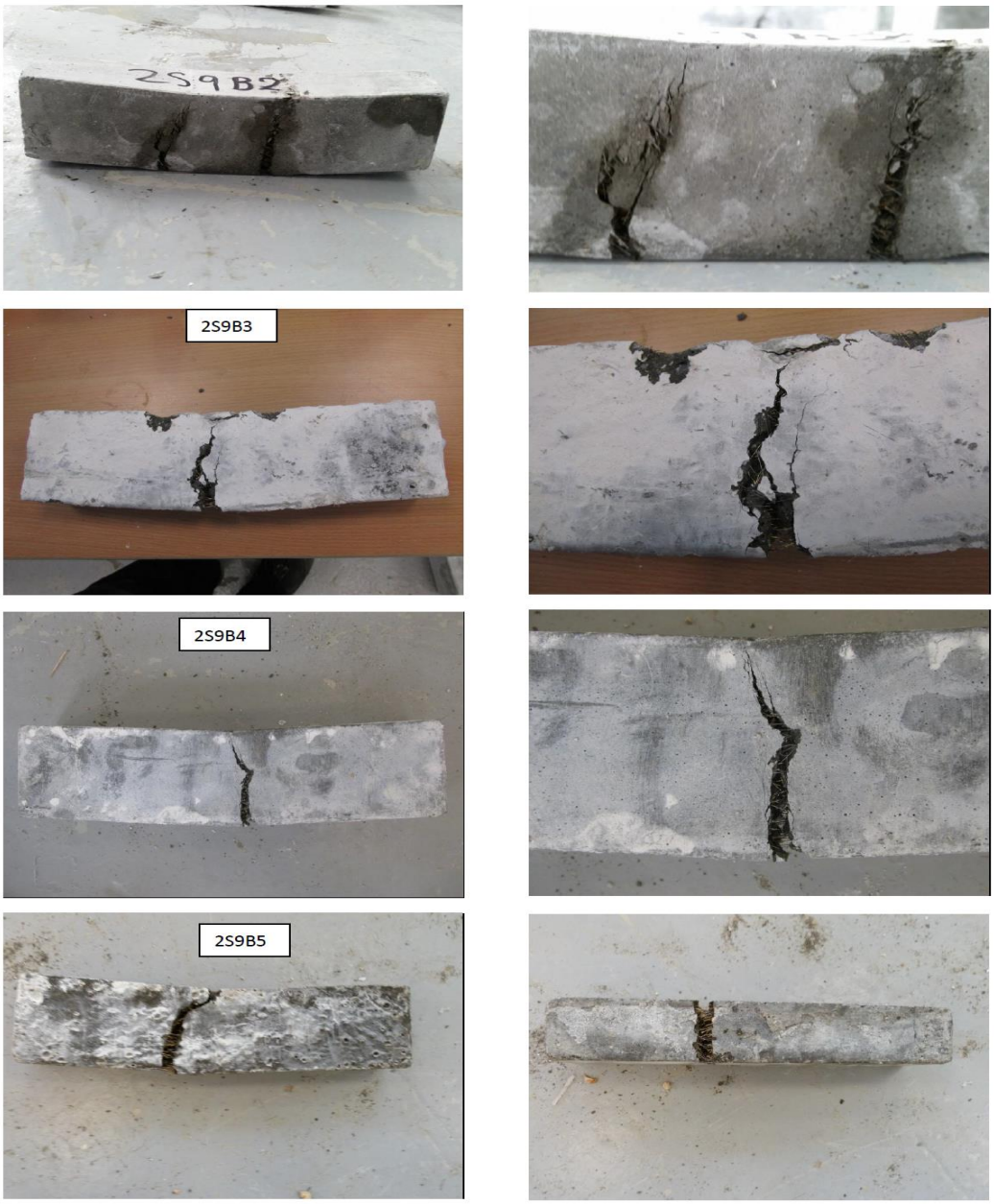

Figure 4.30: Un-notched four point bending test failed specimens (2%)

4.4.5 Discussion

In the previous section, the load deflection responses of three point bending (TPB) and four point bending (FPB) tests were reviewed in relation to the elastic, hardening and post peak phases. In the notched three point bending tests, the average slopes of the initial part of the curves from different batches were roughly the same and linear. However, the linearity of the slopes was only approximate due to the variability in the elastic modulus of the cement paste. The point at which linearity was lost was characterised by a sudden drop in load. This point may sometimes correspond to the occurrence of first cracking but not always as some cracks may also develop earlier in UHPFRC prior to this point.

The load-deflection curves of both un-notched TPB & FPB had an initially shallow slope attributed to local deformation and crushing at load application point which was registered by the crosshead travel measurement. The average slope of the initial curve therefore varied between batches due to the variability in the extent of the local deformation and crushing. However, beyond this initial shallowness, the slopes became steep and smooth with a distinct point marking the end of the initial pre-cracking phase which also corresponded to the first cracking load. Up to this point the stresses in the specimen were mainly resisted by the matrix. When the matrix started to crack, the stress was released resulting in a drop in load before fibre bridging was activated and the stresses were transferred to the fibres.

After the end of proportionality, in most of the tests the loads continued to rise with increasing deflection. However, the rise was very irregular and was marked by several brief drops in load. This was the hardening phase caused by multiple cracking in the matrix each time followed by an intervening bridging action by the fibres whereby loads were transferred from the matrix to the fibres. This resulted in an increase in the load carrying capacity beyond the end of linearity. This deflection hardening process only stopped at peak load when the multiple cracking capacity of the matrix was saturated. This also explained why both size and fibre content were observed not to have any noticeable effect on the hardening response. As long as there were enough fibres within the matrix, the extent of hardening was only limited by the capacity of the matrix to accommodate multiple cracks. As was mentioned in chapter 2, UHPFRC mixes have a relatively high fibre content made possible by their enhanced microstructure. In addition the conditions required to produce deflection hardening are much less onerous compared to those required for strain hardening to occur (Bentur and Mindess, 2007).

There was a noticeable scatter between curves of batches from different batches of the same specimen size typical of UHPFRC (Fehling *et al*, 2004). This is normally attributed to the variability in the orientation of the fibres which is mainly influenced by production factors. More scatter was generally observed in the peak load compared to the load at the

end of linearity. This was because the main influence on load at the end of linearity is the matrix strength though the fibres have some influence through the crack suppression mechanism discussed in chapter 2 (Aitcin, 1998). Homogeneity achieved in the microstructure of UHPFRC matrix is one of the main reasons for its much enhanced strength. On the other hand peak load is influenced significantly by both strength of the matrix and ductility of the composite (Bentur and Mindess, 2007). Ductility depends on the influence of fibres which is in turn dependent on their content, distribution and orientation. The latter two are mainly functions of production factors and are therefore more prone to variability. Therefore, scatter was less in the load at the end of linearity because of the relatively limited influence of fibres on it.

Scatter in both the load at the end of linearity and peak load was observed to decrease with increasing fibre content. As mentioned previously, scatter is mainly influenced by fibre orientation. Possibly fibre content affects scatter by influencing the degree of freedom that fibres have to align themselves within the UHPFRC mix. The higher the fibre content the less room fibres have to take up an orientation of their choice. Fibres in beams have been observed to align parallel to the direction of flow (Fehling *et al*, 2004). The more fibres there are within a UHPFRC mix aligned in this direction the less room there will be for the rest to align in other directions. This means that the higher the fibre content, the less the scatter there will be in the specimen.

Generally, linearity and peak loads increased with size as would be expected. However in the notched three point bending test, significant drops in linearity and peak loads were observed in the largest specimens of some batches further increasing the scatter. This large drop in load was not observed in the un-notched TPB and FPB tests. The drop in peak load in the larger specimens was most likely due to the sequence of casting. Upon stopping the drum mixer once the mixing process was completed (Fig.4.1), some of the fibres may have tended to settle due to gravitational bias (AFGC, 2013). As it is the largest specimens which were cast first (steps 3 and 4 in Fig.4.1) they may have ended up with fewer fibres compared to the rest of mix as illustrated in Fig.4.31. A comparison of the photographic images of the cracked surfaces of specimens ranging in size from the largest (S1) to the smallest (S6) all taken from one of the affected batches, B4 seems to support this explanation (Fig.4.33).

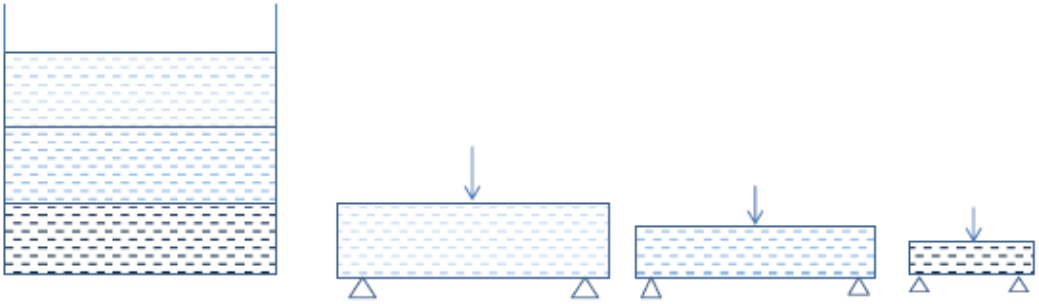

Figure 4.31: Illustration of the effect of gravitational bias and pour sequence on fibre distribution

Batches 3 and 4 of size S1 were the most affected by this gravitational bias and as a result had much less fibres on the crack faces which were less tortuous compared to the rest of the batches (Fig.4.15). This was also the most likely reason for their poor hardening performance. Specimen 2S1B4, for example, in addition to a low peak load also had no noticeable hardening response. In the post peak phase, fibres begin to slip and de-bond from the matrix, resulting in a softening response whereby load-carrying capacity decreases with increasing deformation. The specimens which ended up with much fewer fibres due to gravitational bias as described above therefore also ended up with lower toughness. Therefore, in analysing size effect on the flexural strength of notched TPB test specimens in the next section, the effect of excluding these batches from the analysis was also considered.

The location, direction and number of cracks were influenced by the loading arrangement and whether or not there was a notch. FPB tests introduced pure bending stresses within the middle third of their span producing multiple cracking therein. The cracks were not straight and some branching was observed. In addition to bending stresses a TPB test introduced a shear stress that in the absence of a notch resulted in a straight or diagonal crack within the middle third of the span. A notch introduced a stress concentration at the tip and forced a crack initiation at this location. Once the crack was initiated, the combined effect of bending and shearing stresses generally tended to keep the crack roughly in a vertical direction. However, the effect of matrix heterogeneity and variability in fibre distribution and orientation determined how irregular or tortuous the crack path was. Increased crack tortuosity in UHPFRC was mainly caused by the action of fibres first in suppressing crack formation and then in bridging across potential crack paths. A propagating crack was therefore forced to change direction to find weaker regions resulting in higher failure loads.

All notched beams subject to the TPB test failed in the middle by cracking from the notch tip roughly vertically upwards (Fig.4.15). All Un-notched FPB and TPB test specimens failed by cracking within the middle third as expected indicating that bending was more dominant over shear even for the shortest beams (Figs.4.24 & 4.30). However, in one Un-notched TPB specimen (200mm long and 50mm deep) the crack originated near one of the supports and propagated diagonally towards the loading point on the top surface of the beam (Fig.4.32). This case probably highlights the increasing influence of shear stresses as the beams became shorter. In this case, the combined effects of shear stresses developed in the short beam and its shear capacity within this region were probably enough to cause shear failure. The peak load recorded for this particularly specimen was the highest out of the five specimens with this size and fibre content (4%). Hence shear stresses developed within the beam do not seem to have reduced the beam's ultimate load carrying capacity. The fact that this beam failed in a different way to other beams with similar length and loading was probably due to the variation in fibre distribution and orientation within batches and beam regions.

Figure 4.32 : Failure pattern for beam 4S10B1

Figure 4.33: Notched three point bending test S3 specimens from batch 4

4.5 Size effect analysis

An initial study conducted using data generated by others indicated the existence of a small size effect on the flexural strength of UHPFRC (Awinda et al., 2016). However, only a small range of specimen sizes (50-150mm) with 2% fibre content was considered. Therefore in order to establish size effect more conclusively, this section considers a wider range of sizes and fibre contents (2% - 6%). Data from TPB test specimens on both notched and un-notched specimens described in the previous sections also allowed the extension of the assessment of size effects to more parameters.

Flexural stress was obtained by calculating the nominal stress at the required point based on the elastic beam theory. Hence for the TPB test specimen, the nominal flexural stress was given by Eq.2.14. Based on this equation two flexural stresses were defined corresponding to the load point at which they are calculated namely:

- Flexural stress at the end of linearity
- Flexural stress at peak load (Also referred to as flexural strength in this study)

These two stresses were obtained both for the un-notched and notched specimens and were distinguished by the depth of specimen used. Whereas for the un-notched specimen the overall specimen depth was used, in the notched specimen the crack ligament depth was adopted equal to the overall depth less the notch depth. Table 4.17 summarises information used with Eq. 2.14 to calculate the above mentioned two flexural stresses for notched and un-notched specimens.

Table 4.17: Flexural stresses considered

Flexural stress	**Load (P)**	**Specimen depth (h)**	
		Un-notched	**Notched**
Flexural stress @ end of linearity	Load @ end of linearity	Overall depth	Overall depth less notch depth
Flexural strength	Peak Load		

In the following sections, the effect of specimen size on all the above flexural stresses was analysed by plotting them against specimen depth. A bi-logarithmic plot of flexural stress against specimen depth then enabled the evaluation of size effect on both the flexural strength and the flexural stress at the end of linearity according to the size effect law by Bažant and Planas (1998) discussed in chapter 2. In this framework, the slope of this plot ranges from 0 (no size effect) to -0.5 (maximum size effect).

4.5.1 Size effect on flexural stress at end of linearity

- **Notched TPB test**

The flexural stresses calculated as described above are presented in Table 4.18 and figures in Appendix 9. For specimens with 2% fibre content, apart from batch 1 which had some linearity in the decrease of flexural stress with specimen depth, the rest of the batches did not have a noticeable trend (Appendix 7a). However, the average flexural stress indicated a linear decrease of flexural stress with specimen depth despite the wide scatter (Appendix 7d).

In all the batches of specimens with 4% fibre content, the trend showed flexural stress at end of linearity decreasing with specimen depth (Appendix 7b). However, in batches 2 and 3, the flexural strength of the smallest specimen (S6) was much lower and almost equal to that of the largest size (S6). This large drop in these batches was responsible for the relatively low average flexural strength of the smallest specimen and its large scatter. Apart from the above deviation from the trend, the average flexural strength clearly decreased with increasing specimen depth (Appendix 7d).

Specimens with 6% fibre content also displayed a nearly linear decrease in flexural stress at the end of linearity in all the batches except 2 and 3 (Appendix 7c). In batch 2, the decreasing trend in flexural stress was observed from depths 25mm to 150mm after which there was an increase. In batch 3, there was a drastic decrease in stress from 25mm to 50mm after which the stress stayed almost constant. The average stress reflected the combined effects of above responses within the batches resulting in a relatively small rate of decrease in the flexural stress with increasing size (Appendix 7d). The big drop in stress highlighted in batch 3 resulted in a relatively large scatter in the value of the smallest specimen.

The bi-logarithmic plot of average flexural stress at the end of linearity against specimen depth was linear for all the fibre contents with slopes of -0.23, -0.18 and -0.26 for fibre contents of 2%, 4% and 6% respectively (Fig.4.34). These represented small to medium size effect within the framework proposed by Bažant (1998) in which the slope ranges from 0 (no size effect) to -0.5 (maximum size effect).

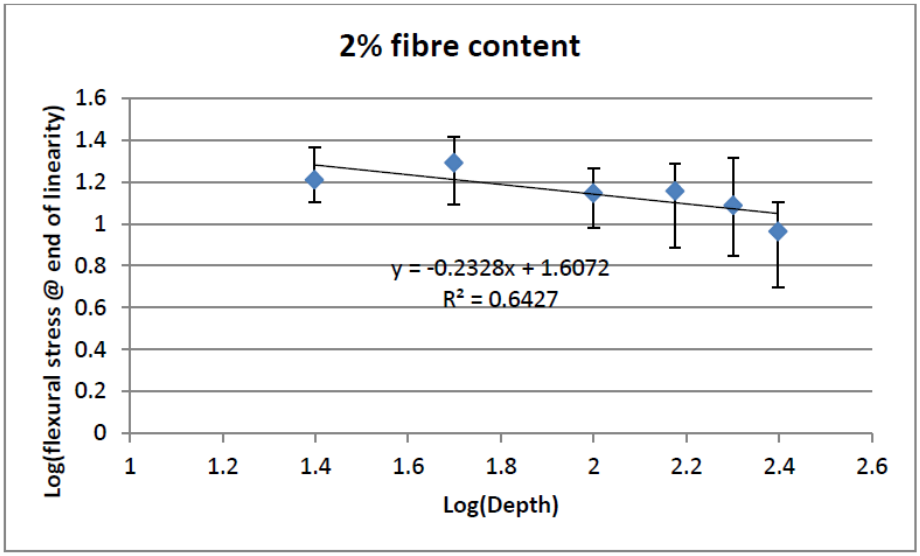

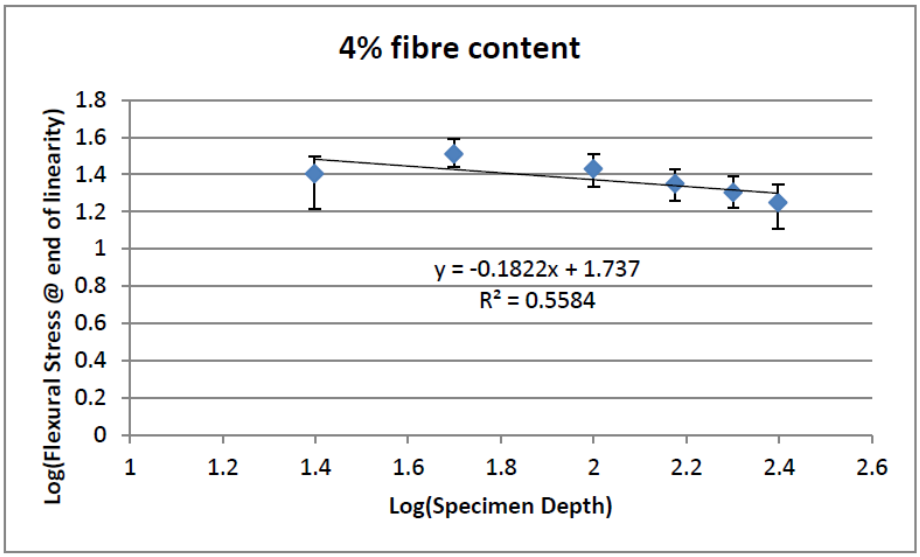

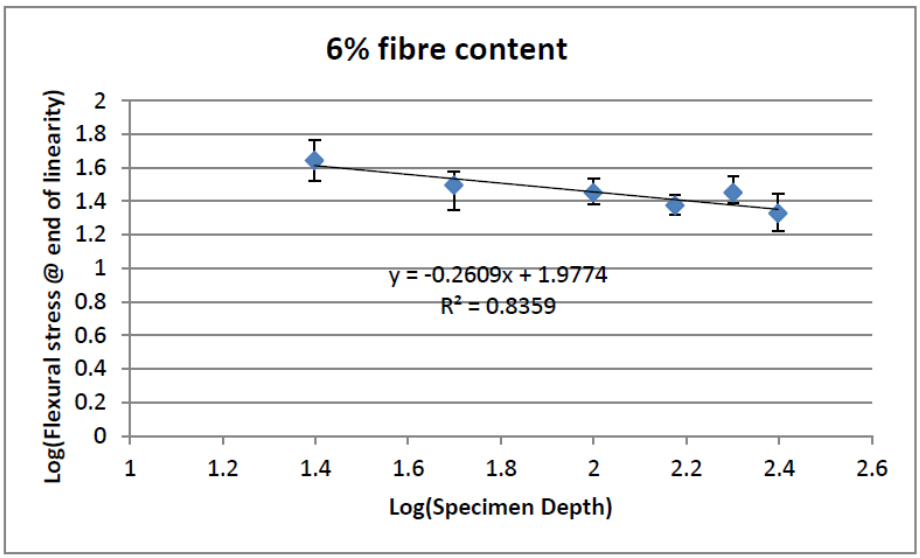

Figure 4.34: Notched TPB bi-logarithmic plot of flexural stress at end of linearity against Depth

Table 4.18: Notched three point bending test flexural stress @ end of linearity

		Stress @ end of linearity (MPa)				
Fibre content (%)	**Depth (mm)**	**Batch 1**	**Batch 2**	**Batch 3**	**Batch 4**	**Batch 5**
2	250	12.74	11.07	4.96	5.07	12.15
	200	20.53	7.03	-	14.40	7.08
	150	19.28	12.49	19.13	7.68	12.99
	100	18.46	-	-	-	9.54
	50	26.08	12.39	13.49	22.40	22.40
	25	23.15	-	12.72	12.81	12.81
4	250	20.76	22.25	17.10	15.61	12.77
	200	17.69	24.72	15.53	16.72	21.14
	150	22.91	23.84	20.37	18.13	26.66
	100	32.09	24.31	24.78	18.71	21.73
	50	27.41	38.67	30.42	33.35	33.35
	25	-	21.85	16.46	31.35	31.35
6	250	16.78	27.91	22.41	20.12	19.17
	200	27.98	35.08	24.92	28.67	24.64
	150	20.75	22.93	27.22	23.99	23.28
	100	27.36	29.11	24.20	34.59	25.53
	50	31.64	34.98	30.00	37.46	37.46
	25	54.68	37.34	58.27	33.30	33.30

- **Un-notched TPB test**

The flexural stress at the end of linearity was calculated from the corresponding load using Eq. 2.14 except that h was now the overall beam depth as indicated in Table 4.17. The flexural stress values obtained thus are presented in Table 4.19 and plots of the same in Appendix 8. Except for batch 3, in all the batches with 2% fibre content the flexural stress at the end of linearity decreased linearly with increasing depth (Appendix 8a). In batch 3 the trend would have been similar but for the smallest size which had a value almost as low as that of the largest size. This value was responsible for the large scatter in the smallest size (S11) as indicated by a plot of the average flexural stress against depth (Appendix 8d). For 4% and 6% fibre content, there was also a general decrease in flexural stress as the size increased though the linearity was not as strong nor the scatter as small as in the specimens with 2% fibre content.

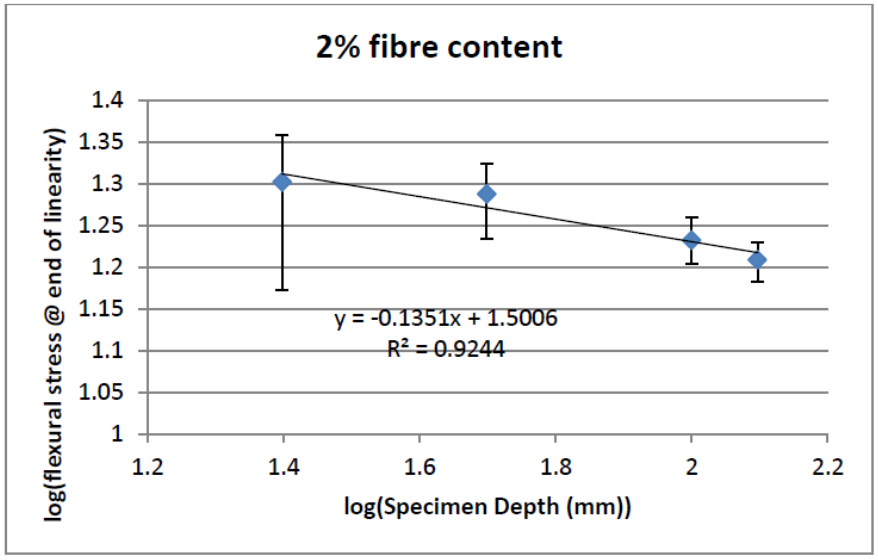

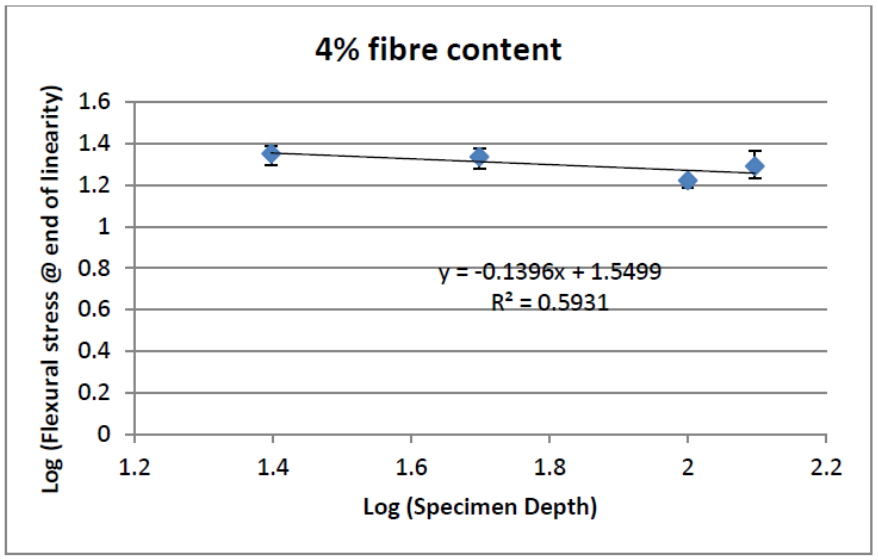

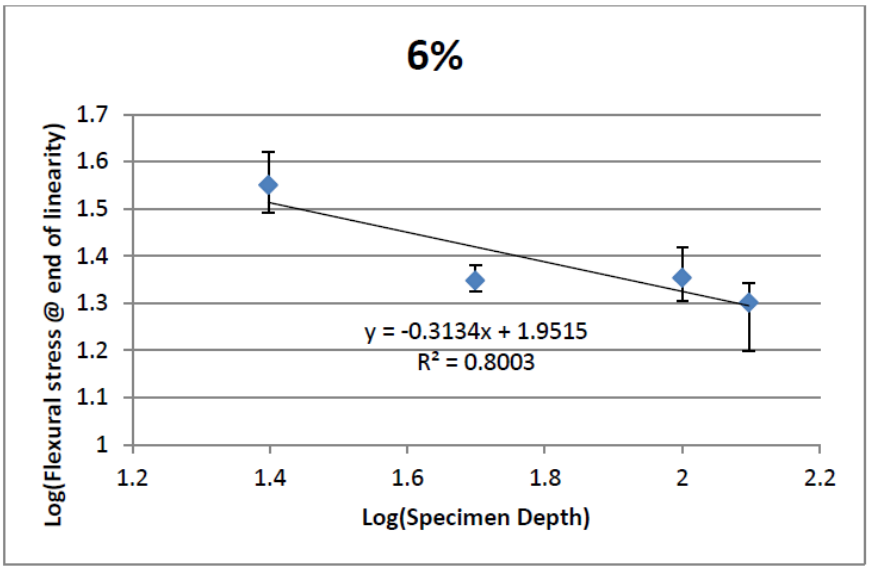

Figure 4.35: Un-notched TPB bi-logarithmic plot of flexural stress at the end of linearity against depth

Even with the scatter taken into account, it was still quite clear from the plots in Appendix 8d that for 2, 4 and 6% fibre contents, the average flexural stress at the end of linearity decreased with specimen depth. Size effects on flexural stress evaluated using a bi-logarithmic plot as in the previous case produced slopes from this plot of -0.13 for 2%, -0.14 for 4% and -0.31 for 6% (Fig.4.35). These values represented small to medium size effects which were significant.

Table 4.19: Un-notched three point bending test flexural stress @ end of linearity

		Flexural stress @ end of linearity (MPa)				
Fibre content	**Depth**	**Batch 1**	**Batch 2**	**Batch 3**	**Batch 4**	**Batch 5**
2	125	16.92	16.98	15.21	15.47	16.23
	100	16.49	18.16	17.67	15.98	17.04
	50	19.80	19.31	19.62	17.12	21.09
	25	18.70	22.44	14.90	22.84	21.35
4	125	23.12	20.14	17.13	0.00	17.70
	100	17.40	16.62	0.00	15.40	17.20
	50	23.84	0.00	18.93	21.33	22.21
	25	23.85	24.46	23.10	20.69	19.71
6	125	15.77	20.27	22.00	21.63	20.29
	100	0.00	23.49	20.18	26.27	20.26
	50	0.00	21.67	0.00	21.14	23.95
	25	40.13	30.93	41.69	33.72	31.07

4.5.2 Size effect on flexural strength

- **Un-notched TPB test**

Flexural strength values for un-notched TPB tests are presented in Table 4.20 with the plots in Appendix 9. For 2% fibre content variation of flexural strength with depth showed no consistent pattern for different batches (Appendix 9a). The average flexural strength had a much higher scatter compared to 1st crack stress (Fig.4.36) which made the size effect on flexural strength inconclusive. Except for batch 2 and 5 of specimens with 4% fibre content which showed some linearity in the decrease of flexural strength with depth, there was no consistent trend in the variation of flexural strength with depth (Appendix 9b). In the average flexural strength however there was an indication of some linearity in the decrease of the average flexural strength with size even considering the scatter within each data point (Fig.4.36). In batch 1 of specimens with 6% fibre content, there was a strong linear decrease in flexural strength with increasing size. Batch 3 showed a similar response though the linearity was not as strong. For the rest of the batches, there was no consistent pattern in the variation of flexural strength with depth. However, there was

some indication that the flexural strength was decreasing with depth though the error margin was too big to make this conclusive.

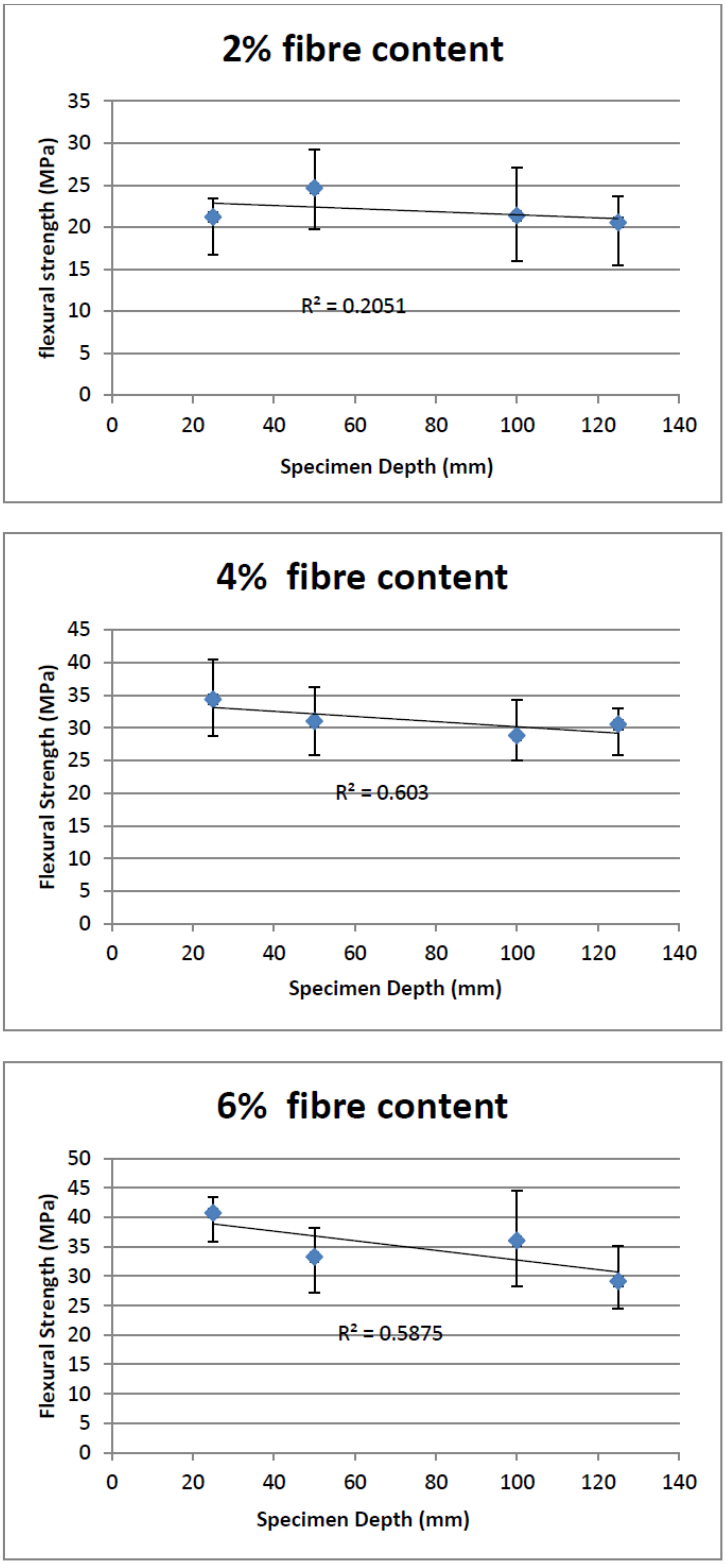

Figure 4.36: Un-notched three point bending test average flexural strength against specimen depth

Table 4.20: Un-notched three point bending test flexural strength

		Flexural strength (MPa)				
Fibre content	**Depth**	**Batch 1**	**Batch 2**	**Batch 3**	**Batch 4**	**Batch 5**
2	125	23.70	22.20	22.28	15.48	19.04
	100	27.05	23.09	19.49	15.98	21.12
	50	19.80	29.25	23.67	26.16	24.34
	25	22.06	22.44	16.69	23.37	21.35
4	125	33.07	31.83	31.84	30.00	25.86
	100	29.78	27.62	34.31	27.32	25.03
	50	31.37	34.98	36.32	26.58	25.81
	25	40.55	34.84	30.94	28.75	36.71
6	125	25.31	31.49	35.16	29.28	24.53
	100	31.92	42.18	33.23	44.57	28.22
	50	38.24	27.28	35.36	29.49	36.00
	25	43.12	40.13	43.46	41.20	35.83

- **Notched TPB test**

Flexural strength values for un-notched TPB tests are presented in Table 4.21 with the plots in Appendix 12. For 2% fibre content specimens, flexural strength decreased almost linearly with specimen size in all the batches except batch 3 where flexural strength dropped in the smallest sizes (Appendix 10a). Despite the wide scatter, the decrease in the average flexural strength with specimen size also seemed linear (Appendix 10d). In batches 1, 4 and 5 of specimens with 4% fibre content, the flexural strength decreased almost linearly with specimen depth (Appendix 10b). Batch 3 showed the same trend except in the smallest size which had a big drop in flexural strength of the same order as that of the biggest specimens. In addition to having a similar drop in flexural strength as Batch 3, the rate of decrease of flexural strength in Batch 2 was much smaller. The effect of all the above was an average flexural strength that decreased linearly with depth but with a larger scatter than that in the flexural stress at the end of linearity (Appendix 10d). This was especially so in the smallest specimen in which drops in flexural strength highlighted above were reflected in a slight drop in the average value.

Except for batch 5, flexural strength decrease with size was almost linear in all the batches with 6% fibre content (Appendix 10c). In Batch 5, there was no consistent pattern though the flexural strength did not change by much between specimen depths 150-250mm. The rate of decrease in the average flexural strength was relatively small with a

much bigger scatter observed in the smallest specimen depths of 25 and 50mm (Appendix 10d).

For all the fibre contents in the notched TPB tests the average flexural strength decreased linearly with increasing depth (Appendix 10d). Adopting the same approach outlined previously to evaluate size effect, the slope of the log plots are: -0.22 for 2%, -0.26 for 4% and -0.27 for 6% fibre contents (Fig.4.37). Even by excluding the batches where there were big drops in the peak load of the largest sizes attributed to gravitational bias, the size effect evaluation did not change much with -0.26 for 2%, -0.25 for 4% and -0.22 for 6% fibre contents. The size effect on flexural strengths from the notched three point tests was medium and therefore quite significant.

Table 4.21: Notched three point bending test flexural strength

		Flexural strength (MPa)				
Fibre content (%)		**Batch 1**	**Batch 2**	**Batch 3**	**Batch 4**	**Batch 5**
2	250	14.40	13.50	8.66	5.07	13.71
	200	23.64	14.54	16.33	15.92	10.13
	150	22.61	17.23	22.00	12.25	15.20
	100	20.19	0.00	23.99	13.47	14.75
	50	27.68	18.53	13.86	23.88	23.88
	25	27.09	24.61	12.73	20.99	20.99
4	250	25.13	24.75	19.69	19.79	13.71
	200	22.28	28.91	21.47	20.86	24.29
	150	35.04	28.00	24.62	19.74	29.35
	100	43.87	26.68	30.70	24.59	27.61
	50	32.31	50.13	43.56	38.97	38.97
	25	47.98	29.07	18.84	38.89	38.89
6	250	22.20	32.30	27.31	30.74	31.32
	200	35.12	37.20	32.95	34.27	30.29
	150	25.21	29.80	34.82	32.03	31.78
	100	34.88	40.90	35.25	41.15	28.74
	50	51.32	45.61	39.30	43.53	43.53
	25	75.86	46.08	65.15	38.58	38.58

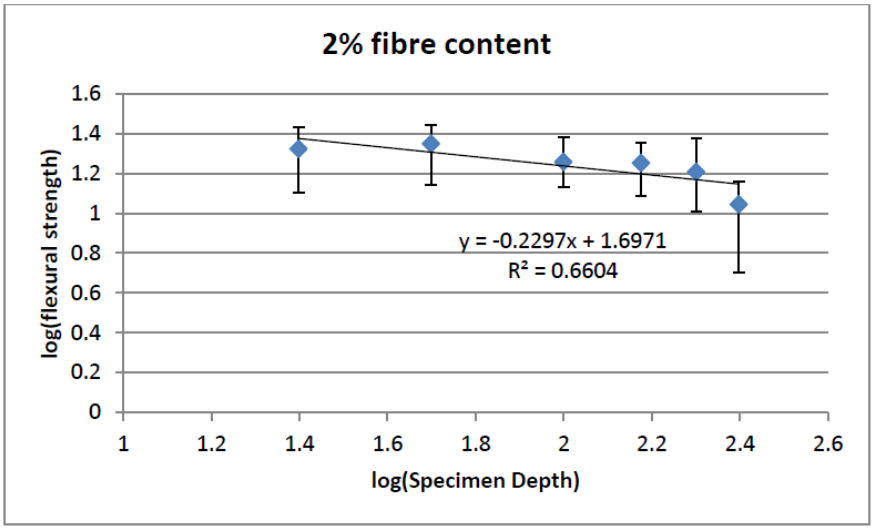

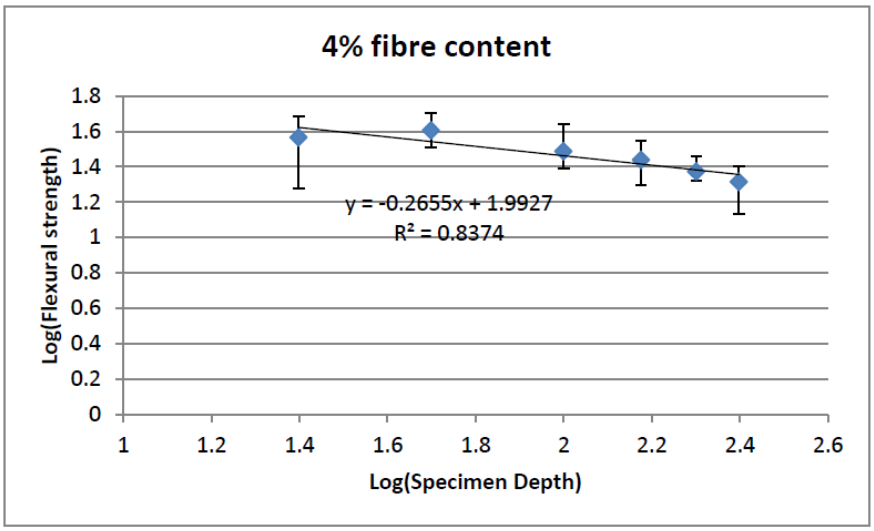

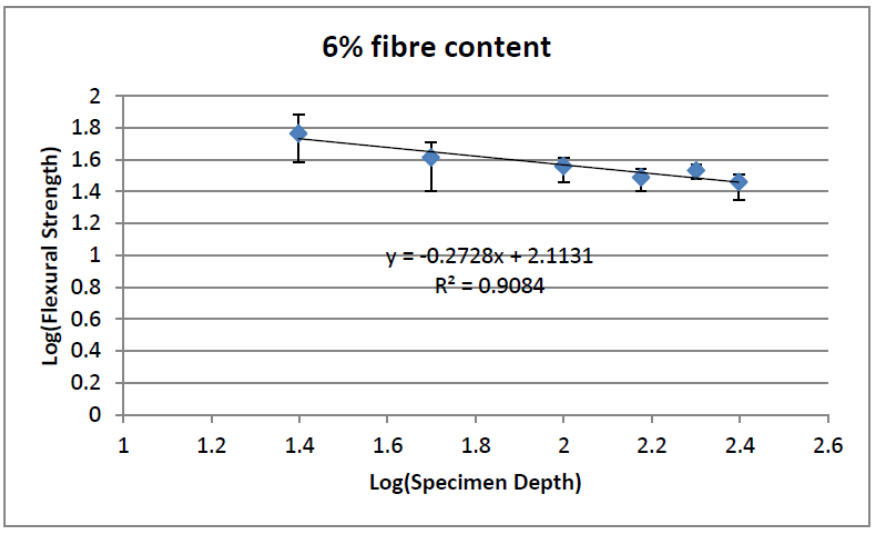

Figure 4.37: Bi-logarithmic plot of flexural strength against depth

4.5.3 Implications of size effect on estimating tensile strength from flexural tests

The UHPFRC specimens tested in this study generally showed a small to medium size effect on both the first crack stress and flexural strength. Size effect response of concrete lies between that of purely ductile materials which exhibit no size effect and that of pure brittle materials that have a strong and constant size effect (Bažant and Planas, 1998). However, studies by Duy et al. (2013) and by Sadegh and Lubell (2012) found only a slight size effect on flexural strength in UHPFRC. Spasojevic et al. (2008) also concluded that the scatter in the results from their study was too large for a size effect on flexural strength to be established. Similarly, a study on size effects on flexural strength by Mahmud et al. (2013) concluded that there was little size effect on the beam nominal strength of UHPFRC specimens due to the material's high ductility. However, the specimens used were geometrically similar only in their notch/depth ratio but not in their depth/span ratio. Similarly studies by Lappa (2007) found no evidence of size effect on the flexural strength of UHPFRC. On the other hand a study by Le et al. (2007) observed the existence of size effect on the flexural strength of UHPFRC beams with depths between 50-150mm tested in four point bending.

These conflicting findings on whether or not there is a size effect on the flexural strength of UHPFRC could be explained by the fact that flexural strength depends on both tensile strength and ductility of the composite. Even for UHPFRC mixes of the same fibre content, distribution and orientation there could be variations in the fibre-matrix bond due to production factors. For fibres of the same aspect ratio, this bond determines not only the critical fibre volume but also their efficiency in improving the material properties. Therefore, a UHPFRC mix with a very strong fibre-matrix bond would result in much higher ductility than one with a relatively weaker bond. UHPFRC mixes with very high ductility would therefore exhibit less size effect than those with lower ductility.

As was discussed in a previous section, the flexural stress at the end of linearity was less prone to scatter compared to flexural strength because it was influenced more by the matrix strength than by ductility. Therefore, the load corresponding to the loss of linearity in the elastic phase of a flexural load-deflection response is normally preferred in estimating the tensile strength of concrete that displays deflection hardening. However, flexural stress values obtained in this way have been observed to still be higher than the actual tensile strength, a fact attributed to the existence of scale effects (Chanvillard and Rigaud, 2003). In the previous sections, the first crack stress obtained from flexural tests had a small to medium size effect. AFGC-SETRA (2013) recommends that the first crack stress obtained from flexural tests needs to be adjusted for scale effects according to Eq.3.27. Values of tensile strength estimated by applying this equation to loads at end of linearity obtained from notched TPB and un-notched TPB and FPB specimens are presented in Table 4.22.

Table 4.22: Average tensile strength values

	Tensile strength (MPa)		
Fibre content (%)	**Notched TPB**	**Un-notched TPB**	**Un-notched FPB**
2	8.08	10.53	7.82
4	13.55	11.60	11.18
6	16.83	14.18	11.95

Several observations can be made which are important in selecting appropriate test arrangements and specimens that would give reliable estimates of tensile strength. Apart from specimens with 2% fibre content, the flexural strength obtained from notched specimens was generally observed to be higher than that from un-notched specimens. This was because notches forced failure by introducing a high stress concentration along a plane that was not necessarily the weakest in the material. Un-notched specimens on the other hand would normally fail along the weakest plane. Therefore, the flexural strength of a notched specimen was generally higher than that of an un-notched one.

The flexural stress obtained from FPB was lower than that from the TPB test. Different from TPB, a FPB test has a continuous bending moment and no shear force in the central span. This results in multiple cracking with failure occurring in the weakest region (Chanvillard and Rigaud, 2003). A TPB test on the other hand introduces a shear stress in the middle of the span and influences the formation of a crack at a point which may not necessarily be the weakest. In estimating tensile strength, a FPB test specimen is therefore preferred to a TPB one because it has pure bending and does not introduce a shear force in the middle third of the specimen. An un-notched specimen is also preferred to a notched one in order allow failure at the weakest region of the specimen rather than forcing failure in the notch tip due to high stress concentration.

4.5.4 Size effect on fracture energy

Though useful as a measure for comparing the post-peak responses and therefore ductility of UHPFRC where the full load-deflection curve is not available, flexural toughness was observed in the previous section to be strongly dependent on specimen size. The post peak performance and hence ductility of notched TPB can be better represented by the fracture energy which is based on the area under the load-deflection curve that includes a full post-peak tail (RILEM, 2002).

Fracture energy values for each batch estimated from the area under the full load deflection curves according to Eq. 4.1 are shown in Table 4.23. Consideration of a suitable range of specimen sizes therefore also enables the assessment of size effect on fracture energy. Average values for each size are plotted with the error bars showing the scatter between batches for each data point (Fig.4.38). There was no noticeable size effect on fracture energy at 2% and 6% fibre contents despite the large scatter in the data. However, the fracture energy at 4% fibre content seemed to be falling with increase in specimen size. The scatter in the data was also comparatively less than at 2% and 6% fibre contents.

If fracture energy is to be considered a material property then by definition it should not vary with size. However, as discussed above, the fracture energy estimated purely based on the area under the load-deflection curve was found in some cases to be size dependent. Various studies have attributed this apparent size dependence on factors from spurious sources (Bažant and Planas (1998); Abdalla and Karihaloo (2003); Petersson (1981)). For UHPFRC, fracture energy is not just that required to cause cracking but includes the total energy needed to cause the fibres to de-bond and slip out of the matrix.

In addition to the energy supplied by the load during the TPB test, Petersson (1981) has shown that the weight of the beam also contributes to the total energy supplied and needs to be accounted for. They have proposed two ways of eliminating the effect of this energy supplied by the beam weight (Fig.4.39):

- Make the span half the length of the beam or
- Use weights to at ends of the beam to compensate for the moment created by the effect of its weight where shorter beam lengths are adopted

The fracture energy can then be obtained directly as follows:

$$G_f = \frac{A}{b(d-a)} \qquad (4.1)$$

where A is the area under the stable load-deflection curve, d the beam depth, a the notch depth and b the width of the beam. However, it is not always practical or economical to eliminate the effect of beam weight as proposed above. Another potential source of error to the determination of G_f is the long 'tail' of the post peak phase of the load-deflection curve.

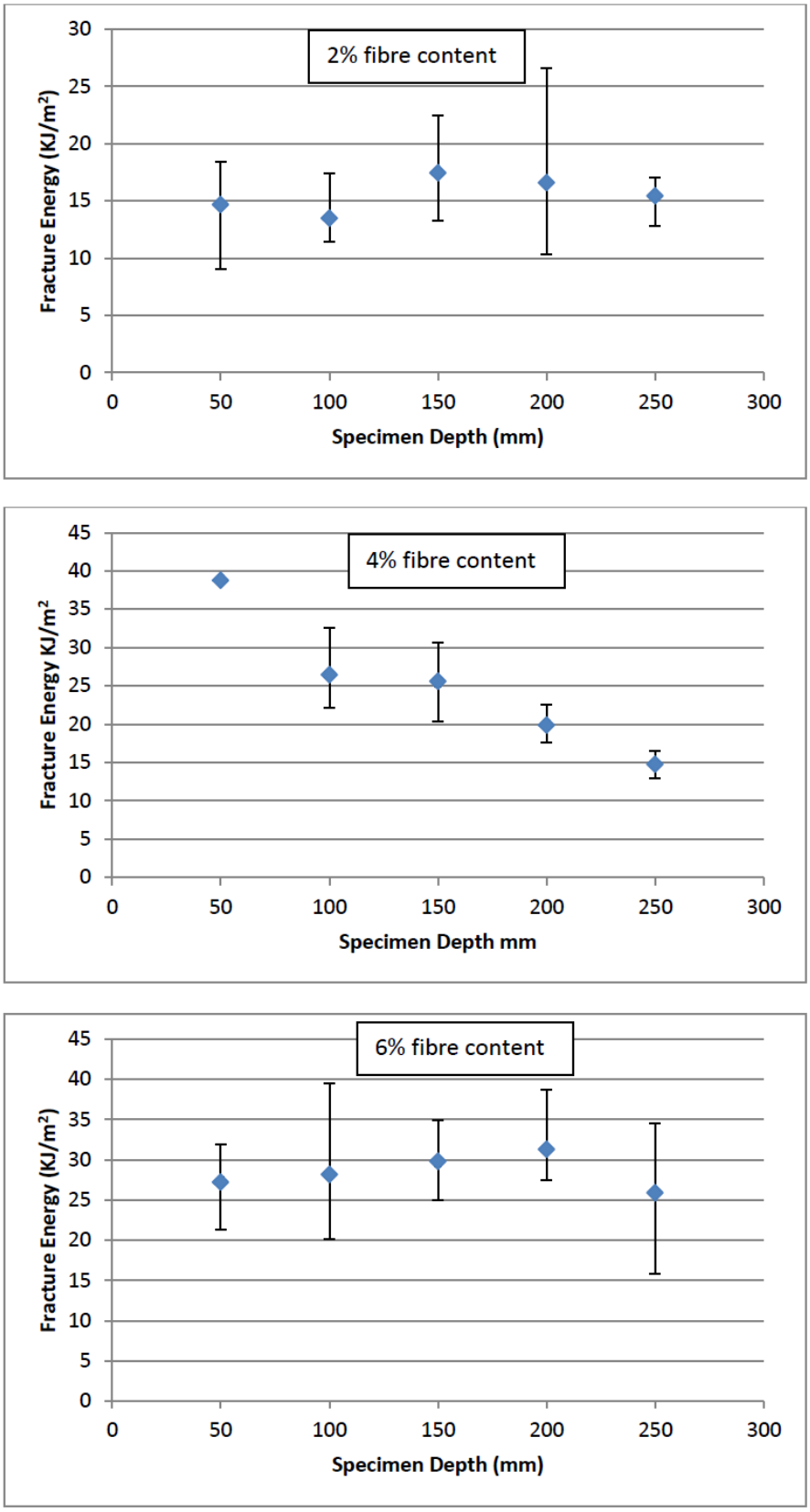

Figure 4.38: Notched TPB test fracture energy against specimen depth

Table 4.23: Fracture energy from notched three point bending tests

Fibre content %	Size	Area under curve (J)	Ligament area (m^2)	Fracture energy (KJ/m^2)
2	1	109857.31	8350	13.16
	2	118891.90	6650	17.88
	3	87717.50	5000	17.54
	4	48869.38	3350	14.59
	5	28842.38	1650	17.48
	6	15166.01	850	17.84
4	1	109857.31	8350	18.34
	2	142120.43	6650	21.37
	3	132733.69	5000	26.55
	4	92214.54	3350	27.53
	5	59130.77	1650	35.84
	6	25421.71	850	29.91
6	1	219782.95	8350	26.32
	2	213522.19	6650	32.11
	3	145974.44	5000	29.19
	4	97334.85	3350	29.06
	5	52520.70	1650	31.83
	6	36361.57	850	42.78

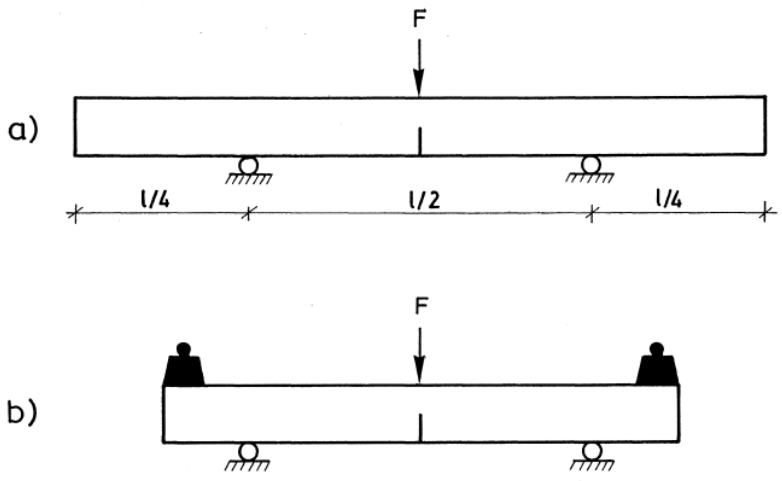

Figure 4.39: Two ways of compensating for energy supplied by weight of beam (Petersson, 1981)

Therefore for an uncompensated TPB test, Petersson (1981) has suggested that both effects of the energy dissipated by the weight of the specimen and the long tail need to be taken into account. Fig.4.40 is a graphical representation of their method which super-imposes the load-deflection curve of an 'uncompensated' beam on to that of a beam tested in one of the two ways mention above. The shaded Area A1 represents the area under the load-deflection curve if the energy supplied by the weight of the beam is not accounted for. The point at which an 'uncompensated' beam fails corresponds to F_0 on the compensated beam. The energy supplied by the weight of the beam is represented by area A2. By treating the beam in the post-peak stage as split into two rectangular pieces connected only by the fracture zone, and further simplifying assumptions, the area A3 is found to equate to A2. Ignoring A4 as negligible (1-2% of total area), the fracture energy is obtained as follows:

$$G_f = \frac{A+W\delta}{b(d-a)} \qquad (4.2)$$

where W is the weight of the specimen between supports and δ is the deflection at the final fracture of the uncompensated beam.

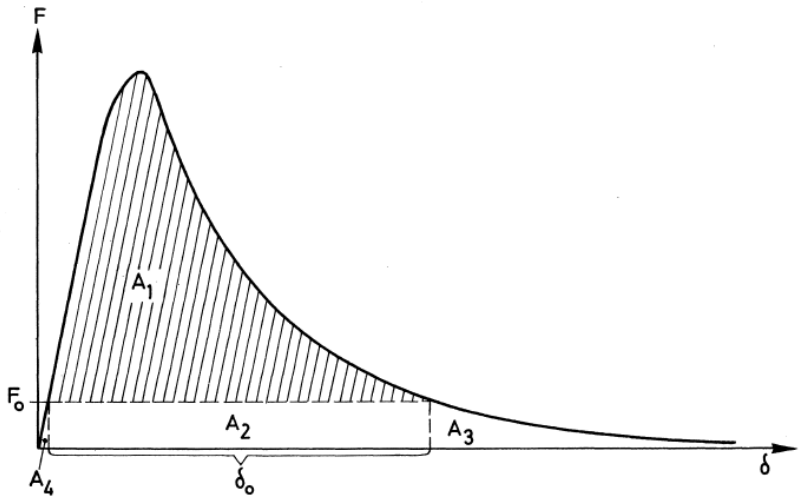

Figure 4.40: Graphical illustration of effect of weight compensation on load deflection curve (Petersson, 1981)

The validity of this approach was confirmed by extensive tests which found values obtained by applying this approach on uncompensated tests to be very close ($\pm 10\%$) to those from compensated tests. They also found that smaller beams (depth=50mm) needed to be compensated by about 50-60% whereas for larger beams (depth=200mm) compensation required was 150-200%. The fracture energy values adjusted for weight of the specimen as outlined above are shown on Table 4.24 and plotted in Fig.4.41.

The effect of weight adjustment can be described as follows:

- Increase in G_f values as observed by Petersson (1981)
- Reduction in the scatter of the values
- The apparent size effect in 4% fibre content is reduced

Clearly some size effect remains because only two sources of the apparent size effect were considered i.e. Specimen weight and the long tail. Abdalla and Karihaloo (2003) suggested that size effect on fracture energy can be entirely removed by taking into account all the sources of size effect. However, Petersson (1981) concluded that size effect on fracture energy cannot be entirely eliminated but only reduced to a value considered free enough of size effects for practical purposes.

Table 4.24: Fracture energy values adjusted for weight of the specimen

Fibre content %	**Size**	**Area under curve (mm^2)**	**Ligament area (mm^2)**	**Mass (Kg)**	**Final displacement (mm)**	**Fracture energy (KJ/m^2)**	**Weight Adjusted fracture energy (KJ/m^2)**
2	1	109857.31	8350	25.77	57.05	13.16	30.07
	2	118891.90	6650	17.44	60.35	17.88	33.08
	3	87717.50	5000	10.09	100.05	17.54	36.93
	4	48869.38	3350	4.32	15.05	14.59	16.45
	5	28842.38	1650	1.27	44.75	17.48	20.78
	6	15166.01	850	-	15.05	17.84	-
Average						**16.13**	**27.46**
4	1	109857.31	8350	27.18	58.35	18.34	31.39
	2	142120.43	6650	18.03	80.15	21.37	42.24
	3	132733.69	5000	10.40	114.85	26.55	49.49
	4	92214.54	3350	4.59	84.95	27.53	38.71
	5	59130.77	1650	1.30	45.65	35.84	39.28
	6	25421.71	850	-	18.55	29.91	29.91
Average						**25.92**	**38.50**
6	1	219782.95	8350	28.80	79.15	26.32	52.54
	2	213522.19	6650	18.48	75.95	32.11	52.38
	3	145974.44	5000	10.96	100.05	29.19	50.25
	4	97334.85	3350	4.76	96.25	29.06	42.18
	5	52520.70	1650	1.33	45.65	31.83	35.36
	6	36361.57	850	-	15.75	42.78	-
Average						**29.70**	**46.54**

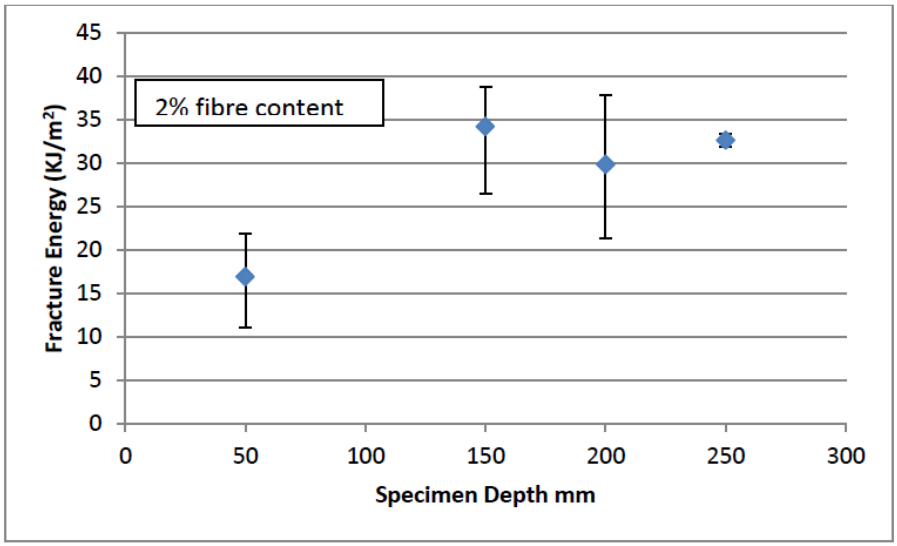

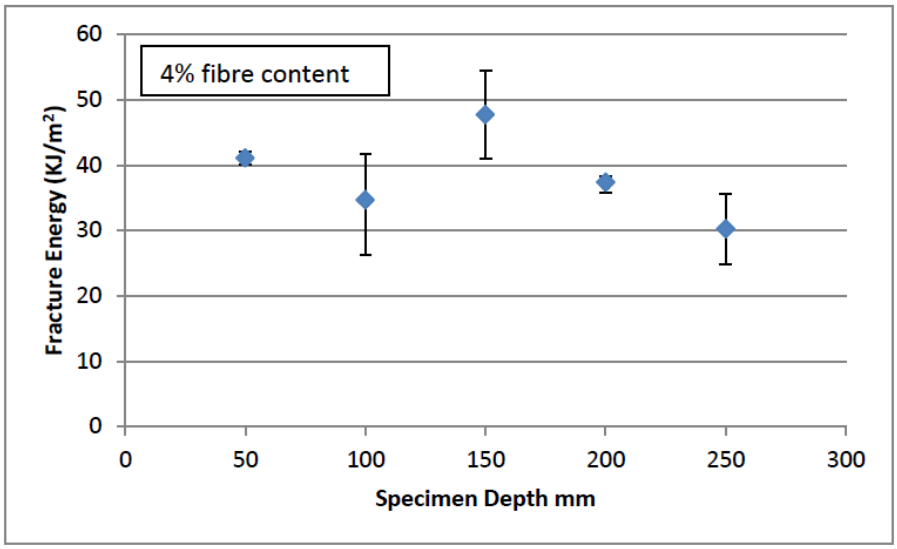

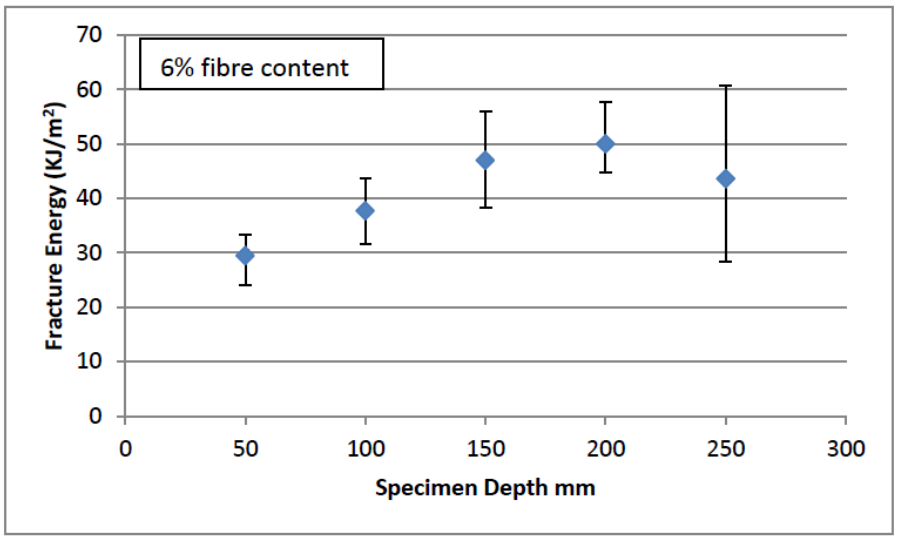

Figure 4.41: Notched TPB test Fracture energy (weight adjusted) with specimen depth

4.6 Effect of Fibre content

In previous sections increasing the fibre content between 2% and 6% was observed to increase both the load carrying capacity and ductility of UHPFRC beam specimens. In this section, fibre content is considered further with the aim of examining its effect on some material properties that can be used to model its flexural behaviour. Its effect on flexural stress values is discussed first due to their importance in estimating the tensile strength of UHPFRC. This is followed by a brief discussion of the effect of fibre content on fracture energy which is also a measure of the material's ductility. Finally the effect of fibre content on compressive strength is considered due to its importance in estimating other material properties such as the elastic modulus.

4.6.1 Effect on flexural stress at end of linearity and flexural strength

For the notched three point bending, and both un-notched three point and four point bending tests, the flexural stress at the end of linearity and flexural strength increased with fibre content in an almost linear way as in Fig.4.42. The almost linear increase in flexural strength with fibre content observed in this study is similar to other studies on UHPFRC (Yoo et al. (2013), Kang et al. (2010)). The linearity can be attributed to conformity with the rule of mixtures discussed chapter 2. It was observed that the rule can be also expressed in the form of Eq. 2.11. Adopting the same approach as Kang (2010), the above equation is conveniently rearranged to express the dependence of flexural strength (σ_f) on fibre content (V_f) more explicitly as follows:

$$\sigma_f = \left(B\left(l_f/d\right) - A\sigma_{f0}\right)V_f + A\sigma_{f0} \qquad (4.3)$$

where l_f and d are the fibre length and diameter respectively and A & B are constants. Therefore, for a constant fibre aspect ratio, the flexural strength is linearly dependent on the fibre content. Plots of average flexural strength against fibre content confirm this strong linear relationship with a high regression coefficient, R^2, (Fig.4.42). For example, the equations obtained from regression of data from the notched three point pending test of specimen S1 are as follows:

$$\sigma_f = 4.47V_f + 2.1 \qquad (4.4)$$

Relating the two Eqs. 4.4 and 4.3 gives

$$A\sigma_{f0} = 2.1 \qquad (4.5)$$

The intercept at the y-axis is the flexural strength at zero fibre content σ_{f0} making $A = 1$. And therefore for $l_f/d = 13/0.2$, $B = 0.032$. Hence it can be concluded that the rule of mixtures can be reliably applied to this UHPFRC mix consisting of fibres with the same aspect ratio. However, this is probably because the deflection hardening in it was

relatively small suggesting that its strain hardening properties would also be relatively small at best (categories b and c in Fig.2.10). As was discussed in chapter 2, it is possible even for a material with no strain hardening to still show deflection hardening. This can happen as long as the residual post-cracking tensile stress is more than about a third of the tensile strength of the matrix (Fig.2.11). A minimum volume of fibres is required to have a noticeable effect on UHPFRC strength as discussed in chapter 2. An increase in fibre volume above the critical volume would make available more fibres to increase the first crack load/stress by crack suppression and the peak load/flexural strength by fibre bridging action. The upper limit of fibre volume would mainly be dictated by the matrix fibre bond strength and the fibre aspect ratio. As the number of fibres increase, a point would be reached beyond which the workability of UHPFRC would not be practical. Between the critical fibre volume and this upper limit, an increase in fibre content would tend to produce an increase in UHPFRC flexural strength.

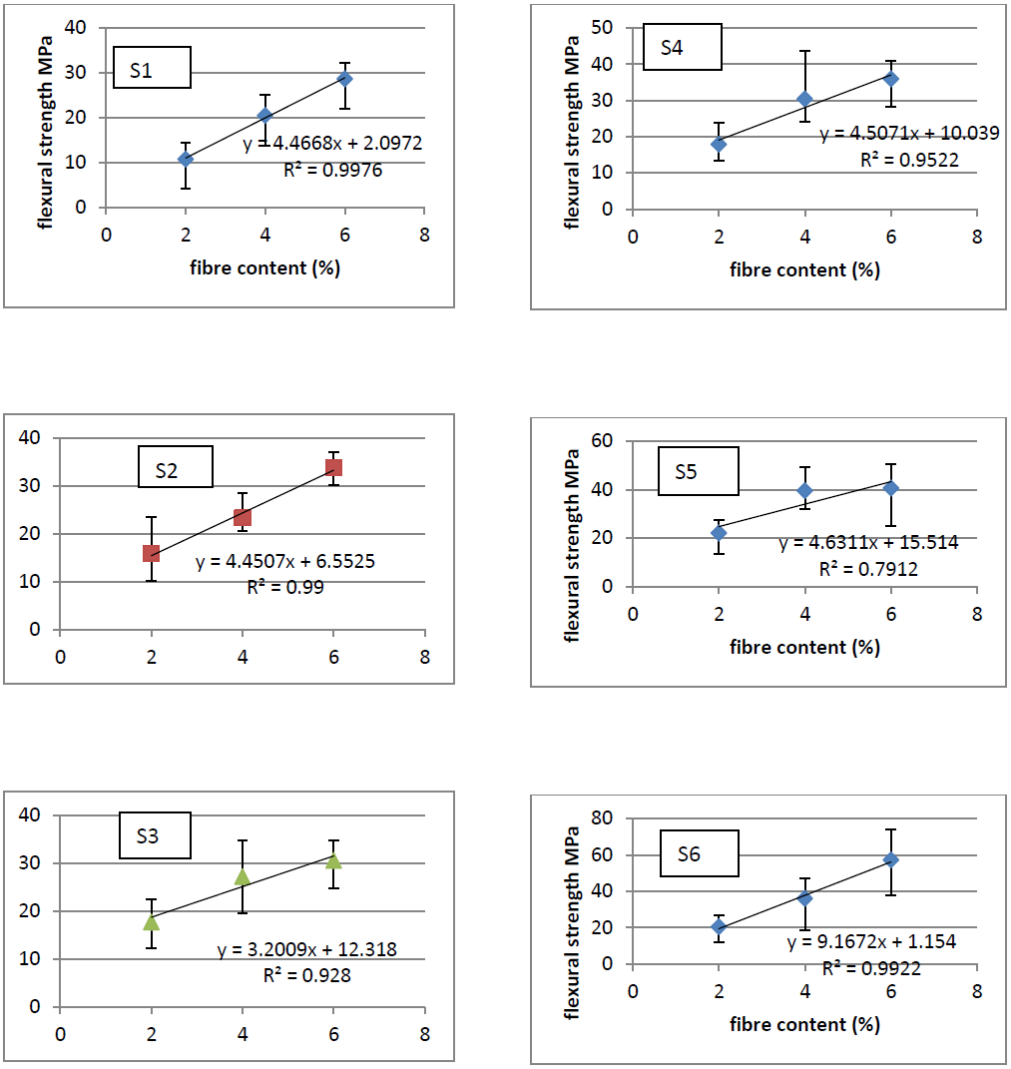

Figure 4.42: Notched three point bending test flexural strength against fibre content for each specimen size

4.6.2 Effect on fracture energy

Consideration of fracture energy values estimated from specimens with 2%, 4% and 6% fibre contents (Tables 4.23 & 4.24) also enabled the assessment of the effect of fibre content on fracture energy. Prior to adjustment accounting for the effect of weight, average fracture energy increases linearly with fibre content (Fig.4.43).

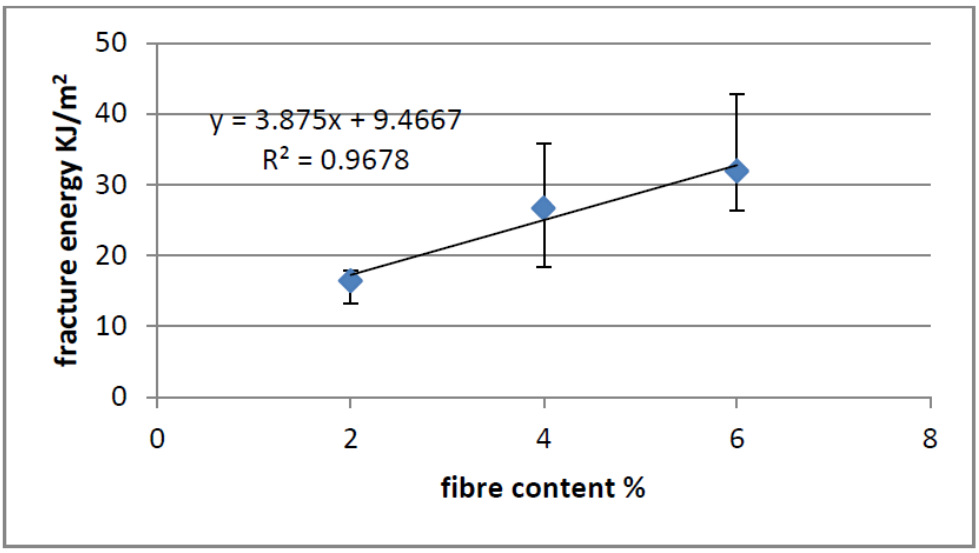

Figure 4.43: Average fracture energy against fibre content

4.6.3 Effect on compressive strength

Unlike in ultra high performance concrete (UHPC) which has no fibres and where the failure is explosive and instantaneous (Le, 2008), in UHPFRC the fibres were observed to hold the matrix together after cracking hence preventing an explosive response. During testing, the load was observed to increase even after the onset of cracking before reaching a maximum value suggesting a hardening behaviour due to multiple cracking (Fig.4.44). From specimens that failed through compressive loading less damage was observed as the fibre content increased. Despite flaking and even crumbling of the concrete matrix, the specimens did not fall apart due to the fibre bridging action. Table 4.25 presents Compressive strength (f_{ck}) values simply calculated according to BS EN 12390-3-2009 as follows:

$$f_{ck} = {}^{F}/_{A} \qquad (4.6)$$

where F is the maximum Load and A is the cross-sectional area of the test specimen.

There was an increase in compressive strength with fibre content in each batch. Despite the wide scatter in the compression failure load within the batches the average compressive strength also increased with fibre content (Fig.4.45). It was noted that there was no correlation between compressive strength and the peak flexural load of the

batches. For example, whereas the lowest peak loads were obtained in specimens 2S1B3 and 2S1B4, the latter had the highest compressive strength of all the batches. The former on the other hand had a higher compressive strength than specimen 2S1B5 which had a much higher peak flexural load.

This result is in line with the reason given for the low peak flexural loads of the above mentioned specimens as due to the fewer fibres observed in their crack faces. Though fibres do have a positive effect in increasing compressive strength, the internal structure of the matrix remains the main factor in achieving a higher strength. Although the maximum compressive strengths obtained in some batches reached or approached 150MPa which is the typical value for UHPFRC, the average compressive strengths for all fibre contents were lower than this value. This could be attributed to the fact that the mix in this study was not subjected to any heat treatment. As was mentioned in chapter 2 heat treatment has been observed to increase the compressive strength of UHPFRC by up to 20% (Fehling, 2014).

2% fibre content **4% fibre content** **6% fibre content**

Figure 4.44: Compression test specimens after test

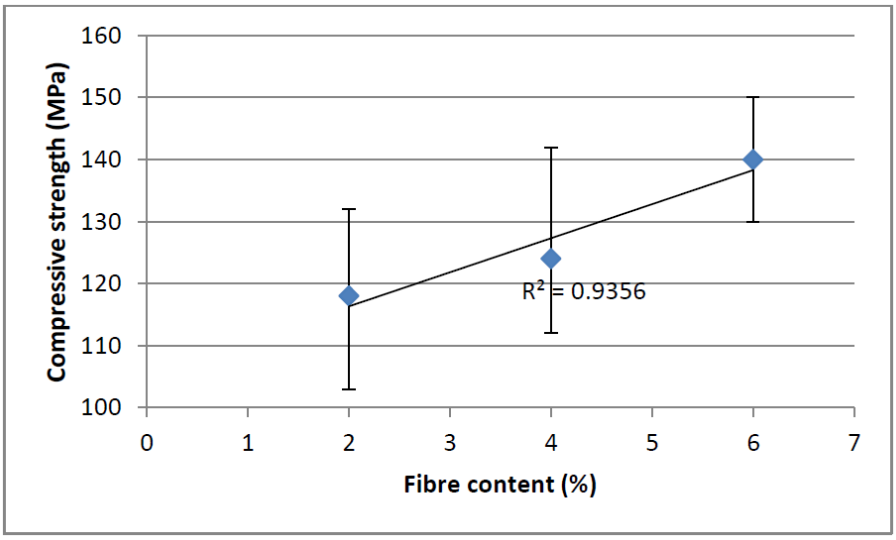

Figure 4.45: Compressive strength against fibre content

Table 4.25: Compressive strengths

Specimen	Mass (air) (Kg)	Mass (water) (Kg)	Density (Kg/m^3)	Max Load (kN)	Compressive Strength (MPa)
2S13B1	2.50	1.49	2482.59	1265	127
2S13B2	2.57	1.55	2513.22	1154	115
2S13B3	2.158	1.533	3452.8	1122	112
2S13B4	2.515	1.507	2495.0	1323	132
2S13B5	2.58	1.554	2514.6	1025	103
Average Compressive Strength					**118**
4S13B1	2.67	1.64	2597.67	1288	129
4S13B2	2.67	1.65	2609.38	1190	119
4S13B3	2.297	1.657	3589.1	1181	118
4S13B4	2.638	1.626	2606.7	1417	142
4S13B5	2.661	1.637	2598.6	1116	112
Average Compressive Strength					**124**
6S13B1	2.70	1.71	2728.01	1448	145
6S13B2	2.72	1.70	2670.26	1358	136
6S13B3	2.358	1.733	3772.8	1303	130
6S13B4	2.777	1.758	2725.2	1499	150
6S13B5	2.734	1.718	2690.9	1416	142
Average Compressive Strength					**140**

4.6.4 Concluding remarks on the effect of fibre content

By means of experimental data, this chapter has confirmed the importance of fibre content in influencing material properties of UHPFRC in relation to its flexural behaviour. Though compression (and by extension elastic modulus) and tensile strength of UHPFRC are mainly influenced by the properties of the matrix, the effect of fibre content has been shown to be important. Chapter 2 examined the enhancements within UHPFRC's internal structure and the mechanisms responsible for its advanced properties. This understanding was used as a basis for explaining the ways by which fibre content influences UHPFRC material properties and flexural behaviour. The enhanced fibre- matrix bond allows more fibres with a higher aspect ratio to be incorporated into the UHPFRC further increasing its compressive and tensile strength. Fibre content has a significant influence on the load and stress at the end of linearity through affecting the spacing between fibres thereby determining the extent of the crack suppression mechanism. The post-cracking response of UHPFRC indicates its ductility and is even more influenced by fibre content. This is because the number of fibres available to bridge across cracks is largely a factor of fibre

content especially when orientation and distribution is carefully controlled by production techniques. As confirmed by experiment, ductility measured by fracture energy increased with fibre content. The combined effect of the tensile strength (or first crack stress) and ductility on the flexural strength of UHPFRC was discussed in chapter 2. By regression analysis of experiment data in this chapter, a direct linear relationship has been established between flexural strength and fibre content. However, only fibre contents between 2% and 6 % by volume were considered in this study. As was discussed in chapter 2, a fibre content below the critical volume will have little effect on the flexural strength (Bentur and Mindess, 2007). A fibre content of 2% is the most commonly adopted in commercial UHPFRC mixes as it is considered the most cost effective (Barnett et al., 2007a). On the other hand exceeding a fibre content of 6% has been observed to adversely affect its rheology and workability (Le, 2008).

Chapter 5 – UHPFRC Model Development

5.1 Introduction

The main aim of this chapter is to present the proposed Ultra High Performance Fibre Reinforced Concrete (UHPFRC) damage model incorporating fibre content (UDMF). First, key features of the model are presented. This is followed by a brief description of the estimation of material properties building on the methods discussed in the initial simulation work in chapter 3. Incorporation of the effect of fibre content is then discussed thereby providing a link to the previous chapter. The model formulation is then presented followed by a description of its implementation through a user defined material model (UMAT) in ABAQUS finite element software. This is followed by a verification of the model using data from tests carried out in the previous chapter. Finally, the model is validated using independent data from case studies chosen to assess the model's capability to simulate test specimens of different fibre contents, sizes and test configurations.

5.2 Key features of the UHPFRC damage model incorporating fibre content (UDMF)

The key features of the proposed model are based on observations from the initial simulation study (chapter 3) and from test data of the effect of fibre content on material properties (chapter 4). These features are highlighted with reference to Fig. 5.1 as follows:

- A bilinear traction-separation (σ-ω) curve using a fracture energy approach is adopted as this was shown in chapter 3 to be able to accurately predict the load-deflection response of UHPFRC test specimens. This was attributed to the material's high fracture energy (G_f) which enabled it to simulate deflection hardening.

- The influence of fibres is taken into account by the way in which they affect the σ-ω curve. Hence fibre content from test data is incorporated into the σ-ω curve through the three main properties (tensile strength [σ_t], fracture energy [G_f] and elastic modulus [E]). These three material properties are expressed as functions of fibre content (λ_f) to reflect the effect of fibres on the material's behaviour.

- The final damage separation w_f is calculated from the three main properties in the above damage law and is therefore also related to the fibre content.

- As observed in chapter 3, for normal UHPFRC flexural behaviour without unloading there is no need to incorporate ability to handle cyclic loading by

including non-recoverable strains. Therefore damage is assumed to occur through degradation of stiffness only such that all strains are recoverable.

- A smeared crack approach is adopted as it lends itself to implementation in the finite element method. In this approach individual cracks are not tracked but the material model is applied to the whole specimen. However, localisation must be limited and this is implemented by using a characteristic length (l_c) to convert strains to displacements as required by the fracture energy approach proposed by Hillerborg et al. (1976). This approach was demonstrated in chapter 3 to be able to predict the flexural response as accurately as the Cohesive Crack model with cohesive elements.

- However, in order to handle the severe convergence difficulties experienced by material models with softening, the smeared crack approach is implemented with viscous regularisation to aid convergence

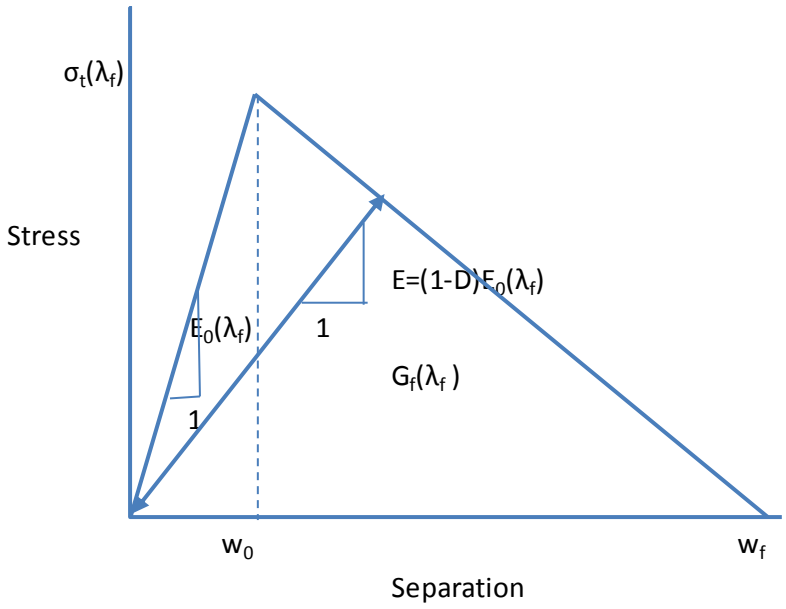

Figure 5.1: Traction separation curve incorporating fibre content

5.3 Summary of material property values

The bilinear σ-ω curve adopted in the UHPFRC model (Fig.5.1) required input of three basic properties i.e. E, G_f and σ_t. These were estimated from the test data presented in chapter 4. The approach used to estimate the material properties was broadly similar to that adopted in the initial simulation study of chapter 3 which was found to be suitable. Hence in the following sections, a summary of the average material properties estimated

in chapter 4 is presented. The values of these properties were the basis for incorporating the effect of fibre content on material properties in the proposed model.

5.3.1 Elastic modulus

As discussed in section 3.5.3 empirical relations are commonly used to estimate the elastic modulus E from compressive strength due to the correlation between the two produced by the common influence of concrete porosity on both properties (Neville, 2012). Therefore E was estimated by applying the same expression used in the initial simulation study (Eq. 3.25) to compressive cube strength values from Table 4.25 in chapter 4. The average E values obtained are summarised in Table 5.1.

5.3.2 Tensile strength

In chapter 4, σ_t was estimated from the flexural stress of an un-notched four point bending (FPB) test specimen corresponding to the end of the linear elastic phase. In line with the approach described in chapter 3, it was then adjusted for scale effects according to Eq. 3.27. These average σ_t values from Table 4.22 are summarised in Table 5.1.

5.3.3 Fracture energy

In chapter 4, fracture energy was estimated from the area under the full load load-deflection curves obtained from three point bending tests on notched UHPFRC specimens. The final fracture energy values were obtained after adjusting for the effect of energy loss from the specimen self-weight following the recommendations of Petersson (1981). The average fracture energy values presented in Table 4.24 are summarised in Table 5.1

Table 5.1: Summary of average material property values

Fibre content	Tensile Strength (MPa)	Fracture Energy (KJ/m^2)	Elastic Modulus (GPa)
2%	7.82	27.46	43.93
4%	11.18	38.50	44.66
6%	11.95	46.54	46.48

5.4 Fibre content

The enhanced crack resistance in UHPFRC is achieved mainly by incorporating fine fibres within the matrix which make the concrete significantly more ductile than normal concrete. The content, distribution and orientation of these fibres within UHPFRC have a significant effect on its properties. Distribution and orientation are a function of the production process. The ideal orientation of fibres should be in the direction of maximum principal stresses. However, as this is difficult to attain without specialised and expensive measures, the aim of normal production processes is to achieve a uniform distribution and

random orientation of the fibres. If this aim is achieved, then the number of fibres per unit area (N) is observed to have the greatest influence on material properties compared to other factors. It is reasonable to expect N to increase with fibre content and decrease with fibre cross-sectional area. Several studies have proposed mathematical relations expressing N in terms of these factors. For example, for 3D configuration with fibres of random orientation, Bentur and Mindess (2007) have suggested that the number of fibres per unit area (N) can be given by:

$$N = \frac{2V_f}{\pi d^2} \qquad (5.1)$$

where d is the fibre diameter and V_f is the fibre volume content. It is evident from the above expression that for a constant aspect ratio with uniform distribution and random orientation, fibre content is the most important factor influencing number of fibres per unit area and hence material properties. The importance of fibre content in influencing material properties of UHPFRC was also confirmed by experimental data in chapter 4 in relation to its flexural behaviour. Therefore the combined effects of fibre content (λ_f) can be related to the material properties measured at the macroscale. The approach developed by Chen (2014) was adapted for this study to incorporate the effect of fibre content into the proposed model. The model by Chen (2014) linked macroscale material properties to measurements of bone pore sizes from experimental data which were then incorporated into a bilinear traction-separation (σ-ω) law. This was then used successfully to simulate the behaviour of a bone-adhesive interface. The above mentioned model however was implemented within the cohesive crack framework such that the traction-separation law was only applied within a crack path known *a priori* using cohesive interface elements. In this study however, the proposed model was implemented within the crack band framework whereby the model was applied to the whole specimen. Hence individual cracks were not tracked but were 'smeared' over the specimen, an approach that required a 'localisation limiter' in the form of a characteristic length.

The average material property values obtained from test data in chapter 4 and summarised in Table 5.1 were plotted against fibre content and the equations of the corresponding curves used as functions of fibre content (Fig.5.2).

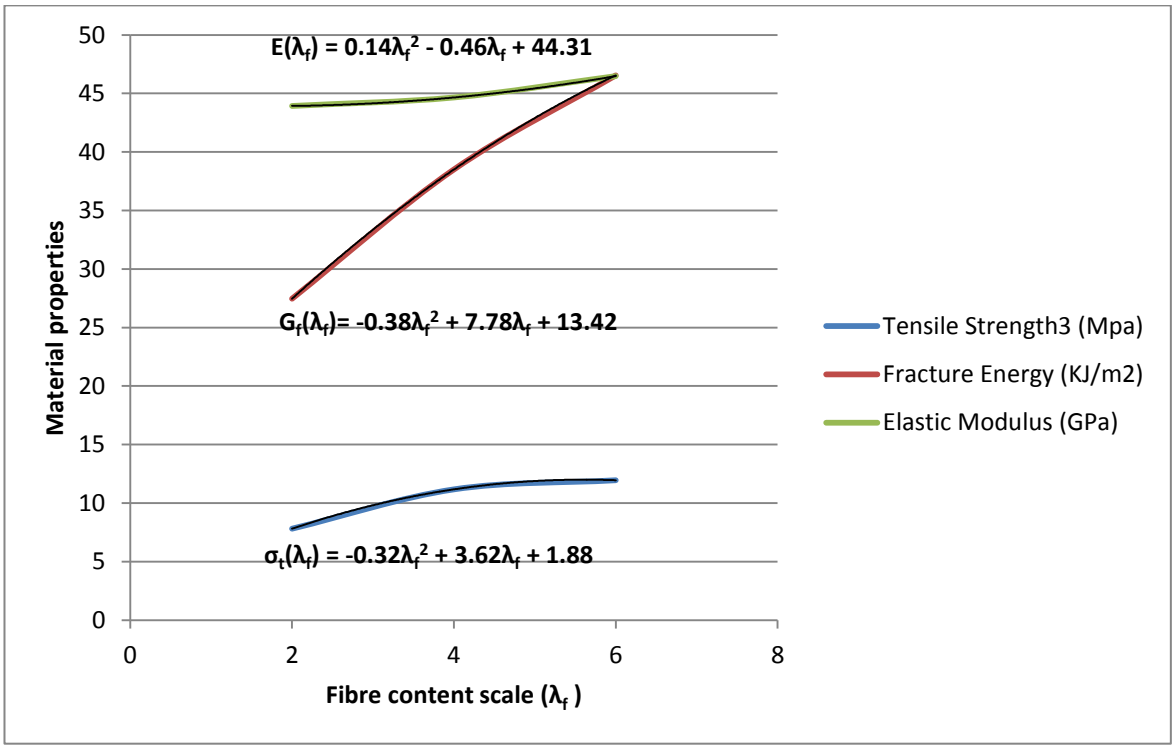

Figure 5.2: Fibre content effect on material properties

The equations from figure 5.2 are presented in Eq. 5.2 below in the usual matrix notation where $\sigma_t(\lambda_f)$, $G_f(\lambda_f)$ and $E(\lambda_f)$ are the tensile strength, fracture energy and elastic modulus respectively based on fibre content (λ_f)

$$\begin{Bmatrix} \sigma_t(\lambda_f) \\ G_f(\lambda_f) \\ E(\lambda_f) \end{Bmatrix} = \begin{Bmatrix} -0.32\lambda_f^2 + 3.62\lambda_f + 1.88 \\ -0.38\lambda_f^2 + 7.78\lambda_f + 13.42 \\ 0.14\lambda_f^2 - 0.46\lambda_f + 44.31 \end{Bmatrix} \tag{5.2}$$

Eq. 5.2 can be written as:

$$\begin{Bmatrix} \sigma_t(\lambda_f) \\ G_f(\lambda_f) \\ E(\lambda_f) \end{Bmatrix} = [A]\{\lambda_f\} = \begin{bmatrix} -a_1 & a_2 & -a_3 \\ -b_1 & b_2 & b_3 \\ c_1 & -c_2 & c_3 \end{bmatrix} \begin{Bmatrix} \lambda_f^{\,2} \\ \lambda_f \\ 1 \end{Bmatrix} \tag{5.3}$$

The matrix $[A]$ contains the coefficients of fibre content (λ_f) from Eq. 5.2 as follows:

$$[A] = \begin{bmatrix} -a_1 & a_2 & -a_3 \\ -b_1 & b_2 & b_3 \\ c_1 & -c_2 & c_3 \end{bmatrix} = \begin{bmatrix} -0.32 & 3.62 & 1.88 \\ -0.38 & 7.78 & 13.42 \\ 0.14 & -0.46 & 44.31 \end{bmatrix} \tag{5.4}$$

These coefficients were adopted as constants in the subsequent model where the effect of fibre content was considered by the way in which it affected the traction separation law.

5.5 Model formulation

The model formulation is adapted from the general framework for progressive damage and failure as described in ABAQUS Analysis manual (ABAQUS, 2013). The model assumes an initially linear elastic behaviour followed by the initiation and evolution of damage.

5.5.1 Linear elastic behaviour

The elastic behaviour is written in terms of an elastic constitutive matrix that relates the nominal stresses to the nominal strains at each point. The nominal stresses are the force components divided by the original area at each integration point. The nominal strains are the separation (w) divided by the characteristic length (l_c).

$$\varepsilon = {}^{w}/_{l_c} \tag{5.5}$$

The characteristic length (l_c) associated with a material point is required in order to implement a stress-displacement concept in a finite element model (Bažant and Planas, 1998). It is based on the element geometry and formulation. For a first order element, for example, It is defined as typical length of a line across the element (ABAQUS, 2013) .

The elastic behaviour can be written in the form of the generalised Hooke's law relating the stresses to strains at a point as follows (Astley, 1992):

$$\begin{Bmatrix} \sigma_x \\ \sigma_y \\ \sigma_z \\ \tau_{xy} \\ \tau_{yz} \\ \tau_{zx} \end{Bmatrix} = [M] \begin{Bmatrix} \varepsilon_x \\ \varepsilon_y \\ \varepsilon_z \\ \gamma_{xy} \\ \gamma_{yz} \\ \gamma_{zx} \end{Bmatrix} \tag{5.6}$$

where σ_x, σ_y , σ_z and τ_{xy} , τ_{yz}, τ_{zx} are the normal and shearing stresses respectively while ε_x ,ε_y ,ε_z and γ_{xy},γ_{yz} , γ_{zx} are the corresponding normal and shearing strains at a point.

$[M]$ is the elastic matrix given by:

$$[M] = \begin{bmatrix} (1-v)c & vc & vc & & & \\ vc & (1-v)c & vc & & & \\ vc & vc & (1-v)c & & & \\ & & & G & & \\ & & & & G & \\ & & & & & G \end{bmatrix} \tag{5.7}$$

where $c = \frac{E}{(1+v)(1-2v)}$ and $G = \frac{E}{2(1+v)}$

The inverse of Eq. 5.6 can be written as follows (Zienkiewicz, 2005):

$$\begin{Bmatrix} \varepsilon_x \\ \varepsilon_y \\ \varepsilon_z \\ \gamma_{xy} \\ \gamma_{yz} \\ \gamma_{zx} \end{Bmatrix} = \frac{1}{E} \begin{bmatrix} 1 & -v & -v & 0 & 0 & 0 \\ -v & 1 & -v & 0 & 0 & 0 \\ -v & -v & 1 & 0 & 0 & 0 \\ 0 & 0 & 0 & 2(1+v) & 0 & 0 \\ 0 & 0 & 0 & 0 & 2(1+v) & 0 \\ 0 & 0 & 0 & 0 & 0 & 2(1+v) \end{bmatrix} \begin{Bmatrix} \sigma_x \\ \sigma_y \\ \sigma_z \\ \tau_{xy} \\ \tau_{yz} \\ \tau_{zx} \end{Bmatrix} \tag{5.8}$$

For two-dimensional cases, the last two rows and columns can be ignored to give the following:

$$\begin{Bmatrix} \varepsilon_x \\ \varepsilon_y \\ \varepsilon_z \\ \gamma_{xy} \end{Bmatrix} = \frac{1}{E} \begin{bmatrix} 1 & -v & -v & 0 \\ -v & 1 & -v & 0 \\ -v & -v & 1 & 0 \\ 0 & 0 & 0 & 2(1+v) \end{bmatrix} \begin{Bmatrix} \sigma_x \\ \sigma_y \\ \sigma_z \\ \tau_{xy} \end{Bmatrix} \tag{5.9}$$

In the plane stress case, $\sigma_z = 0$ so that

$$\varepsilon_z = -\frac{v}{E}(\sigma_x + \sigma_y) \tag{5.10}$$

Substituting Eq.5.10 into the inverse of Eq. 5.9 produces the expression for the plane stress case as follows:

$$\begin{Bmatrix} \sigma_x \\ \sigma_y \\ \tau_{xy} \end{Bmatrix} = \frac{E}{(1-v^2)} \begin{bmatrix} 1 & v & 0 \\ v & 1 & 0 \\ 0 & 0 & (1-v)/2 \end{bmatrix} \begin{Bmatrix} \varepsilon_x \\ \varepsilon_y \\ \gamma_{xy} \end{Bmatrix} \tag{5.11}$$

Similarly the expression for the plane strain case can be obtained from taking the inverse of Eq. 5.9 with $\varepsilon_z = 0$ as follows:

$$\begin{Bmatrix}\sigma_x\\ \sigma_y\\ \tau_{xy}\end{Bmatrix} = \frac{E}{(1+v)(1-2v)}\begin{bmatrix}(1-v) & v & 0\\ v & (1-v) & 0\\ 0 & 0 & (1-2v)/2\end{bmatrix}\begin{Bmatrix}\varepsilon_x\\ \varepsilon_y\\ \gamma_{xy}\end{Bmatrix} \quad (5.12)$$

5.5.2 Damage modelling

Damage refers to the loss of load-carrying capacity due to the progressive degradation of the material stiffness (Lemaître and Chaboche, 1994). Material failure occurs when there is complete loss of the load-carrying capacity at the end of this process. The stiffness degradation process is modelled using damage mechanics by considering the degraded response of the curve that the material would have followed in the absence of damage (Fig.5.3). The failure mechanism consists of a damage initiation criteria and a damage evolution law.

5.5.3 Damage initiation

Damage is assumed to begin when a quadratic interaction function involving the nominal strain ratios reaches a value of one as follows (ABAQUS, 2013) :

$$\left\{\frac{\varepsilon_x}{\varepsilon_x^0}\right\}^2 + \left\{\frac{\varepsilon_y}{\varepsilon_y^0}\right\}^2 + \left\{\frac{\varepsilon_z}{\varepsilon_z^0}\right\}^2 = 1 \quad (5.13)$$

ε_x^0, ε_y^0, ε_z^0 are the failure normal strains defined as the maximum stress divided by the corresponding elastic modulus (figure 5.3).

$$\varepsilon_0 = \frac{\sigma_{max}}{E} \quad (5.14)$$

From which the corresponding separation w_0 is calculated as follows:

$$w_0 = \varepsilon_0 \times l_c \quad (5.15)$$

5.5.4 Damage evolution

This is described by the rate at which the material stiffness is degraded after the damage initiation criterion is met. Damage evolution is defined based on the energy that is dissipated as a result of the damage forces (also called fracture energy,G_f). The fracture energy is equal to the area under the traction-separation curve of the linear damaged law (see Fig.5.1). The maximum strain is calculated from Fig.5.3 as follows:

$$\varepsilon_f = \frac{2G_f}{\sigma_{max} l_c} \quad (5.16)$$

Formulation is based on a scalar damage approach whereby post damage-initiation stress (σ_1) is related to stress without damage (σ_E) as:

$$\sigma_1 = (1 - D)\sigma_E \tag{5.17}$$

where D is the scalar damage variable which incorporates the combined effect of all damage mechanisms. For linear softening, damage evolution is modelled such that D evolves monotonically from 0 (undamaged) to 1 (fully damaged) upon further loading after damage initiation.

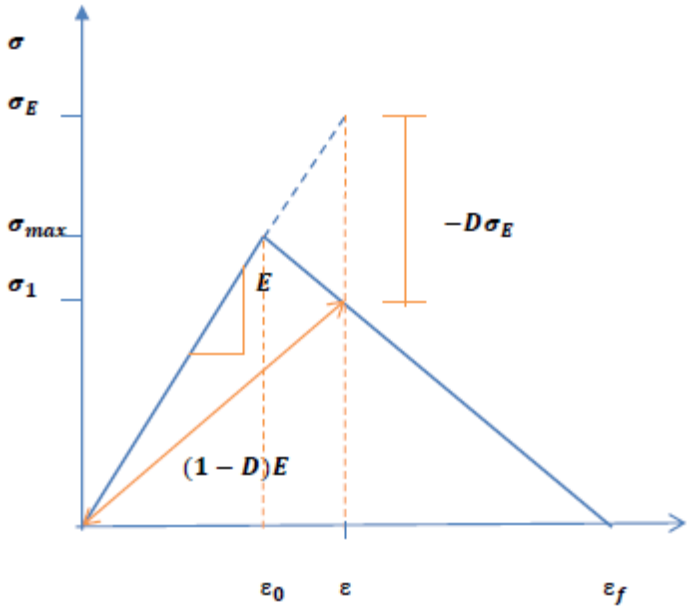

Figure 5.3: Defining the damaged response

From figure 5.3

$$\frac{E\varepsilon_0}{(\varepsilon_f - \varepsilon_0)} = \frac{(1-D)E\varepsilon}{(\varepsilon_f - \varepsilon)} \tag{5.18}$$

which reduces to:

$$D = \frac{\varepsilon_f(\varepsilon - \varepsilon_f)}{\varepsilon(\varepsilon_f - \varepsilon_0)} \tag{5.19}$$

(See Appendix 11 for derivation)

5.6 Implementation of model in ABAQUS

In implementing the finite element equations for quasi-static problems ($Ku = F$), the stiffness matrix changes in non-linear cases so that an incremental approach has to be adopted (Dunne and Petrinic, 2005). The equation is therefore solved incrementally ($K\Delta u = \Delta F$), and the stiffness matrix has to be updated at each step. However, the above incremental equilibrium equation will generally not be satisfied until convergence occurs. Implicit integration is commonly preferred to explicit integration because it involves the determination of a residual force at each step and iteration within the step to minimise the residual force to within a specified tolerance. This can be conveniently expressed in terms of residual forces (Ψ) as follows:

$$k(u)u - f = \Psi \neq 0. \qquad (5.20)$$

One of the commonly used techniques used in implicit integration is the Newton-Raphson method reviewed below. From Eq.5.20, residual forces (Ψ) are given by:

$$\Psi = k(u)u - f \qquad (5.21)$$

Ψ can be expanded using the Taylor series as follows:

$$\Psi(u) + \frac{\partial \Psi(u)}{\partial u}\Delta u + O(\Delta u^2) = 0 \qquad (5.22)$$

The matrix $J = \frac{\partial \Psi(u)}{\partial u}$ is called the Jacobian or effective tangent stiffness. It comprises of two terms; the first corresponds to internal forces (tangent stiffness matrix) and the second to external forces (load stiffness matrix). A linear form of Eq.5.22 can therefore be written as:

$$\Psi + J\Delta u = 0 \qquad (5.23)$$

Hence

$$J(u_n)\Delta u_n = -\Psi(u_n) \qquad (5.24)$$

where the displacement is updated by:

$$u_{n+1} = u_n + \Delta u_n \qquad (5.25)$$

The iteration carries on until the residual force is within the specified tolerance.

For many practical purposes, the Jacobian need only be accurate enough to give good convergence. In ABAQUS finite element code, the material Jacobian is defined as $\partial\Delta\sigma/\partial\Delta\varepsilon$ (ABAQUS, 2013) where

$$d\Delta\sigma = \frac{\partial \Delta\sigma}{\partial \Delta\varepsilon} d\Delta\varepsilon \tag{5.26}$$

In the above, shear strains are changed to engineering strains (i.e. the latter are twice the former). Using the above incremental form of Hooke's law, the material Jacobian for the plane strain case (ΔY_{13}=ΔY_{23}=0) in Eq. 5.12 can be written in the vector notation as:

$$\frac{\boldsymbol{\partial \Delta\sigma}}{\boldsymbol{\partial \Delta\varepsilon}} = \begin{bmatrix} \frac{\partial \Delta\sigma_{11}}{\partial \Delta\varepsilon_{11}} & \frac{\partial \Delta\sigma_{11}}{\partial \Delta\varepsilon_{22}} & \frac{\partial \Delta\sigma_{11}}{\partial \Delta\varepsilon_{33}} & \frac{\partial \Delta\sigma_{11}}{\partial \Delta\varepsilon_{12}} \\ \frac{\partial \Delta\sigma_{22}}{\partial \Delta\varepsilon_{11}} & \frac{\partial \Delta\sigma_{22}}{\partial \Delta\varepsilon_{22}} & \frac{\partial \Delta\sigma_{22}}{\partial \Delta\varepsilon_{33}} & \frac{\partial \Delta\sigma_{22}}{\partial \Delta\varepsilon_{12}} \\ \frac{\partial \Delta\sigma_{33}}{\partial \Delta\varepsilon_{11}} & \frac{\partial \Delta\sigma_{33}}{\partial \Delta\varepsilon_{22}} & \frac{\partial \Delta\sigma_{33}}{\partial \Delta\varepsilon_{33}} & \frac{\partial \Delta\sigma_{33}}{\partial \Delta\varepsilon_{12}} \\ \frac{\partial \Delta\sigma_{12}}{\partial \Delta\varepsilon_{11}} & \frac{\partial \Delta\sigma_{12}}{\partial \Delta\varepsilon_{22}} & \frac{\partial \Delta\sigma_{12}}{\partial \Delta\varepsilon_{33}} & \frac{\partial \Delta\sigma_{12}}{\partial \Delta\varepsilon_{12}} \end{bmatrix} = \begin{bmatrix} 2G+c & c & c & 0 \\ c & 2G+c & c & 0 \\ c & c & 2G+c & 0 \\ 0 & 0 & 0 & \frac{1}{2}2G \end{bmatrix} \tag{5.27}$$

where $G = \frac{E}{2(1+\upsilon)}$ and $c = \frac{E\upsilon}{(1+\upsilon)(1-2\upsilon)}$

If values of strain increment, and elastic constants (E and υ) are provided to the UMAT, the stress increment $\Delta\sigma$ is obtained by Hooke's law as follows:

$$\Delta\sigma = \boldsymbol{C}\Delta\varepsilon^e = \begin{bmatrix} 2G+c & c & c & 0 \\ c & 2G+c & c & 0 \\ c & c & 2G+c & 0 \\ 0 & 0 & 0 & \frac{1}{2}2G \end{bmatrix} \begin{bmatrix} \Delta\varepsilon_{11} \\ \Delta\varepsilon_{22} \\ \Delta\varepsilon_{33} \\ \Delta\varepsilon_{12} \end{bmatrix} \tag{5.28}$$

where $\boldsymbol{C}$ is the consistent material Jacobian in ABAQUS/Standard.

The above order of the shear quantities is only applicable to plane strain and axisymmetric elements but not for plane stress or 3D elements. The type of element used will determine the order according to the stiffness matrix required. However, for linear elasticity the material Jacobian is just the elastic stiffness hence easily specified in the UMAT. As discussed in chapter 3, damaged elasticity can be treated in the same way as linear elasticity as long as the degraded (damaged) stiffness replaces the elastic stiffness (Lemaître and Chaboche, 1994). The Jacobian for damaged elasticity then equals the damaged stiffness matrix.

The model was implemented as a user defined material model (UMAT) in ABAQUS/Standard finite element software and specified as a FORTRAN subroutine. A basic UMAT developed by Chen (2014) in their work mentioned in section 5.4 was adopted as the starting point for this study. However, the formulation in his model was similar to that of cohesive elements reviewed in section 3.5.5. It was also applied using

the cohesive crack approach whereby the cohesive elements were inserted in a crack path known *a priori*. On the other hand the model in this study adopted a smeared crack approach whereby it was applied to the whole specimen and individual cracks were not tracked. Therefore initial modelling was undertaken to validate the ability of the UMAT developed by Chen (2014) for application in the smeared crack approach. As part of this process the UMAT was found to make reasonably accurate predictions of the flexural response of the UHPFRC specimen described in section 3.5.2. This was in line with the observations made in chapter 3 where the predictions of the cohesive crack model using cohesive elements were found to be equivalent to that of the concrete smeared cracking model. After the success of this initial validation, the effect of fibre content (Eq. 5.2) was incorporated into the UMAT using a FORTRAN code. To run the model, an input file defining the geometry, loading conditions, etc. is also submitted to the ABAQUS solver (Fig.5.4).

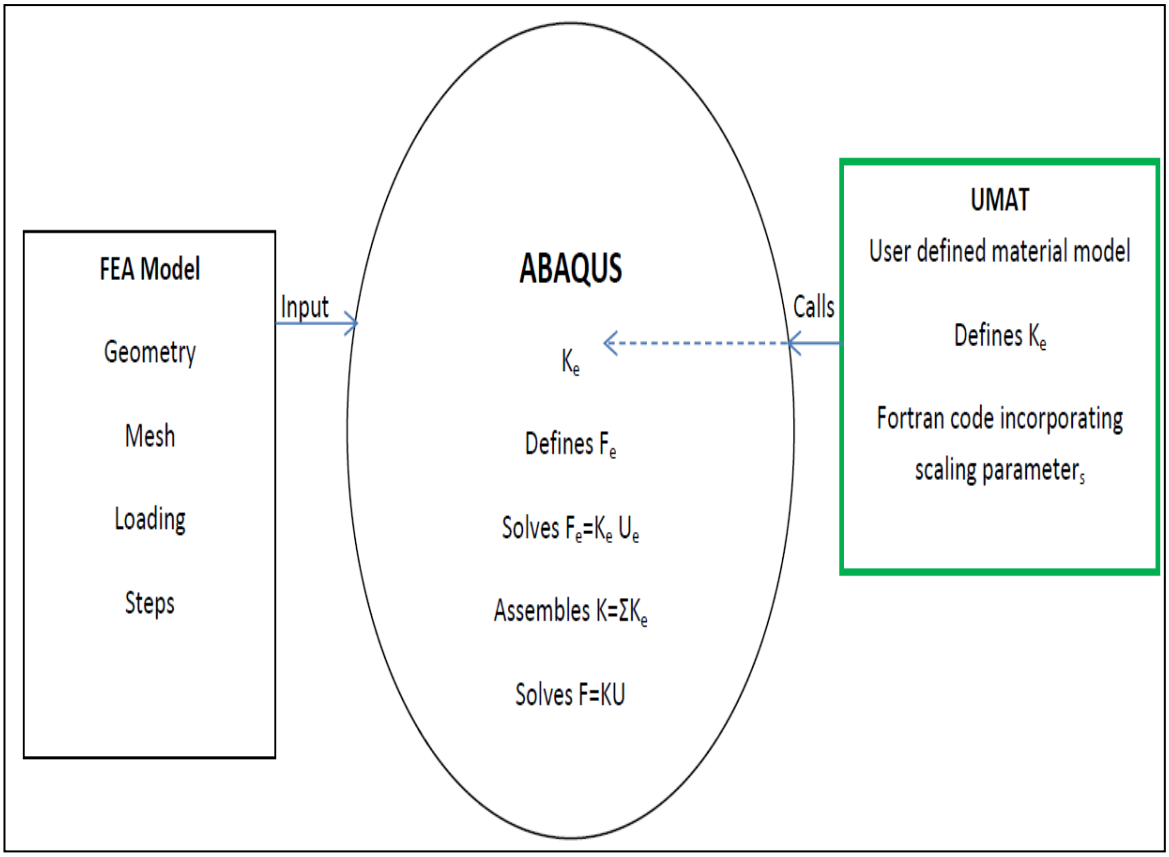

Figure 5.4: overview of ABAQUS solution process

The aim of the UMAT is to specify the material behaviour in terms of the constitutive response relating the stress in the material for any given deformation (Dunne and Petrinic, 2005). The proposed UMAT for UHPFRC therefore makes use of inputs of or calculated material properties to model linear elasticity, damage initiation and damage evolution

according to the bilinear traction separation law in figure 5.1. The main material properties influencing each of these three phases is calculated from fibre content according to Eq. 5.2. The UMAT specifies material behaviour by updating the stress, Jacobian and other state variables. This process is summarised in figures 5.5 and 5.6.

In order for the UMAT in ABAQUS to be able to achieve the above aim, it needs to be provided with the following information (Dunne and Petrinic, 2005):

- Stress, strain and deformation gradient at the beginning of time increment
- Strain and deformation gradient at the end of the time increment

With the above information, the role of the UMAT is then to carry out the following:

- Calculate the stress at the end of the time increment
- Determine the material Jacobian or tangent stiffness
- Update any state variables to the end of the time increment

As is common in finite element code, a modular structure was adopted with the following implemented as sub-routines:

- Failure initiation
- Damage evaluation
- Stress calculation
- Calculation of the derivative of damaged elasticity

The implementation of UDMF is described below with reference to Fig.5.5

a) Input fibre content (fc), Poisson's ratio (ν) and viscosity parameter (η)
b) Using fibre content (Eq. 5.2) calculate elastic modulus (E), tensile strength (σ_t) and fracture energy (G_f)
c) Using material constants (E and ν), generate full elastic stiffness matrix (Eq. 5.7)
d) Calculate strain at the end of an increment
e) Check failure initiation criteria (Eq. 5.13) based on failure strain calculated using failure stress (Eq. 5.14)

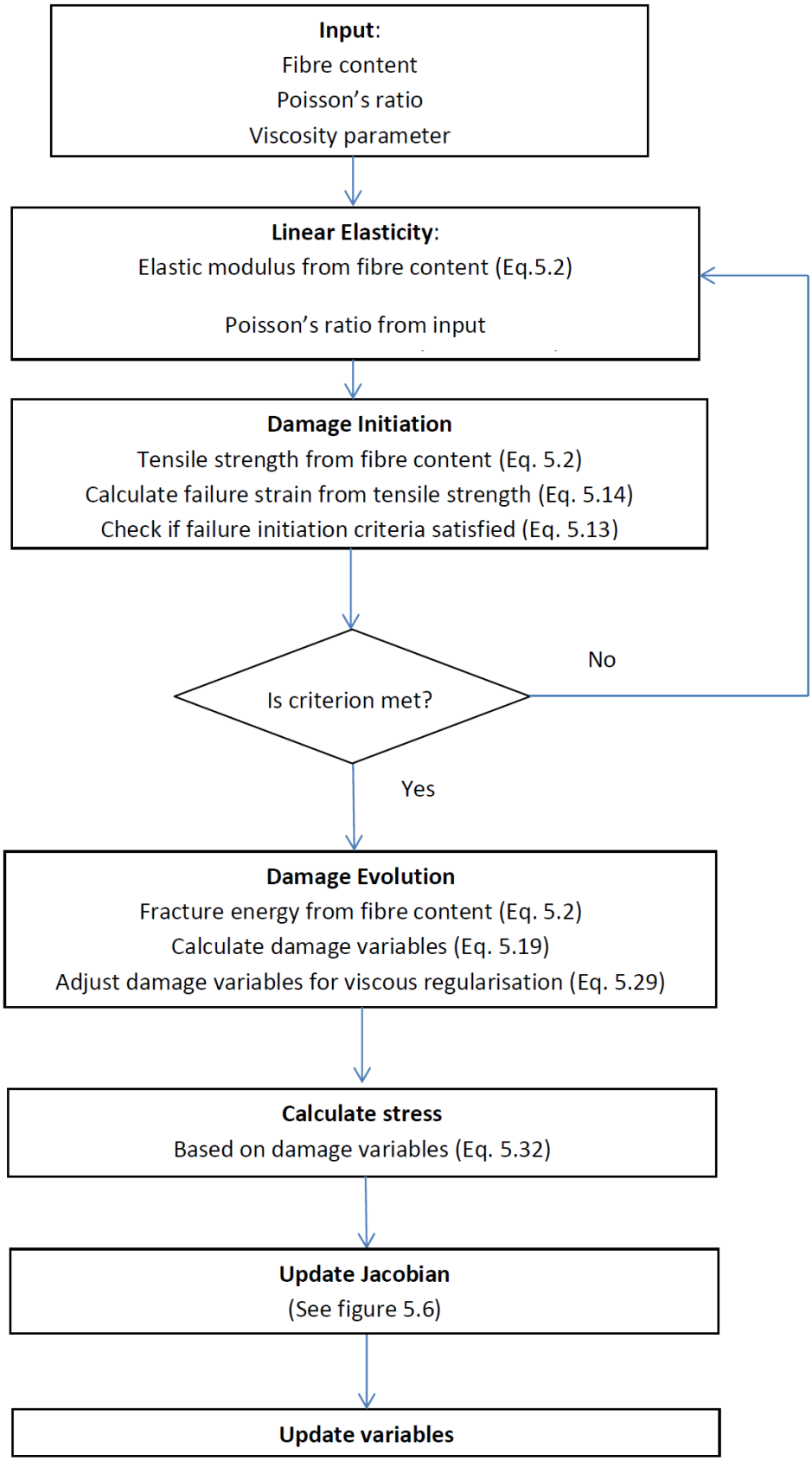

Figure 5.5: Overview of UDMF process

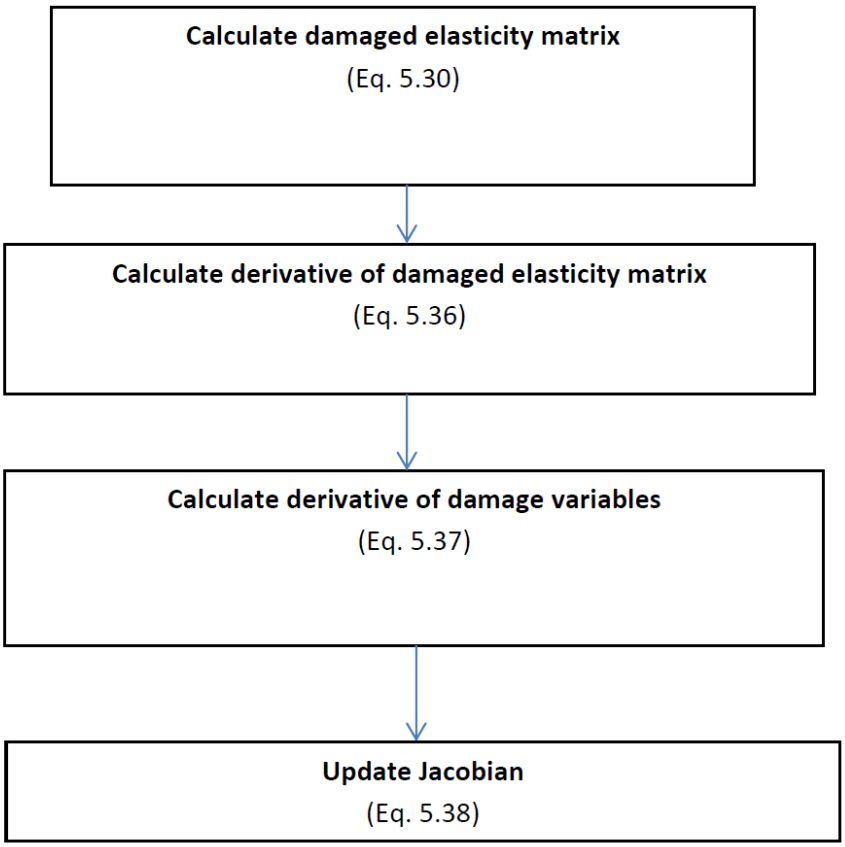

Figure 5.6: UDMF process in updating Jacobian

If failure has not occurred, calculate strain at end of next increment

f) If failure has occurred:

1. Calculate the damage variables (Eq. 5.19)
2. Calculate damage variables with viscous regularisation (D_R) as follows (ABAQUS, 2013):

$$D_R = \left(\frac{\Delta t}{\eta+\Delta t}\right) * D + \left(\frac{\eta}{\eta+\Delta t}\right) * D_{R0} \quad (5.29)$$

where Δt is the time increment and D_{R0} is the regularised damage variable at the start of the time increment

3. Generate full damaged stiffness matrix E_d (Fig.5.3) as follows:

$$E_d = (1 - D)E \quad (5.30)$$

This gives for the plane strain case from Eq. 5.27

$$E_d = \begin{bmatrix} (1-Dx)(1-v)c & (1-Dx)(1-Dy)vc & (1-Dx)vc & 0 \\ (1-Dx)(1-Dy)vc & (1-Dy)(1-v)c & (1-Dy)vc & 0 \\ (1-Dx)vc & (1-Dy)vc & (1-v)c & 0 \\ 0 & 0 & 0 & (1-Dx)(1-Dy)G \end{bmatrix} \quad (5.31)$$

where $c = \frac{E}{(1+v)(1-2v)}$ and $G = \frac{E}{2(1+v)}$

4. Calculate stress at the end of increment based on damage scale by adding to the previous stress the stress increment (∆σ) calculated from the strain increment (∆ε) as follows:

$$\Delta\sigma = E_d \Delta\varepsilon \quad (5.32)$$

g) Update all quantities (strains, damage scales, energy) to the end of time increment

h) Update Jacobian

In order to update the Jacobian, it can be written as follows:

From Eq. 5.32,

$$\frac{\partial \Delta\boldsymbol{\sigma}}{\partial \Delta\boldsymbol{\varepsilon}} = \frac{\partial (E_d \Delta\varepsilon)}{\partial \Delta\varepsilon} \quad (5.33)$$

This can also be conveniently written as:

$$\frac{\partial \Delta\boldsymbol{\sigma}}{\partial \Delta\boldsymbol{\varepsilon}} = \frac{\partial (E_d \Delta\varepsilon)}{\partial D} \frac{\partial D}{\partial \Delta\varepsilon} \quad (5.34)$$

Re-arranging Eq.5.34 gives:

$$\frac{\partial \Delta\boldsymbol{\sigma}}{\partial \Delta\boldsymbol{\varepsilon}} = \left(\frac{\partial E_d}{\partial D}\right) \Delta\varepsilon \left(\frac{\partial D}{\partial \Delta\varepsilon}\right) \quad (5.35)$$

where $\frac{\partial E_d}{\partial D}$ is the partial derivative of the damaged stiffness matrix (E_d) with respect to the damage scale (D) and $\frac{\partial D}{\partial \Delta\varepsilon}$ is the partial derivative of the damage scale relative to strain increment.

These two terms are obtained as follows:

1. Calculate partial derivative of the damaged stiffness matrix (Eq. 5.30) with respect to damage scales ($\partial E_d/\partial D$) giving for D_x for example:

$$\frac{\partial E_d}{\partial D_x} = \begin{bmatrix} (-1)(1-v)c & (-1)(1-Dy)vc & (-1)vc & 0 \\ (-1)(1-Dy)vc & 0 & (0 & 0 \\ (-1)vc & 0 & 0 & 0 \\ 0 & 0 & 0 & (-1)(1-Dy)G \end{bmatrix} \quad (5.36)$$

2. Calculate partial derivative of damage scale with respect to strain($\partial D/\partial \varepsilon$).

Therefore the partial derivative of damage scale D (Eq. 5.19) relative to strain in the x direction ε_x , for example, would be

$$\frac{\partial D_x}{\partial \varepsilon_x} = \frac{(\varepsilon_f * \varepsilon_x * (\varepsilon_f - \varepsilon_0) - (\varepsilon_f - \varepsilon_0) * (\varepsilon_x - \varepsilon_0) * \varepsilon_f)}{(\varepsilon_x * (\varepsilon_f - \varepsilon_0))^2} \quad (5.37)$$

The increment to the damaged stiffness ΔE_d is then given by Eq. 5.34 above. The Jacobian is therefore updated as:

$$J = E_d + \Delta E_d \quad (5.38)$$

However, as mentioned in chapter 3, material models exhibiting softening behaviour and stiffness degradation often lead to severe convergence difficulties in implicit analysis. A common technique to overcome some of these convergence difficulties is the use of a viscous regularization of the constitutive equations, which causes the consistent tangent stiffness of the softening material to become positive for sufficiently small time increments (Δt). Therefore, in order to introduce viscous regularisation, the increment to the damaged stiffness is adjusted using a viscosity parameter η as follows:

$$\Delta E_d = \frac{\Delta t}{(\Delta t + \eta)} \quad (5.39)$$

Using viscous regularization with a small value (compared to the characteristic time increment) for the viscosity parameter η usually helps improve the rate of convergence of the model in the softening regime, without compromising results (ABAQUS, 2013) .

5.7 Model verification

Verification of the model was carried out by simulating the three point bending tests carried out on notched specimens as described in the previous chapter. Model predictions of the load deflection response were compared to test data presented in chapter 4. For comparison with model prediction, average test data was used.

5.7.1 Problem description

First the developed model was used to simulate a 50x100x350 notched UHPFRC specimen with 4% fibre content under three point bending. A simply supported test arrangement was adopted as shown in Fig.5.7.

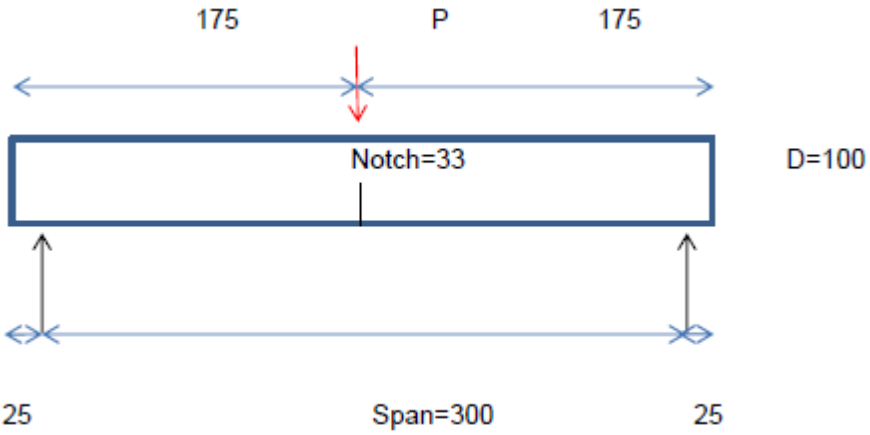

Figure 5.7: Load arrangement geometry

5.7.2 Modelling techniques

- **Meshing**

For 2D analysis ABAQUS guide recommends using either plane strain elements with incompatibility or plane stress elements with reduced integration for bending (ABAQUS, 2013). In this section plane strain elements with incompatibility (CPE4I) were adopted as a starting point with mesh consisting of 1114 elements (Fig.5.8).

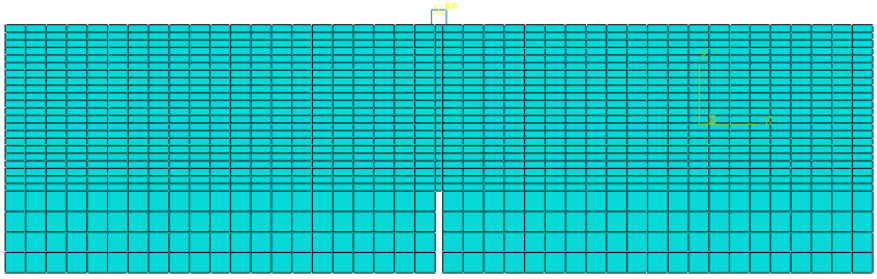

Figure 5.8: Un-deformed mesh

- **Load and boundary conditions**

Direct application of a point load can cause convergence difficulties due to stress singularities. Two techniques available in ABAQUS were considered in deciding the one to adopt in applying point loads namely the multiple point constraints (mpc) and use of rigid bodies. Use of multiple point constraints (mpc) was observed to need much higher viscous regularisation to achieve convergence but at the expense of accuracy. Hence an analytical rigid body was adopted (Fig.5.8) as it was found to produce much quicker convergence with better accuracy using only minimal regularisation. However, the size of the rigid block relative to element size was important to minimise sticking or penetration errors. The point load was applied at the top centre point of the rigid body designated as the reference point (RP) and implemented by a displacement boundary condition. The bottom of the rigid body and the top of the beam were designated as the master and slave contact surfaces respectively. Tangential contact behaviour was adopted with friction as the interaction property initially setting the friction coefficient at 0.1.

- **Convergence aids**

As mentioned previously, viscous regularisation is needed with material models exhibiting softening behaviour and stiffness degradation to overcome severe convergence difficulties in implicit analysis programs. Only a small value of the viscosity parameter η is necessary to help improve the rate of convergence of the model in the softening phase without compromising results. Hence initially the value of the viscosity parameter η was adopted as 0.001.

- **Non-linear analysis**

As explained in section 5.6 a numerical approach is needed to solve non-linear FE equations. One of the commonly used numerical methods available in ABAQUS is the Newton-Raphson approach the basics of which were highlighted previously and which was also adopted in this simulation.

5.7.3 Results

An image of the deformed shape of the model prediction is shown below (Fig.5.9) alongside that of the actual specimen (Fig.5.10).

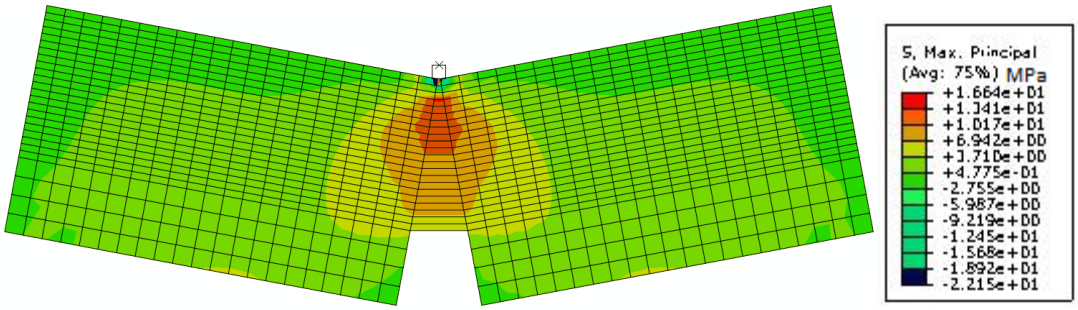

Figure 5.9: Deformed shape with stress state

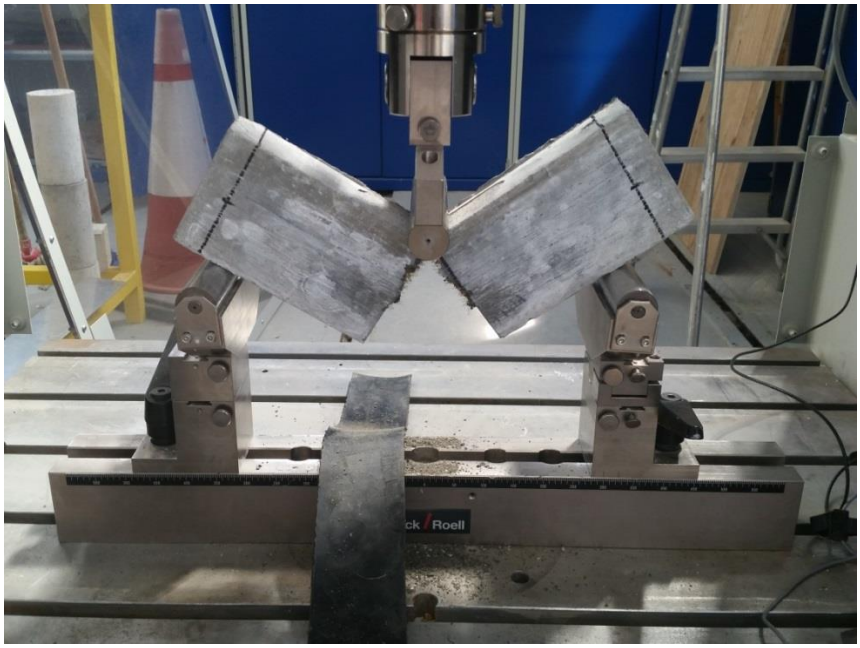

Figure 5.10 : Testing of specimen 4S4B4 to failure

The bilinear traction-separation law adopted in the model generally predicted the shape of the Load-deflection curve well (Fig.5.11). The model predicted only the average behaviour of the UHPFRC beam specimens. It did not indicate scatter which could only be considered by adopting probabilistic approaches such as that by Behloul (1996). Neither did it capture variations due to the material's inherent heterogeneity. In relation to the average test, however, the model predicted the peak load to within less than 1% (Table 5.2).

Similarly, model prediction of the material's toughness represented as the area under the curve up to a deflection of 1/150 of span (JSCE-SF4) was just over 1% of the test average.

The slope of the linear elastic phase was mainly influenced by the prescribed elastic modulus. As was mentioned previously, this linearity was only approximate due to inherent variations within the cement paste. The end of linearity in the flexural response (load deflection curve) coincided with the maximum tensile stress in the bilinear traction-separation curve. After this point, softening started in the tensile stress. However, due to the high fracture energy of UHPFRC, the flexural load/stress did not drop immediately but continued to rise though at an increasingly slower rate. This decreasing rate of rise of the flexural load continued until at one point the rate became zero. This point at which the slope of the load-deflection curve was zero corresponded to the attainment of the peak load. Therefore the model was able to simulate deflection hardening quite close to the UHPFRC mix considered. This was despite the fact that the traction separation curve did not incorporate strain hardening. The reason for this was that the material's fracture energy was high enough to delay the onset of softening in flexure despite a softening in the tensile stress thereby enabling an increase in bending load carrying capacity (Fig. 5.11). This was in line with the material's ability to display deflection hardening even with little or no strain hardening capacity as discussed in chapter 2. This ability was related to a critical fibre volume required to produce hardening behaviour. The critical fibre volume required for deflection hardening was described to be much less onerous than that required for strain hardening. Thereafter, the slope of the flexural response became negative and the load decreased with increasing deflection.

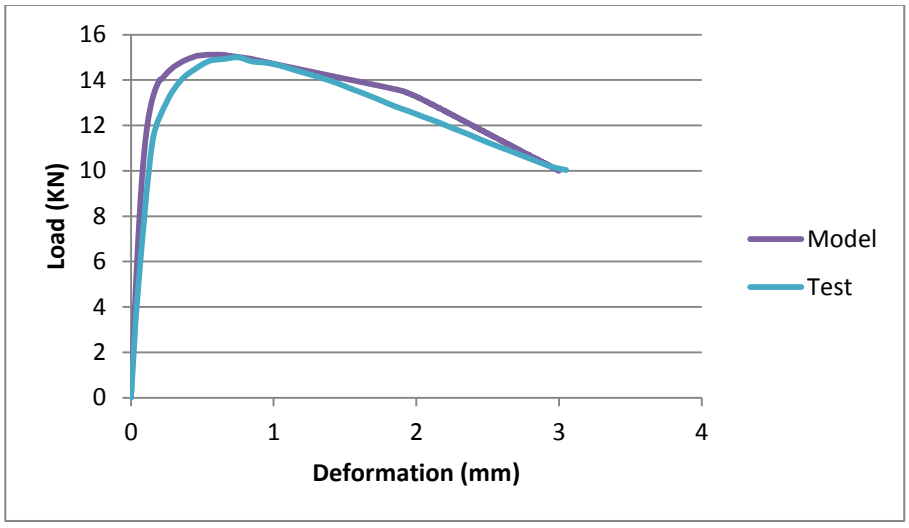

Figure 5.11: Comparison of model and test load-deflection curve for 100x100x350 specimen

Table 5.2: Comparison of model and test average leak load and toughness

	Test Average	Model	Difference (%)
Peak Load (KN)	15	15.12	0.8
Area under curve to 2mm (J)	26.7	27.9	1.2

5.7.4 Sensitivity analysis

The next step in the verification was to analyse the sensitivity of the model both to input and in-built parameters. Input parameters examined pertained to the mesh and convergence aids while in-built parameters related to the values of material properties adopted in the model.

- **Mesh sensitivity**

Three meshes with increasing number of elements (Fig. 5.12) were used in simulation and the resulting load-deflection response is presented in Fig. 5.13 and Table 5.3. They show that the mesh density had little effect on the results.

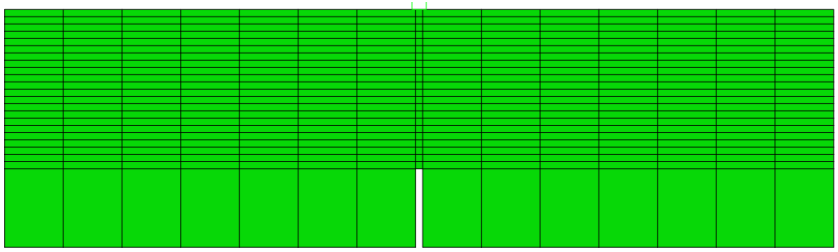

Mesh 1 (384 elements)

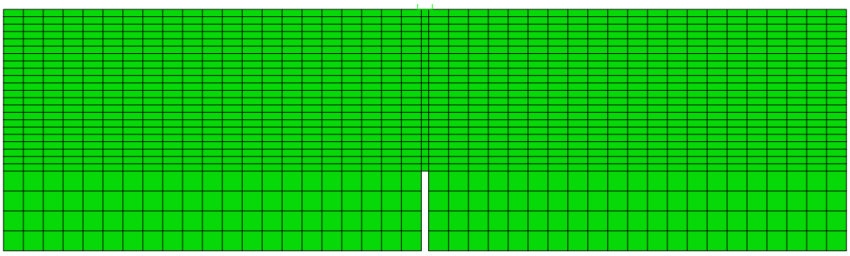

Mesh 2(1114 elements)

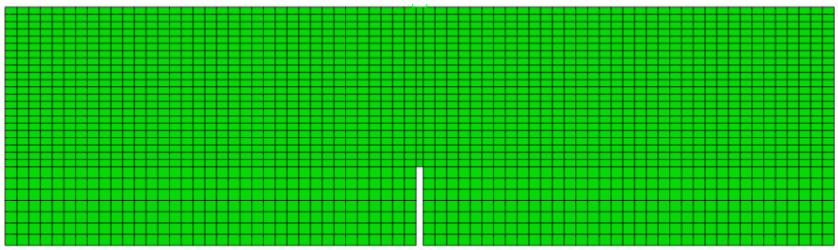

Mesh 3 (2052 elements)

Figure 5.12: Mesh sensitivity study cases

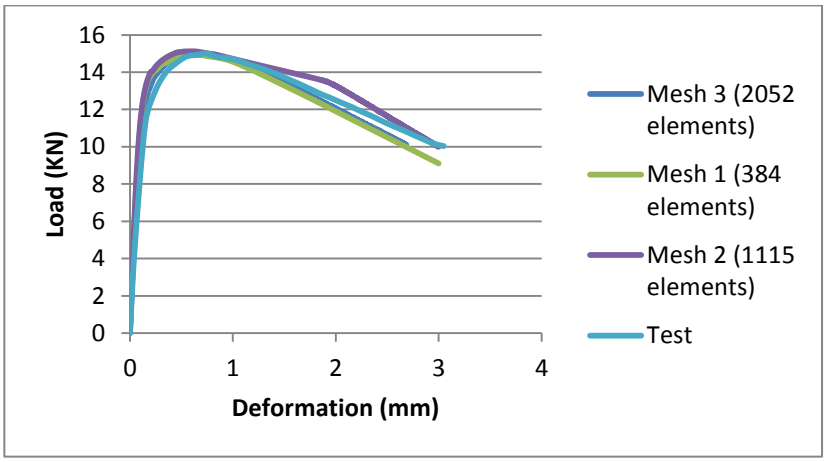

Figure 5.13: Mesh sensitivity study

Table 5.3: Mesh sensitivity on peak load and flexural toughness

Mesh	No. of elements	Peak Load (kN)	Difference with test (%)
1	384	14.94	0.4
2	1115	15.12	0.8
3	2052	14.93	0.4

- **Convergence aids**

The influence of convergence aids was assessed by comparing the energy dissipated by viscous regularisation for the whole model (designated as ALLVD in ABAQUS history output) with the total internal energy of the whole model (ALLIE) (Fig. 5.14). It showed that very little viscous energy was dissipated thereby confirming that the influence of this convergence aid on the results was negligible.

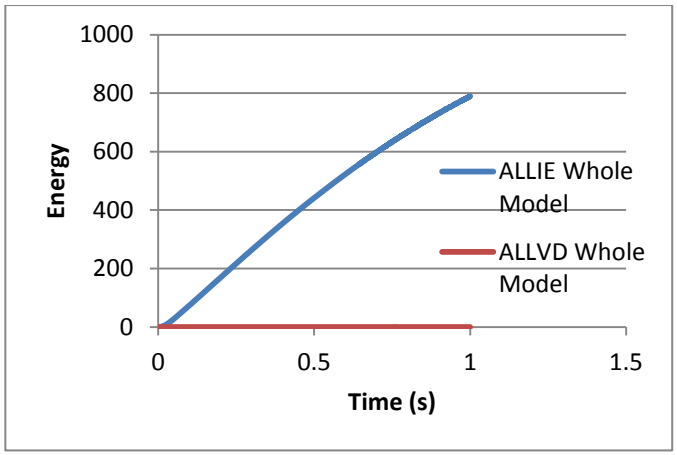

Figure 5.14: Effect of convergence aids

- **Parametric study within scatter zone**

As is typical of UHPFRC, the experimental data showed significant scatter. The material properties, however, were calculated from average values. The scatter in the material properties arising from all the batches with 4% fibre content are presented in the table 5.4 below and provided the range of values employed in the sensitivity study.

Table 5.4: Input values for parametric study

	E1	E2	σ_t1	σ_t2	G_f1	G_f2
Elastic Modulus, E	**43.2**	**46.7**	44.66	44.66	44.66	44.66
Tensile Strength, σ_t	11.18	11.18	**10.3**	**12.3**	11.18	11.18
Fracture Energy, G_f	38.5	38.5	38.5	38.5	**29.1**	**39.3**

As can be seen in Fig. 5.15, varying the elastic modulus within the zone had little noticeable effect on the slope of the linear elastic phase of the load-deflection curve. The peak load was dependent on both the tensile strength and fracture energy. As shown in the sensitivity study, tensile strength had the biggest influence on the peak load prediction mainly by increasing the linear elastic phase (Fig.5.16). As described above, the fracture energy if high enough can also increase the peak load by introducing deflection hardening. As expected a decrease in the fracture energy made the post peak slope steeper and the material less ductile (Fig.5.17). While increasing the tensile strength tended to make the post peak curve steeper (i.e. reduces the ductility), the counteracting flattening influence on the curve from increasing the fracture energy was more dominant. The response of the model here also matched the material behaviour in which higher fracture energy required more work in de-bonding and pulling out the fibres from the matrix to cause softening.

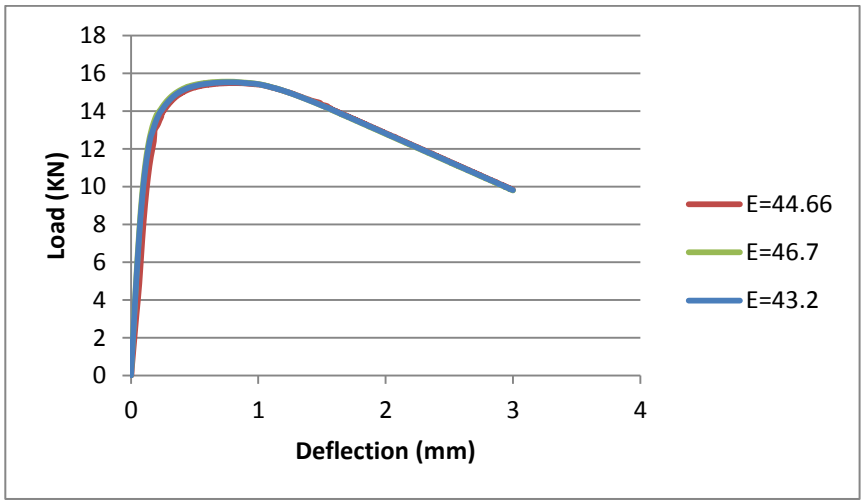

Figure 5.15: Variation in elastic modulus

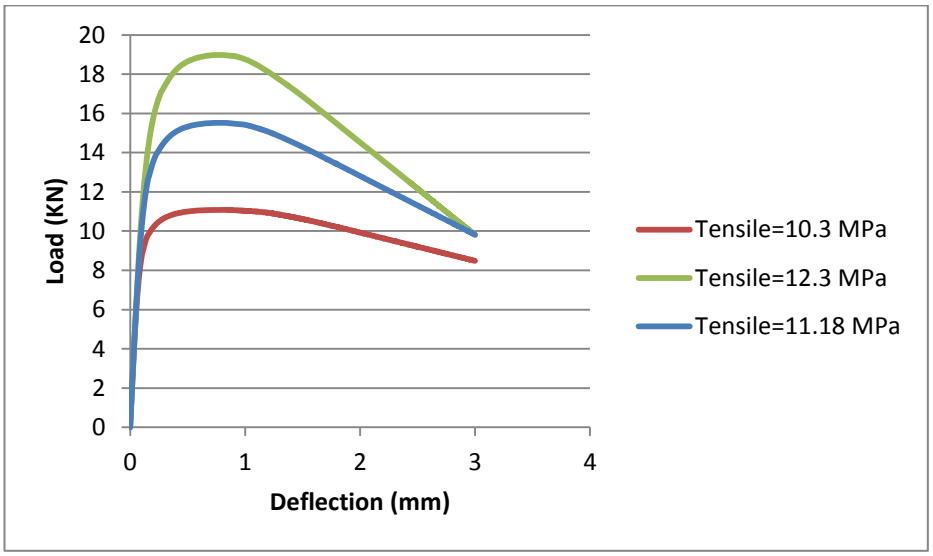

Figure 5.16: Variation in tensile strength

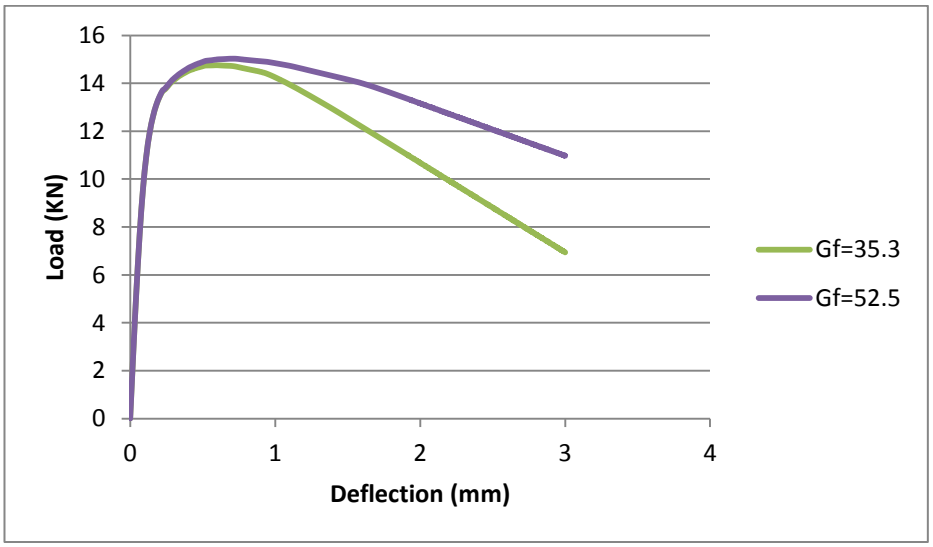

Figure 5.17: Variation in fracture energy

5.7.5 Further verification

In the previous section, a specimen of size 50x100x350 with 4% fibre content was used in the first stage of verification. The verification was then extended to the rest of the fibre contents tested (2% and 6%) and to 50x100x550 specimens (fig 5.18). In chapter 5 it was observed that these two middle sized specimens were least affected by gravitational bias of the fibres which occurred mostly in the largest and smallest specimens following the sequence in which they were cast.

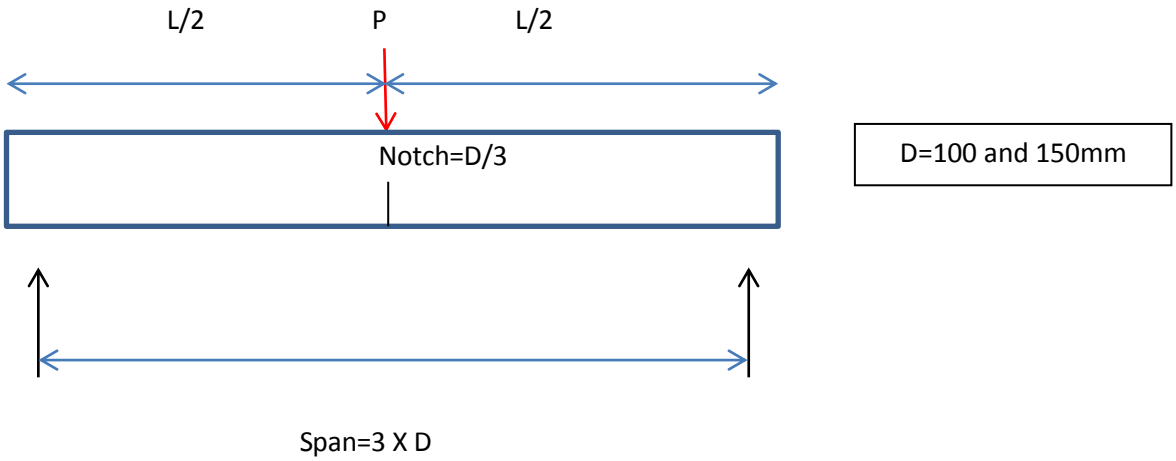

Figure 5.18: Load and support geometry

- **Simulation techniques**

The type of elements, non-linear solution technique and convergence aids adopted in this stage of verification were similar to those of the first stage and are summarised in Table 5. 5. The number of elements used for each specimen was selected based on an element size in the middle range of that used in the mesh sensitivity study. These are presented in Table 5.6. As in the previous section, the load was applied using an analytical rigid body.

Table 5.5: Some simulation parameters

Type of elements	Plane strain incompatible elements (CPE4i)
Non-linear solution	Newton-Raphson
Convergence aids	Viscous regularisation (0.001); Automatic stabilisation

Table 5.6: No. of elements

Specimen	**No. of elements**
100x50x350	1114
150x50x550	2607

- **Results**

A summary of the model predictions of the load deflection curves for all these notched three point bending test specimens is presented in Figs. 5.19 and 5.20. In terms of slope of the elastic phase, the peak load and the area under the curve, model predictions of the middle range of sizes were very good for all the fibre contents (Table 5.7). As observed in section 5.7.4, these three parameters were directly influenced by the elastic modulus (E),

tensile strength (σ_t) and fracture energy (G_f) respectively. These material properties were made functions of fibre content based on test data and inbuilt into the model's traction separation law. The ability of the model to accurately predict the elastic phase, peak and post peak phases across the range of fibre contents therefore also verified that the effect of fibre content adopted was appropriate.

Table 5.7: Model predictions of peak load and flexural toughness compared to test

			Peak Load (KN)			Toughness (J)		
Fibre Content (%)	**Size**	**Depth (mm)**	**Test Average**	**Model**	**Difference (%)**	**Test Average**	**Model**	**Difference (%)**
2	S3	150	13.10	13.09	-0.07	33.27	34.22	2.86
	S4	100	8.92	9.92	11.17	15.42	18.78	21.79
4	S3	150	20.13	19.92	-1.06	52.39	52.04	-0.67
	S4	100	15.16	15.12	-0.27	26.74	27.90	4.34
6	S3	150	22.59	21.52	-4.74	56.15	56.80	1.16
	S4	100	17.91	16.34	-8.77	31.70	29.78	-6.06

However, disparities between test data and model predictions were observed for very small and for very large specimens (fig 5.21). These disparities were explained in chapter 4 as a consequence of the gravitational bias of the fibres during production and the sequence of casting which started from the largest going down the sizes to the smallest specimens. The general effect of these factors was for the larger specimens which were cast first to have fewer fibres which settled to the bottom resulting in the smallest sizes having proportionally more fibres.

The peak load disparities observed in very small specimens could also possibly be explained by the 'surface layer or skin' effect where fibres close to the formed surface of the specimen tend to be aligned parallel to the formwork surface. This resulted in a surface layer (skin) that was stronger than the middle of the specimen where the fibres were randomly oriented. This skin or surface layer made up a bigger proportion of the smaller specimens in which its effect was more noticeable.

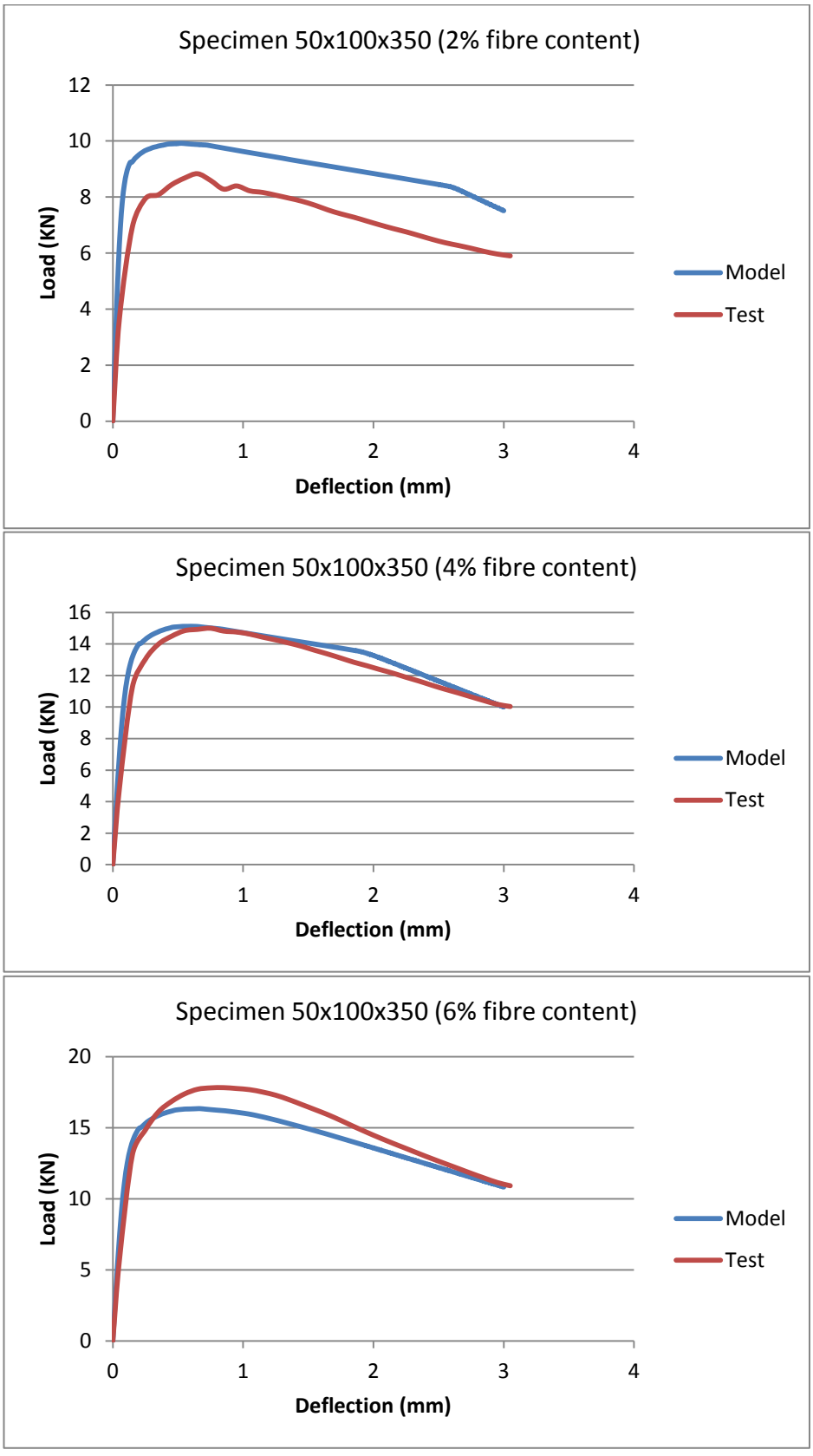

Figure 5.19: Model prediction of load deflection curves for 100mm deep specimens with 2%, 4% and 6% fibre content

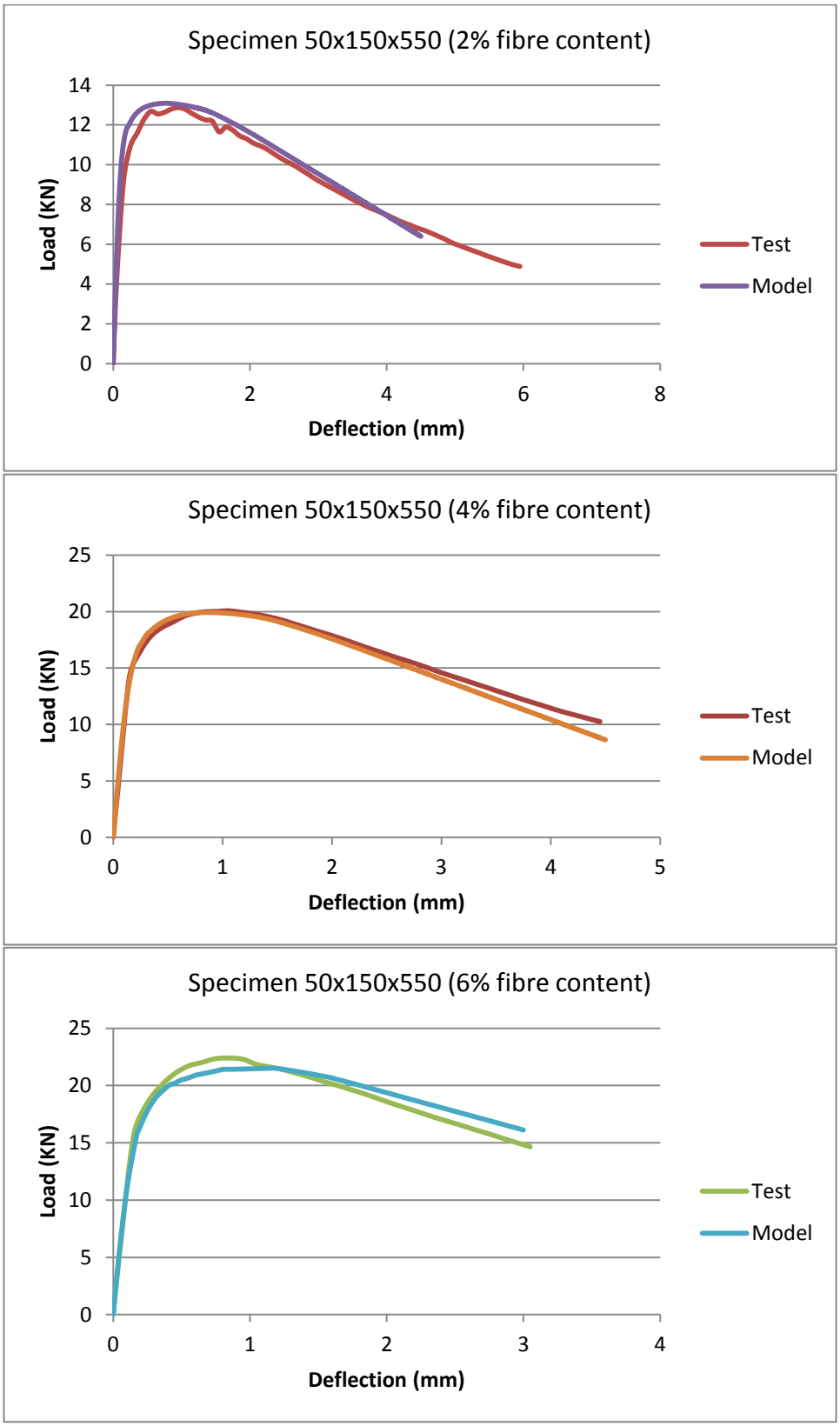

Figure 5.20: Model prediction of load deflection curves for 150mm deep specimens with 2%, 4% and 6% fibre content

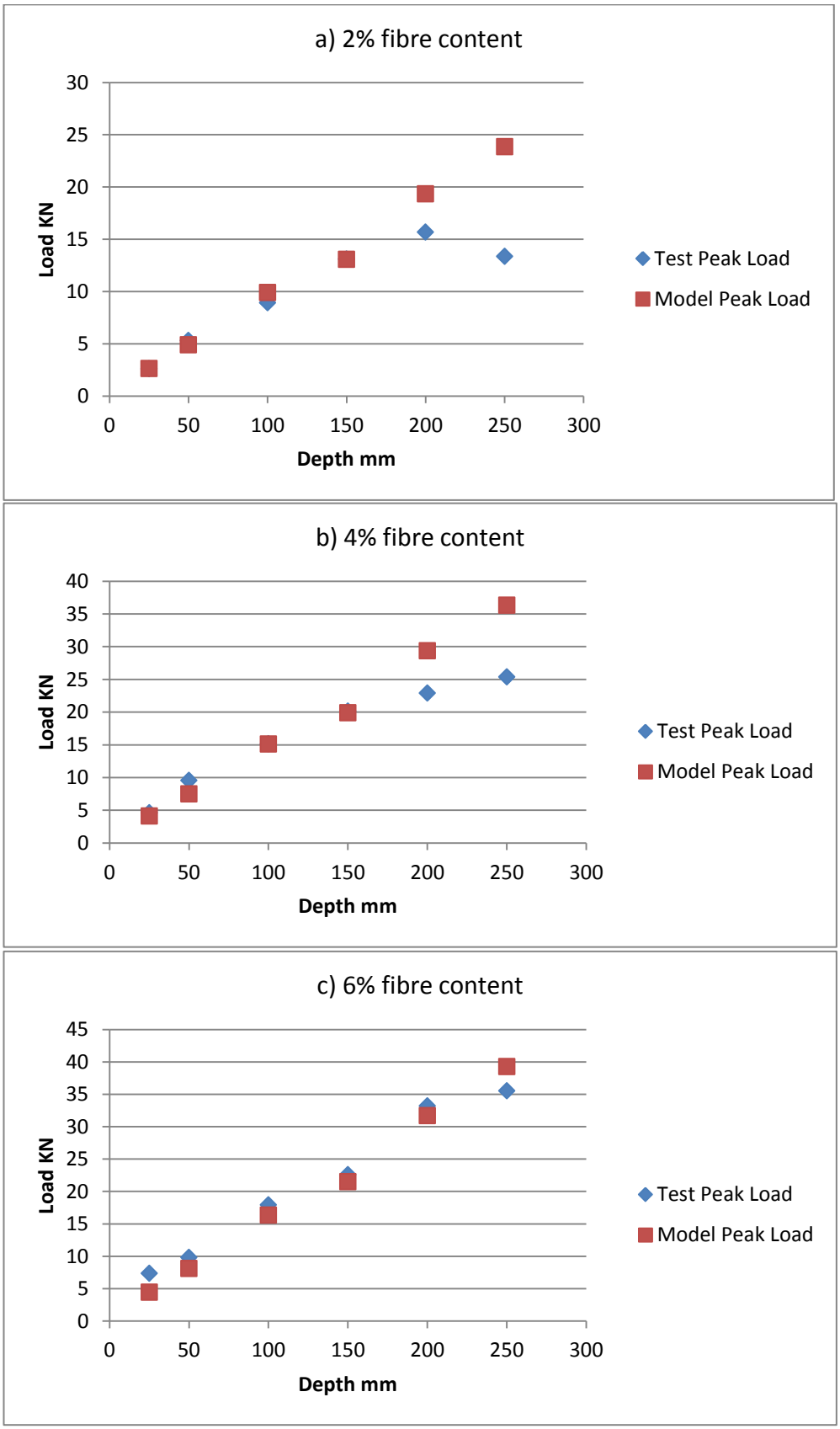

Figure 5.21: Comparison of model prediction of peak load with test for a) 2% fibre content b) 4% fibre content c) 6% fibre content

5.8 Model validation

5.8.1 CASE STUDY 1

The work of Mahmud et al. (2013) involving experimental and numerical studies of size effect of UHPFRC beams was used as the first case study to validate the model. This work was chosen for validation because they tested a range of notched specimen sizes in three point bending. Notched specimens varying in depth from 30mm-150mm (Fig. 5.22) were prepared from a UHPFRC mix shown in Table 5.8 below. While the water/binder content was similar for both mixes, some cement was replaced by Ground Granulated Blast Furnace Slag (GGBFS) in the mix used in the case study. Due to the relatively high cement content in UHPFRC mixes, some research has been carried to replace part of it with industrial waste products such as GGBFS in order to enhance their sustainability (Barnett et al. (2007a); Oner and Akyuz (2007)). The use of these cement replacements at the levels adopted in their studies has been found to have no significant effect on final strength. Displacement controlled TPB tests were then carried out in a study of the size effects on the flexural strength of UHPFRC. In addition to the test data, the study also presented results of test simulations using the concrete damaged plasticity (CDP) model in ABAQUS with the following material property inputs:

Mean Tensile Strength, σ_t = 9MPa; mean Compressive Strength, σ_c = 150MPa and mean elastic modulus, E = 45GPa. The traction-separation curve in Fig. 5.23 obtained from a direct tensile test was also used.

Table 5.8: UHPFRC mix proportions (Mahmoud et al, 2013)

Mix content	**Kg/m^3**
Cement	657
Ground Granulated Blast Furnace Slag (GGBFS)	418
Microsilica (Silica fume)	119
Silica sand	1051
Superplasticiser	40
Water	185
Steel fibres (2%)	157
Total	2627

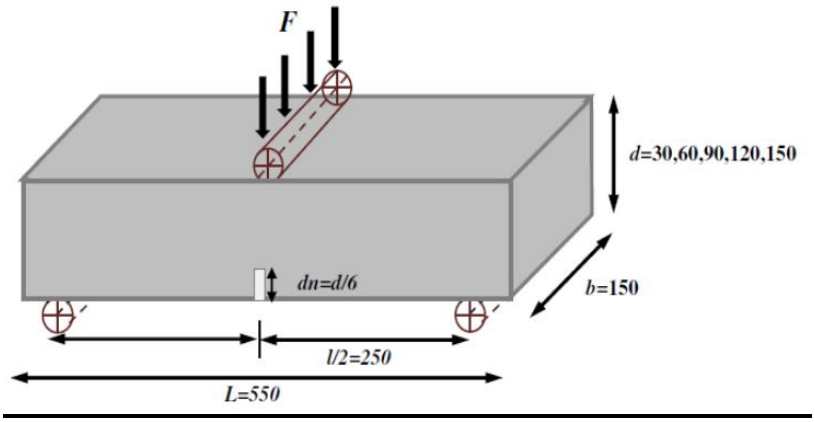

Figure 5.22: Load and support arrangement (Mahmoud et al, 2013)

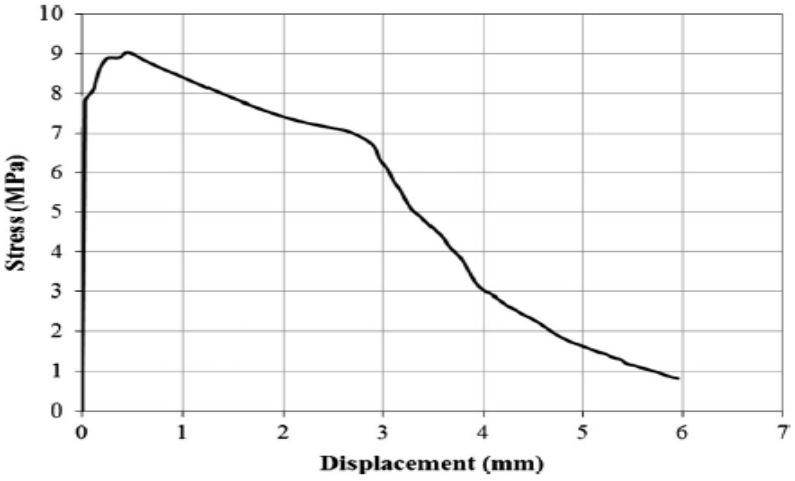

Figure 5.23: Traction separation curve from tensile test (Mahmoud et al, 2013)

- **Simulation techniques**

The geometry and load arrangement of the above work are simulated according to Fig. 5.24 with the load application via the rigid blocks as discussed previously in the verification. The type of element, numerical solution technique and convergence aids adopted are presented in Table 5.9 and the number of elements in Table 5.10. A typical mesh used in the simulation is also shown in Fig.5.25.

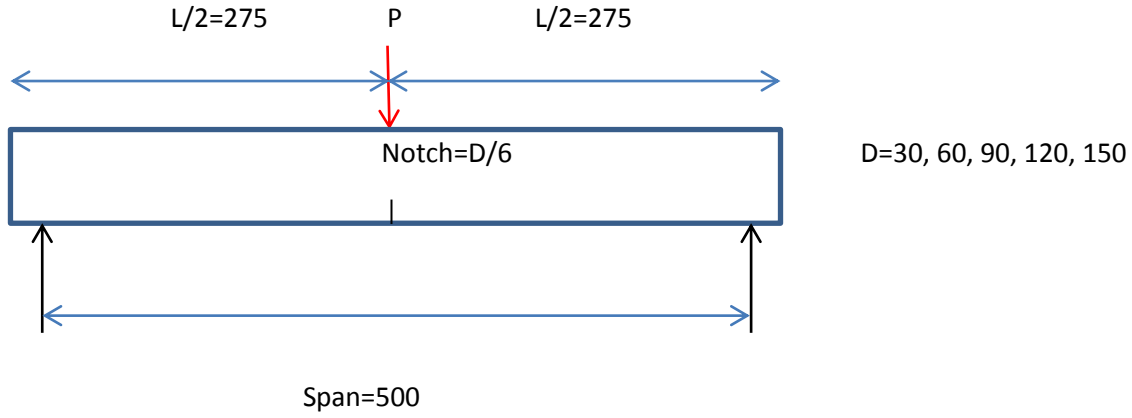

Figure 5.24: Load and support arrangement

Table 5.9: Some simulation parameters

Type of elements	Plane strain incompatible elements (CPE4i)
Non-linear solver	Newton-Raphson
Convergence aids	Viscous regularisation (0.001); Automatic stabilisation

Table 5.10: Number of elements

Specimen	**No. of elements**
30x150x550	1221
60x150x550	2330
90x150x550	3328
120x150x550	4326
150x150x550	5435

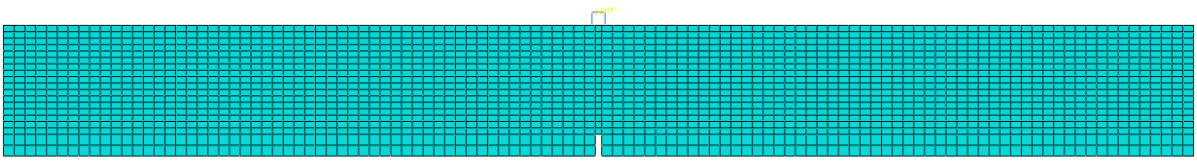

Figure 5.25: Typical un-deformed mesh diagram

- **Results**

Fig.5.26 shows a typical deformed shape from one of the specimens simulated and the flexural response for all the specimens is shown in Fig.5.27. Mahmud et al (2013) used measurements of crack mouth opening displacement (CMOD) instead of specimen deflection in their study.

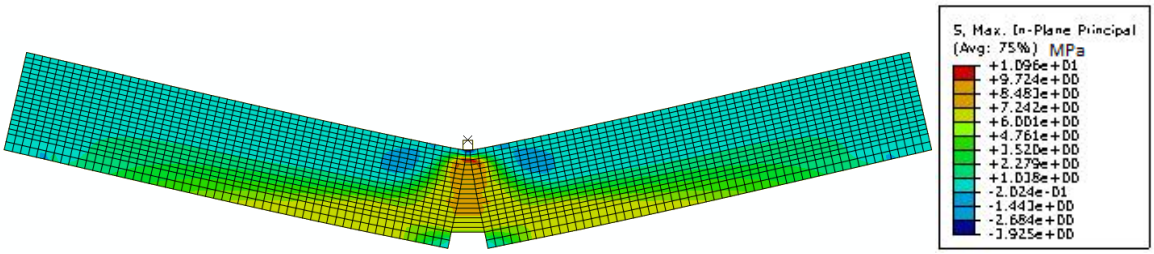

Figure 5.26: Typical deformed shape with stress state

UDMF model predictions of the load-CMOD curves are compared in Table 5.11 with test data and that of the CDP model by Mahmud et al. (2013). Apart from the smallest specimen (depth=30), the shapes of the load deflection curves predicted by the model matched reasonably well those from both the test data and the CDP model. In their study they noted that for the smallest specimen (d=30) the test pre-load of 2KN was quite close in magnitude to the specimen load capacity (as observed by its peak load in Table 5.11) making test values less accurate. For the rest of the specimens (depths 60-150) UDMF slightly under-predicted the slope of the initial curve compared to both test and CDP model (Fig.5.27). In UDMF the initial pre-damage phase was assumed to be linearly elastic so that its prediction of slope was mainly governed by the elastic modulus adopted. Therefore the lower elastic modulus adopted in UDMF (43.3GPa) compared to their CDP model (45GPa) could account for some of the under prediction of the slope.

UDMF also slightly over-predicted the point at the end of linearity resulting in a longer linear elastic phase compared to test. While CDP uses a crack detection surface based on plasticity, UDMF on the other hand adopts a much simpler damage initiation criteria based on the quadratic function of strain ratios (Eq. 5.13). Given the relative simplicity of the damage initiation criteria, UDMF prediction test was reasonable. Generally, UDMF predicted the peak load to within +10% of test value (Table 5.11). Peak load as was noted in section 5.7.4 was most sensitive to tensile strength.

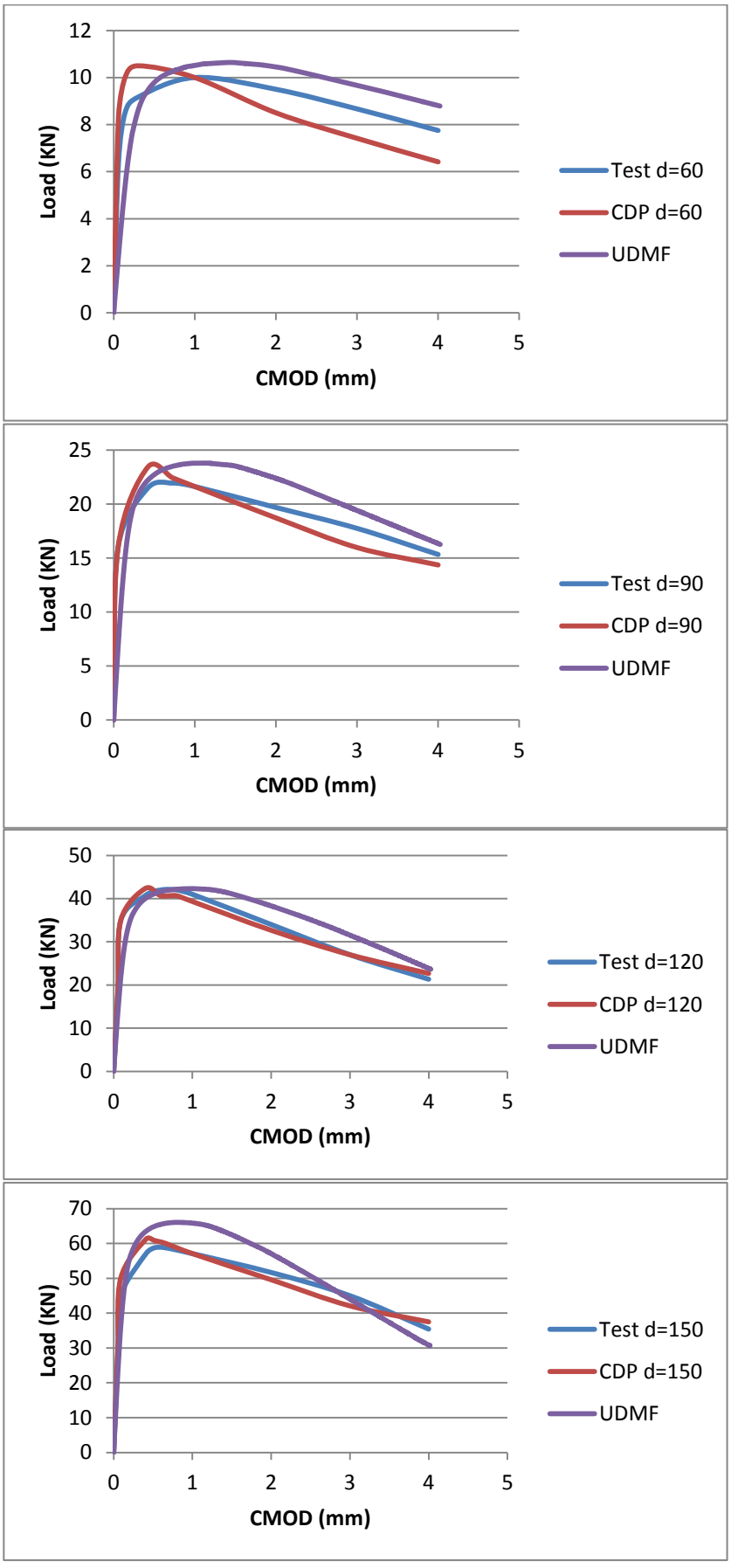

Figure 5.27: Model prediction compared to test and CDP

However fracture energy also had some influence though to a lesser extent. Once failure was initiated, the fibre bridging action responsible for the high fracture energy in UHPFRC also increased flexural load capacity by enabling load transfer in cracked zones. Hence while the end of linearity corresponded to the maximum stress (σ_{max}) in Fig.5.3, the peak load occurred at a point on the softening phase of the traction separation curve. The traction separation curve input by Mahmud et al (2013) however showed a small strain hardening (Fig.5.23). They adopted for their CDP model the ultimate strength (9MPa) which was higher than that used in UDMF (7.8MPa).

The post peak response was again evaluated based on the area under the load-deflection curve up to a deflection equal to 1/150 of span in accordance to the Japanese standard (JSCE-SF4). These are also presented in Table 5.11. UDMF again over-predicted the post peak response but to within 10 % of test. UDMF predictions of peak load and toughness also generally matched CDP's (Fig.5.28 &5.29) despite the small differences in the input values compared in Table 5.12.

Table 5.11: Model predictions of peak load and flexural toughness compared to test data

	Peak Load (KN)					Toughness (J)				
Depth (mm)	**Test**	**CDP**	**Difference (%)**	**UDMF**	**Difference (%)**	**Test**	**CDP**	**Difference (%)**	**UDMF**	**Difference (%)**
30	3.17	2.81	-11.36	2.73	-13.82	9.28	8.53	-8.08	9.84	6.03
60	10.13	10.52	3.85	10.64	5.03	35.95	33.92	-5.65	38.63	7.45
90	22.03	23.07	4.72	23.79	7.97	75.77	73.34	-3.21	82.77	9.24
120	40.73	40.23	-1.23	42.31	3.88	130.33	128.55	-1.37	141.07	8.24
150	60.13	61.75	2.69	66.06	9.86	195.70	194.08	-0.83	209.03	6.81

The bilinear traction separation curve adopted in UDMF was compared to that used by Mahmud et al (2013) in figure 5.30. The tensile strength of 9MPa used by the latter is based on the ultimate stress after strain hardening. It is worth noting that the stress at the end of linearity from their traction-separation curve is quite close to the tensile strength adopted in UDMF at 2% fibre content (7.8 MPa).

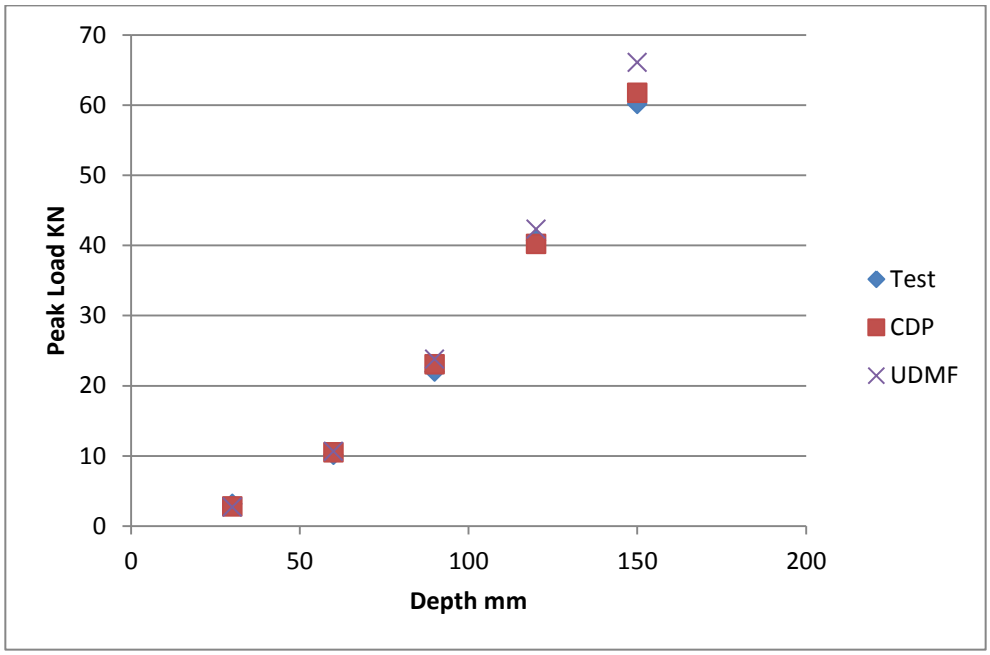

Figure 5.28: Peak load against specimen size

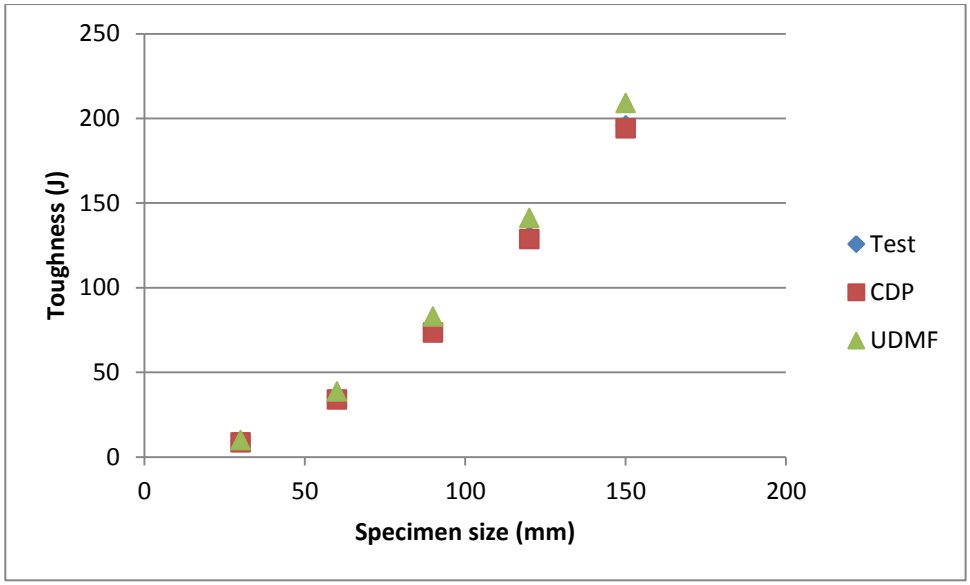

Figure 5.29: Toughness against specimen size

Table 5.12: Input parameters for cohesive modelling compared to CDP's

	UDMF	CDP used by Mahmud et al
Tensile strength	7.8 MPa	9MPa
Elastic Modulus	43GPa	45GPa
Type of elements	Plane strain incompatible elements (CPE4I)	Plane stress (CPS4)
Non-linear solver	Newton-Raphson	RIKS

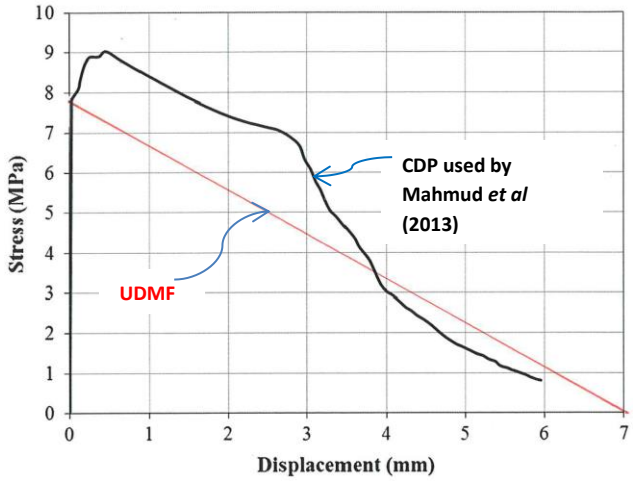

Figure 5.30: Traction separation response of UDMF compared to CDP

UHPFRC's tensile response can be defined by either by the value at end of linearity (or 1st cracking) or at the maximum value after strain hardening. While the former indicates the tensile strength of the matrix, the maximum tensile strength provides an indication of the largest uniaxial stress that can be applied to the UHPFRC prior to the initiation of fibre pull-out (Graybeal and Baby, 2013). Design guidance of UHPFRC currently is based on estimation of the tensile strength of the matrix (AFGC-SETRA, 2013). Therefore as further validation, cohesive elements in ABAQUS were employed in simulating the same specimens in order to assess the most the appropriate tensile strength between 7.8 and 9MPa to be used for modelling. Fracture energy of 32 KJ/m^2 was used based on the area under the traction separation curve in Fig. 5.23 while the elastic modulus E remained 45GPa as used by Mahmud et al (2013). Plane strain incompatible elements were used in the bulk of the model. Newton-Raphson solution technique was used with viscous a regularisation value of 0.001. Predictions by the model using cohesive elements compared to that of other models and to test data are presented in Fig. 5.31. It can be seen that simulation with cohesive elements using a tensile strength of 7.8MPa corresponding to the end of linearity predicted the peak load closer to test than that using the ultimate tensile strength (9MPa). This suggests that when a bilinear traction separation law is used with a fracture energy approach then tensile strength based on the matrix strength as recommended by AFGC-SETRA (2013) seems most appropriate. However, CDP even with tensile strength of 9MPa generally predicted a lower peak load than both CE and UDMF. This may be because damaged plasticity assumes that some of the deformations are not recovered on unloading. This is illustrated in Fig.5.32 comparing two cases with the same damaged stiffness one with unrecoverable deformation and the other without. For a bilinear traction separation curve, the maximum stress corresponds to the end of the linear elastic phase of the flexural load deflection response.

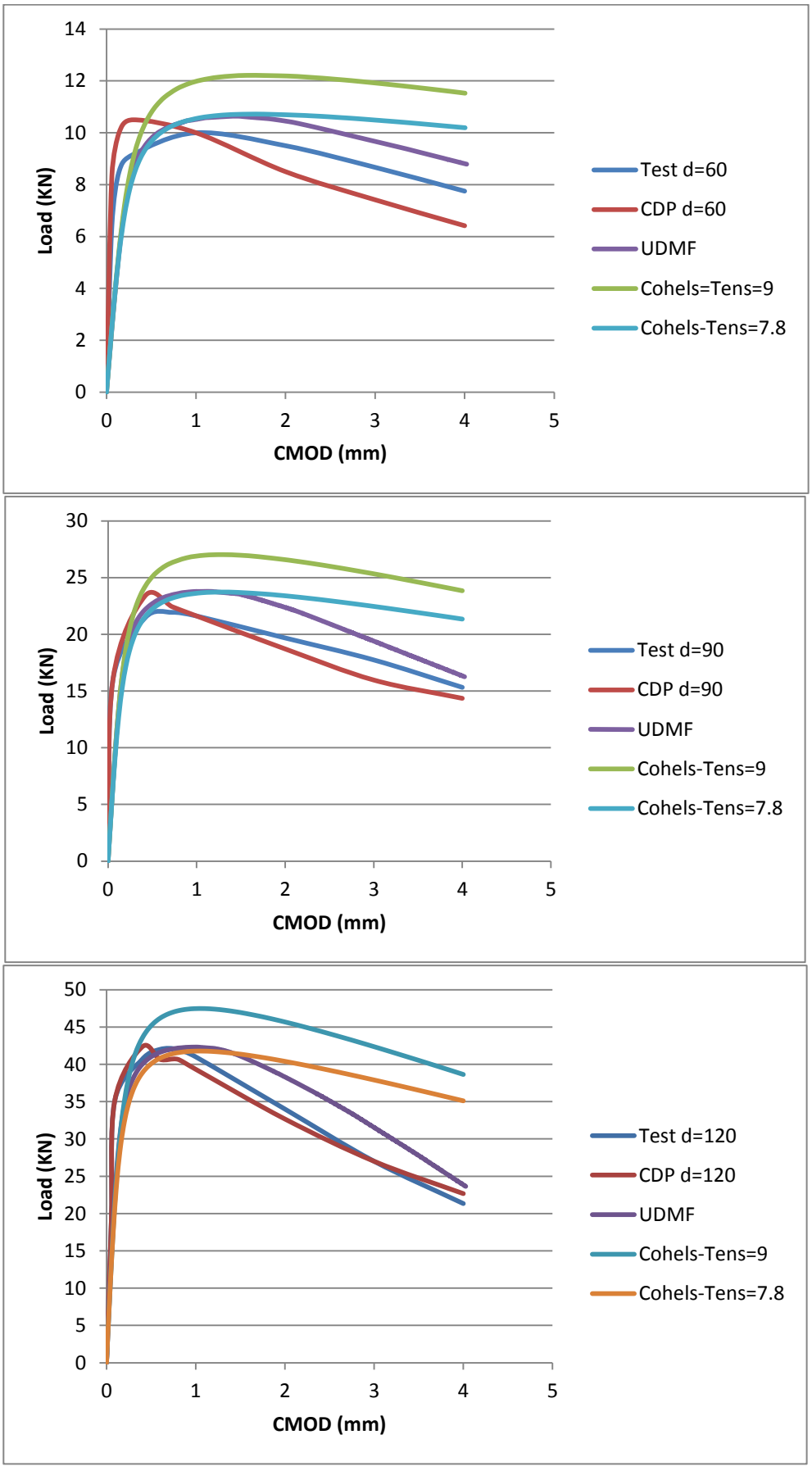

Figure 5.31: Comparison of predictions by different models with test

The load carrying capacity beyond this point however, is dependent on the material's ductility. The absence of suitable mechanisms to sustain higher loads after the onset of damage would result in a brittle failure typical of materials with low fracture energy. In UHPFRC however, fibre bridging action enables the transfer of loads even in cracked zones resulting in the ability to sustain increased load be it at an ever decreasing rate. This is the hardening phase characterised by multiple cracking. At a point along the softening curve this multi-cracking capacity is exhausted and this is the point corresponding to the peak flexural load. It can be seen that at this point the case with unrecoverable deformation results in a lower stress than the one without. So while damaged plasticity may be justified where there is cyclic loading, in concrete under normal loading damaged elasticity as used in UDMF model is observed to be more representative of concrete behaviour (Lemaître and Chaboche, 1994). Therefore the simulation by Mahmud et al (2013) using the CDP model had to adopt a higher tensile strength of 9MPa in order to predict values close to the test data.

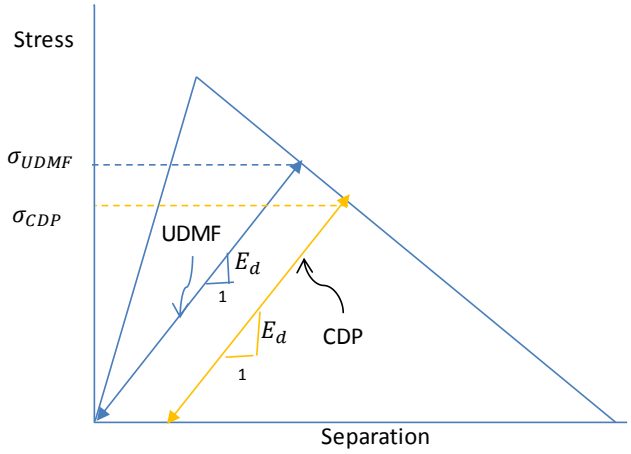

Figure 5.32: Comparing stress at peak load between UDMF and CDP

However, even with a tensile strength value of 7.8MPa, simulation with cohesive elements over predicted the post peak response (Fig.5.31). Cohesive elements were implemented within the cohesive crack framework such that the traction-separation law was only applied within a crack path known *a priori*. UDMF on the other hand was implemented within the crack band framework whereby the model was applied to the whole specimen. Hence individual cracks were not tracked but were 'smeared' over the elements in which they occurred in the specimen. Hence while damage was limited to the cohesive elements, in UDMF damage was 'smeared' over more elements potentially resulting in more energy loss post peak compared to that from only cohesive elements. This could be the reason for the prediction of a lower post peak response by UDMF which was more representative of UHPFRC.

5.8.2 CASE STUDY 2

Data from tests carried out by Le (2008) in relation to the effect of fibre content on flexural strength of UHPFRC beams was selected for the next stage of validation thereby enabling an assessment of the suitability of the fibre content effect adopted in the model. In addition this data provided an opportunity to validate the model's ability to simulate four point bending (FPB) tests carried out on un-notched specimens. In the above mentioned study fibre content was varied between 1% and 3.5% and its effect on flexural strength measured. The UHPFRC mix used by Le (2008) was very similar to that adopted in chapter 4 (Table 5.13).

Table 5.13: UHPFRC mix proportions

	1% fibre content	2% fibre content	3.5% fibre content
Cement	955	955	955
Silica fume	239	239	239
Total binder	**1194**	**1194**	**1194**
Silica sand	1051	1051	1051
Superplasticiser	51.8	51.8	51.8
Water	212.6	212.6	212.6
Steel fibres	78.5	157	274.5

In their study, 100x100x350 specimens were cast by placing the fresh mix at one end of the mould and allowed to flow to the other end. The specimens were subjected to post-set heat treatment at 90^0C. The un-notched specimens were then subjected to displacement controlled four point bending (FPB) tests (Fig. 5.33).

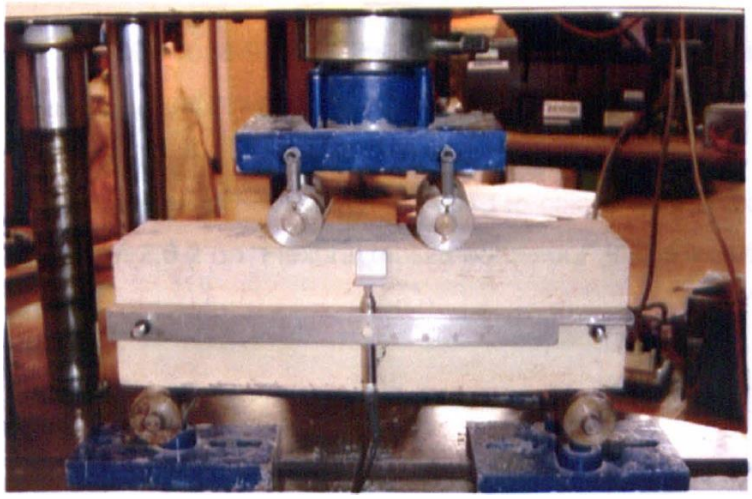

Figure 5.33: Four point bending test arrangement (Le, 2008)

- **Simulation techniques**

The geometry and load arrangement of the above work were simulated according to Fig. 5.34. A simply supported system was assumed for the boundary conditions. The load was also applied using a displacement boundary condition. The type of element, numerical solution technique and convergence aids adopted were similar to those used in model verification (section 5.7). These are summarised in Table 5.14. A typical mesh used in the simulation is also shown in Fig.5.35 consisting of 224 elements.

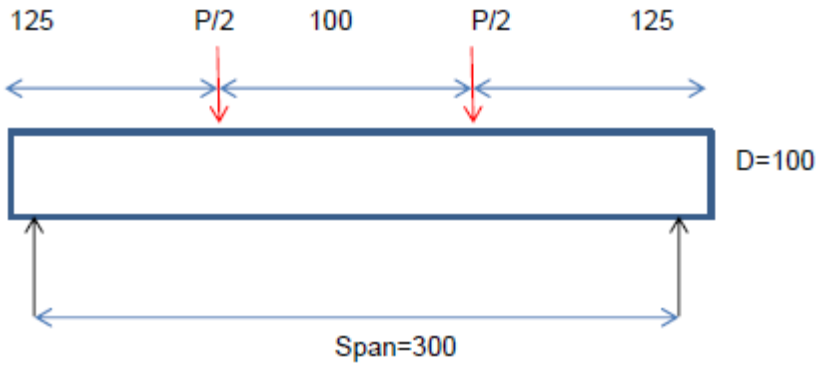

Figure 5.34: Load and support arrangement

Table 5.14: Some simulation parameters

Type of elements	Plane strain incompatible elements (CPE4i)
No. of elements	224
Non-linear solver	Newton-Raphson
Convergence aids	Viscous regularisation (0.001); Automatic stabilisation

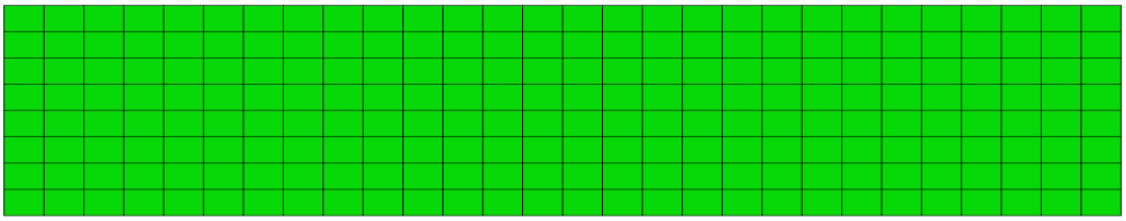

Figure 5.35: Typical un-deformed mesh diagram

- **Results**

A typical model deformed shape and stress contours from one of the specimens simulated is shown in Fig. 5.36. Unlike the three point bending test, the four point bending test produces pure bending within the middle third and does not introduce a shear stress in the middle. Also unlike a notched specimen where a high stress concentration forces a crack from the notch tip, multiple cracks could occur within the middle third of the un-notched specimen. However, most often a dominant crack occurs with minor cracks branching off it (Fig.4.30). There were no photos of these failed specimens available for comparison but the high compressive stress at the supports seen in the deformed shape (Fig. 5.36) could cause local deformation and crushing similar to that see in Fig.4.30.

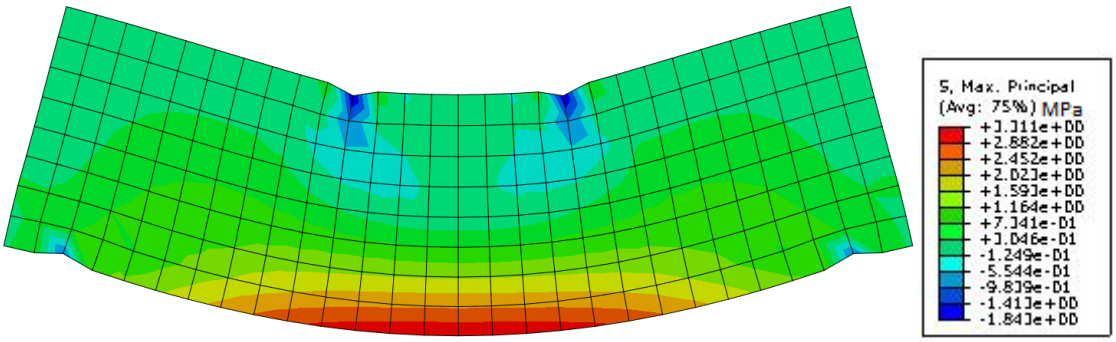

Figure 5.36: Typical deformed mesh with stress state

The model predicted the load deflection response very well when compared with the test curves in Fig. 5.37. A fibre content effect was incorporated into the model's traction-separation curve by making the elastic modulus (E), tensile strength (σ_t), and fracture energy (G_f) its function. As observed in the parametric study in section 5.7.4, these three properties were most influential in the elastic, peak and post peak phases respectively of the flexural response. Therefore, in order to assess the specific performance of the fibre content effect, the model's prediction was compared against test data in the elastic, peak, and post peak phases across all fibre contents.

For all the fibre contents, the model predictions of the initial linear elastic phase compared very well with the test data. It can be clearly seen in Fig. 5.36 that the model's prediction of the slope of the elastic phase was virtually indistinguishable to that of the test in all the fibre contents considered. Similarly, the model prediction of the end of the linear elastic phase was excellent for all the fibre contents. While Le (2008) did not provide any tensile strength estimates, the accurate model prediction of the point at the end of linearity suggests that the tensile strength values adopted in the model were very close to that of the material.

The model's predictions of the peak load and flexural toughness are presented in Table 5.15 for all the fibre contents. The material's deflection hardening phase was also predicted well by the model with the predicted peak loads being within 7% or less of the test value for all the fibre contents considered. As was shown by the sensitivity study in section 5.7.4 peak loads predictions by the model were mainly influenced by the value of tensile strength adopted. Model flexural strength values plotted against fibre content also compared very well with test values in Fig. 5.38. The flexural strength increased with fibre content almost linearly and in conformity with the rule of mixtures similar to the test results described in chapter 4. The model was able to predict flexural strength across fibre contents. As in the previous examples, the post peak response was compared based on the area under the load deflection curve up to a deflection equal to 1/150 of the span (Table 5.15). Similarly the model flexural toughness values calculated up to a deflection of 2mm (JSCE-SF4) were within 15% of the test values. That the model predictions closely matched test values in the elastic, peak and post peak phases confirmed that the effect of fibre content incorporated in the model was appropriate for this class of UHPFRC.

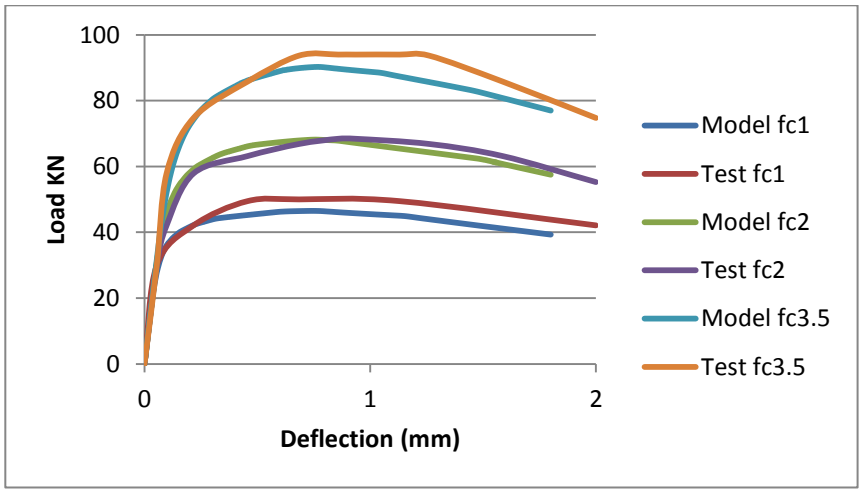

Figure 5.37: UDMF predictions compared to test for different fibre contents (fc)

Table 5.15: : Model prediction of peak load and flexural toughness compared to test

	Peak Load (KN)			Toughness (J)		
Fibre content (%)	Test	Model	Difference (%)	Test	Model	Difference (%)
1	50.00	46.50	-7.00	90.98	76.64	-15.76
2	68.42	68.17	-0.37	122.35	110.94	-9.33
3.5	94.00	90.26	-3.98	166.85	145.24	-12.95

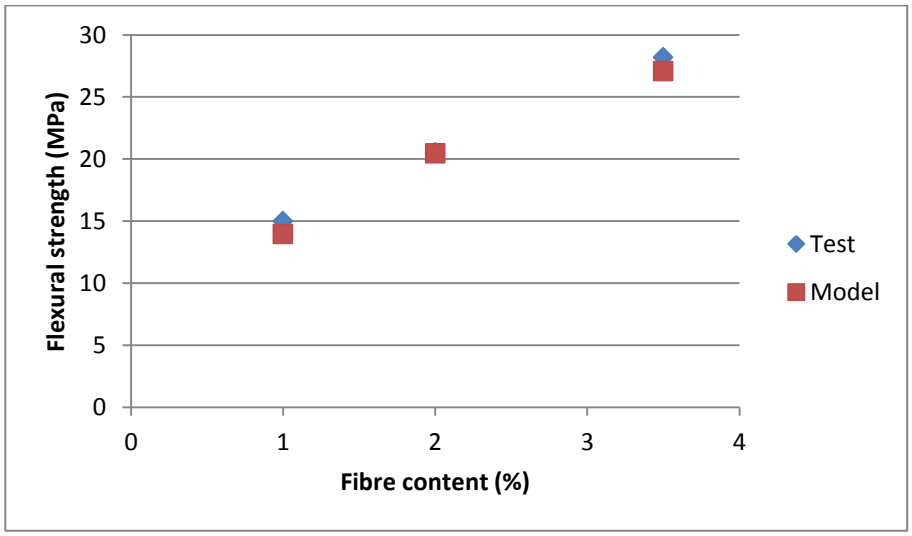

Figure 5.38: Model prediction of fibre content effect on flexural strength compared to test

Chapter 6 – Conclusions

6.1 Overview

This study has presented a UHPFRC damage model incorporating fibre content (UDMF) thereby achieving its main aim. The objectives identified in the introduction as necessary to deliver this overall aim were grouped into three phases which also reflected the chronological order in which they were addressed namely:

- Initial simulation study
- Experimental investigations
- UHPFRC model development

In the following sections, a summary of the findings from each of these phases is presented in relation to each objective. These findings are the basis for the subsequent outlining of the study's contribution to knowledge and recommendations for future work.

6.2 Initial simulation study

A bilinear $\sigma - w$ curve was adopted in the initial simulation requiring the input of values of elastic modulus (E), tensile strength (σ_t) and fracture energy (G_f). Values of E estimated from compression tests, σ_t from un-notched FPB tests and G_f from notched TPB test were found to be reasonably close to those from literature. Based on their subsequent use in initial simulation, these values of material properties were observed to be appropriate for modelling the flexural behaviour of UHPFRC thereby also justifying the adoption of the bilinear $\sigma - w$ curve. In order to identify a suitable modelling approach to be used as a basis for developing a UHPFRC model, the cohesive crack model (CCM), crack band model and damage models were considered within the framework proposed by Elices and Planas (1989). ABAQUS cohesive elements, ABAQUS concrete smeared crack model (CSM) and ABAQUS concrete damaged plasticity model (CDP) were selected and investigated as representative of each the three categories respectively from the above mentioned framework. A comparison of these three modelling approaches found that they predicted equivalent load deflection curves that closely matched the test data. Therefore, in addition to its ability to make accurate predictions, the smeared crack approach was identified as suitable for modelling UHPFRC due to the relative ease of implementing it within the finite element method. However, it was proposed that implementing it with viscous regularisation, for example could minimise convergence difficulties associated with strain softening models.

6.3 Experimental investigations

The study of size effect in UHPFRC was identified in the literature review as one of the areas in which there was limited research. With the aid of CCM, an initial study of geometrically similar UHPFRC specimens with 2% fibre content had indicated a small

geometrical size effect on the flexural strength (Awinda et al., 2016). However, a more detailed study was necessary in order to establish the existence of size effect more conclusively. Therefore a comprehensive experimental investigation was carried out to study size effects in UHPFRC specimens taking into account a wider range of geometrically similar specimens. The size effect investigation was extended to cover the entire load deflection response namely pre-peak, peak and post peak phases. The flexural stress at the end of linearity, flexural strength and fracture energy respectively were adopted to represent these three phases. In addition UHPFRC specimens with fibre contents of 2%, 4% and 6% were investigated. An evaluation of the size effects based on the framework proposed by Bažant and Planas (1998) found that the flexural stress at the end of linearity was subject to small to medium size effects. The size effect in the flexural strength of notched TPB test specimens was medium while that in un-notched specimens was inconclusive due to the large scatter in the data.

The large scatter in UHPFRC test data has been cited as the reason in several studies for invalidating the existence of size effects in the material. In this study also a large scatter in the test data was observed. However, even by allowing for the large scatter in the data, the trend indicating size effects was still evident. Yoo et al. (2016) found the same trend but suggested that it may have been due to the different fibre distribution characteristics within the specimens. However, the tests they used in their further study to verify their suggestion were limited in both the range of sizes and fibre contents adopted. While fibre distribution may indeed be an influencing factor in size effect studies, the varying strength of the fibre-matrix bond within the ITZ is also a possible reason for the differences in findings from different studies. These observations identify a need for more research at the mesoscale and microscale to provide more insight on the phenomena that seem to cause the size effects in some studies but not in others.

The flexural stress at the end of linearity was also observed to be prone to less scatter than flexural strength a fact attributed to the relatively bigger influence of fibres on the latter whereas the former is mainly influenced by the matrix strength. This is the rationale for its adoption in estimating the tensile strength in standards such as AFGC-SETRA (2013). Such standards also recommend the use of this value of stress obtained from un-notched FPB test specimens. The value of tensile strength obtained from un-notched FPB test specimens was confirmed in this study to be lower than that from both un-notched and notched TPB test specimens. This was attributed to the pure bending stresses in FPB test specimens different from those in the TPB test which also introduced shearing stresses in the middle of the specimens. The absence of a notch further enabled failure within specimens to occur in the weakest region rather than being forced to originate from a notch tip. This is more desirable as it is more representative of real life structures.

Experimental investigation of the effect of fibre content on flexural stresses at the end of linearity and at peak indicated their conformity to the rule of mixtures.

Fracture energy (G_f) estimated from only the area under the full load deflection curve was found to be size dependent at 4% fibre content, an observation that others have attributed to energy loss from spurious sources (Bažant and Planas, 1998). When the effect of specimen weight was taken into account as proposed by Petersson (1981), the scatter in the fracture energy values was noticeably reduced. However, size effect on fracture energy was not completely eliminated. As mentioned in 3.5.3, because of the difficulties in defining the location of a propagating crack, in practice G_f is estimated by measuring the total energy consumed from crack initiation to complete propagation through a specimen. Fracture energy is then calculated by assuming that the crack occurs vertically upwards within the crack ligament. However, even for the case of notched specimens under the TPB test where the crack propagated roughly in a vertical direction from the notch tip, the crack path was observed to be tortuous. Therefore the G_f values obtained by the above calculations would most likely have been on the higher side as the straight and vertical crack area assumed was probably lower than the actual area of the tortuous crack. Fibre content was also found to be a major influence on the elastic modulus, tensile strength and fracture energy.

6.4 UHPFRC damage model incorporating fibre content (UDMF).

Insights into the role of fibre content on the failure mechanisms within UHPFRC (as discussed in chapter 2) and observations of their influence on material properties at the macro level provided a justification for incorporating fibre content into the UHPFRC model. Values of elastic modulus (E), tensile strength (σ_t) and fracture energy (G_f) were estimated by applying the methods recommended in the initial simulation study (Chapter 3) to the test data from chapter 4. Expressions defining the effect of fibre content on the three material properties were then incorporated into a bilinear $\sigma - w$ curve with stiffness degradation following the approach developed by Chen (2014). Hence the values of elastic modulus (E), tensile strength (σ_t) and fracture energy (G_f) were now a function of fibre content. In doing this, the damage also varied according to fibre content.

UDMF adopted a smeared crack approach in that individual cracks were not tracked. Following observations from the initial simulation study in chapter 3, a capacity for viscous regularisation was built in to aid convergence. The model was implemented as a UMAT in ABAQUS using a FORTRAN code. The model was verified by simulating the TPB tests on notched specimens from chapter 4. Predictions of the model load deflection response matched the test data reasonably well for all the fibre contents (2%, 4% and 6%). Model predictions of both peak load and toughness were generally within 10% of test data.

The model was found to be most sensitive to variations in tensile strength relative to that in fracture energy and elastic modulus. A sensitivity analysis also found the model to be generally insensitive to mesh density. The energy dissipated by viscous regularisation was also negligible compared to the total energy in the model.

The ability of the model to simulate UHPFRC notched test specimens of different sizes subject to three point bending was validated using the work of Mahmud et al (2012). The model's prediction of the load deflection curves matched the test curves reasonably well. The model predicted the peak load and toughness to within 10% of the test values. In the case study, Mahmud et al (2012) adopted a $\sigma - w$ curve idealised from a direct tensile test which had a small strain hardening. In their work, the ultimate tensile stress rather than the stress at end of linearity was adopted as the tensile strength. They used this information within the CDP model in ABAQUS to simulate the tests. However, design standards such as AFGC-SETRA (2013) base their estimates of tensile strength on the stress at the end of linearity. Therefore as part of UDMF's validation it was compared to the above CDP modelling work. With the help of additional modelling work using cohesive elements, it was concluded that the tensile strength corresponding to the stress at end of linearity was more appropriate for use in a model with a bilinear $\sigma - w$ curve.

The suitability of the effect of fibre content adopted in UDMF was validated using the work of Le (2008). Un-notched FPB UHPFRC test specimens with fibre contents ranging from 1% - 3.5% were simulated and compared to test data from the above mentioned work. The modelling predictions of the load deflection curves were excellent for all the fibre contents thus validating the effect of fibre content as adopted in UDMF. In addition, the model's ability to simulate un-notched specimens under the four point bending test arrangement was validated.

6.5 Contributions

The main contributions of this study are highlighted as follows:

a) A validated UHPFRC damage model incorporating fibre content to accurately simulate the flexural response of un-notched and notched test specimens of different sizes and fibre contents, and to predict their failure loads.

b) Establishment of the existence and evaluation of size effects on the flexural stress at linearity and flexural strength of geometrically similar UHPFRC specimens with 2%, 4% and 6% fibre content. This contributes to the limited studies available of size effects on UHPFRC.

c) Estimates of values of elastic modulus (E), tensile strength (σ_t) and fracture energy (G_f) at 2%, 4% and 6% fibre content from standard tests which have been confirmed as

appropriate inputs for modelling UHPFRC using a bilinear $\sigma - w$ curve. UHPFRC being still a relatively new material whose adoption is still limited, this is an important contribution in making more test data available in literature for further research and development of modelling tools.

d) Comparison of the cohesive crack model using cohesive elements (CCM), ABAQUS concrete smeared crack model (CSM) and ABAQUS concrete damaged plasticity (CDP) model in simulating the flexural response of UHPFRC. Lessons learnt have been documented based on the experience of employing the above models and these will be useful for similar studies in future.

6.6 Recommendations for future work

Some of the findings of this study have highlighted the important role of mechanisms at the mesoscale and microscale on the flexural behaviour of UHPFRC at the macroscale. Examples include the large scatter observed in UHPFRC's test data, and crack tortuosity which can be mainly explained by matrix heterogeneity and variability in fibre distribution and orientation. A means of measuring these aspects of UHPFRC can provide more insight into the underlying phenomena. For example a recent study based on a multiscale modelling framework combined mesoscale measurements of UHPFRC specimens by μ-XCT with FEM to estimate reasonably accurate values of the material's elastic modulus (Qsymah et al., 2017). Another study has dealt with the heterogeneity of UHPFRC by coupling different models suited to different constituents of UHPFRC (Zhang et al., 2018). In the above mentioned work, the CDP model was adopted for the concrete matrix and the cohesive crack model for the ITZ. Fibre orientation was also modelled by an innovative technique that could generate many meshes with randomly oriented two-noded beam elements representing fibres. This approach was used successfully to simulate the direct tensile test, and both notched and un-notched three-point bending beam tests.

In this study, qualitative descriptions of crack patterns provided insights into some observations making it possible to link the low failure loads in some specimens to the poor fibre distribution along crack paths. The poor fibre distribution in some batches was attributed to gravitational bias typical of UHPFRC mixes. However, this study did not measure any mesoscale or microscale parameters but mainly relied on theoretical understanding of UHPFRCs internal structure to explain observations and measurements at the macro-scale. In line with the multiscale framework cited above, the varying fibre content within a batch or specimen can be measured using a method like μ-XCT. This measure can then be incorporated into the model as a fibre content scale that can be used to study the effect of fibre content and distribution on its flexural behaviour. In the same way a mesoscale measure of fibre orientation could be incorporated into the model in future. Microscale and mesoscale measurements of fibre distribution, orientation and

bond strength could also be used in future studies to explain the phenomena underlying the size effects observed in some UHPFRC mixes and not in others.

A bilinear traction separation ($\sigma - w$) curve adopted in this work was able to simulate the flexural behaviour of UHPFRC reasonably well. In future refinements to the traction-separation curve could be made either by:

- Introducing a non-linear elastic phase in the traction-separation curve to model a bigger strain hardening.
- Determining traction separation curves from tensile test or inverse analysis of flexural tests.

References

Aarup, B., 2004. CRC -A Specimen Fibre Reinforced High Performance Concrete, International Symposium: Advances in Concrete through Science and Engineering Illinois, USA.

ABAQUS, 2013. ABQUS Documentation. Simulia, Providence, RI, USA.

Abdalla, H.M., Karihaloo, B.L., 2003. Determination of size-independent specific fracture energy of concrete from three-point bend and wedge splitting tests. Mag. Concr. Res., 55(2): 133-141.

Acker, P., Behloul, M., 2004. Ductal Technology. A Large Spectrum of Properties, A Wide Range of Applications, Ultra High Performance Concrete, Kassel, Germany, pp. 13-23.

Adeline, R., Behloul, M., 1996. High ductile beams without passive reinforcement. In: De Larrard, F., Lacroix, R. (Eds.), Fourth International Symposium on Utilization of High-Strength/High-performance Concrete, Paris, France, pp. 1383-1390.

AFGC-SETRA, 2013. Ultra High Performance Fibre-Reinforced Concretes Recommendations, SETRA, Bagneux, France.

AFGC, 2013. Documents Scientifiques et Techniques: Recommadations. , Association Francaise De Genie Civil Paris.

Aitcin, P.-C., 1998. High-performance concrete. E&FN Spon, London.

Astley, R.J., 1992. Finite elements in solids and structures: an introduction. Chapman & Hall, London.

Awinda, K., Chen, J., Barnett, S.J., 2016. Investigating geometrical size effect on the flexural strength of the ultra high performance fibre reinforced concrete using the cohesive crack model. Construction and Building Materials, 105: 123-131.

Bache, H.H., 1981. Densified Cement/ Ultra-Fine Particle Based Materials., 2nd International Conference on Superplasticisers in Concrete, Ottawa, Canada.

Barnett, S.J., Lataste, J.-F., Parry, T., Millard, S.G., Soutsos, M.N., 2010. Assessment of fibre orientation in ultra high performance fibre reinforced concrete and its effect on flexural strength. Materials and Structures 43: 1009–1023.

Barnett, S.J., Millard, S.G., Soutsos, M.N., Schleyer, G.K., Tyas, A., 2007a. Flexural Performance of UHPFRC PROTECT2007: Structures under Extreme Loading, Whistler, BC, Canada, pp. 99.

Barnett, S.J. et al., 2007b. Ultra high performance fibre reinforced concrete for explosion resistant structures. In: Russell, M.I., Basheer, P.A.M. (Eds.), Concrete Platform. Queen's University of Belfast, Belfast, UK, pp. 565-573.

Bažant, Z.P., 1998. Size effect in tensile and compression fracture of concrete structures: computational modeling and design. In: Mihashi, H., Rokugo, K. (Eds.), Fracture Mechanics of Concrete Structures (FraMCoS-3). Fracture Mechanics of Concrete Structures Aedificatio, Gifu, Japan, pp. 1905-1922.

Bažant, Z.P., 2002. Concrete fracture models: testing and practice. Engineering Fracture Mechanics, 69(2): 165-205.

Bažant, Z.P., Kazemi, M.T., 1990. Determination of fracture energy, process zone length and brittleness number from sixe effect, with application to rock and concrete. International Journal of Fracture, 44(2): 111-131.

Bažant, Z.P., Oh, B.H., 1983. Crack band theory for fracture of concrete. Materials and Structures, 16: 23.

Bažant, Z.P., Planas, J., 1998. Fracture and size effect in concrete and other quasibrittle materials. CRC Press, London.

Behloul, M., 1996. Analysis and modelling of the behaviour of Ultra High Performance Fibre-Reinforced Cement Matrix Material (Reactive Powder Concretes), Paris.

Benson, S.D.P., Karihaloo, B.L., 2005. CARDIFRC-Development and mechanical properties. Part III: Uniaxial tensile response and other mechanical properties. Mag. Concr. Res., 57(8): 433-443.

Bentur, A., Mindess, S., 2007. Fibre reinforced cementitious composites. Taylor & Francis, London; New York.

Benzeggagh, M.L., Kenane, M., 1996. Measurement of Mixed-Mode Delamination Fracture Toughness of Unidirectional Glass/Epoxy Composites with Mixed-Mode Bending Apparatus. Composites Science and Technology, 56: 439–449.

Bonneau, O., Lachemi, M., Dallaire, E., Dugat, J., Aitcin, P.-C., 1997. Mechanical properties and durability of two industrial reactive powder concretes. ACI Mater J, 94(4): 286-290.

Bruhwiler, E., Denarie, E., 2008. Rehabilitation of concrete structures using ultra high performance fibre reinforced concrete. In: Fehling, E., Schmidt, M., Sturwald, S. (Eds.), Second International Symposium on Ultra High Performance Concrete, Kassel, Germany.

BSI, 2009. Testing hardened concrete. Making and curing specimens for strength tests. BSI.

Chanvillard, G., Rigaud, S., 2003. Complete characterisation of tensile properties of Ductal® UHPFRC according to the French recommendations. In: Naaman, A.E., Reinhardt, H.W. (Eds.), International Workshop High Performance Fiber Reinforced Cement Composites. RILEM Publications SARL.

Chen, J., 2014. An extended cohesive damage model with a length scale in fracture analysis of adhesively bonded joints. Engineering Fracture Mechanics, 119: 202–213.

Chen, J., Ravey, E.,Hallet, S.,Wisnom, M.,Grassi, M., 2009. Prediction of delamination in braided composite T-piece specimens. Composites Science and Technology, 69: 5.

Crisfield, M.A., 1986. Snap-through and snap-back response in concrete structures and the dangers of under-integration. International Journal for Numerical and Analytical Methods in Engineering, Volume 22(Issue 3): 751-767.

Denneman, E., Kearsley, E.P., Visser, A.T., 2012. Definition and application of a cohesive crack model allowing improved prediction of the fl exural capacity of high-performance fibre-reinforced concrete pavement materials. Journal of the South African Institution of Civil Engineering, 54(811): 11.

Denneman, E., Wu, R., Kearsley, E.P., Viser, A.T., 2011. Discrete fracture in high performance fibre reinforced concrete materials. Engineering Fracture Mechanics, 78: 11.

Dunne, F., Petrinic, N., 2005. Introduction to computational plasticity. Oxford University Press, Oxford; New York.

Duy, L.N., Dong, J.K., Gum, S.R., Kyung, T.K., 2013. Size effect on flexural behavior of ultra-high-performance hybrid fiber-reinforced concrete. Composites Part B: Engineering, 45(1): 1104-1116.

Einsfeld, R.A., Velasco, M.S.L., 2006. Fracture parameters for high-performance concrete. Cem Concr Res, 36(3): 576-583.

Elices, M., Planas, J., 1989. Material Models. In: Efgren, L. (Ed.), Fracture Mechanics of Concrete Structures - From theory to applications. Chapman and Hall, London, pp. 16-66.

Elices, M., Planas, J., 1996. Fracture mechanics parameters of concrete. Advanced Cement Based Materials, 4: 116-127.

Ellis, B.D., DiPaolo, B.P., McDowell, D.L., Zhou, M., 2014. Experimental investigation and multiscale modeling of ultra-highperformance concrete panels subject to blast loading. Int J Impact Engng, 69 95-103.

Fehling, E., Schmidt, Michael , Walraven, J., Ãhlich, S., 2015. Ultra-High Performance Concrete UHPC : Fundamentals, Design, Examples. Beton-Kalender Ser. Wilhelm Ernst & Sohn Verlag fur Architektur und Technische, Berlin, Germany.

Graybeal, B., 2007. Compressive behavior of ultra-high-performance-fiber-reinforced concrete. ACI Mater J, 104(3): 146-152.

Graybeal, B.A., 2005. Characterisation of The Behaviour of Ultra High Performance Concrete. Concrete Repair, Rehabilitation and Retrofitting Ii. University of Maryland, USA.

Graybeal, B.A., Baby, F., 2013. Development of Direct Tension Test Method for Ultra-High-Performance Fiber-Reinforced Concrete. ACI Mater J, Title no. 110-M17.

Habel, K., 2004. Structural behaviour of elements combining ultra-high performance fibre reinforced concretes (uhpfrc) and reinforced concrete, École polytechnique fédérale de lausanne, Lausanne, EPFL.

Hassan, A., Jones, S., Mahmud, G., 2012. Experimental test methods to determine the uniaxial tensile and compressive behaviour of ultra high performance fibre reinforced concrete (UHPFRC). . Construction and Building Materials: 874-882.

Hillerborg, A., 1980. Analysis of fracture by means of the fictitious crack model, particularly for fibre reinforced concrete. International Journal of cement composites, 2: 8.

Hillerborg, A., Modeer, M., Petersson, P.E., 1976. Analysis of crack formation and crack growth in concrete by means of fracture mechanics and finite elements. Cem Concr Res, 6(6): 773-781.

Ikeda, S., Tanaka, Y., Shimoyama, Y., Kobayashi, T., 2004. Innovative design and construction of a 50m span footbridge using reactive powder concrete. In: Liu, T.C. (Ed.), George C. Hoff Symposium on High-Performance Concrete and Concrete for Marine Environment. ACI, Las Vegas, USA, pp. 93-108.

JSCE-SF4, Method of tests for flexural strength and flexural toughness of steel fiber reinforced concrete, Japanese Society of Civil Engineers.

Kabele, P., Li, V.C., 1998. Fracture energy of strain-hardening cementitious composites. In: Mihashi, H., Rokugo, K. (Eds.), Fracture Mechanics of Concrete Structures (FraMCoS-3). Fracture Mechanics of Concrete Structures Aedificatio, Gifu, Japan, pp. 487-498.

Kang, S.T., Kim, J.-K., 2012. Investigation on the flexural behavior of UHPCC considering the effect of fiber orientation distribution. Construction and Building Materials, 28(1): 57-65.

Kang, S.T., Lee, Y., Park, Y.-D., Kim, J.-K., 2010. Tensile fracture properties of an Ultra High Performance Fiber Reinforced Concrete (UHPFRC) with steel fiber. Compos Struct, 92: 11.

Karihaloo, B.L., De Vriese, K.M.B., 1999. Short-fibre reinforced reactive powder concrete. Rilem Proc, 6: 53-63.

Karihaloo, B.L., Wang, J., 2000a. Micromechanics of fiber-reinforced cementitious composites. Advanced Engineering Materials, 2(11): 726-732.

Karihaloo, B.L., Wang, J.X., 2000b. Micromechanics of fiber-reinforced cementitious composites. Advanced Engineering Materials, 2(11): 726-732.

Kazemi, S., Lubell, A.S., 2012. Influence of Specimen Size and Fiber Content on Mechanical Properties of Ultra-High-Performance Fiber-Reinforced Concrete. ACI Mater J.

Lange-Kornbak, D., Karihaloo, B.L., 1998. Design of fiber-reinforced DSP mixes for minimum brittleness. Advanced Cement Based Materials, 7(3-4): 89-101.

Lappa, E.S., 2007. High Strength Fibre Reinforced Concrete Static and fatigue behaviour in bending, Technische Universiteit Delft.

Le, T.T., 2008. Ultra high performance fibre reinforced concrete paving flags, University of Liverpool.

Le, T.T., Soutsos, M.N., Millard, S.G., Barnett, S.J., 2007. UHPFRC - Optimisation of mix proportions. In: Russell, M.I., Basheer, P.A.M. (Eds.), Concrete Platform. Queen's University of Belfast, Belfast, pp. 339-348.

Le, T.T., Soutsos, M.N., Millard, S.G., Tang, K.K., 2008. Structural behaviour of a UHPFRC flag pavement. In: Fehling, E., Schmidt, M., Stürwald, S. (Eds.), Second International Symposium on Ultra High Performance Concrete. Structural Materials and Engineering Series. Kassel University Press, Kassel, Germany, pp. 663-670.

Lee, J., Lopez, M.M., 2014. An Experimental Study on Fracture Energy of Plain Concrete. International Journal of Concrete Structures and Materials, 8(2): 129-139.

Lemaître, J., Chaboche, J.-L., 1994. Mechanics of solid materials. Cambridge University Press, Cambridge.

Li, V., Wang, Y., Backer, S., 1990. Effect of inclining angle, bundling and surface treatment on synthetic fibre pull-out from a cement matrix. . Composites, 21(2): 132-40.

Li, V.C., Stang, H., 2004. Elevating FRC material ductility to infrastructure durability. In: Di Prisco, M., Felicetti, R., Plizzari, G.A. (Eds.), 6th RILEM Symposium on Fibre-Reinforced Concretes (FRC). RILEM Publications S.A.R.L., Varenna, Italy, pp. 171-186.

Li, X., 2016. An extended cohesive damage model for simulating crack propagation in fibre reinforced composies, University of Portsmouth.

Lofgren, I., Stang, H., Olesen, J.F., 2004. Wedge splitting test - a test to determine fracture properties of FRC. In: Di Prisco, M., Felicetti, R., Plizzari, G.A. (Eds.), 6th RILEM Symposium on Fibre-Reinforced Concretes (FRC). RILEM Publications S.A.R.L., Varenna, Italy, pp. 379-388.

Lubliner, J.J., S.O., O., E., O., 1989. A plastic-damage model for concrete. International Journal of Solids and Structures, 25(3): 229-326.

Maca, P., Sovjak, R., Vavrinik, T., 2013. Experimental investigation of mechanical properties of ultra high performance fibre reinforced concrete. Procedia Engineering, 65: 14-19.

Magureanu, C., Sosa, J., Negrutiu, C., Heghes, B., 2012. Mechanical Properties and Durability of Ultra-High-Performance Concrete. ACI Mater J, 109(2).

Mahmud, G.H., Yang, Z., Hassan, A.M.T., 2013. Experimental and numerical studies of size effects of Ultra High Performance Steel Fibre Reinforced Concrete (UHPFRC) beams. Construction and Building Materials, 48: 1027-1034.

Marcinkiewitcz, K., Wells, M., 2014. Staircase showcase for ultra-high-strength-fibre-reinforced concrete. ICE Civil Engineering proceedings, 167(CE3).

Markovic, I., 2006. High-Performance Hybrid-Fibre Concrete - Development and Utilisation. Delft University Press, Netherlands.

Mazars, J., 1981. Mechanical damage and fracture of concrete structures, Proceedings ICF 5, Cannes, pp. 1499-1506.

Mazars, J., 1985. A model for a unilateral elastic damageable material and its application to concrete. In: Wittmann, F.H. (Ed.), Fracture Toughness and Fracture Energy of Concrete. Elsevier.

Mier, J.G.M.v., 2013. Concrete fracture: a multiscale approach. CRC Press, Boca Raton, FL.

Morin, V., Cohen Tenoudji, F., Feylessoufi, A., 7 Richard, P., 2011. Superplasticizer effects on setting and structuration mechanisms of ultrahigh-performance concrete. . Cem Concr Res, 31: 63-71.

Naaman , A., Reinhardt, H.W., 2015. International workshop series on high performance fiber reinforced cement composites (HPFRCC): History and evolution, High Performance Fiber Reinforced Cement Compsites (HPFRCC7), Stuttgart, Germany.

Neville, A.M., 2012. Properties of concrete Pearson Education Limited, Harlow.

Neville, A.M., Brooks, J.J., 2010. Concrete Technology Pearson Education Limited, Harlow.

Niazi, M.S., Wisselink, H.H., Meinders, T., 2013. Viscoplastic regularization of local damage models: revisited. Computational Mechanics, 51(2): 203-216.

Oliver, J., 1995. Modeling strong discontinuities in solid mechanics via strain softening constitutive equations, CIMNE.

Oner, A., Akyuz, S., 2007. An experimental study on optimum usage of GGBS for the compressive strength of concrete. Cement & Concrete Composites, 29: 505-514.

Perry, V., Seibert, P., 2008. The use of UHPFRC (Ductal) for bridges in North America: Technology, applications and challenges facing commercialisation, Second International Symposium on Ultra High Performance Concrete, Kassel, Germany.

Petersson, P.E., 1981. Crack growth and development of fracture zones in plain concrete and similar materials, Division of Building Materials, Lund Institute of Technology Lund, Sweden.

Planas, J., Elices, M., Guinea, G.V., 1995. The extended cohesive crack. In: Bakker, G., Karihalo.B.L (Eds.), Fracture of Brittle Disordered Materials: Concrete, Rock and Ceramics. E & FN Spon, London, pp. 51-65.

Qsymah, A., Sharma, R., Yang, Z., Margetts, L., Mummery, P., 2017. Micro X-ray computed tomography image-based two-scale homogenisation of ultra high performance fibre reinforced concrete. Construction and Building Materials, 130: 230-240.

Radtke, F.K.F., Simone, A., Sluys, L.J., 2010. A computational model for failure analysis of fibre reinforced concrete with discrete treatment of fibres. Engineering Fracture Mechanics: 597-620.

Richard, P., Cheyrezy, M., 1994. Reactive powder concretes with high ductility and 200-800 MPa compressive strength. In: Mehta, P.K. (Ed.), Concrete Technology Past, Present and Future. American Concrete Institute, Detroit, Michigan, pp. 507-518.

Richard, P., Cheyrezy, M., 1995. Composition of reactive powder concretes. Cem Concr Res, 25(7): 1501-1511.

RILEM, 2002. RILEM TC 162-TDF: Test and design methods for steel fibre reinforced concrete. Bending test. Materials and Structures, 35(11): 579-582.

Romualdi, J.P., Batson, G.B., 1963. Behaviour of reinforced concrete beams with closely spaced reinforcement. J. Amer. Concr. Inst. , 60: 775–789.

Rossi, P., 1997. High performance multimodal fiber reinforced cement composites (HPMFRCC): The LCPC experience. ACI Mater J, 94(6): 478-483.

Rots, J.G., 1989. Stress rotation and stress locking in smeared crack analysis of separation. In: Mihashi, H., Takahashi, H., Wittmann, F.H. (Eds.), Fracture Toughness and Fracture Energy Test Methods. Balkema, Rotterdam, pp. 367-382.

Sadegh, K., Lubell, A., 2012. Influence of Specimen Size and Fiber Content on Mechanical Properties of Ultra-High-Performance Fiber-Reinforced Concrete. ACI Mater J(November-December): 675-684.

Soutsos, M.N., Millard, S.G., Karaiskos, K., 2005. Mix design, mechanical properties and impact resistance of reactive powder concrete (RPC), International Workshop on High Performance Fiber Reinforced Cementitious Composites in Structural Applications.

Spasojević, A., 2008. Structural Implications of Ultra-High Performance Fibre-Reinforced Concrete in Bridge Design, École Polytechnique Fédérale de Lausanne, Suisse.

Spasojevic, A., Redaelli, D., Ruiz, M.F., Muttoni, A., 2008. Influence of tensile properties of UHPFRC on size effect in bending. In: Fehling, E., Schmidt, M., Stürwald, S. (Eds.), Second International Symposium on Ultra High Performance Concrete. Structural Materials and Engineering Series. Kassel University Press, Kassel, Germany, pp. 303-310.

Su, X., Yang, Z., Liu, G., 2010. Finite Element Modelling of Complex 3D Static and Dynamic Crack Propagation By Embedding Cohesive Elements in Abaqus. Acta Mechanica Solida Sinica, 23(3)(12).

Taylor, H.F.W., 1997. Cement chemistry. Thomas Telford, London.

Tjiptobroto, P., Hansen, W., 1993. Tensile strain hardening and multiple cracking in highperformance cement-based composites containing discontinuous fibers. ACI Materials Journal, 90: 16025.

Trivedi, N., Singh, R., Chattopadhyay, J., 2015. A comparative study on three approaches to investigate the size independent fracture energy of concrete. . Engineering Fracture Mechanics, 138: 49-64.

VSL, P.P.L., 2008. Ductal Parameters. In: Ltd, V.P.P. (Ed.).

Wecharatana, M., Shah, S.P., 1983. A model for predicting fracture resistance of fibre reinforced concrete. Cem Concr Res, 13: 819–829.

Wille, K., Parra-Montesinos, G., 2012. Effect of Beam Size, Casting Method, and Support Conditions on Flexural Behaviour of Ultra-High-Performance Fiber-Reinforced Concrete. ACI Mater J, 109(3): 10.

Wuest, J., Denarie, E., Bruhwiler, E., 2008. Model for predicting the UHPFRC tensile hardening response. In: Fehling, E., Schmidt, M., Stürwald, S. (Eds.), Second International Symposium on Ultra High Performance Concrete. Structural Materials and Engineering Series. Kassel University Press, Kassel, Germany, pp. 153-160.

Yang, Z.J., Chen, J., 2005. Finite element modelling of multiple cohesive discrete crack propagation in reinforced concrete beams. Engineering Fracture Mechanics 72 2280–2297.

Yang, Z.J., Su, X.T., Chen, J.F., Liu, G.H., 2009. Monte Carlo simulations of complex cohesive fracture in random heterogeneous quasi-brittle materials. International Journal of Solids and Structures, 46.

Yoo, D.-Y., Lee, J.-H., Yoon, Y.-S., 2013. Effect of fiber content on mechanical and fracture properties of ultra high performance fiber reinforced cementitious composites. Compos Struct, 106: 12.

Yoo, D., Banthia, N., Kang, S., Yoon, Y., 2016. Size effect in ultra-high-performance concrete beams. Engineering Fracture Mechanics, 157: 86-106.

Yoo, D., Shin, H., Yang, J., & Yoon, S., 2014. Material and bond properties of ultra high performance fibre reinforced concrete with micro steel fibres. Compos Part a-Appl S, Part B(80): 116-125.

Zhang, H., Huang, Y.J., Yang, Z.J., Xu, S.L., Chen, X.W., 2018. A discrete-continuum coupled finite element modelling approach for fibre reinforced concrete. Cem Concr Res, 106: 130-143.

Zienkiewicz, O.C., 2005. The finite element method: its basis and fundamentals. Elsevier Butterworth-Heinemann, Amsterdam. London.

Appendices

APPENDIX 1(a) Notched Three Point Bending test Peak Load against Specimen Depth (2%) for batches 1-5

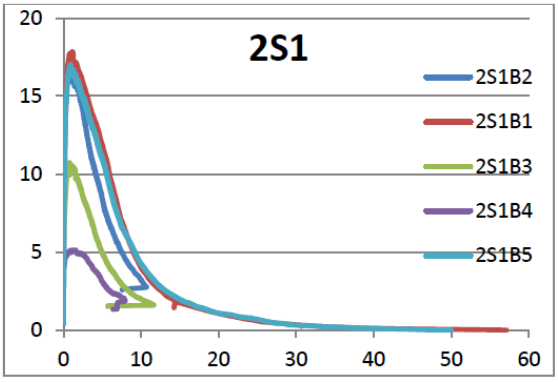

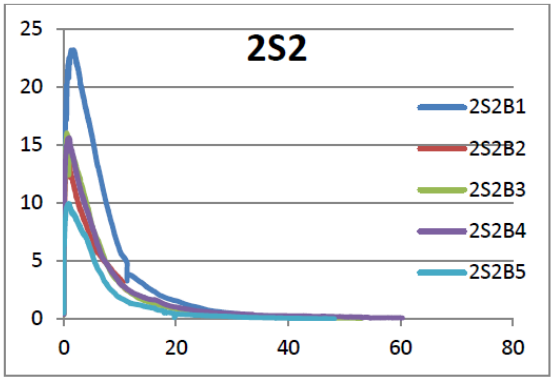

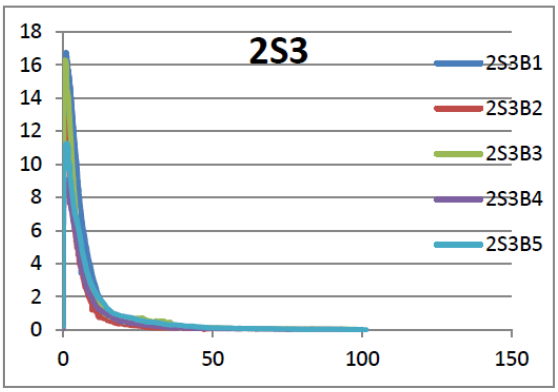

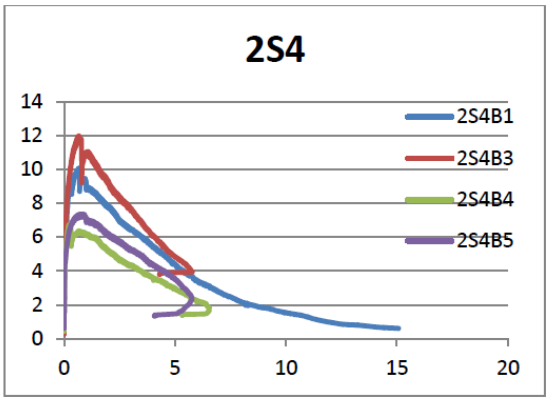

Load (KN)

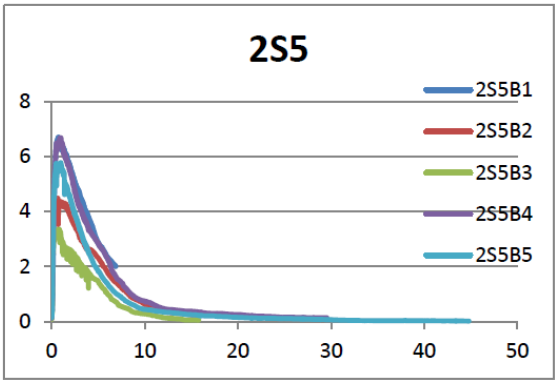

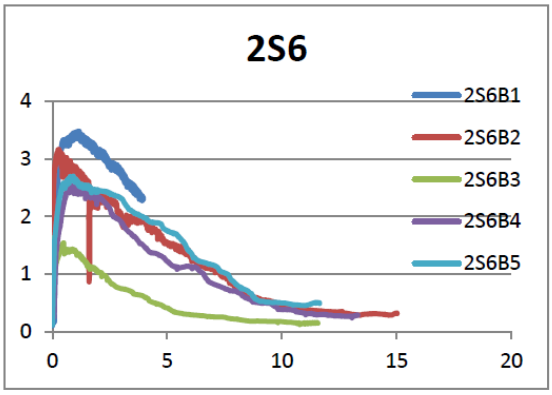

Deflection (mm)

APPENDIX 1(b): Notched Three Point Bending test Peak Load against Specimen Depth (4%) for batches 1-5

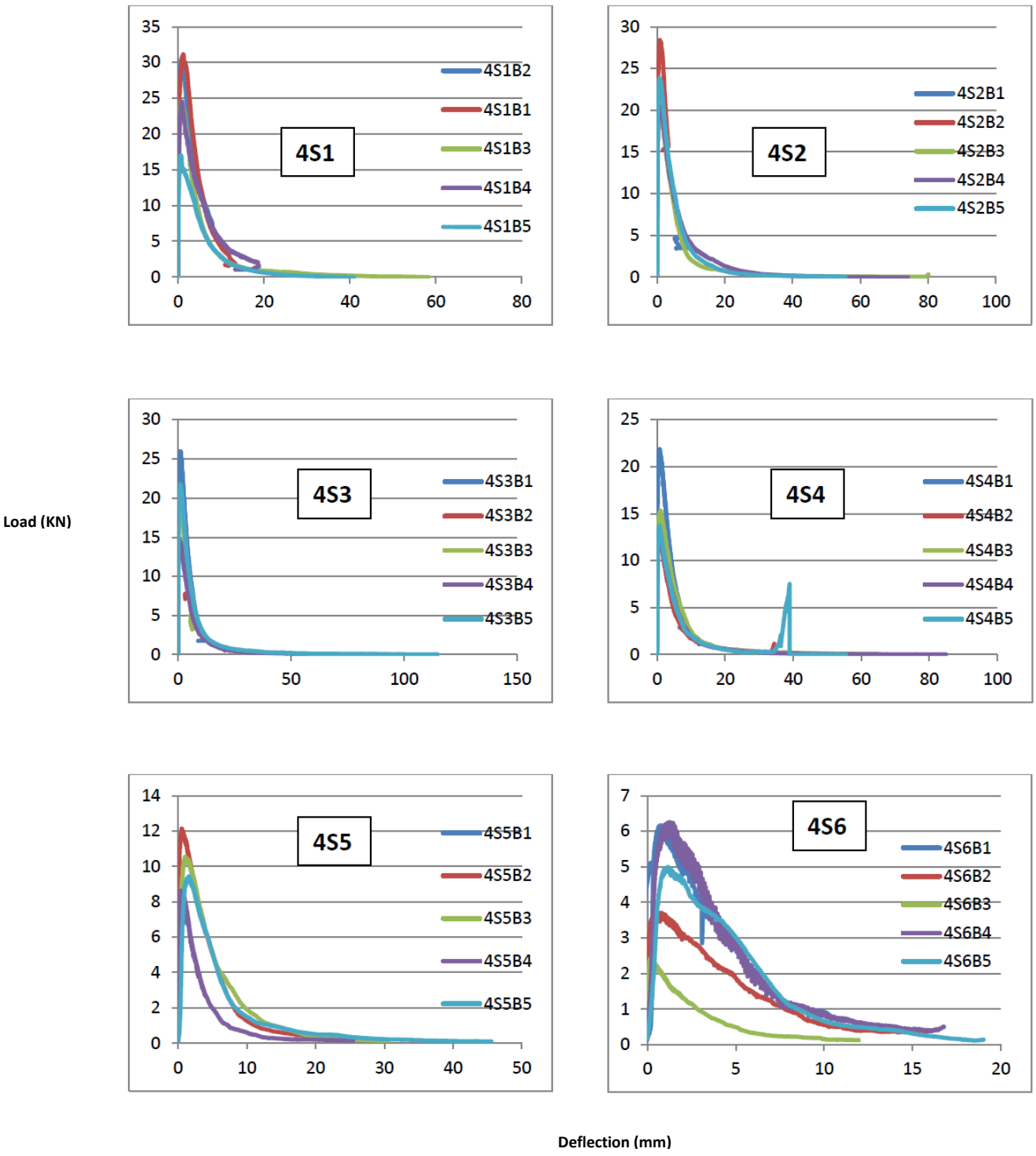

APPENDIX 1(c): Notched Three Point Bending test Peak Load against Specimen Depth (6%) for batches 1-5

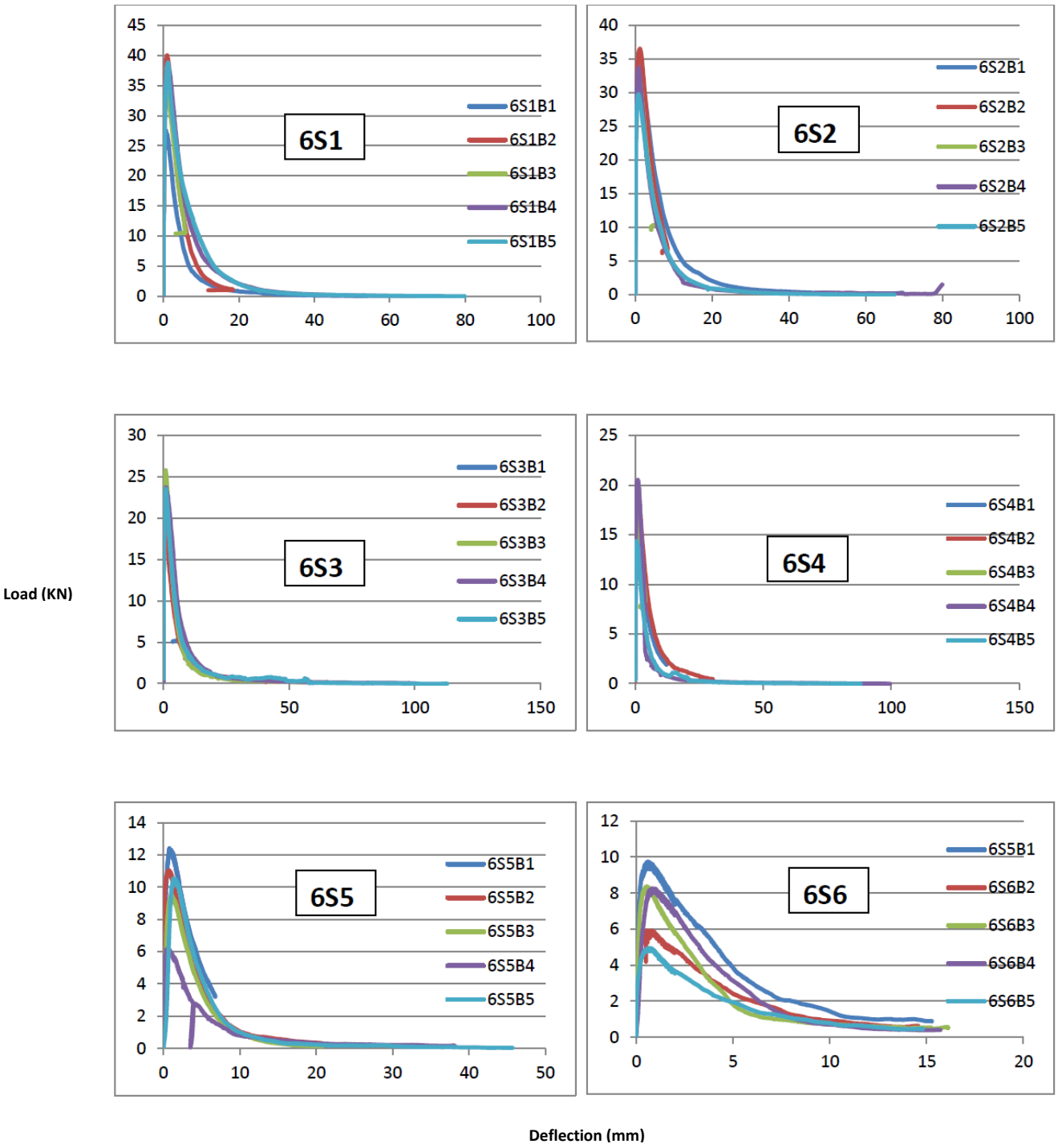

APPENDIX 2(a): Notched Three Point Bending test load @ linearity against Specimen Depth (2%) for batches 1-5

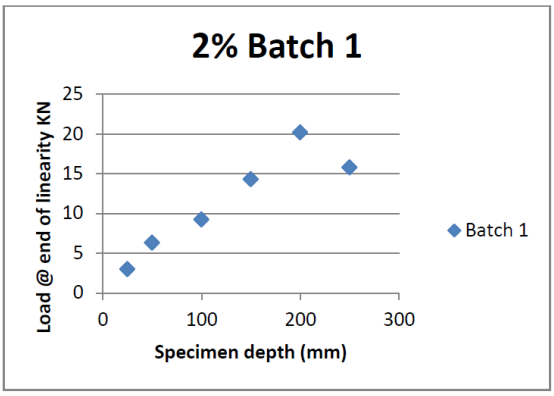

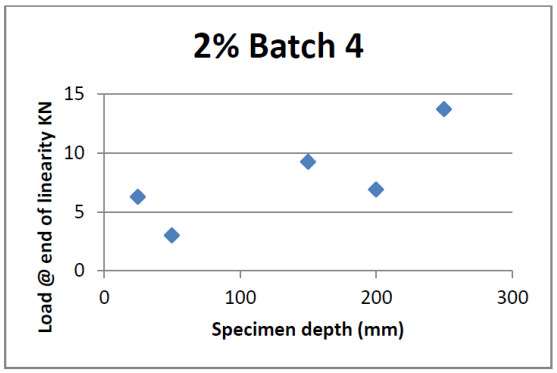

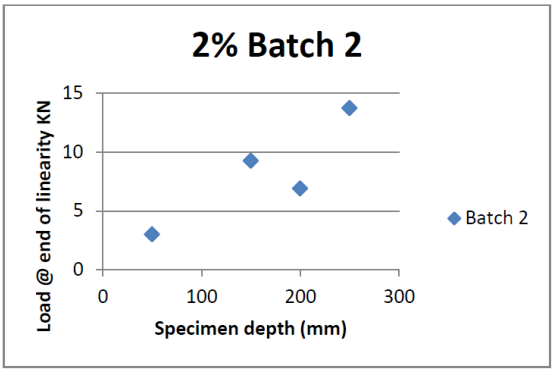

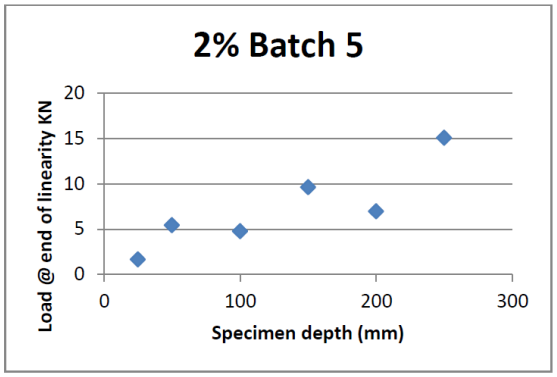

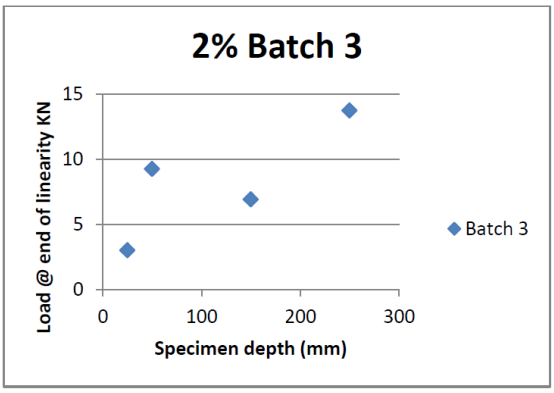

APPENDIX 2(b): Notched Three Point Bending test load @ linearity against Specimen Depth (4%) for batches 1-5

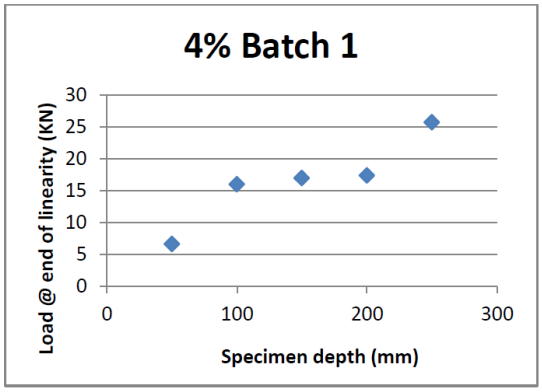

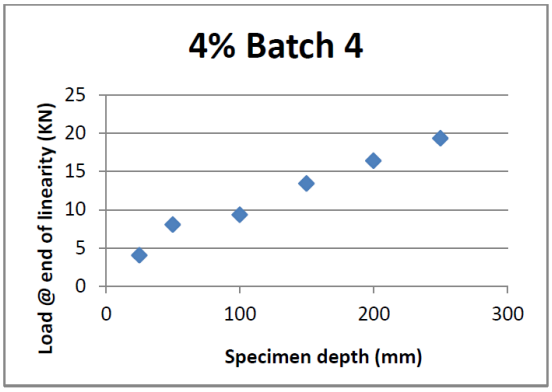

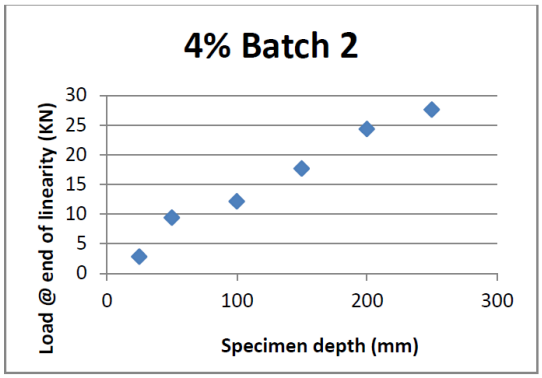

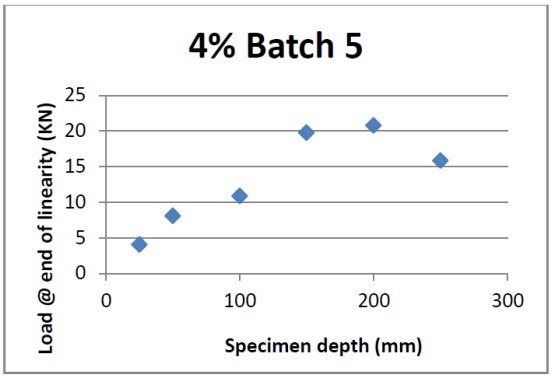

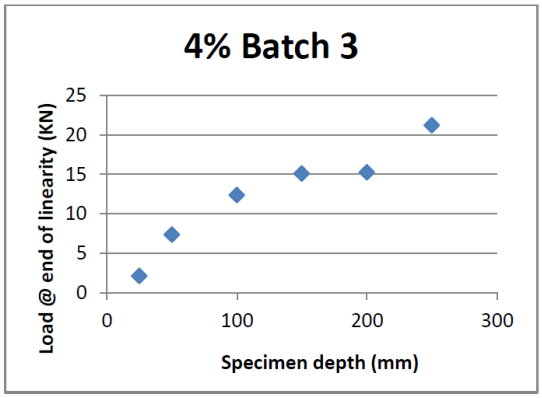

APPENDIX 2(c): Notched Three Point Bending test load @ linearity against Specimen Depth (6%) for batches 1-5

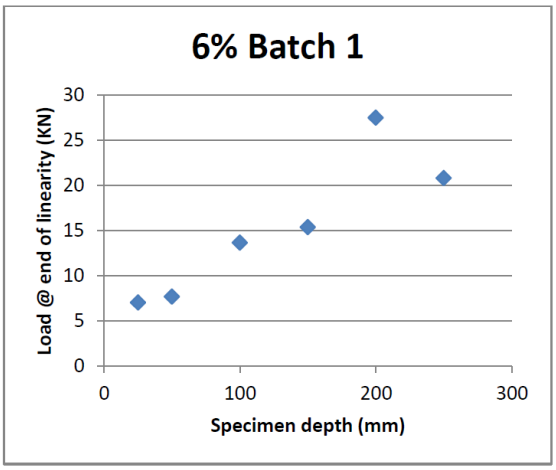

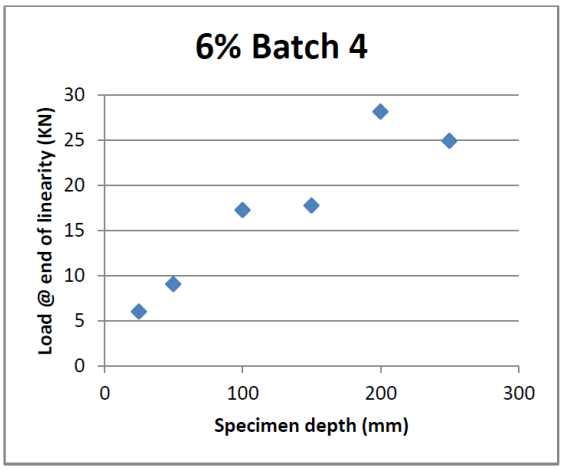

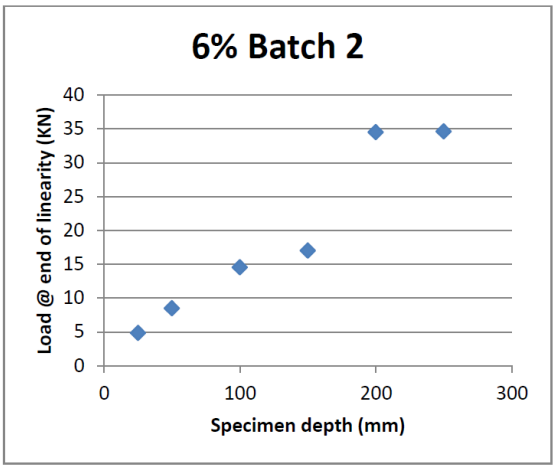

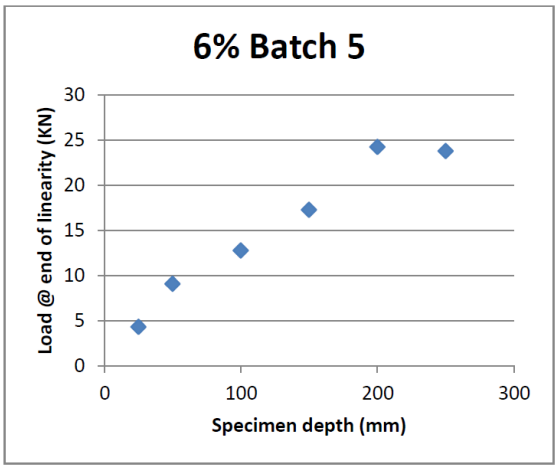

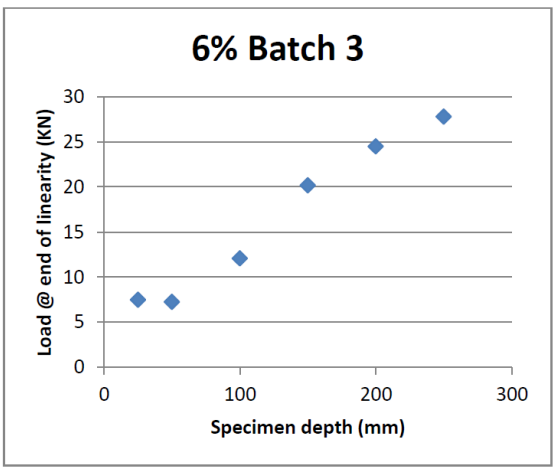

APPENDIX 3(a): Notched Three Point Bending test Peak Load against Specimen Depth (2%) for batches 1-5

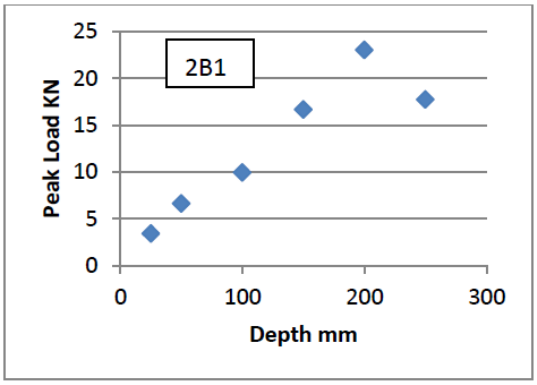

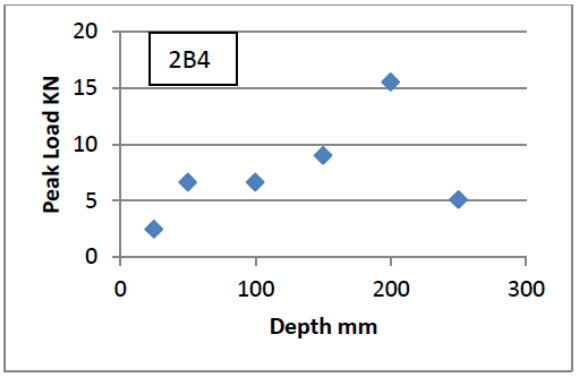

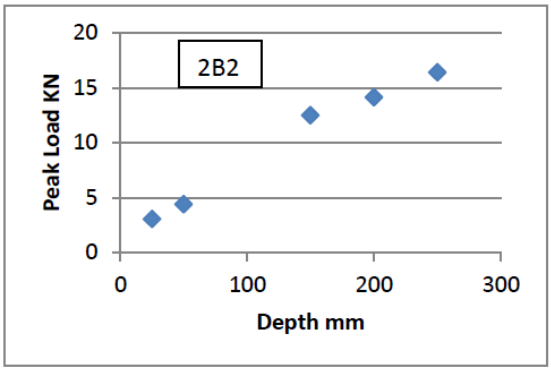

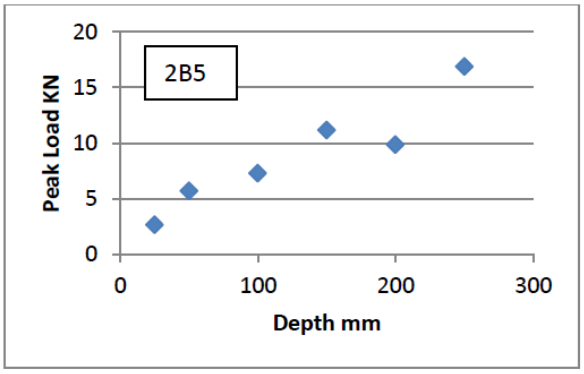

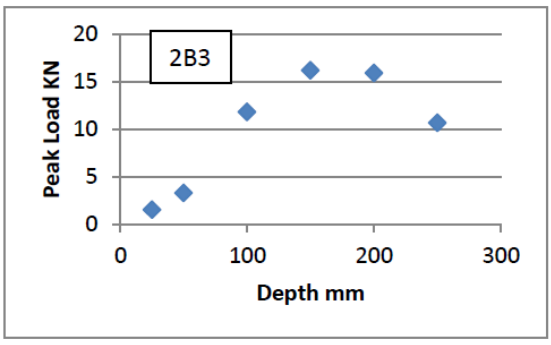

APPENDIX 3(b): Notched Three Point Bending test Peak Load against Specimen Depth (4%) for batches 1-5

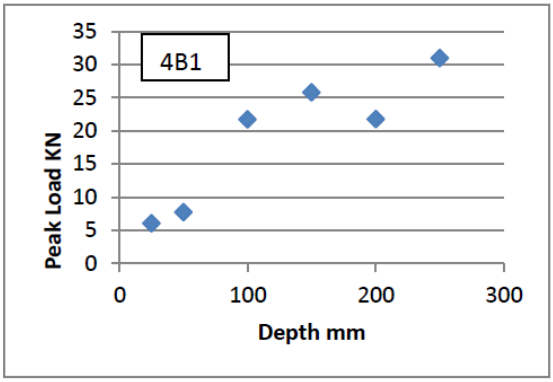

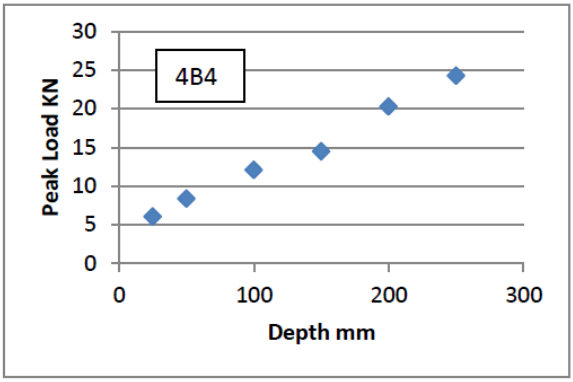

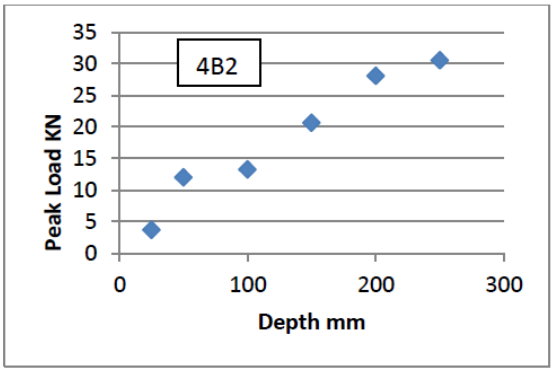

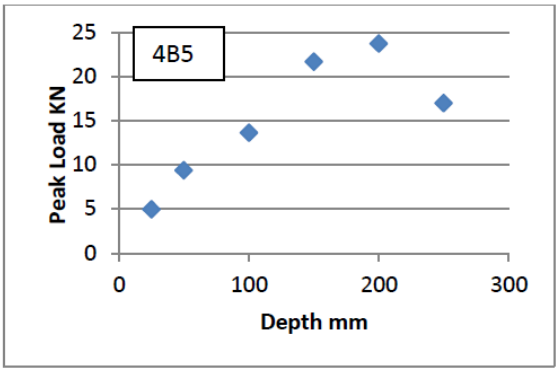

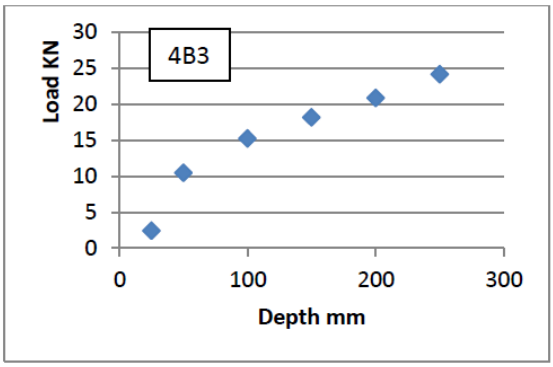

APPENDIX 3(c): Notched Three Point Bending test Peak Load against Specimen depth (6%) for batches 1-5

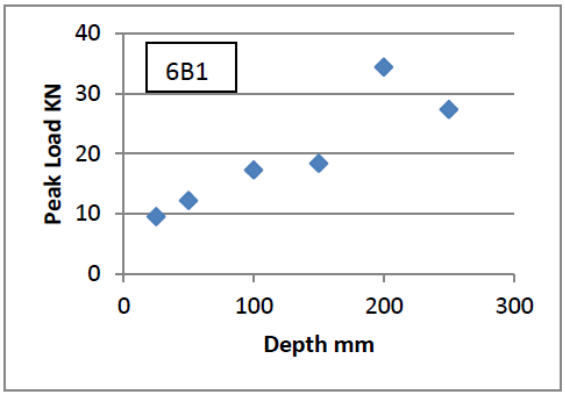

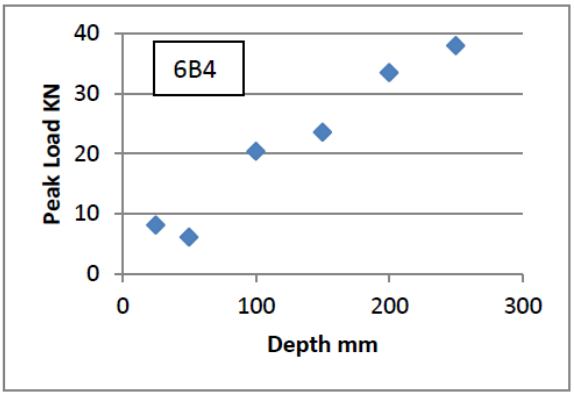

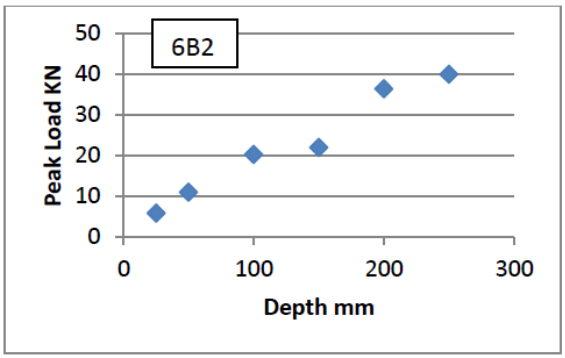

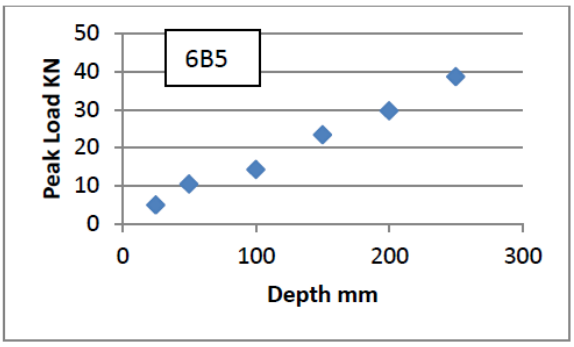

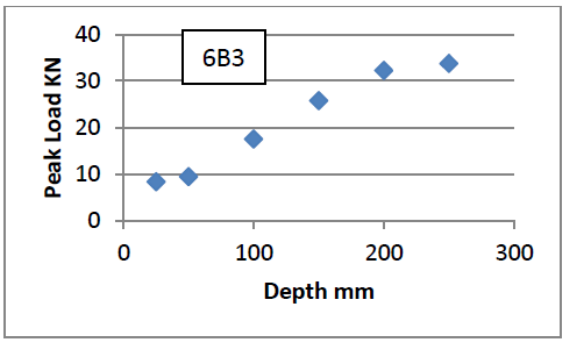

APPENDIX 4(a): Un-notched Three Point Bending test Load at end of linearity against Specimen Depth Batches 1-5 (2% fibre content)

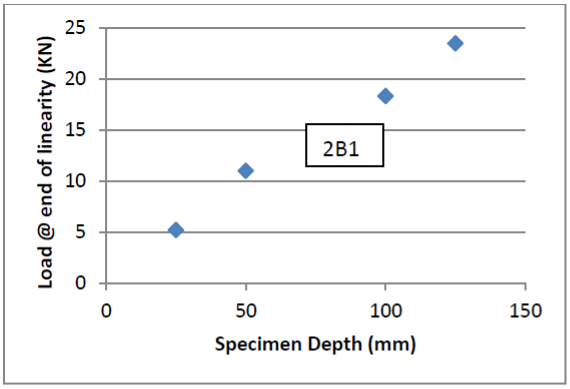

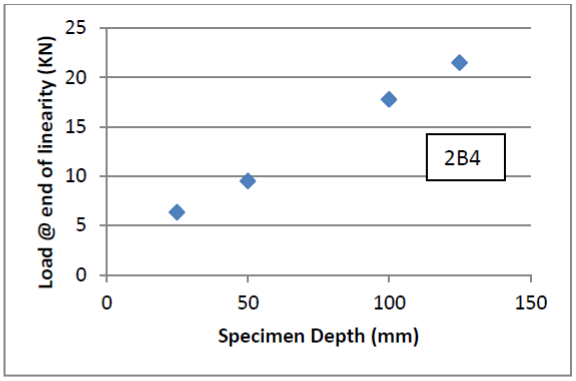

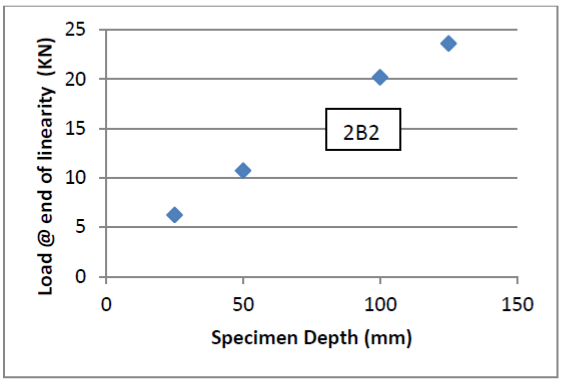

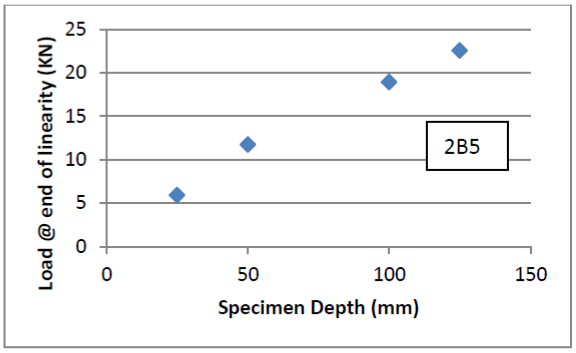

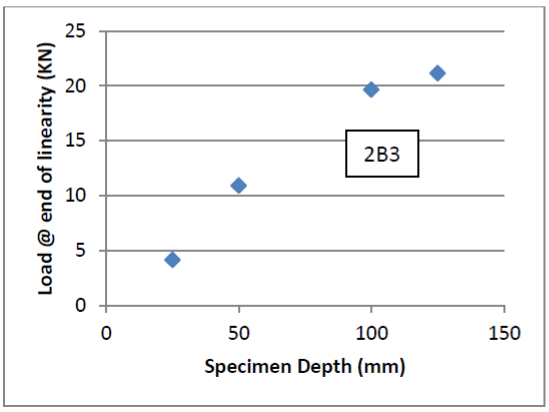

APPENDIX 4(b): Un-notched Three Point Bending test Load at end of linearity against Specimen Depth Batches 1-5 (4% fibre content)

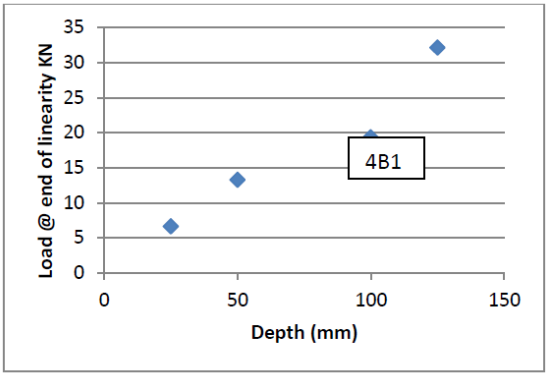

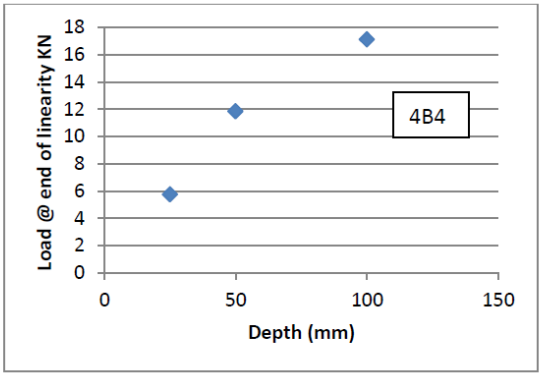

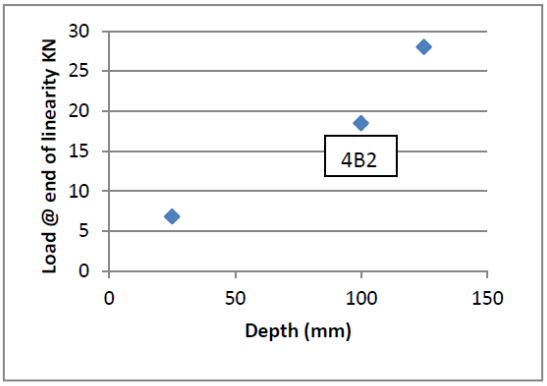

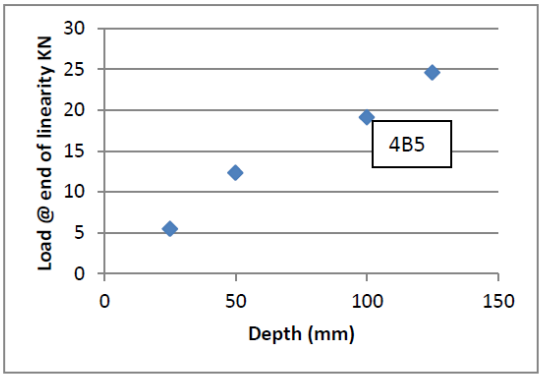

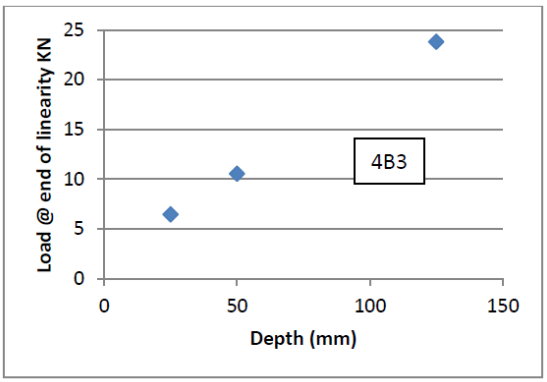

APPENDIX 4(c): Un-notched Three Point Bending test Load at end of linearity against Specimen Depth Batches 1-5 (6% fibre content)

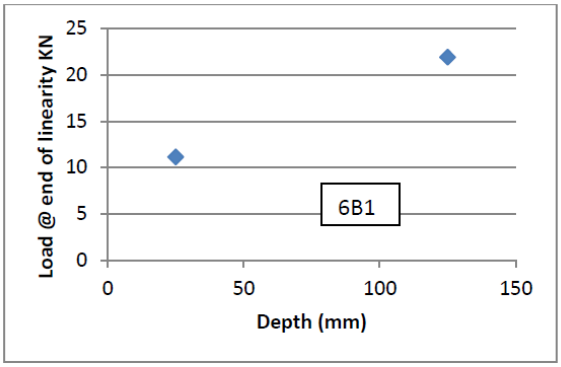

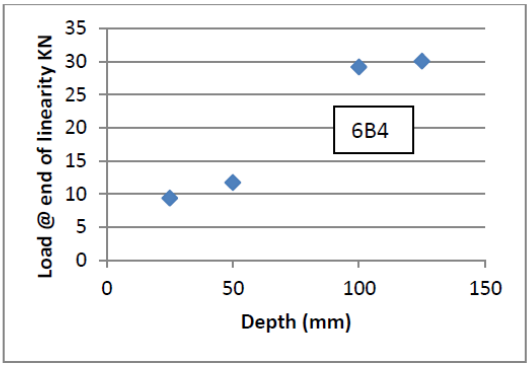

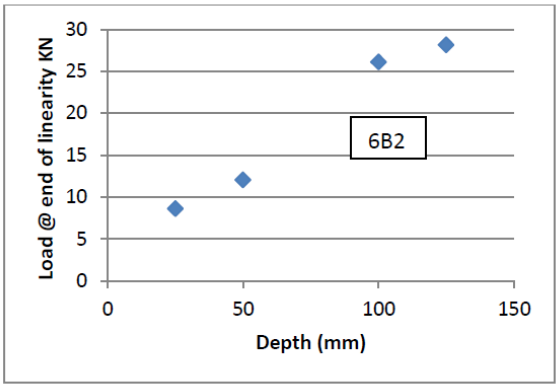

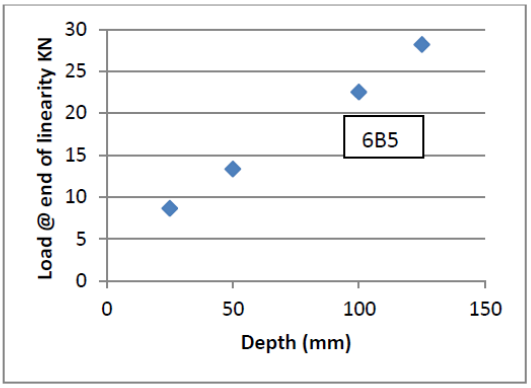

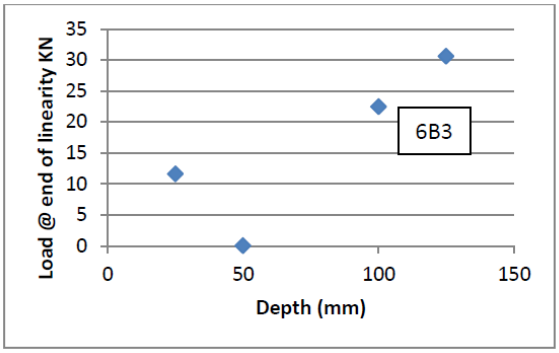

APPENDIX 5(a): Un-notched Three Point Bending test Peak Load against Specimen Depth Batches 1-5 (2% fibre content)

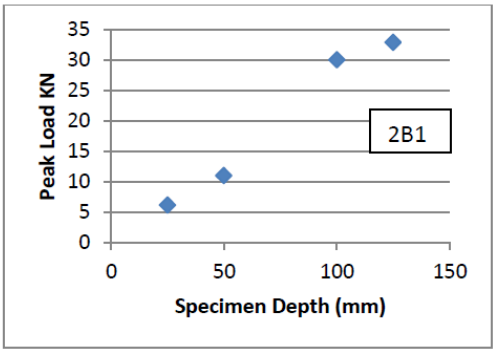

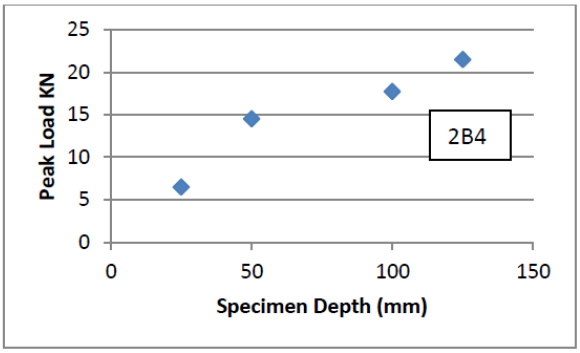

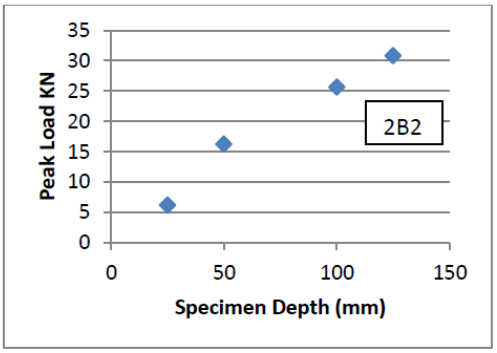

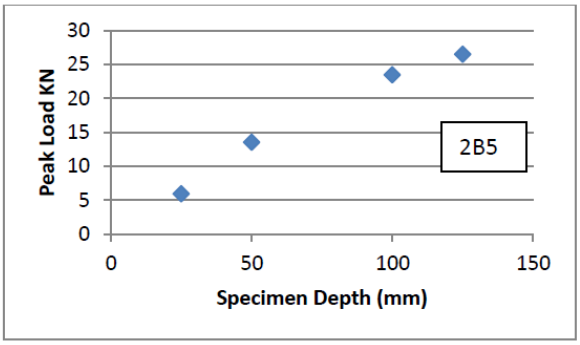

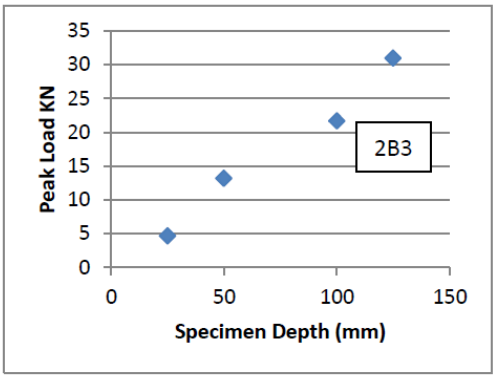

APPENDIX 5(b): Un-notched Three Point Bending test Peak Load against Specimen Depth Batches 1-5 (4% fibre content)

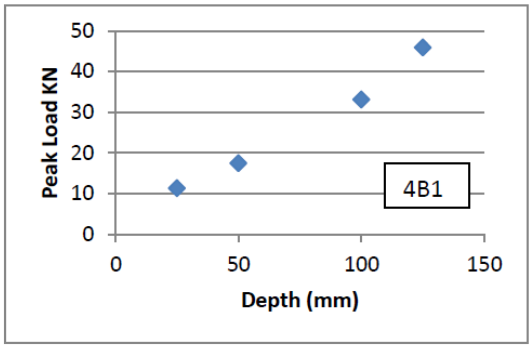

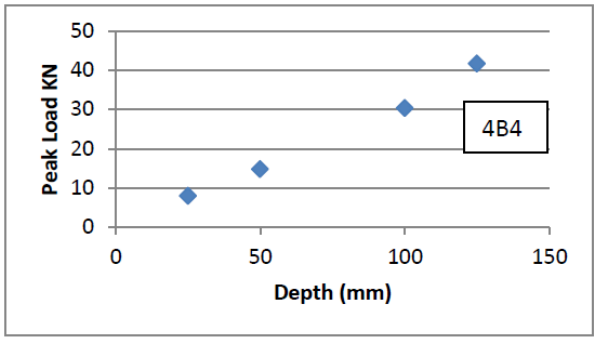

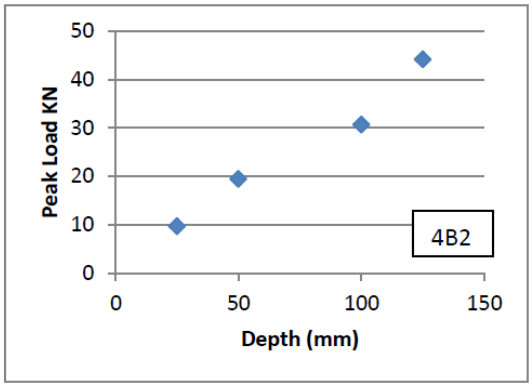

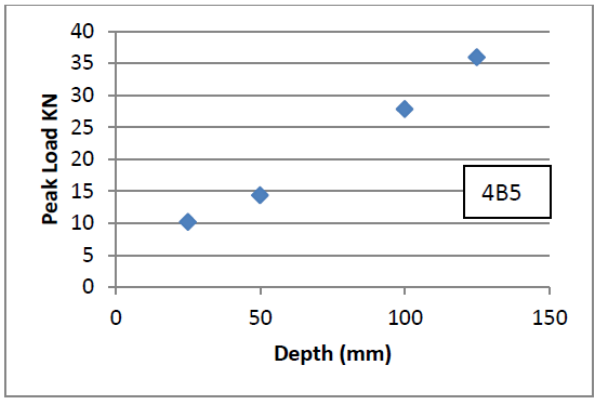

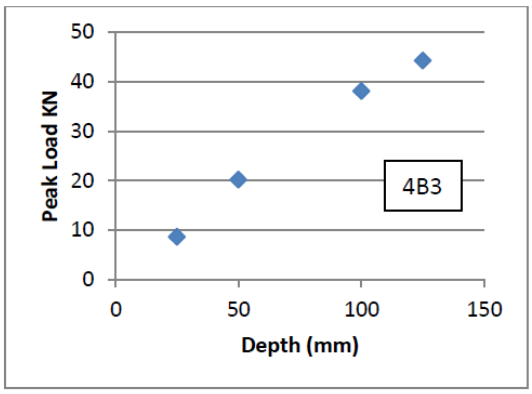

APPENDIX 5(c): Un-notched Three Point Bending test Peak Load against Specimen Depth Batches 1-5 (6% fibre content)

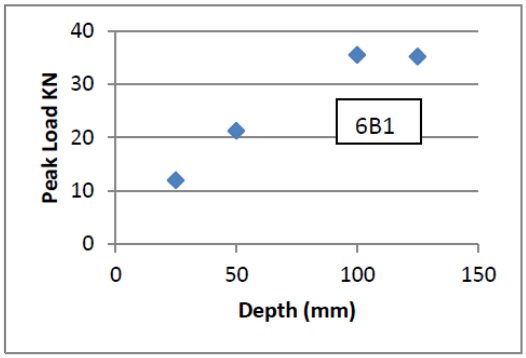

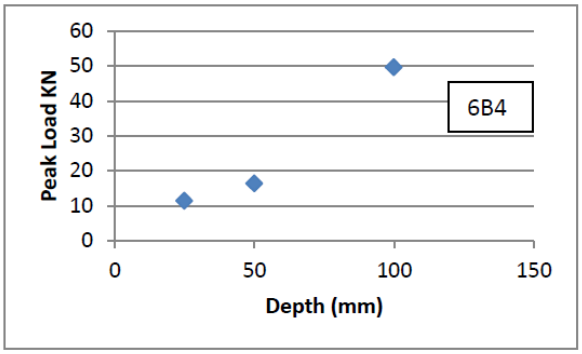

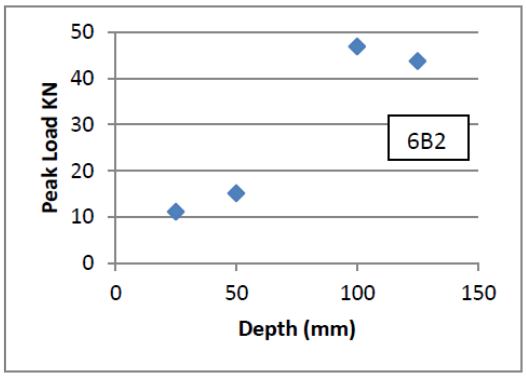

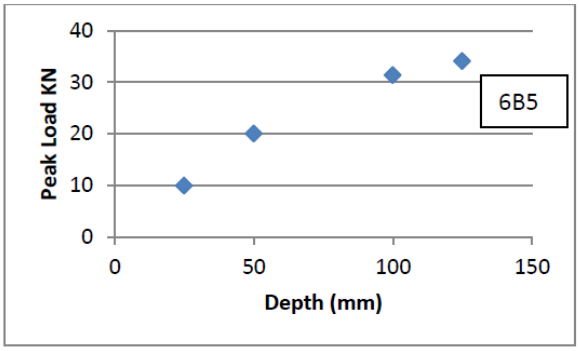

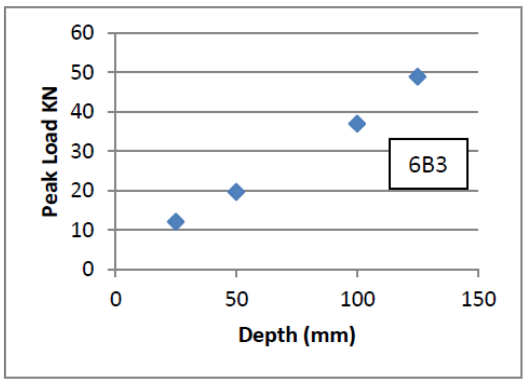

APPENDIX 6 (a): Un-notched Four Point Bending test Load @ end of linearity against batch no.

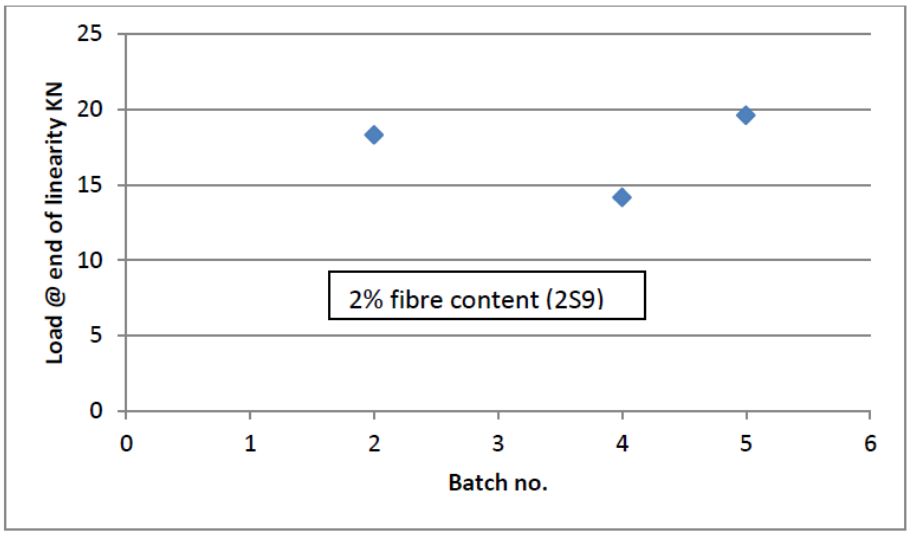

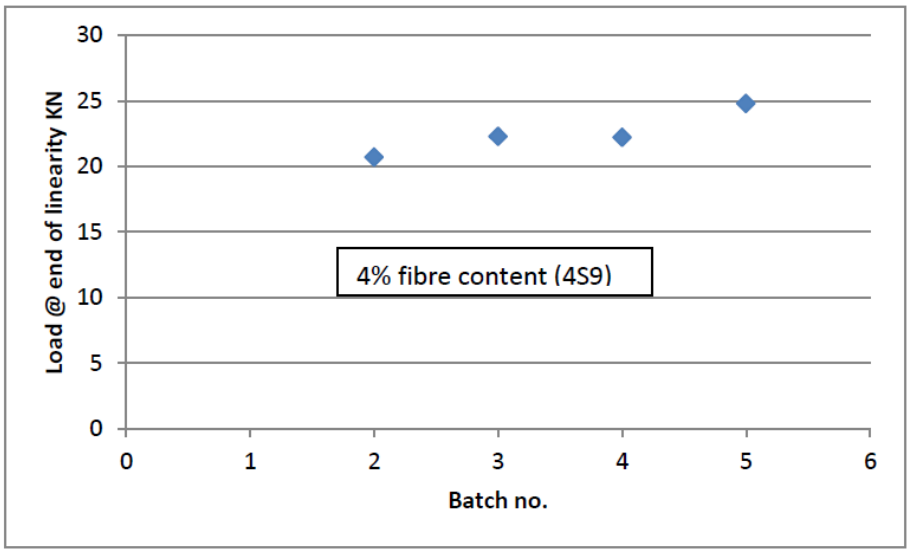

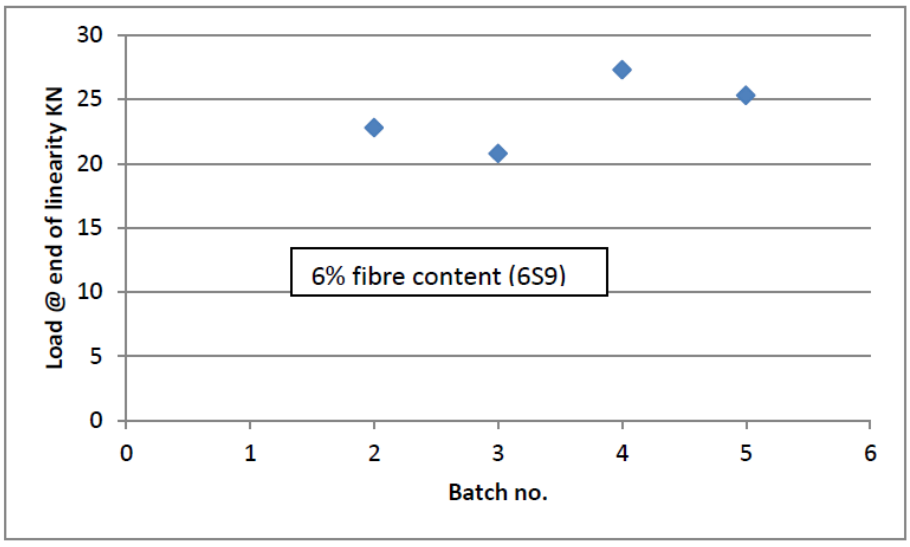

APPENDIX 6(b): Un-notched Four Point Bending test Peak load against batch no.

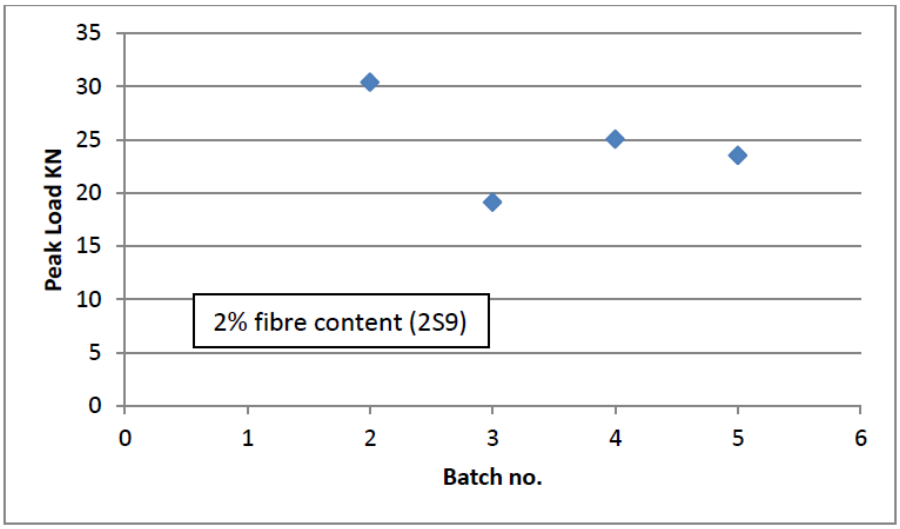

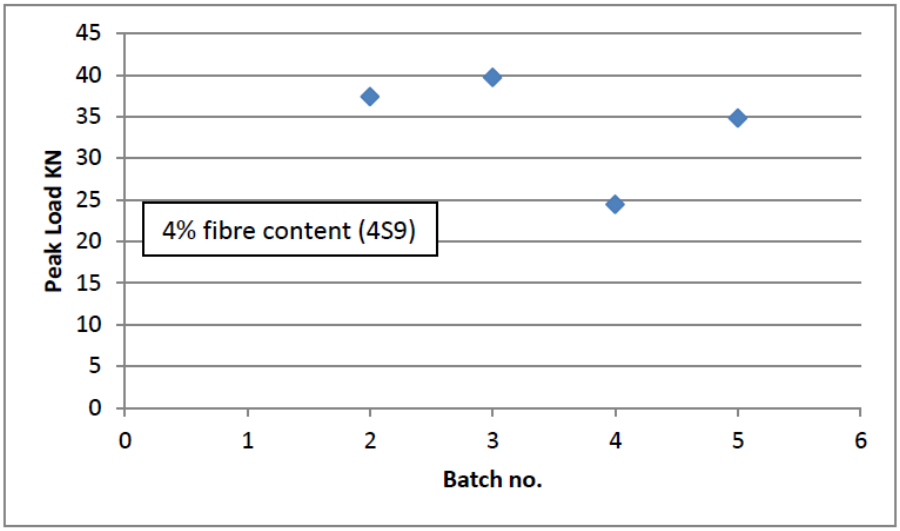

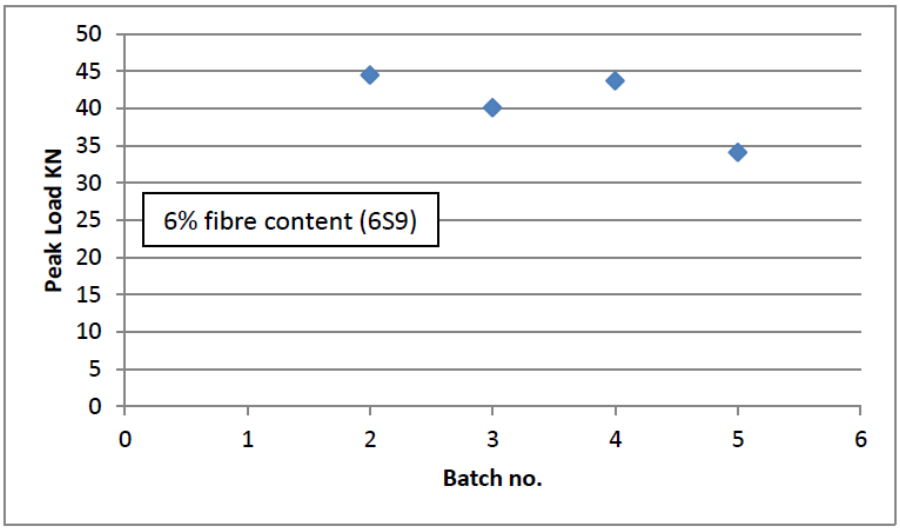

APPENDIX 7(a): Notched Three Point Bending test flexural stress @ end of linearity against specimen depth (2%)

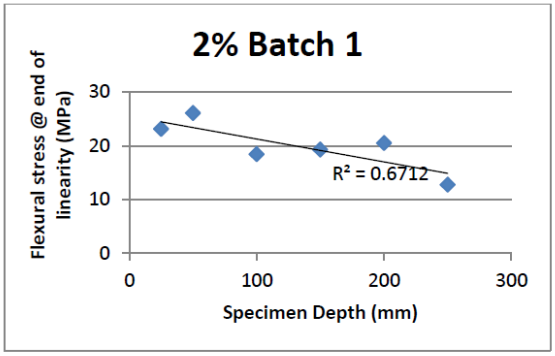

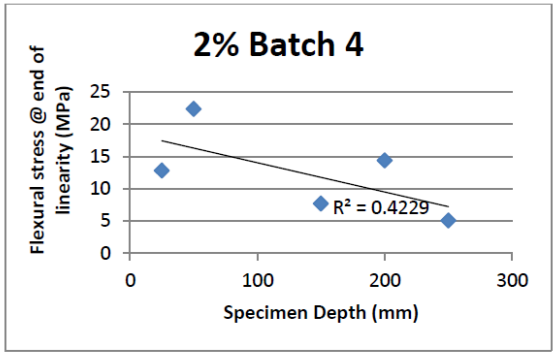

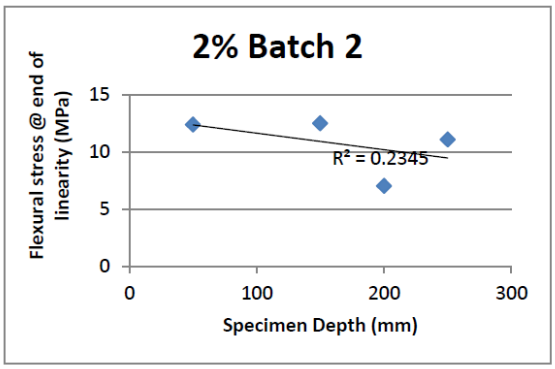

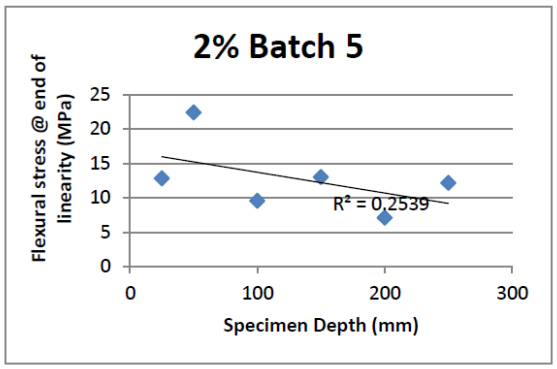

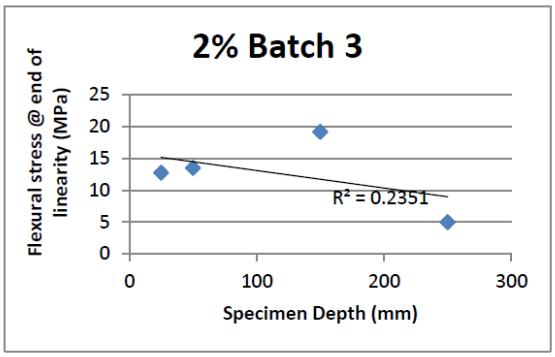

APPENDIX 7(b): Notched Three Point Bending test flexural stress @ end of linearity against specimen depth (4%)

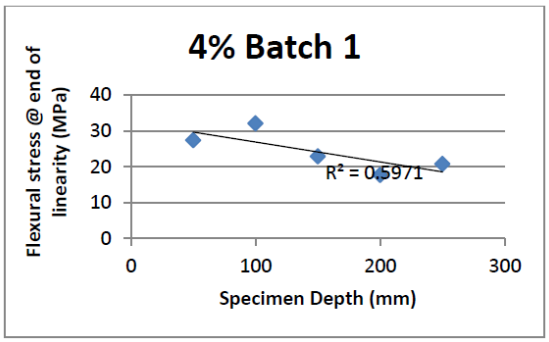

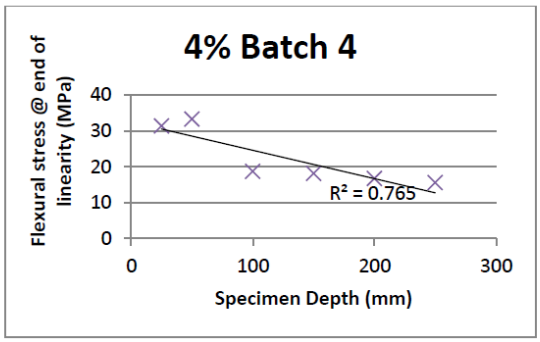

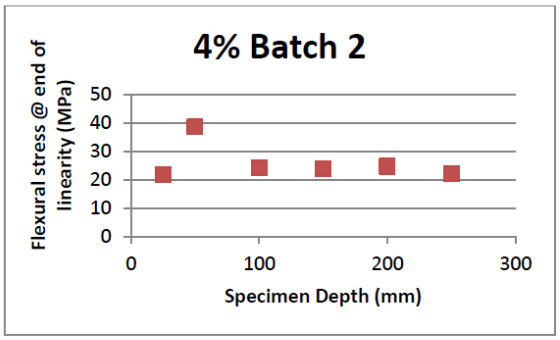

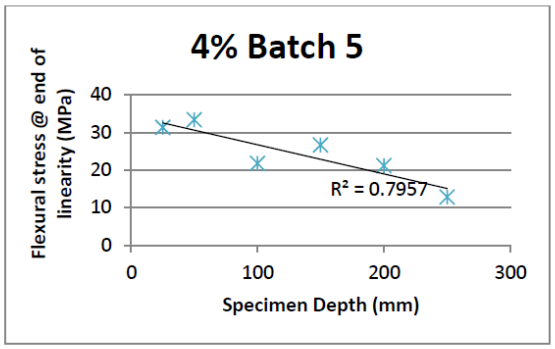

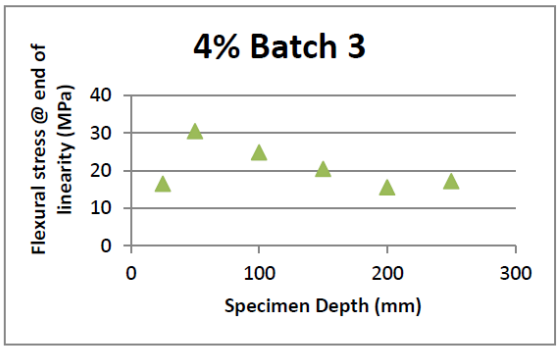

APPENDIX 7(c): Notched Three Point Bending test flexural stress @ end of linearity against specimen depth (6%)

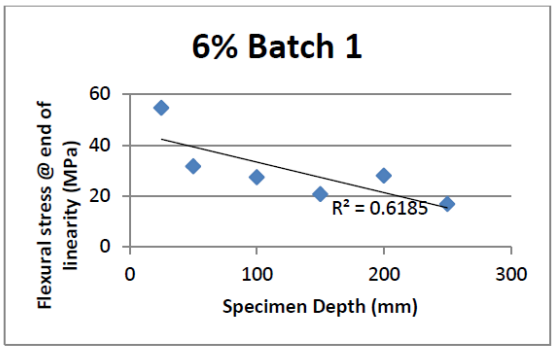

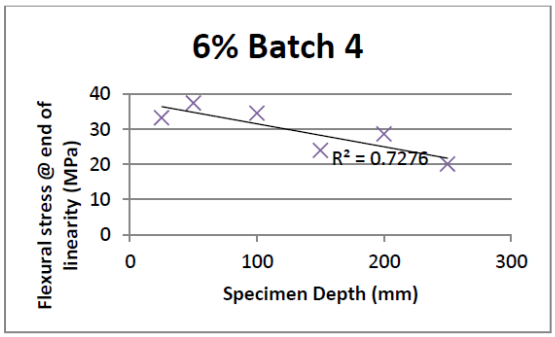

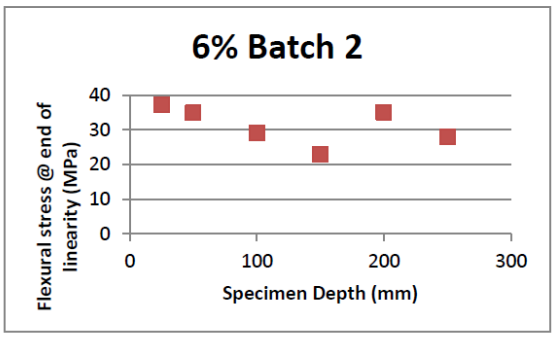

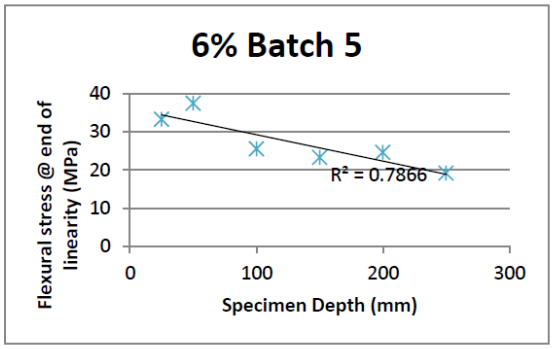

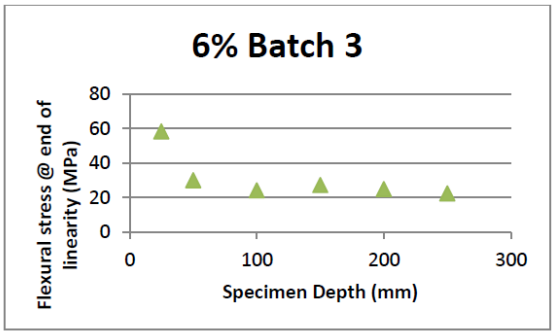

APPENDIX 7(d): Notched Three Point Bending test avg. flexural stress @ end of linearity against specimen depth

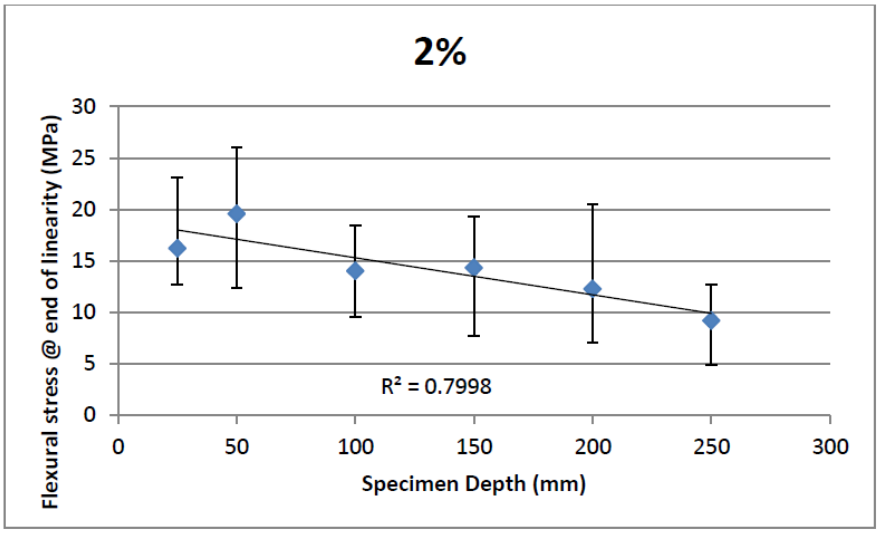

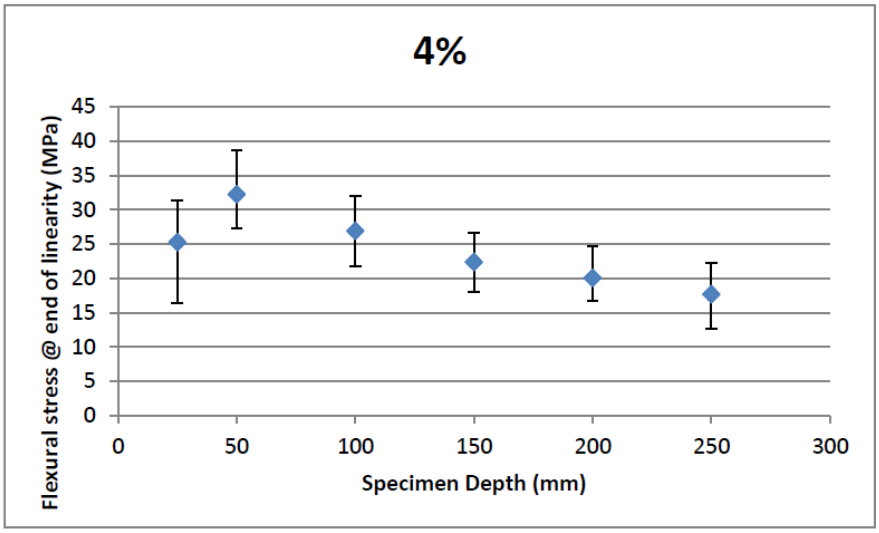

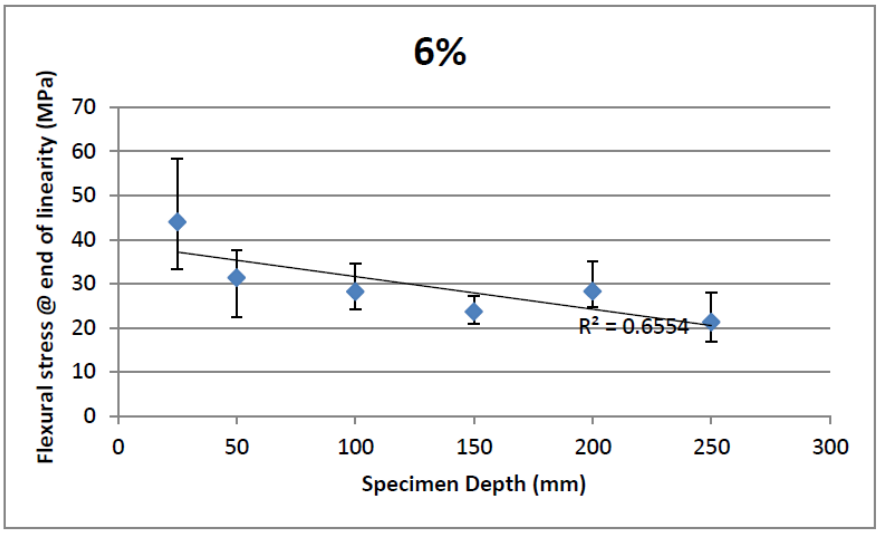

APPENDIX 8(a): Un-notched Three Point Bending test flexural stress @ end of linearity against specimen depth (2%)

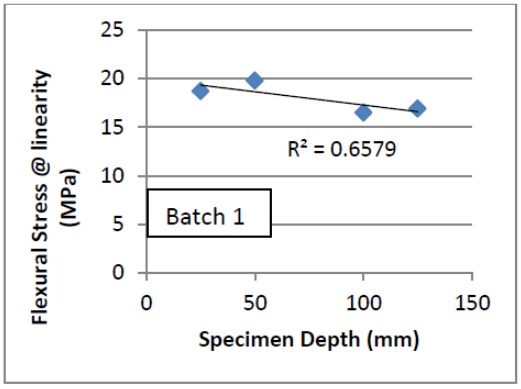

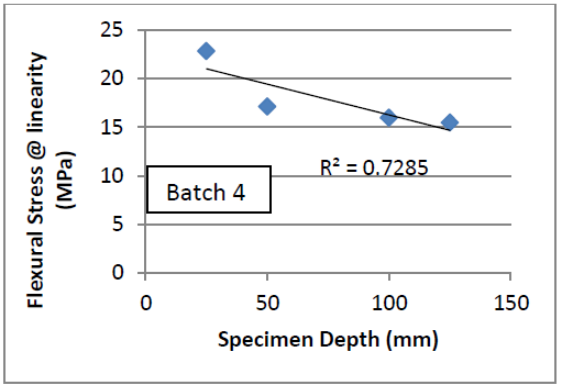

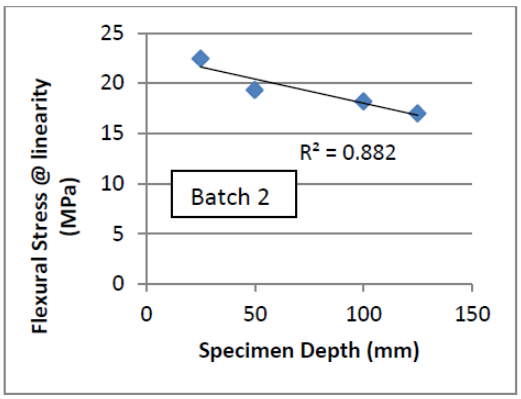

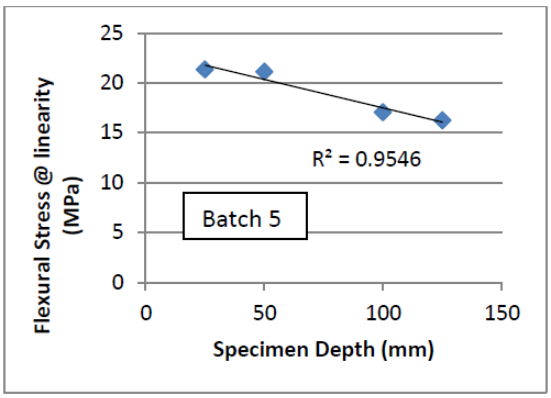

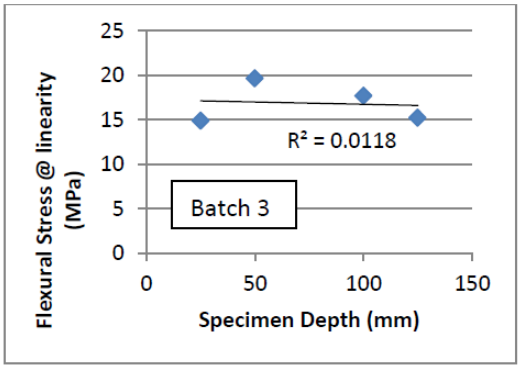

APPENDIX 8(b): Un-notched Three Point Bending test flexural stress @ end of linearity against specimen depth (4%)

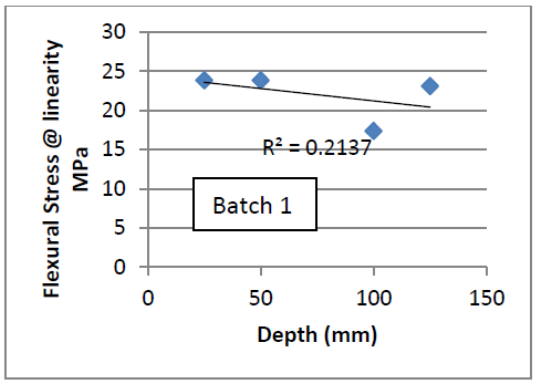

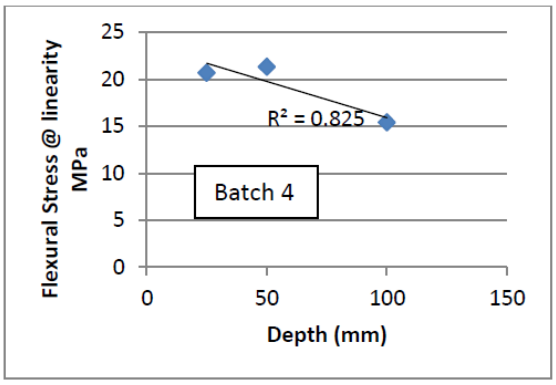

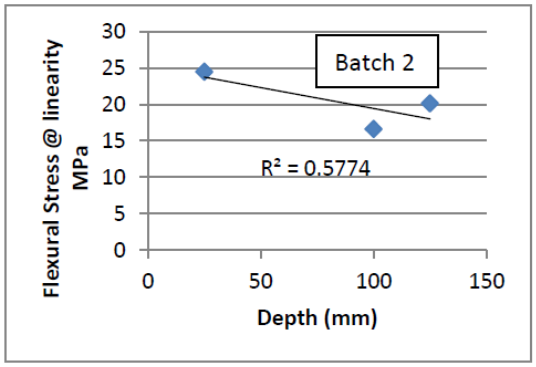

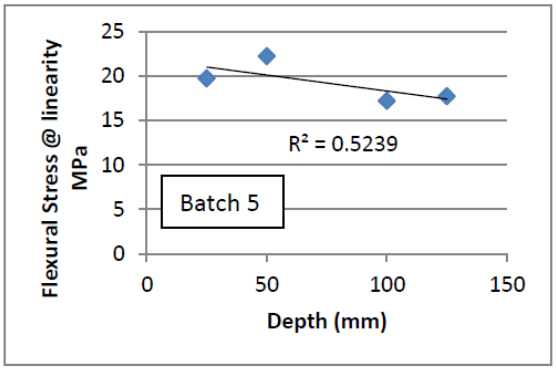

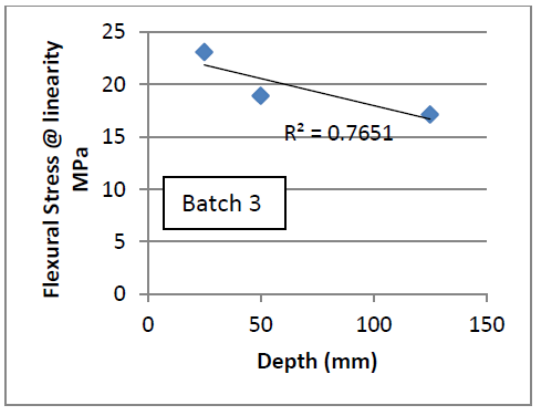

APPENDIX 8(c): Un-notched Three Point Bending test flexural stress @ end of linearity against specimen depth (6%)

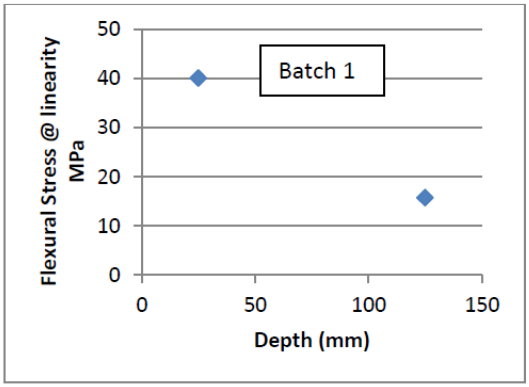

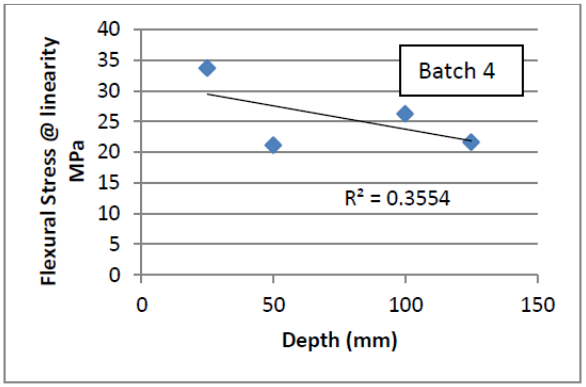

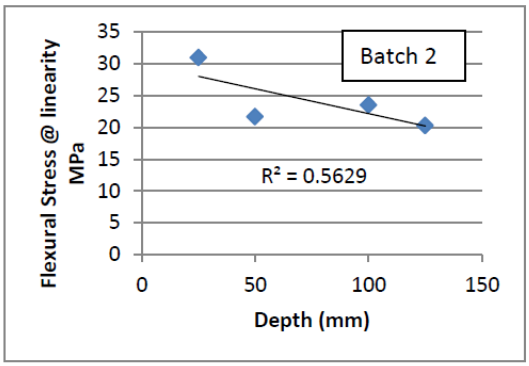

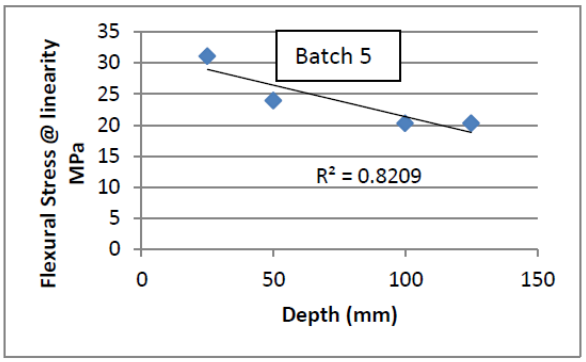

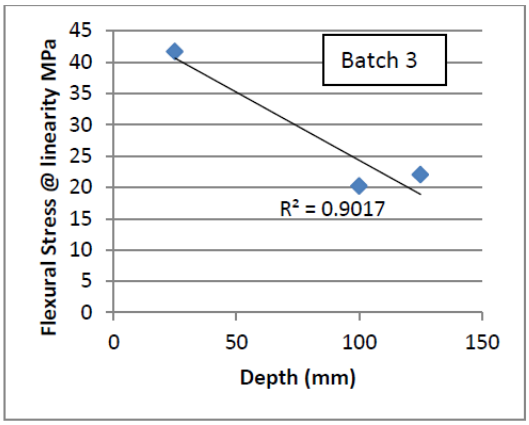

APPENDIX 8(d): Un-notched Three Point Bending test avg. flexural stress @ end of linearity against specimen depth

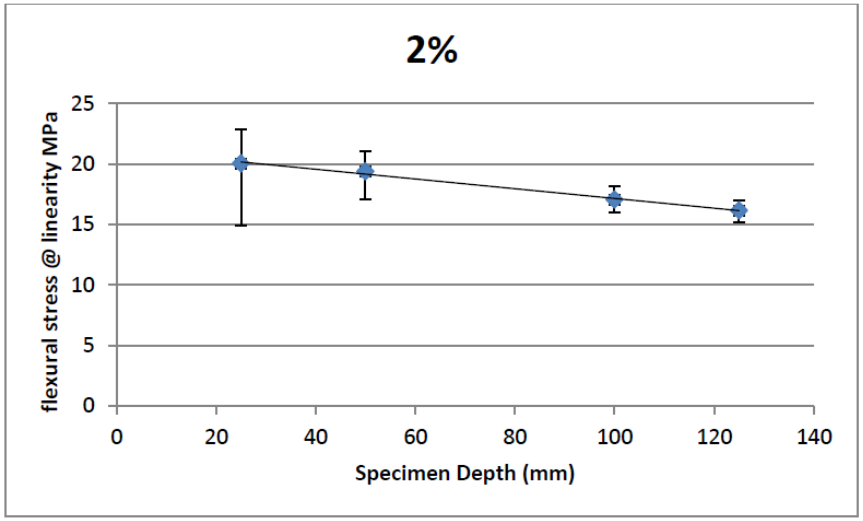

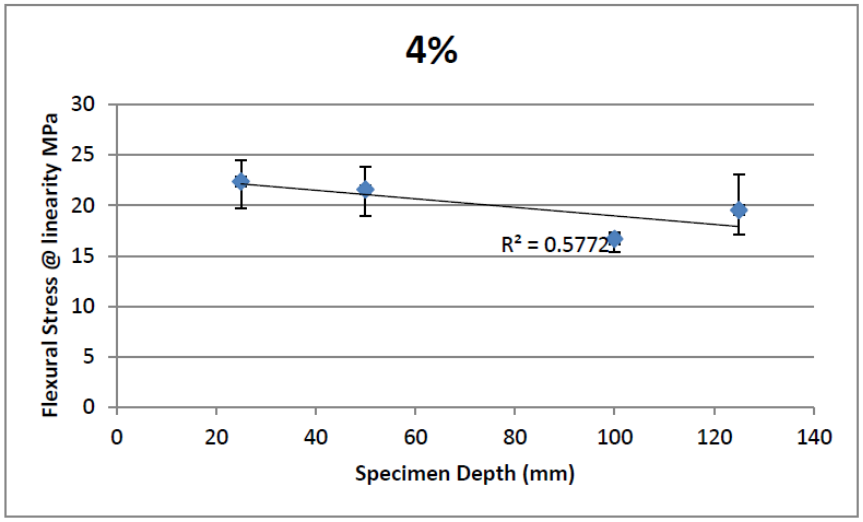

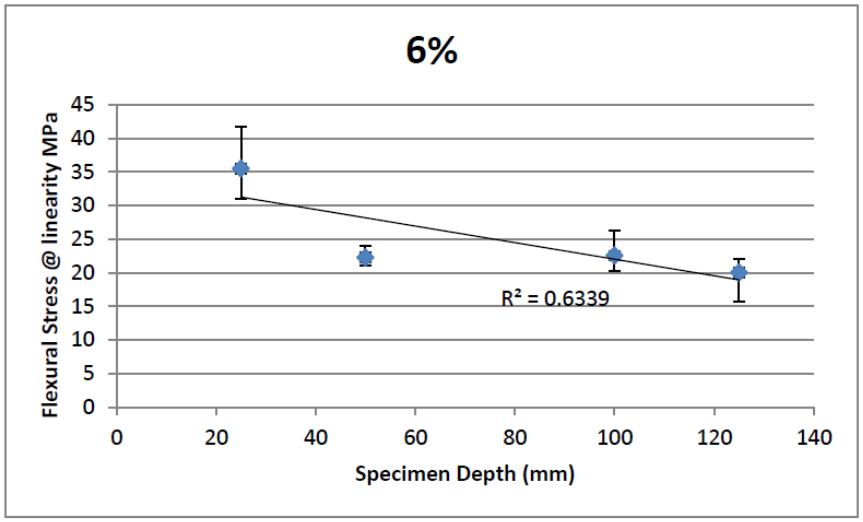

APPENDIX 9(a): Un-notched Three Point Bending test flexural strength against specimen depth (2%)

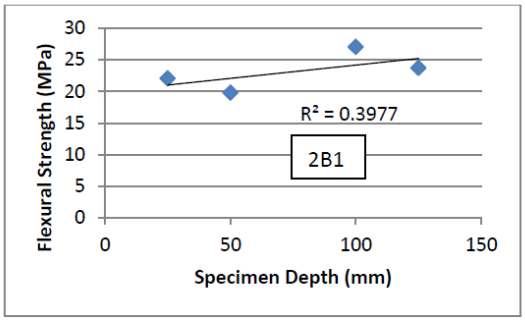

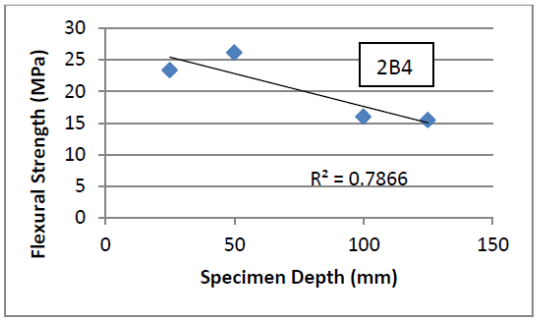

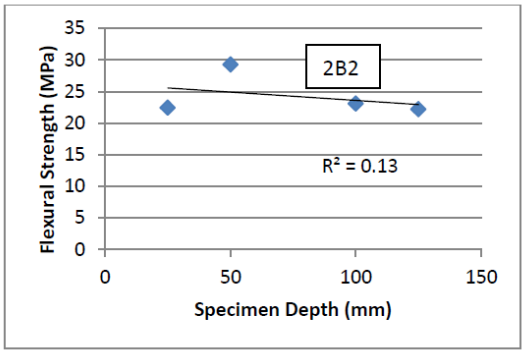

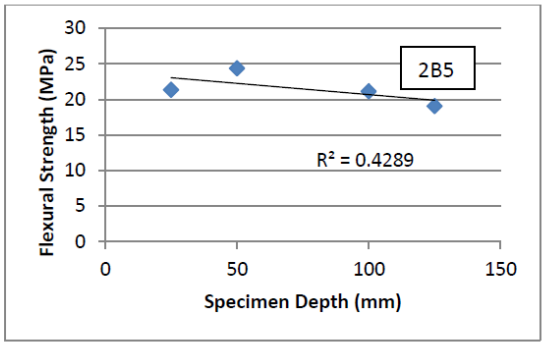

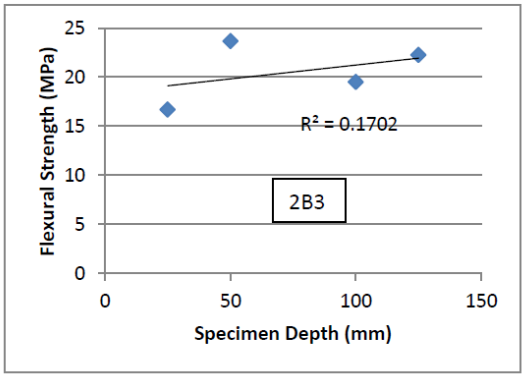

APPENDIX 9(b): Un-notched Three Point Bending test flexural strength against specimen depth (4%)

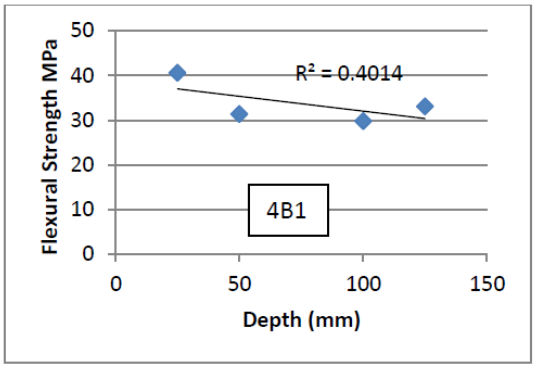

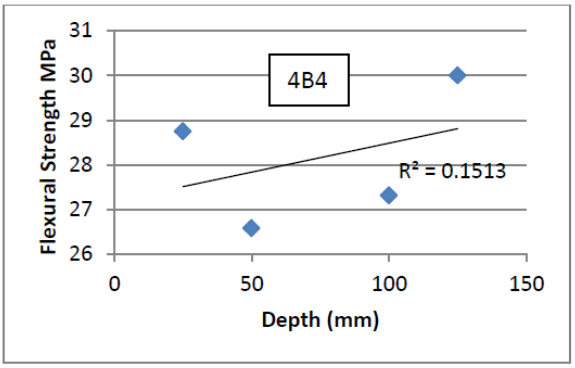

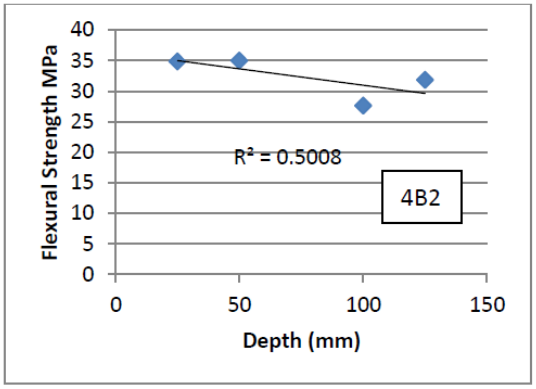

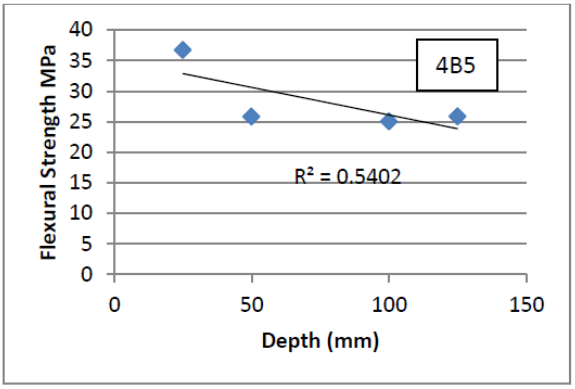

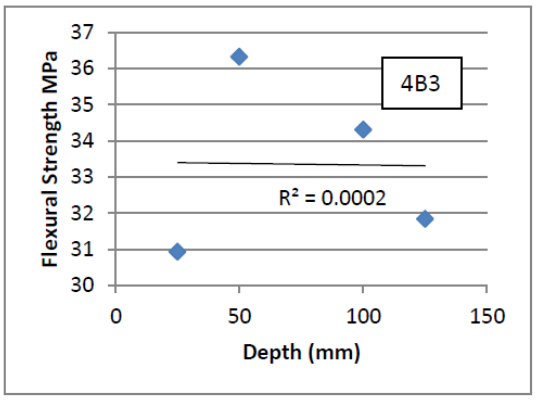

APPENDIX 9(c): Un-notched Three Point Bending test flexural strength against specimen depth (6%)

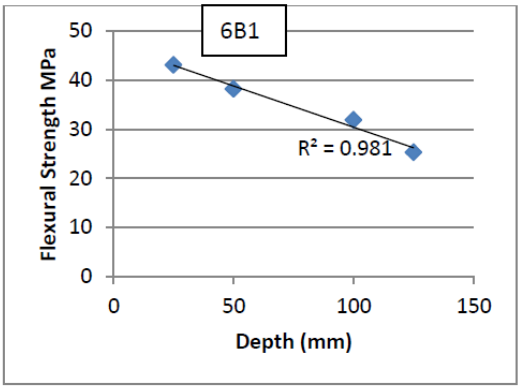

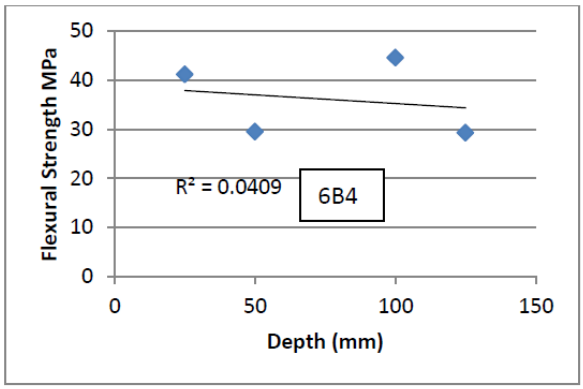

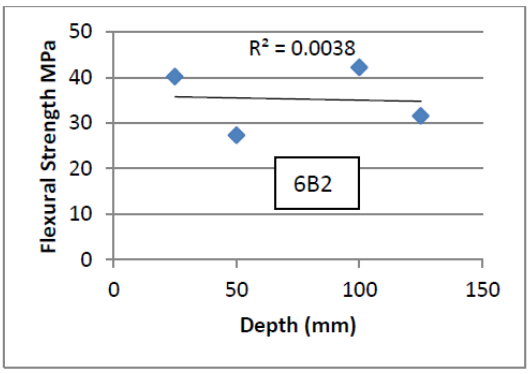

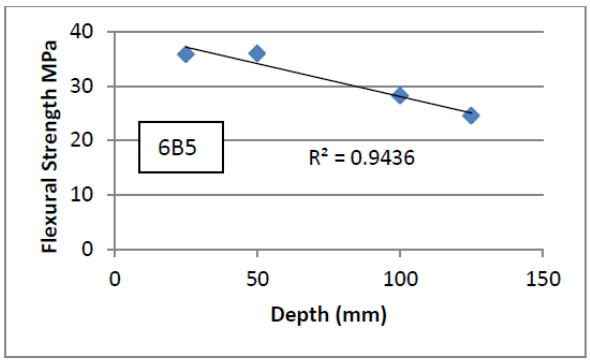

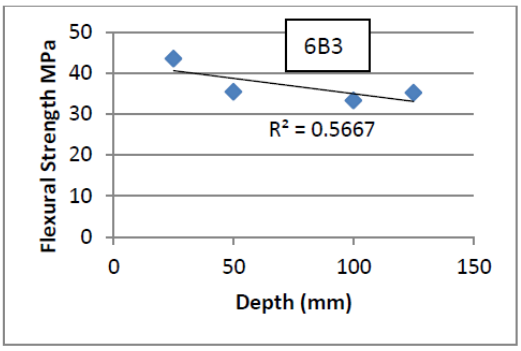

APPENDIX 9(d): Un-notched Three Point Bending test avg. flexural strength against specimen depth

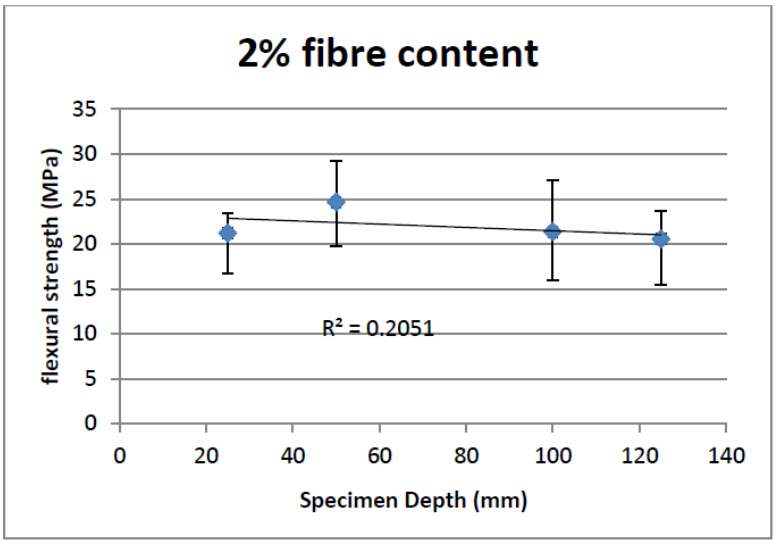

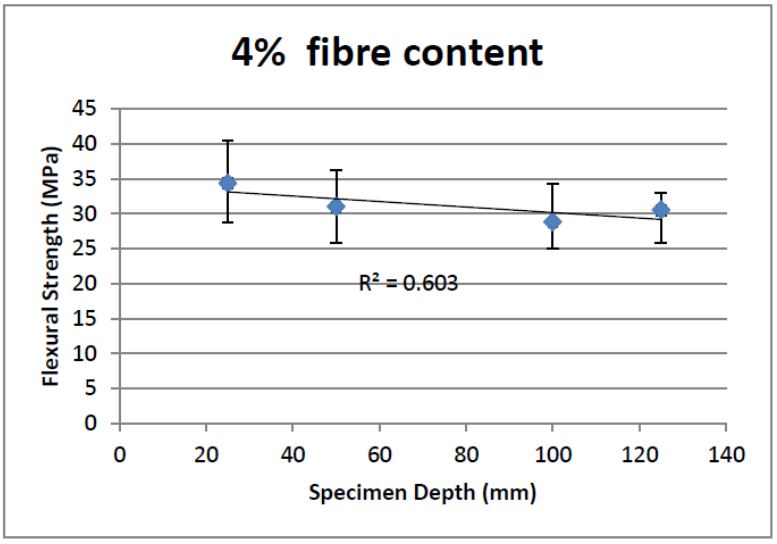

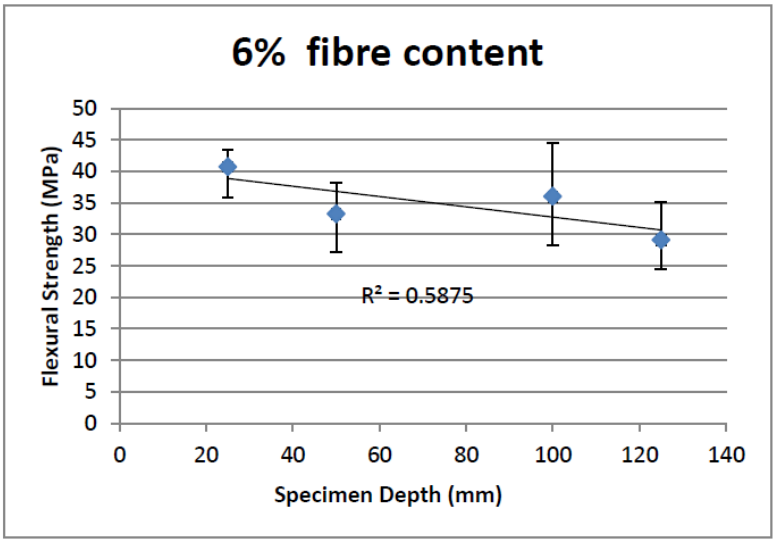

APPENDIX 10(a): Notched Three Point Bending test flexural strength against specimen depth (2%)

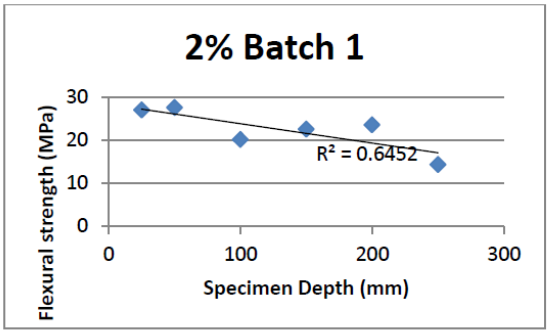

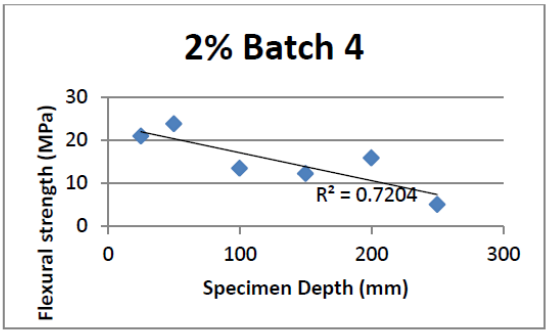

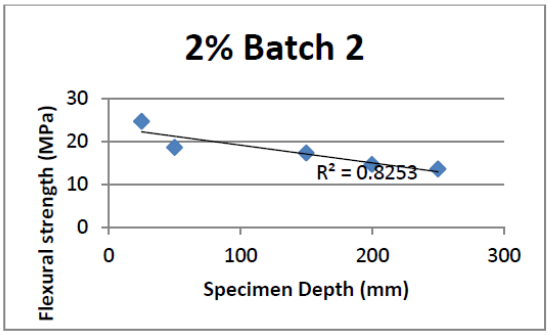

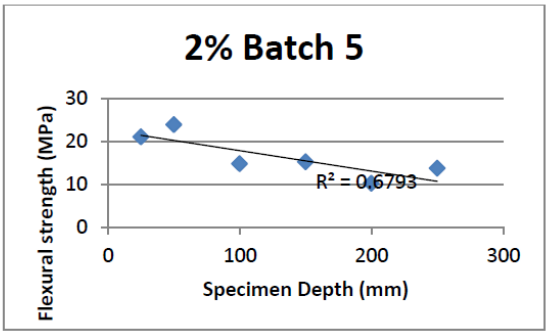

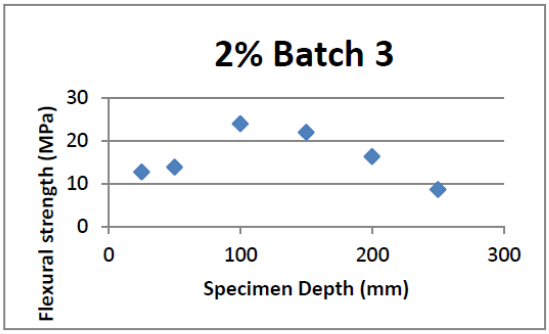

APPENDIX 10(b): Notched Three Point Bending test flexural strength against specimen depth (4%)

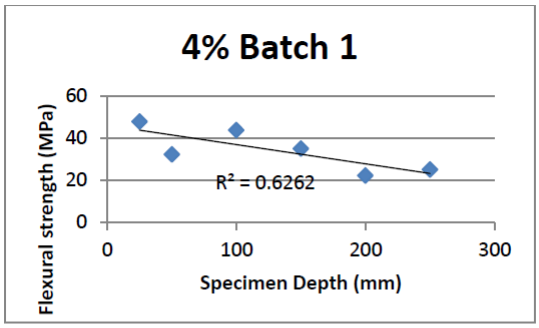

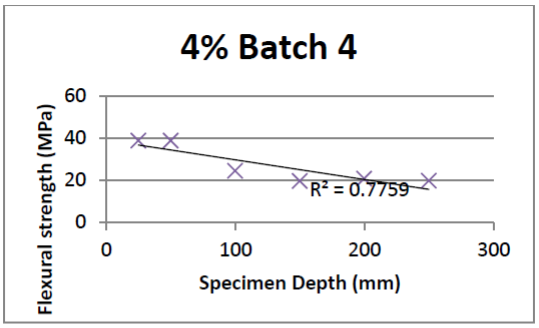

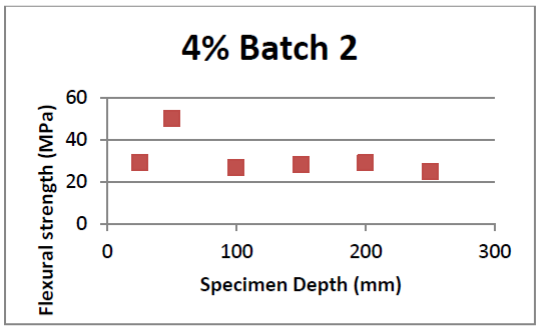

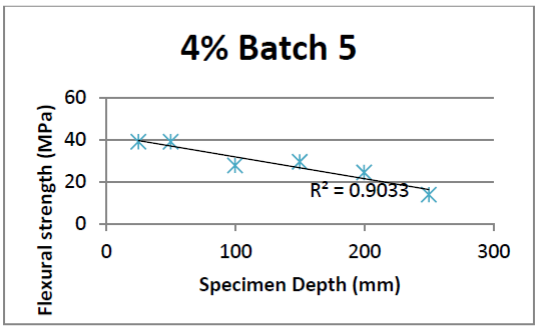

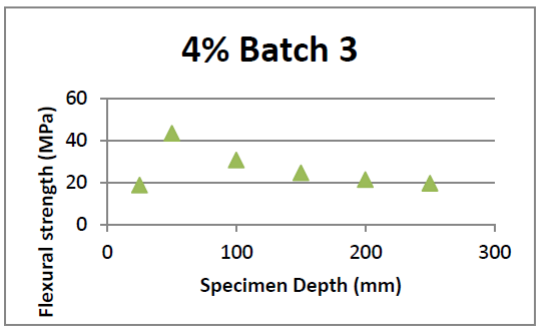

APPENDIX 10(c): Notched Three Point Bending test flexural strength against specimen depth (6%)

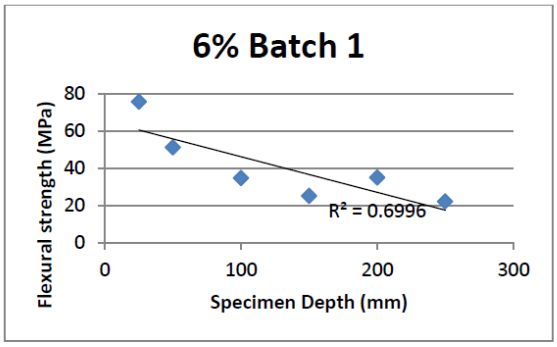

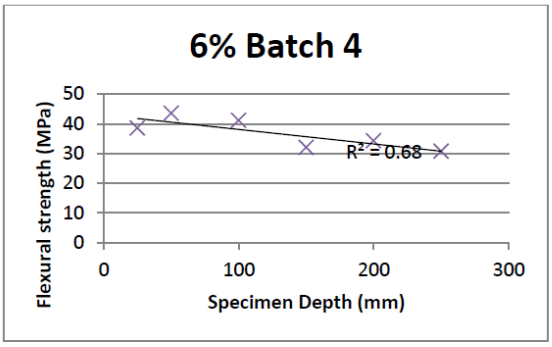

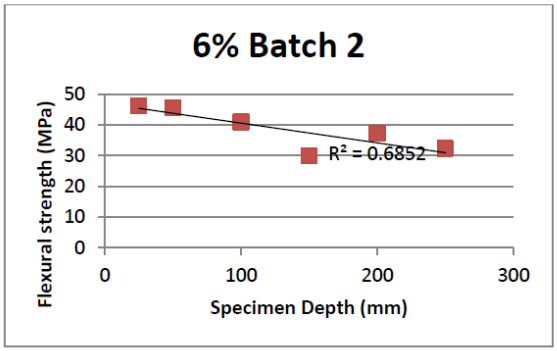

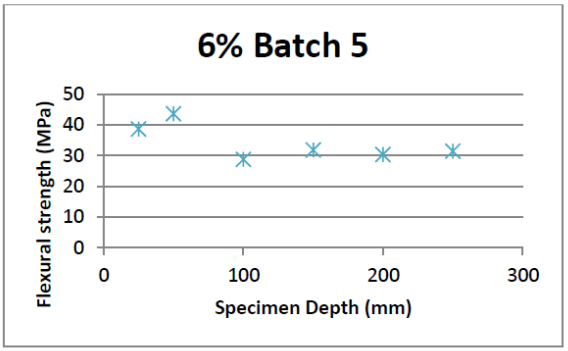

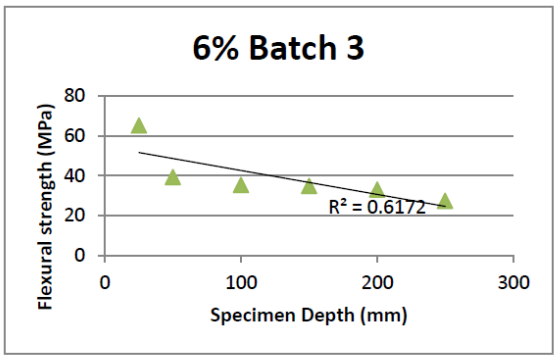

APPENDIX 10(d): Notched Three Point Bending test avg. flexural strength against specimen depth

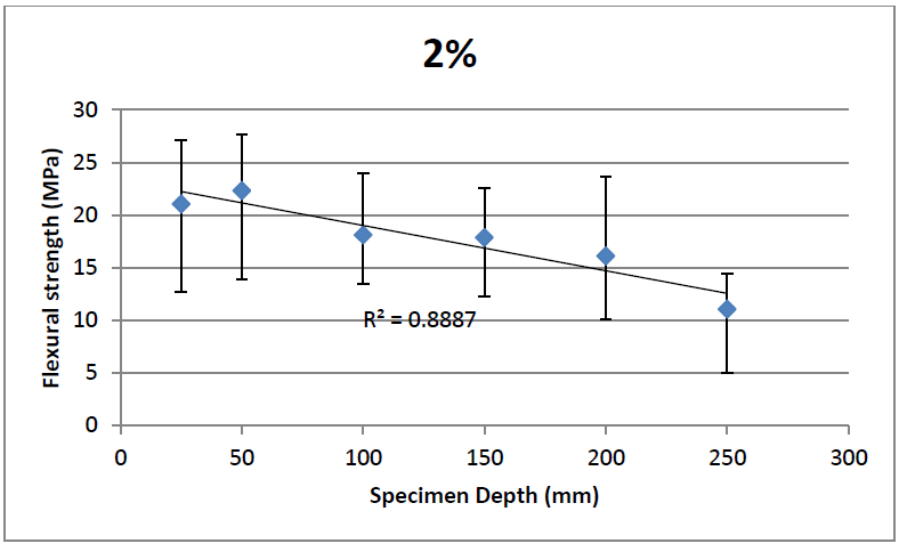

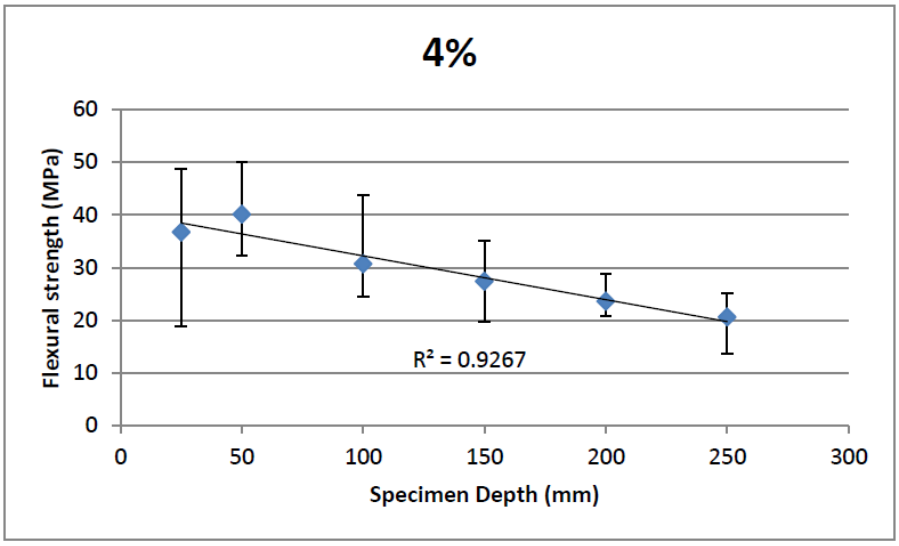

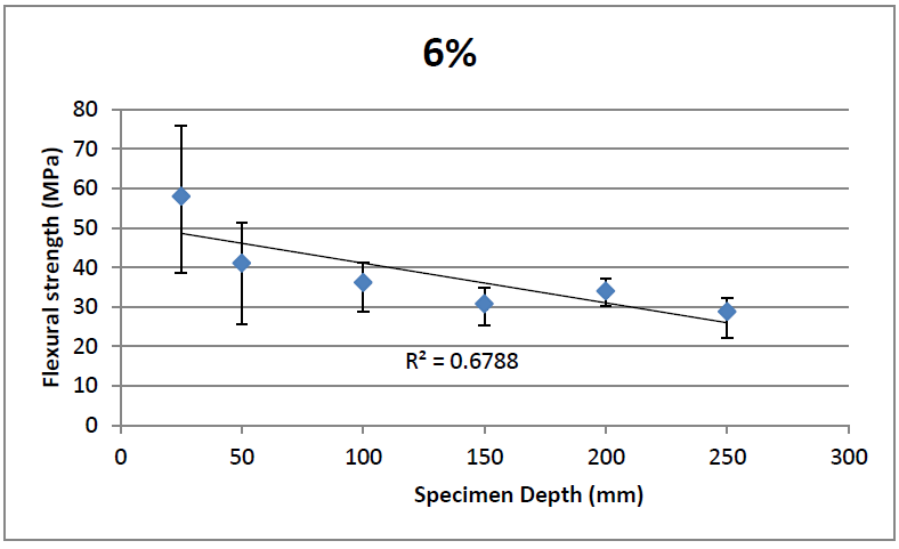

APPENDIX 11: Deriving the damage scale (D)

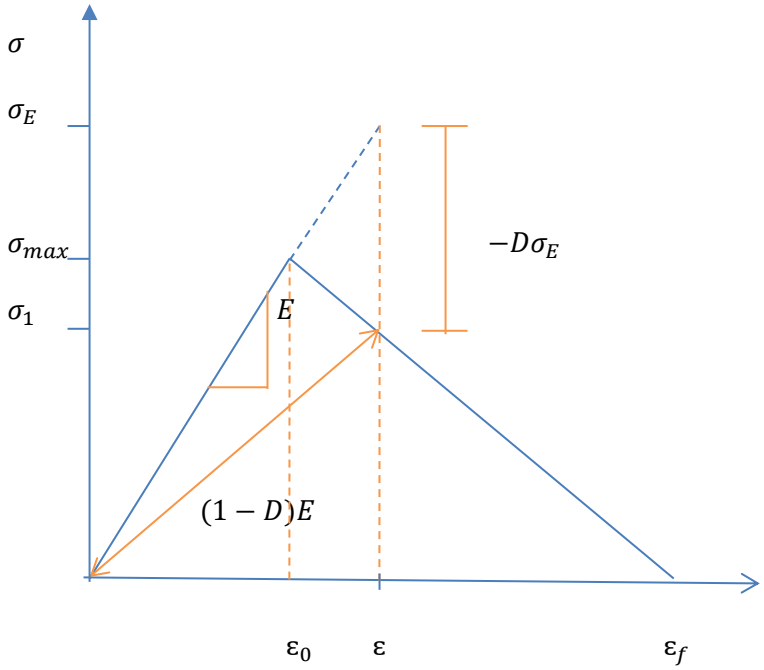

Typical damaged response

$$\sigma_{max} = E * \varepsilon_0$$

$$\sigma_1 = (1 - D) * E * \varepsilon$$

$$\frac{E * \varepsilon_0}{(\varepsilon_f - \varepsilon_0)} = \frac{(1 - D) * E * \varepsilon}{(\varepsilon_f - \varepsilon)}$$

$$(\varepsilon_f - \varepsilon) * \cancel{E} * \varepsilon_0 = (1 - D) * \cancel{E} * \varepsilon * (\varepsilon_f - \varepsilon_0)$$

$$\varepsilon_0 * \varepsilon_f - \varepsilon_0 * \varepsilon = (1 - D)(\varepsilon_f * \varepsilon - \varepsilon_0 * \varepsilon)$$

$$\varepsilon_0 * \varepsilon_f - \varepsilon_0 * \varepsilon = \varepsilon_f * \varepsilon - \varepsilon_0 * \varepsilon - \varepsilon_f * \varepsilon * D + \varepsilon_0 * \varepsilon * D$$

$$\varepsilon_0 * \varepsilon_f - \varepsilon_0 * \varepsilon = \varepsilon_f * \varepsilon - \varepsilon_0 * \varepsilon - D * (\varepsilon_f * \varepsilon - \varepsilon_0 * \varepsilon)$$

$$\varepsilon_0 * (\varepsilon_f - \varepsilon) = \varepsilon(\varepsilon_f - \varepsilon_0) - \varepsilon(\varepsilon_f - \varepsilon_0) * D$$

$$\varepsilon(\varepsilon_f - \varepsilon_0) * D = \varepsilon(\varepsilon_f - \varepsilon_0) - \varepsilon_0 * (\varepsilon_f - \varepsilon)$$

$$\varepsilon(\varepsilon_f - \varepsilon_0) * D = \varepsilon * \varepsilon_f - \varepsilon_0 * \varepsilon - \varepsilon_0 * \varepsilon_f + \varepsilon_0 * \varepsilon$$

$$\varepsilon(\varepsilon_f - \varepsilon_0) * D = \varepsilon_f(\varepsilon - \varepsilon_0)$$

$$D = \frac{\varepsilon_f}{\varepsilon} * \frac{(\varepsilon - \varepsilon_0)}{(\varepsilon_f - \varepsilon_0)}$$

APPENDIX 12: Example of an input file for the un-notched FPB test (fibre content =1%) used in UDMF validation (CASE STUDY 2)

```
                        SCM-2DunnotchedFPB-D100-L350-fc1
*Heading
** Job name: SCM-2DunnotchedFPB-D100-L350-fc1 Model name: Model-1
** Generated by: Abaqus/CAE 6.13-3
*Preprint, echo=NO, model=NO, history=NO, contact=NO
**
** PARTS
**
*Part, name=Part-1
*End Part
**
**
** ASSEMBLY
**
*Assembly, name=Assembly
**
*Instance, name=Part-1-1, part=Part-1
*Node
      1,           50.,           0.
      2,         37.5,            0.
      3,          25.,            0.
      4,         12.5,            0.
      5,           0.,            0.
      6,        -12.5,            0.
      7,         -25.,            0.
      8,        -37.5,            0.
      9,         -50.,            0.
     10,        -62.5,            0.
     11,         -75.,            0.
     12,        -87.5,            0.
     13,        -100.,            0.
     14,       -112.5,            0.
     15,        -125.,            0.
     16,       -137.5,            0.
     17,        -150.,            0.
     18,       -162.5,            0.
     19,        -175.,            0.
     20,       -187.5,            0.
     21,        -200.,            0.
     22,       -212.5,            0.
     23,        -225.,            0.
     24,       -237.5,            0.
     25,        -250.,            0.
     26,       -262.5,            0.
     27,        -275.,            0.
     28,       -287.5,            0.
     29,        -300.,            0.
     30,          50.,         -12.5
     31,         37.5,         -12.5
     32,          25.,         -12.5
     33,         12.5,         -12.5
     34,           0.,         -12.5
     35,        -12.5,         -12.5
     36,         -25.,         -12.5
     37,        -37.5,         -12.5
     38,         -50.,         -12.5
     39,        -62.5,         -12.5
     40,         -75.,         -12.5
     41,        -87.5,         -12.5
     42,        -100.,         -12.5
     43,       -112.5,         -12.5
     44,        -125.,         -12.5
     45,       -137.5,         -12.5
     46,        -150.,         -12.5
     47,       -162.5,         -12.5
     48,        -175.,         -12.5
     49,       -187.5,         -12.5
     50,        -200.,         -12.5
     51,       -212.5,         -12.5
```

52,	-225.,	-12.5
53,	-237.5,	-12.5
54,	-250.,	-12.5
55,	-262.5,	-12.5
56,	-275.,	-12.5
57,	-287.5,	-12.5
58,	-300.,	-12.5
59,	50.,	-25.
60,	37.5,	-25.
61,	25.,	-25.
62,	12.5,	-25.
63,	0.,	-25.
64,	-12.5,	-25.
65,	-25.,	-25.
66,	-37.5,	-25.
67,	-50.,	-25.
68,	-62.5,	-25.
69,	-75.,	-25.
70,	-87.5,	-25.
71,	-100.,	-25.
72,	-112.5,	-25.
73,	-125.,	-25.
74,	-137.5,	-25.
75,	-150.,	-25.
76,	-162.5,	-25.
77,	-175.,	-25.
78,	-187.5,	-25.
79,	-200.,	-25.
80,	-212.5,	-25.
81,	-225.,	-25.
82,	-237.5,	-25.
83,	-250.,	-25.
84,	-262.5,	-25.
85,	-275.,	-25.
86,	-287.5,	-25.
87,	-300.,	-25.
88,	50.,	-37.5
89,	37.5,	-37.5
90,	25.,	-37.5
91,	12.5,	-37.5
92,	0.,	-37.5
93,	-12.5,	-37.5
94,	-25.,	-37.5
95,	-37.5,	-37.5
96,	-50.,	-37.5
97,	-62.5,	-37.5
98,	-75.,	-37.5
99,	-87.5,	-37.5
100,	-100.,	-37.5
101,	-112.5,	-37.5
102,	-125.,	-37.5
103,	-137.5,	-37.5
104,	-150.,	-37.5
105,	-162.5,	-37.5
106,	-175.,	-37.5
107,	-187.5,	-37.5
108,	-200.,	-37.5
109,	-212.5,	-37.5
110,	-225.,	-37.5
111,	-237.5,	-37.5
112,	-250.,	-37.5
113,	-262.5,	-37.5
114,	-275.,	-37.5
115,	-287.5,	-37.5
116,	-300.,	-37.5
117,	50.,	-50.
118,	37.5,	-50.
119,	25.,	-50.

```
120,         12.5,         -50.
121,           0.,         -50.
122,        -12.5,         -50.
123,         -25.,         -50.
124,        -37.5,         -50.
125,         -50.,         -50.
126,        -62.5,         -50.
127,         -75.,         -50.
128,        -87.5,         -50.
129,        -100.,         -50.
130,       -112.5,         -50.
131,        -125.,         -50.
132,       -137.5,         -50.
133,        -150.,         -50.
134,       -162.5,         -50.
135,        -175.,         -50.
136,       -187.5,         -50.
137,        -200.,         -50.
138,       -212.5,         -50.
139,        -225.,         -50.
140,       -237.5,         -50.
141,        -250.,         -50.
142,       -262.5,         -50.
143,        -275.,         -50.
144,       -287.5,         -50.
145,        -300.,         -50.
146,          50.,        -62.5
147,         37.5,        -62.5
148,          25.,        -62.5
149,         12.5,        -62.5
150,           0.,        -62.5
151,        -12.5,        -62.5
152,         -25.,        -62.5
153,        -37.5,        -62.5
154,         -50.,        -62.5
155,        -62.5,        -62.5
156,         -75.,        -62.5
157,        -87.5,        -62.5
158,        -100.,        -62.5
159,       -112.5,        -62.5
160,        -125.,        -62.5
161,       -137.5,        -62.5
162,        -150.,        -62.5
163,       -162.5,        -62.5
164,        -175.,        -62.5
165,       -187.5,        -62.5
166,        -200.,        -62.5
167,       -212.5,        -62.5
168,        -225.,        -62.5
169,       -237.5,        -62.5
170,        -250.,        -62.5
171,       -262.5,        -62.5
172,        -275.,        -62.5
173,       -287.5,        -62.5
174,        -300.,        -62.5
175,          50.,         -75.
176,         37.5,         -75.
177,          25.,         -75.
178,         12.5,         -75.
179,           0.,         -75.
180,        -12.5,         -75.
181,         -25.,         -75.
182,        -37.5,         -75.
183,         -50.,         -75.
184,        -62.5,         -75.
185,         -75.,         -75.
186,        -87.5,         -75.
187,        -100.,         -75.
```

```
188,       -112.5,          -75.
189,        -125.,          -75.
190,       -137.5,          -75.
191,        -150.,          -75.
192,       -162.5,          -75.
193,        -175.,          -75.
194,       -187.5,          -75.
195,        -200.,          -75.
196,       -212.5,          -75.
197,        -225.,          -75.
198,       -237.5,          -75.
199,        -250.,          -75.
200,       -262.5,          -75.
201,        -275.,          -75.
202,       -287.5,          -75.
203,        -300.,          -75.
204,         50.,         -87.5
205,        37.5,         -87.5
206,         25.,         -87.5
207,        12.5,         -87.5
208,          0.,         -87.5
209,       -12.5,         -87.5
210,        -25.,         -87.5
211,       -37.5,         -87.5
212,        -50.,         -87.5
213,       -62.5,         -87.5
214,        -75.,         -87.5
215,       -87.5,         -87.5
216,        -100.,        -87.5
217,       -112.5,        -87.5
218,        -125.,        -87.5
219,       -137.5,        -87.5
220,        -150.,        -87.5
221,       -162.5,        -87.5
222,        -175.,        -87.5
223,       -187.5,        -87.5
224,        -200.,        -87.5
225,       -212.5,        -87.5
226,        -225.,        -87.5
227,       -237.5,        -87.5
228,        -250.,        -87.5
229,       -262.5,        -87.5
230,        -275.,        -87.5
231,       -287.5,        -87.5
232,        -300.,        -87.5
233,         50.,         -100.
234,        37.5,         -100.
235,         25.,         -100.
236,        12.5,         -100.
237,          0.,         -100.
238,       -12.5,         -100.
239,        -25.,         -100.
240,       -37.5,         -100.
241,        -50.,         -100.
242,       -62.5,         -100.
243,        -75.,         -100.
244,       -87.5,         -100.
245,        -100.,        -100.
246,       -112.5,        -100.
247,        -125.,        -100.
248,       -137.5,        -100.
249,        -150.,        -100.
250,       -162.5,        -100.
251,        -175.,        -100.
252,       -187.5,        -100.
253,        -200.,        -100.
254,       -212.5,        -100.
255,        -225.,        -100.
```

```
    256,        -237.5,         -100.
    257,         -250.,         -100.
    258,        -262.5,         -100.
    259,         -275.,         -100.
    260,        -287.5,         -100.
    261,         -300.,         -100.
*Element, type=CPE4I
  1,   1,   2,  31,  30
  2,   2,   3,  32,  31
  3,   3,   4,  33,  32
  4,   4,   5,  34,  33
  5,   5,   6,  35,  34
  6,   6,   7,  36,  35
  7,   7,   8,  37,  36
  8,   8,   9,  38,  37
  9,   9,  10,  39,  38
 10,  10,  11,  40,  39
 11,  11,  12,  41,  40
 12,  12,  13,  42,  41
 13,  13,  14,  43,  42
 14,  14,  15,  44,  43
 15,  15,  16,  45,  44
 16,  16,  17,  46,  45
 17,  17,  18,  47,  46
 18,  18,  19,  48,  47
 19,  19,  20,  49,  48
 20,  20,  21,  50,  49
 21,  21,  22,  51,  50
 22,  22,  23,  52,  51
 23,  23,  24,  53,  52
 24,  24,  25,  54,  53
 25,  25,  26,  55,  54
 26,  26,  27,  56,  55
 27,  27,  28,  57,  56
 28,  28,  29,  58,  57
 29,  30,  31,  60,  59
 30,  31,  32,  61,  60
 31,  32,  33,  62,  61
 32,  33,  34,  63,  62
 33,  34,  35,  64,  63
 34,  35,  36,  65,  64
 35,  36,  37,  66,  65
 36,  37,  38,  67,  66
 37,  38,  39,  68,  67
 38,  39,  40,  69,  68
 39,  40,  41,  70,  69
 40,  41,  42,  71,  70
 41,  42,  43,  72,  71
 42,  43,  44,  73,  72
 43,  44,  45,  74,  73
 44,  45,  46,  75,  74
 45,  46,  47,  76,  75
 46,  47,  48,  77,  76
 47,  48,  49,  78,  77
 48,  49,  50,  79,  78
 49,  50,  51,  80,  79
 50,  51,  52,  81,  80
 51,  52,  53,  82,  81
 52,  53,  54,  83,  82
 53,  54,  55,  84,  83
 54,  55,  56,  85,  84
 55,  56,  57,  86,  85
 56,  57,  58,  87,  86
 57,  59,  60,  89,  88
 58,  60,  61,  90,  89
 59,  61,  62,  91,  90
 60,  62,  63,  92,  91
 61,  63,  64,  93,  92
```

```
 62,  64,  65,  94,  93
 63,  65,  66,  95,  94
 64,  66,  67,  96,  95
 65,  67,  68,  97,  96
 66,  68,  69,  98,  97
 67,  69,  70,  99,  98
 68,  70,  71, 100,  99
 69,  71,  72, 101, 100
 70,  72,  73, 102, 101
 71,  73,  74, 103, 102
 72,  74,  75, 104, 103
 73,  75,  76, 105, 104
 74,  76,  77, 106, 105
 75,  77,  78, 107, 106
 76,  78,  79, 108, 107
 77,  79,  80, 109, 108
 78,  80,  81, 110, 109
 79,  81,  82, 111, 110
 80,  82,  83, 112, 111
 81,  83,  84, 113, 112
 82,  84,  85, 114, 113
 83,  85,  86, 115, 114
 84,  86,  87, 116, 115
 85,  88,  89, 118, 117
 86,  89,  90, 119, 118
 87,  90,  91, 120, 119
 88,  91,  92, 121, 120
 89,  92,  93, 122, 121
 90,  93,  94, 123, 122
 91,  94,  95, 124, 123
 92,  95,  96, 125, 124
 93,  96,  97, 126, 125
 94,  97,  98, 127, 126
 95,  98,  99, 128, 127
 96,  99, 100, 129, 128
 97, 100, 101, 130, 129
 98, 101, 102, 131, 130
 99, 102, 103, 132, 131
100, 103, 104, 133, 132
101, 104, 105, 134, 133
102, 105, 106, 135, 134
103, 106, 107, 136, 135
104, 107, 108, 137, 136
105, 108, 109, 138, 137
106, 109, 110, 139, 138
107, 110, 111, 140, 139
108, 111, 112, 141, 140
109, 112, 113, 142, 141
110, 113, 114, 143, 142
111, 114, 115, 144, 143
112, 115, 116, 145, 144
113, 117, 118, 147, 146
114, 118, 119, 148, 147
115, 119, 120, 149, 148
116, 120, 121, 150, 149
117, 121, 122, 151, 150
118, 122, 123, 152, 151
119, 123, 124, 153, 152
120, 124, 125, 154, 153
121, 125, 126, 155, 154
122, 126, 127, 156, 155
123, 127, 128, 157, 156
124, 128, 129, 158, 157
125, 129, 130, 159, 158
126, 130, 131, 160, 159
127, 131, 132, 161, 160
128, 132, 133, 162, 161
129, 133, 134, 163, 162
```

130, 134, 135, 164, 163
131, 135, 136, 165, 164
132, 136, 137, 166, 165
133, 137, 138, 167, 166
134, 138, 139, 168, 167
135, 139, 140, 169, 168
136, 140, 141, 170, 169
137, 141, 142, 171, 170
138, 142, 143, 172, 171
139, 143, 144, 173, 172
140, 144, 145, 174, 173
141, 146, 147, 176, 175
142, 147, 148, 177, 176
143, 148, 149, 178, 177
144, 149, 150, 179, 178
145, 150, 151, 180, 179
146, 151, 152, 181, 180
147, 152, 153, 182, 181
148, 153, 154, 183, 182
149, 154, 155, 184, 183
150, 155, 156, 185, 184
151, 156, 157, 186, 185
152, 157, 158, 187, 186
153, 158, 159, 188, 187
154, 159, 160, 189, 188
155, 160, 161, 190, 189
156, 161, 162, 191, 190
157, 162, 163, 192, 191
158, 163, 164, 193, 192
159, 164, 165, 194, 193
160, 165, 166, 195, 194
161, 166, 167, 196, 195
162, 167, 168, 197, 196
163, 168, 169, 198, 197
164, 169, 170, 199, 198
165, 170, 171, 200, 199
166, 171, 172, 201, 200
167, 172, 173, 202, 201
168, 173, 174, 203, 202
169, 175, 176, 205, 204
170, 176, 177, 206, 205
171, 177, 178, 207, 206
172, 178, 179, 208, 207
173, 179, 180, 209, 208
174, 180, 181, 210, 209
175, 181, 182, 211, 210
176, 182, 183, 212, 211
177, 183, 184, 213, 212
178, 184, 185, 214, 213
179, 185, 186, 215, 214
180, 186, 187, 216, 215
181, 187, 188, 217, 216
182, 188, 189, 218, 217
183, 189, 190, 219, 218
184, 190, 191, 220, 219
185, 191, 192, 221, 220
186, 192, 193, 222, 221
187, 193, 194, 223, 222
188, 194, 195, 224, 223
189, 195, 196, 225, 224
190, 196, 197, 226, 225
191, 197, 198, 227, 226
192, 198, 199, 228, 227
193, 199, 200, 229, 228
194, 200, 201, 230, 229
195, 201, 202, 231, 230
196, 202, 203, 232, 231
197, 204, 205, 234, 233

```
198, 205, 206, 235, 234
199, 206, 207, 236, 235
200, 207, 208, 237, 236
201, 208, 209, 238, 237
202, 209, 210, 239, 238
203, 210, 211, 240, 239
204, 211, 212, 241, 240
205, 212, 213, 242, 241
206, 213, 214, 243, 242
207, 214, 215, 244, 243
208, 215, 216, 245, 244
209, 216, 217, 246, 245
210, 217, 218, 247, 246
211, 218, 219, 248, 247
212, 219, 220, 249, 248
213, 220, 221, 250, 249
214, 221, 222, 251, 250
215, 222, 223, 252, 251
216, 223, 224, 253, 252
217, 224, 225, 254, 253
218, 225, 226, 255, 254
219, 226, 227, 256, 255
220, 227, 228, 257, 256
221, 228, 229, 258, 257
222, 229, 230, 259, 258
223, 230, 231, 260, 259
224, 231, 232, 261, 260
*Nset, nset=Set-2, generate
   1,  261,    1
*Elset, elset=Set-2, generate
   1,  224,    1
** Section: Section-1
*Solid Section, elset=Set-2, material=Material-1
,
*End Instance
**
*Nset, nset=LHSMidTop, instance=Part-1-1
 19,
*Nset, nset=LHSupport, instance=Part-1-1
 259,
*Nset, nset=RHSMidTop, instance=Part-1-1
 11,
*Nset, nset=RHSupport, instance=Part-1-1
 235,
*End Assembly
**
** MATERIALS
**
*Material, name=Material-1
*Depvar
     12,
*User Material, constants=3
1.,   0.2, 0.001
**
** BOUNDARY CONDITIONS
**
** Name: LHSupport Type: Displacement/Rotation
*Boundary
LHSupport, 1, 1
LHSupport, 2, 2
** Name: RHSupport Type: Displacement/Rotation
*Boundary
RHSupport, 2, 2
** ----------------------------------------------------------------
**
** STEP: Step-1
**
*Step, name=Step-1, nlgeom=NO, inc=8000
```

```
*Static
0.01, 1., 1e-12, 1.
**
** BOUNDARY CONDITIONS
**
** Name: LHSMidTopDisp Type: Displacement/Rotation
*Boundary
LHSMidTop, 2, 2, -1.8
** Name: RHSMidTopDisp Type: Displacement/Rotation
*Boundary
RHSMidTop, 2, 2, -1.8
**
** OUTPUT REQUESTS
**
*Restart, write, frequency=0
**
** FIELD OUTPUT: F-Output-1
**
*Output, field, variable=PRESELECT
**
** HISTORY OUTPUT: LHSMidTopRF2
**
*Output, history
*Node Output, nset=LHSMidTop
RF2,
**
** HISTORY OUTPUT: LHSMidTopDisp
**
*Node Output, nset=LHSMidTop
U2,
**
** HISTORY OUTPUT: LHSReaction
**
*Node Output, nset=LHSupport
RF2,
*End Step
```

University of Portsmouth

Certificate of Ethics Review

Project Title:	Modelling the behaviour of ultra high performance fibre reinforced concrete
User ID:	489433
Name:	kenneth odero awinda
Application Date:	09/03/2015 15:17:30

You must download your referral certificate, print a copy and keep it as a record of this review.

The FEC representatives for the School of Civil Engineering & Surveying are Tim Whitehead and John Williams

It is your responsibility to follow the University Code of Practice on Ethical Standards and any Department/School or professional guidelines in the conduct of your study including relevant guidelines regarding health and safety of researchers including the following:

- University Policy
- Safety on Geological Fieldwork

It is also your responsibility to follow University guidance on Data Protection Policy:

- General guidance for all data protection issues
- University Data Protection Policy

SchoolOrDepartment: SCES
PrimaryRole: Other
SupervisorName: Dr Jiye Chen
HumanParticipants: No
PhysicalEcologicalDamage: No
HistoricalOrCulturalDamage: No
HarmToAnimal: No
HarmfulToThirdParties: No
OutputsPotentiallyAdaptedAndMisused: No
Confirmation-ConsideredDataUse: Confirmed
Confirmation-ConsideredImpactAndMitigationOfPontentialMisuse: Confirmed
Confirmation-ActingEthicallyAndHonestly: Confirmed

Certificate Code: 6CC9-CFE5-F0D0-5A13-16BF-48BB-939A-0E2E Page 1

Supervisor Review

As supervisor, I will ensure that this work will be conducted in an ethical manner in line with the University Ethics Policy.

Supervisor signature:

Date: 26/01/2015

FORM UPR16

Research Ethics Review Checklist

University of Portsmouth

Please include this completed form as an appendix to your thesis (see the Postgraduate Research Student Handbook for more information

Postgraduate Research Student (PGRS) Information				**Student ID:**	489433
PGRS Name:	Kenneth Odero Awinda				
Department:	School of Civil Engineering & Surveying	**First Supervisor:**	Dr Jiye Chen		
Start Date: (or progression date for Prof Doc students)	**February 2012**				
Study Mode and Route:	Part-time ☒	MPhil ☐	MD ☐		
	Full-time ☐	PhD ☐	Professional Doctorate ☐		

Title of Thesis:	Modelling the behaviour of Ultra High Performance Fibre Reinforced Concrete
Thesis Word Count: (excluding ancillary data)	52754

If you are unsure about any of the following, please contact the local representative on your Faculty Ethics Committee for advice. Please note that it is your responsibility to follow the University's Ethics Policy and any relevant University, academic or professional guidelines in the conduct of your study

Although the Ethics Committee may have given your study a favourable opinion, the final responsibility for the ethical conduct of this work lies with the researcher(s).

UKRIO Finished Research Checklist:
(If you would like to know more about the checklist, please see your Faculty or Departmental Ethics Committee rep or see the online version of the full checklist at: http://www.ukrio.org/what-we-do/code-of-practice-for-research/)

a) Have all of your research and findings been reported accurately, honestly and within a reasonable time frame?	YES ☒ NO ☐
b) Have all contributions to knowledge been acknowledged?	YES ☒ NO ☐
c) Have you complied with all agreements relating to intellectual property, publication and authorship?	YES ☒ NO ☐
d) Has your research data been retained in a secure and accessible form and will it remain so for the required duration?	YES ☒ NO ☐
e) Does your research comply with all legal, ethical, and contractual requirements?	YES ☒ NO ☐

Candidate Statement:

I have considered the ethical dimensions of the above named research project, and have successfully obtained the necessary ethical approval(s)

Ethical review number(s) from Faculty Ethics Committee (or from NRES/SCREC):	6CC9-CFE5-F0D0-5A13-16BF-48BB-939A-0E2E

If you have *not* submitted your work for ethical review, and/or you have answered 'No' to one or more of questions a) to e), please explain below why this is so:

Signed *(PGRS)*:	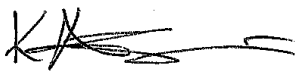	**Date:** 26/01/18